

Alma Mater Studiorum – Università di Bologna

DOTTORATO DI RICERCA IN

GEOFISICA

Ciclo 34

Settore Concorsuale: 04/A4 - GEOFISICA

Settore Scientifico Disciplinare: GEO/10 – GEOFISICA DELLA TERRA SOLIDA

**Seismotectonic study on two
strategic infrastructures in Southern Italy**

Presentata da: Giulia Alessandrini

Coordinatore Dottorato

Nadia Pinardi

Supervisore

Silvia Castellaro

Esame finale anno 2022

ABSTRACT

With the entry into force of the latest Italian Building Code (NTC 2008, 2018), innovative criteria were provided, especially for what concerns the seismic verifications of large infrastructures. In particular, for buildings considered as strategic, such as large dams, a seismotectonic study of the site was declared necessary, which involves a re-assessment of the basic seismic hazard. This PhD project fits into this context, being part of the seismic re-evaluation process of large dams launched on a national scale following the O.P.C.M. 3274/2003, D.L. 79/2004. A full seismotectonic study in the region of two large earth dams in Southern Italy was carried out. Being seismotectonics the study of the relationship between seismicity, active tectonics and individual faults of an area, we identified and characterized the structures that could generate earthquakes in our study area, together with the definition of the local seismic history. This information was used for the reassessment of the basic seismic hazard, defining the expected maximum accelerations expected in free field conditions at bedrock, using probabilistic seismic hazard assessment approaches. We tested different combinations in terms of subdivision into seismic zones and attenuation laws, in order to arrive to an estimate that could take into account the various uncertainties. In recent years, fault-based models for the seismic hazard assessment have been proposed all over the world as a new emerging methodology. For this reason, we decided to test the innovative SHERIFS approach on our study area. Four different fault-based seismicity rates were obtained, based on four different fault and multi-fault rupture scenarios, which were then compared with the seismicity rates from the historical and instrumental regional catalogs. The occasion of the seismotectonic study gave also the opportunity to focus on the characteristics of the seismic stations that provided the data for the study itself. In the context of the work presented here, we focused on the 10 stations that had been active for the longest time and we carried out a geophysical characterization, the data of which merged into a more general study on the soil-structure interaction at seismic stations and on the ways in which it could affect the SHA. Lastly, an additional experimental study on the two dams and their associated minor structures is also presented, aimed at defining their main dynamic parameters, useful for subsequent dynamic structural and geotechnical studies.

Contents

1.	INTRODUCTION.....	6
2.	SEISMOTECTONIC SETTING.....	8
2.1	Geological setting	8
2.2	Seismic history	10
2.2.1	Macroseismic intensities at locations close to the area of interest	15
2.3	Structural setting.....	21
2.3.1	Focus on active and capable faults.....	24
3.	PROBABILISTIC SEISMIC HAZARD ANALYSIS	27
3.1	Seismotectonic probabilism (or standard) approach.....	27
3.1.1	Earthquake catalog.....	28
3.1.2	Identification and characterization of seismogenic sources	31
3.1.3	Seismicity rates and maximum expected magnitude.....	35
3.1.4	Ground Motion Models (GMMs).....	39
3.1.5	Discussion of the uncertainties	40
3.1.5.1	San Pietro sull’Osento dam	41
3.1.5.2	Marana Capacciotti dam.....	42
3.1.6	Seismic hazard results.....	43
3.1.6.1	San Pietro sull’Osento dam	44
3.1.6.2	Marana Capacciotti dam.....	49
3.2	Fault-based approach.....	53
3.2.1	SHERIFS approach	54
3.2.2	Case study: the Irpinia region.....	54
3.2.3	Model performance and final remarks	56
4.	SEISMIC STATIONS AND SEISMIC HAZARD.....	59
4.1	Seismic soil classification	59
4.1.1	Surveyed seismic stations.....	62
4.2	Soil-structure interaction	63
5.	ADDITIONAL SURVEYS	65
5.1	San Pietro sull’Osento dam	66
5.1.1	Existent surveys	66

5.1.2	New surveys.....	69
5.1.2.1	Ground – Left bank	69
5.1.2.2	Ground - Right bank	74
5.1.2.3	Embankment	76
5.1.2.4	Dam	78
5.1.2.5	Access bridge to the well	79
5.1.2.6	Well.....	80
5.1.2.7	Accelerograms for SSR (Site Seismic Response) studies referring to stiff ground ..	81
5.2	Marana Capacciotti dam.....	88
5.2.1	Existent surveys	88
5.2.2	New surveys.....	88
5.2.2.1	Ground	88
5.2.2.2	Embankment	91
5.2.2.3	Dam	92
5.2.2.4	Accelerograms for SSR (Site Seismic Response) studies referring to stiff ground ..	93
6.	DELIVERABLES AND CONCLUSIONS.....	100
	REFERENCES.....	101
	APPENDIX A.....	112
	APPENDIX B	113
	APPENDIX C.....	114
	ADDITIONAL MATERIAL	115

1. INTRODUCTION

The Seismic Hazard Analysis (SHA), or Assessment, is a multidisciplinary subject, whose aim is to forecast the earthquake occurrence and to quantitatively estimate the ground shaking at a particular site. The results from SHA are typically used in the earthquake-resistant building design. The plan of critical facilities such as nuclear power plants, dams, pipelines, offshore platforms requires *ad hoc* geo-hazard studies that include SHA. The design of more standard constructions is also based on more general (usually nation-wide) SH studies. The specification of design ground motion parameters is a critical issue also in geotechnical earthquake engineering (Kramer, 1996; Gerstenberger *et al.*, 2020) and several attempts and progress have been done over the years.

It is possible to trace the evolution of SHA in a series of different methodological generations, which will be here briefly reviewed. An SHA may be carried out deterministically, as when a particular earthquake scenario is assumed, or probabilistically, where uncertainties in earthquake size, location and time of occurrence are explicitly considered. In the early years of earthquake engineering, the use of Deterministic Seismic Hazard Analysis (DSHA) was prevalent (Kramer, 1996). This approach involves the development of a particular earthquake scenario (magnitude and location) upon which a ground motion hazard evaluation is based. The approach is “deterministic”, since the scenario consists of the postulated occurrence of an earthquake of a specific size at a specific location (Reiter, 1991; Abrahamson, 2006).

When a Probabilistic Seismic Hazard Assessment (PSHA) approach is preferred, one needs a time-occurrence model for the earthquake occurrence. This can be modelled either as a time-dependent (e.g., Cornell & Winterstein, 1988; Pace *et al.*, 2006; Barani *et al.*, 2014) or a time-independent process (e.g., Gruppo di Lavoro MPS, 2004; Petersen *et al.*, 2007). Over the years, several earthquake prediction models have been proposed. In 1911 it was hypothesized that earthquakes followed a seismic cycle (Reid, 1911), that is a sequence of events affecting repeatedly the same fault or the same seismogenic area: from this concept, the “characteristic earthquake” model was conceived (Schwartz & Coppersmith, 1984). In the early ‘80s, two semideterministic models were proposed: the time-predictable (Shimazaki & Nakata, 1980) and the slip-predictable (Kiremidjian & Anagnos, 1984) models. The first one is supposed to predict the time interval that will separate a shock characterized by a certain stress drop value from the following shock; the slip-predictable model is supposed to predict the slip (hence, the magnitude) in relation to the time elapsed since the last earthquake. However, none of these models showed real applicability.

In the past 50-60 years the use of probabilistic concepts allowed uncertainties in the size, location and rate of recurrence of earthquakes and in the variation of ground motion characteristics with earthquake size and location to be explicitly considered in the evaluation of seismic hazards. PSHA is now commonly used to indicate a method to assess the ground-motion level expected with different likelihood at rocky or non-rocky site during a given period of time. In 1966 Allin Cornell, civil engineer who was studying probability distributions, met Luis Esteva, a PhD student dealing with earthquake ground motions and their dependence on magnitude and distance (McGuire, 2006,

2007). From the collaboration of these two researchers, the fundamental concepts of PSHA arose and its basic formulation was then published in 1968 (Cornell, 1968); a description of this approach is given in chapter 3.1. At present, the PSHA conceived by Cornell and Esteva still holds and over the years some other elements were added to the model, such as the logic tree method (Power *et al.*, 1981) to account for the epistemic uncertainty and the introduction of sensitivity and uncertainty analyses aimed at the identification of the input elements having the highest influence on the hazard and its uncertainty (Barani *et al.*, 2014). Despite some critical aspects of the model emerged (Mulargia *et al.*, 2017), PSHA is nowadays the only method officially adopted worldwide for hazard estimates addressed to seismic design (McGuire & Arabasz, 1990; Reiter, 1991; Abrahamson, 2006; McGuire, 2007; Baker, 2013). This applies, just to quote a few examples, to Eurocode 8 in Europe (CEN, 2003), to the National Earthquake Hazard Reduction Program in USA (BSSC, 2003), to the Norme Tecniche sulle Costruzioni (referred to hereafter as NTC) in Italy (NTC, 2008, 2018). In Italy, the provisions introduced with the NTC2008 and NTC2018 provided innovative criteria, in particular for the seismic safety verification of large facilities. For buildings deemed as strategic, such as large dams or nuclear power plants, they require specific seismotectonic studies, which involves a reassessment of the basic seismic hazard.

This PhD project fits into this context: we carried out a full seismotectonic study in the region of two large earth dams in Southern Italy, being seismotectonics a highly specialized sector of Earth Sciences that deals with the relationships between tectonics and seismicity of an area (Vannoli & Burrato, 2018). This study is part of the seismic re-evaluation process of large dams launched on a national scale following the O.P.C.M. 3274/2003, D.L. 79/2004, for which the Ministry of Infrastructure and Transportation, the Direzione Generale per le Dighe e le Infrastrutture Idriche ed Elettriche and the Istituto Nazionale di Geofisica e Vulcanologia provided specific guidelines named “*Linee-guida per la redazione e le istruttorie degli studi sismotettonici relativi alle grandi dighe*” (Basili *et al.*, 2007).

The first part of this thesis focuses on the definition of the local seismic history, with particular attention to the most destructive events reported in the historical and instrumental catalogs. The main tectonic setting and the main faulting systems have been also described (chapter 2). The second phase of this research focused on the reassessment of the basic seismic hazard, defining the expected maximum horizontal acceleration in free field conditions at bedrock, expected for the two sites, using the probabilistic approach, according to the requests of the Ministry of Infrastructure and Transport. The key points in defining the uncertainties associated with the assessment of the basic seismic hazard and the site by using the logical tree approach have been also analysed. Furthermore, during a research period spent at the University of Barcelona (29/03/21 – 29/07/21), it was possible to study and test a fault-based PSHA approach on this study area (chapter 3). We also present the geophysical characterization of ten seismic stations, in the frame of the bigger context of the seismic soil classification and the soil-structure interaction, discussing how these aspects could affect the SHA (chapter 4). Lastly, an additional experimental study on the two buildings and their associated minor structures is also presented, aimed at defining their main dynamic parameters (chapter 5).

2. SEISMOTECTONIC SETTING

The study area is centred around the hydraulic dams named Marana Capacciotti, (located in Bellaveduta, in the countryside of Cerignola, Foggia), and San Pietro sull'Oseinto (in the countryside of the municipalities of Monteverde and Aquilonia, Avellino), in southern Italy (Figure 1a). These facilities accumulate and distribute water in the Capitanata district (Figure 1b), a consortium that extends for about 450'000 hectares, within the province of Foggia. They are earth dams, typically larger than concrete ones; by their nature, they have a much more heterogeneous and complex structure, a further reason for a site-specific hazard study. In this chapter, we first present the geological setting of the study area; then, we show its seismic history and the structural setting that is responsible for such sequence of seismic events, and that in turn has been shaped by those events.

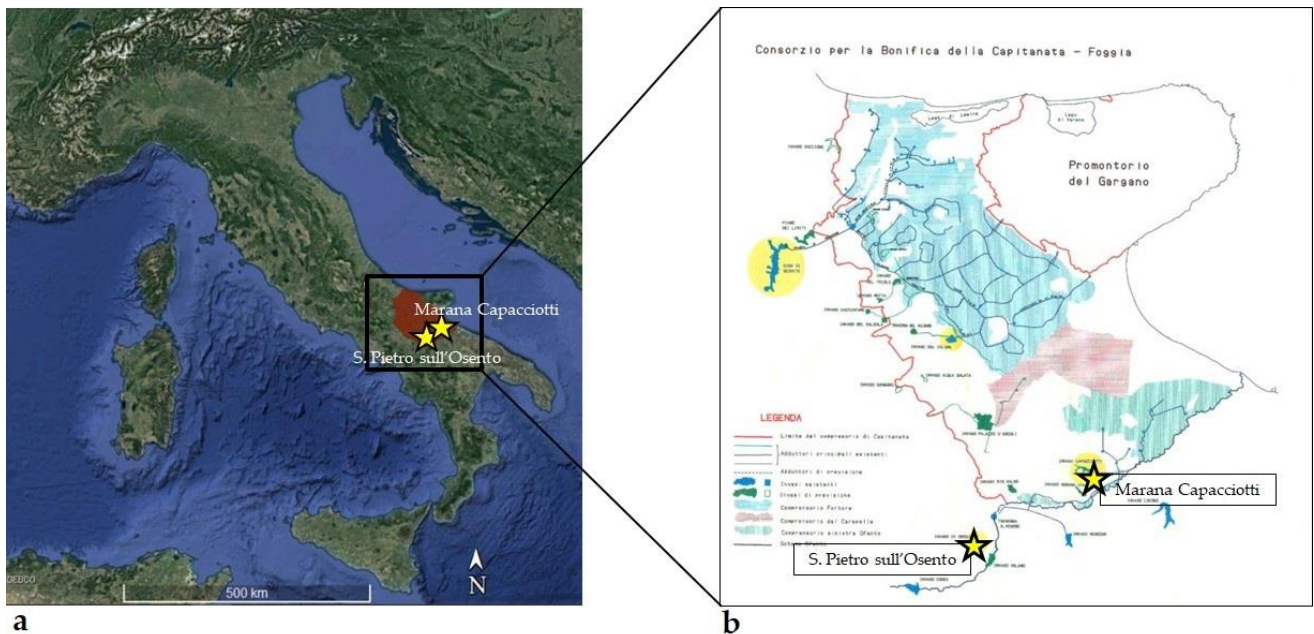


Figure 1. (a) Map of Italy. The study area is centred around two earth dams marked by the yellow stars; the red area indicates the 'Consorzio per la Bonifica della Capitanata'. (b) Zoom of the 'Consorzio per la Bonifica della Capitanata'.

2.1 Geological setting

The Italian geotectonics is the result of the collision between the northern Mesozoic margin of the African continental plate, to the South, which moved relatively against the European continental plate, located to the North. From this collision, the Alps and the Apennines originated; they are still rising nowadays and their external compressive fronts are active, involving increasingly external portions of foreland areas (Vannoli & Burrato, 2018). Our study area is located in the southern Apennines, an East-verging thrust belt related to the West-dipping subduction of the Apulian lithosphere (Doglioni *et al.*, 1996). The area where the two hydraulic facilities are located is characterized by the complex nature of the regional tectonics. From West to East (Figure 2), the

regional geology consist of: Sicilide Units, an oceanic domain capped by Miocene flysch, where the San Pietro sull'Osento dam is; a carbonate platform (Apenninic platform); deep-sea sediments, that represents the infill of the Lagonegro basin; a carbonate platform (Apulian platform) capped by late Miocene to Pliocene– Pleistocene foredeep deposits, where the Marana Capacciotti is (Di Luccio *et al.*, 2005). Below, a more detailed description of the geological and topographic setting of the two facilities is provided.

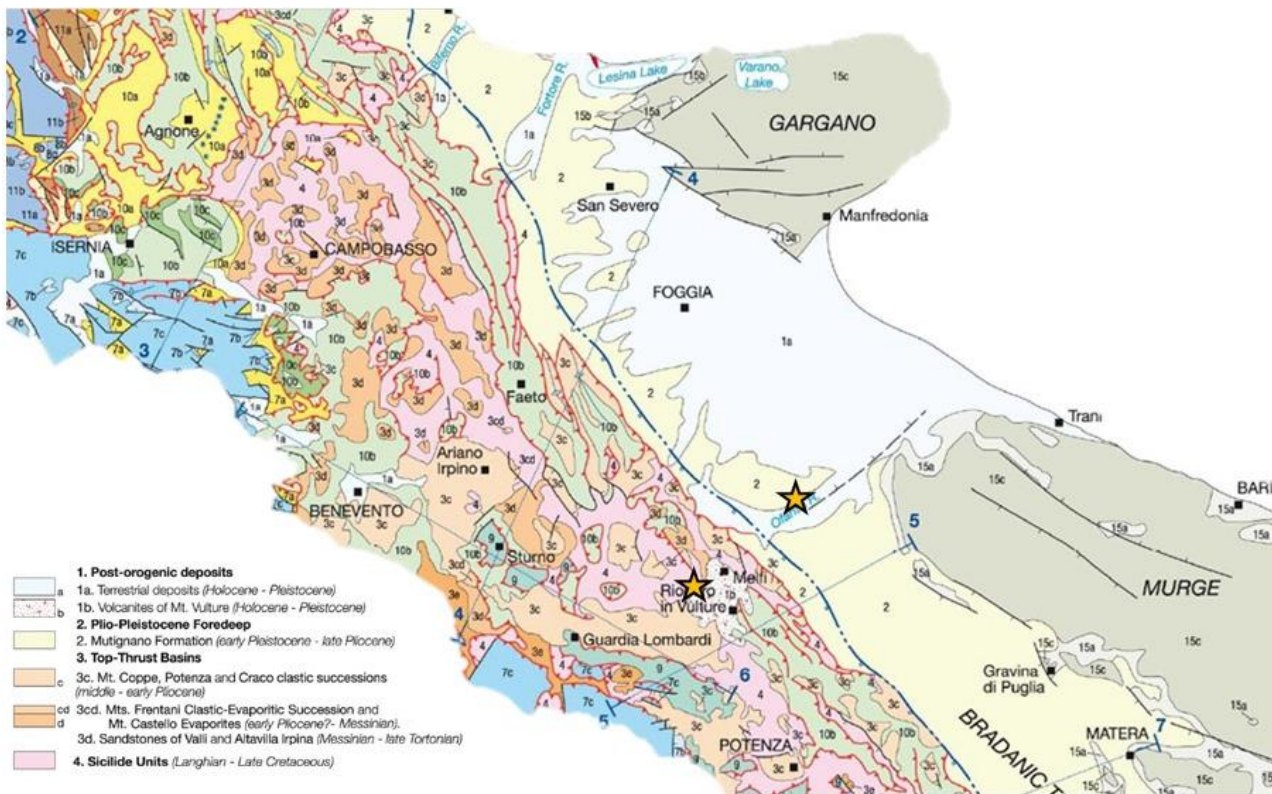


Figure 2. Geological-structural map of Southern Apennines (from Vezzani *et al.*, 2010).

The reservoir of the San Pietro dam receives water from its tributary, the Osento river, on the left bank of the Ofanto river (Figure 3a). The reservoir lies in a narrow valley, arranged in the N-NW (mountain) S-SE (valley) direction and it is surrounded by a series of medium-elevation hills, with altitudes between 460 and 860 m asl. The geological surveys performed during the construction of the dam suggested the existence of a tectonic discontinuity between the geological formations of the hydrographic left side and those of the hydrographic right side of the dam (Cotecchia, 1959). This hypothesis was based on the observation of the different lithologies on the two sides of the riverbed. This difference is also reflected on the different topography: steep and rocky walls are present on the left side, consisting of Miocene marly-arenaceous Flysch surmounted by Oligocene Varicolored Clays, while on the right bank Miocene yellowish sandbanks with some banks of crystalline pebble conglomerate have been identified (see chapter 5, Figure 34). Even if there is no knowledge of specific studies concerning the seismogenic potential of this tectonic discontinuity, the presence of a

NW-SE structure, as suggested by Cotecchia (1959), is also confirmed by other studies. For example, in the bulletin of the Italian Geological Society of 1974 (Ortolani, 1974), Franco Ortolani recognizes an NNW-SSE thrust, East of the Osento river, which places the Varicolored Clays unit in overthrust on the Messinian deposits of the Molasse of Anzano. In any case, it is difficult to say with certainty whether this structure is the same as in the studies cited so far. The study by Vezzani *et al.* (2010) identifies a NW-SE tectonic structure East of lake of San Pietro, however in a relaxing regime. The geological map produced by the study from Vitale & Ciarcia (2018) shows several fault segments: among these, a feature seems to have been traced along the lake of San Pietro, with NNW-SSE trend, in accordance with the observations of Cotecchia (1959) and of Ciaranfi *et al.* (1973). The area under examination is not covered by the studies included in the CARG project. However, from the “Melfi” sheet (ISPRA), immediately South of the area of interest, it is possible to hypothesize an extension of the fault marked West of the town of Monteverde. In light of these considerations, we carried out a geophysical characterization to make sure of the presence of two different lithologies between the two banks, which is discussed in chapter 5.

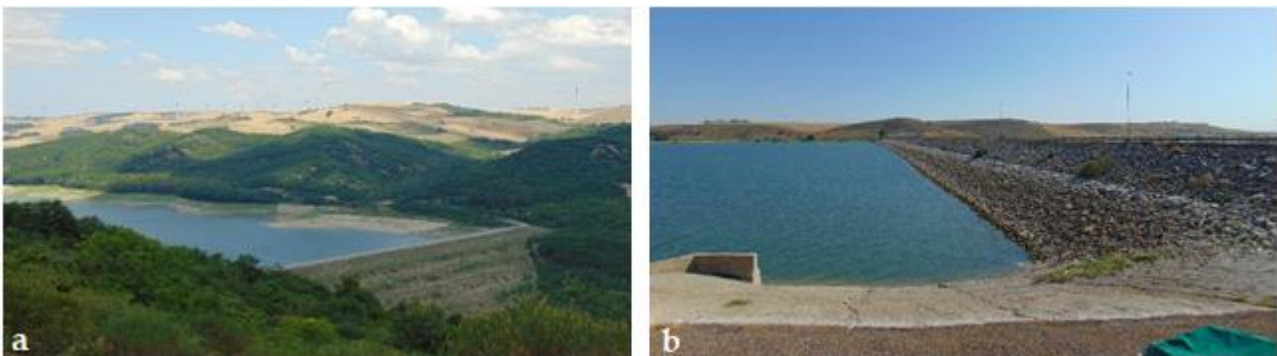


Figure 3. (a) San Pietro sull’Osento dam; (b) Marana Capacciotti dam.

The Marana Capacciotti dam, built between 1969-1976, receives water from the Ofanto river. The basin has an elongated shape and a flat morphology, with altitudes between 150 and 410 m asl. The entire area of the basin is home to crops. It is located within the Mutignano Formation (Vezzani *et al.*, 2010), made up of blue clays that shade laterally and upwards to yellow sands (Sabbie di Serracapriola) and downwards to conglomerates (Conglomerates di Turrivalignani), dating back to the Lower Pleistocene – late Pliocene. As in the case of the San Pietro dam, the 1:50 000 scale cartography of the CARG project unfortunately does not cover the area under examination. However, it is possible to relocate the Capacciotti dam within Sheet 175 “Cerignola” of the Geological Map of Italy on a scale of 1: 100 000 (ISPRA), in which the presence of sands, clayey sands and polygenic conglomerates is confirmed.

2.2 Seismic history

Thanks to its history, Italy boasts the most documented and most temporally extended (25 centuries) seismic catalogs in the world. The seismic history of the area under examination has been here

reconstructed starting from the information related to the epicentres of historical earthquakes and their macroseismic effects, reported in the Parametric Catalog of Italian Earthquakes – CPTI15 v3.0 (Rovida *et al.*, 2020, 2021), in the Database of Italian Macroseismic – DBMI15 v3.0 (Locati *et al.*, 2021) and in the Catalog of Italian and Mediterranean Strong Earthquakes – CFTI5Med (Guidoboni *et al.*, 2018, 2019). Further information on earthquake-induced macroseismic effects on the ground has been extracted from the Italian Catalog of Earthquake-Induced Ground Failures (CEDIT, Martino *et al.*, 2021).

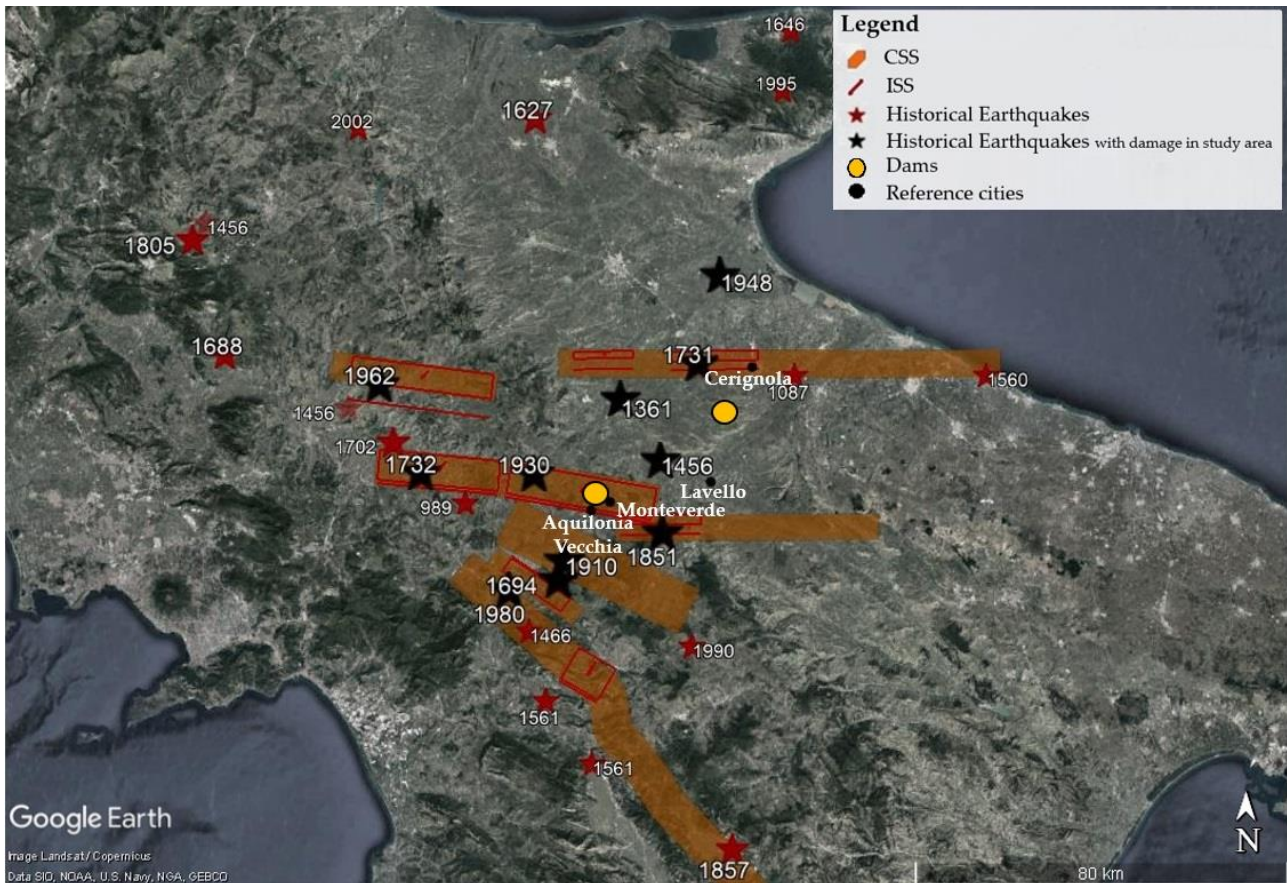


Figure 4. Seismic history map. Stars mark the epicentres of historical events with intensity effects > VI (Mercalli – Cancani – Sieberg scale; Sieberg, 1930). The events have a temporal distribution ranging from 989 to 2002 A.D. Larger earthquakes are represented by larger symbols. The black stars distinguish the historical earthquakes presumably having the greatest impact on the dams (Cerignola and Lavello, for the Marana Capacciotti dam; Monteverde and Aquilonia Vecchia for the San Pietro sull’Osento dam) from the other historical earthquakes, marked by red stars. The single (ISS) and composite (CSS) seismogenic sources responsible for the historical earthquakes with damage in study area are also shown. Data from Fracassi & Valensise (2007); Pino *et al.* (2008); CFTI (Guidoboni *et al.*, 2018, 2019); DISS Working Group (2021).

The Capitanata district lies in one of the most seismically active region of the southern Apennines and large seismic events occurred in historical and more recent times (Fracassi & Valensise, 2007; Pino *et al.*, 2008). In Figure 4 the epicentres of historical earthquakes with intensity effects > VI, according to the Mercalli – Cancani – Sieberg scale (see paragraph 2.2.1; Sieberg, 1930) are shown, in a distance range of about 150 km from the two dams object of study. Among them, the ones that had destructive effects for the study locations are discussed in the following paragraphs. For

historical earthquakes, i.e. pre-instrumental events, the magnitude is estimated from the epicentral intensity and from the areas enclosed by the isoseismals of a given epicentral intensity (Rovida *et al.*, 2020). This magnitude is called equivalent (M_e) and the uncertainty at 1σ confidence level is generally estimated at ± 0.46 m.u. (unit of magnitude). The following earthquake descriptions are extracted from the CFTI5Med (Guidoboni *et al.*, 2018, 2019) and from the Database of Individual Seismogenic Sources (DISS), Version 3.3.0 (DISS Working Group, 2021).

1361 (M_e 6) Ascoli Satriano. Despite being characterized by a low rate of seismicity, the Tavoliere delle Puglie area was hit in historical times by two important destructive events. The first, in chronological order, is the 1361 Ascoli Satriano earthquake. To date, there are no specific studies in the literature for this earthquake. This is partly due to the fact that attention has only recently been paid to the active deformation of the Apulian foreland, following the 2002 sequence that affected the Molise region. The area hit by the 1361 earthquake was relatively sparsely inhabited at the time and macroseismic information is rather limited. The extension of the epicentral area – which certainly includes Ascoli Satriano and Bovino – is still very poorly defined. Towards the South, two discrete constraints on the limits of the damage area are placed by the not very serious damage of Sant’Agata di Puglia and Rionero in Vulture. To the East, the only constraint is placed by Canosa di Puglia. The most affected city was Ascoli Satriano, where most of the buildings collapsed and there were thousands of deaths.

1456 (M_e 7.1) Sannio-Irpinia. The 1456 sequence is one of the most destructive events that took place in the Italian peninsula. The analysis of the sources, the reconstruction of the large damage area and the localization of the effects led to the hypothesis that it was not a single macro-event but several shocks close to each other. This makes the reconstruction of the single seismogenic sources problematic. Those shown in Figure 4 are the possible epicentres of the earthquakes attributed to the seismic sequence of 5-30 December 1456. On the basis of the research developed in Guidoboni & Ferrari (2004) and the geological considerations from Fracassi & Valensise (2007), it was possible to delineate different areas of damage, assuming a correspondence with four epicentral areas: the area around the extinct volcano Vulture, including part of the Capitanata and the Murge, represents one of the areas in which one of the epicentres is assumed to be. This is the closest hypothetical epicentre to the two dams. The areas were identified by locating both the damage attested by direct sources and all the sites existing at the time of the earthquake.

1694 (M_e 6.8) Irpinia-Basilicata. The destructive event that occurred in 1694 is considered the “ancestor” of the 1980 Irpinia earthquake (M_e 6.7). It caused extensive damage in the Apennine area, on the border between the current provinces of Avellino and Potenza, where the city of Muro Lucano (shown in Figure 5) is located. Significant damage was found in large part of Campania, Basilicata and Apulia as well. The area where the maximum effects have been experienced was located in the upper Ofanto valley.



Figure 5. Representation of Muro Lucano, less than ten years after the 1694 earthquake, from CFTILab (Tarabusi et al., 2020).

1731 (M_e 6.5) Foggiano. The Foggiano earthquake of 1731 is the second destructive historical event of the Tavoliere delle Puglie. The most serious effects occurred in the cities of Foggia and Cerignola. In many centres of the Capitanata and of the Adriatic coast, the earthquake caused huge damage to the buildings. A mechanism with two rupture events has been proposed for this earthquake, justified by the presence of two fault segments active in recent times (“Foggia-Cerignola” system, see paragraph 2.3). According to Patacca & Scandone (2001), a mechanism of this type would be in good agreement with the magnitude attributed to the earthquake.

1732 (M_e 6.6) Irpinia. This earthquake mainly affected the Irpinia area, but it caused damage in a very large area, extending from the Tyrrhenian towns of Campania to Foggia, and from Benevento to some centres of northern Basilicata. The towns of Carife and Mirabella Eclano were totally destroyed. In other ten localities (Apice, Ariano Irpino, Bonito, Flumeri, Grottaminarda, Guardia Lombardi, San Mango sul Calore, Lioni, Montorsi, Vallata) the destruction was very extensive and the few buildings that had not collapsed became unusable.

1851 (M_e 6.4) Basilicata. The two destructive mainshock of 1851 struck northern Basilicata, devastating the region of Mount Vulture. The earthquake almost completely destroyed the villages of Barile and Melfi. Collapses and serious injuries in almost all the houses were found in Venosa, Atella, Lavello and Ripacandida, in the province of Potenza. The area in which significant damage to the buildings was found extended further North, towards the northern Capitanata, and

eastwards, towards the Ofanto valley, affecting a large area of Apulia up to the Adriatic coast; much less damage towards the South and West, where only a limited part of Irpinia was affected.

1910 (M_e 5.7) Irpinia-Basilicata. The 1910 earthquake affected a large area of the southern Apennines between Irpinia and Basilicata. The most serious effects were in Calitri, in the Ofanto valley, where about 30% of the houses collapsed. In about 40 other places the earthquake caused injuries, cracks, ledges and walls falling. The most damaged villages turned out to be those located in a direction parallel to the Apennine chain. Overall 53 municipalities were damaged: 41 in the province of Avellino and 12 in the province of Potenza.

1930 (M_e 6.7) Irpinia. The 1930 earthquake struck upper Irpinia, Vulture, Sannio, Salerno, Napoli, Matera and upper Apulia. The mainshock had its maximum effects in the mountainous area between Melfi (Figure 6) and Ariano Irpino, in the provinces of Benevento, Avellino and Foggia. The greatest damage occurred in Aquilonia Vecchia, Lacedonia, Villanova del Battista and Trevico, where about 70% of the houses collapsed completely. In 68 towns in the provinces of Avellino, Potenza, Foggia, Benevento and Salerno, collapses and deep lesions were found, extending to a large part of the building heritage. The most serious damages, in the various provinces, are located as follows: in the province of Avellino, the most affected town was Ariano Irpino, where the percentage of damaged houses was 66%; in Rionero in Vulture, where 90% of the buildings were damaged, many buildings collapsed and many others were unusable.



Figure 6. Historical photos of the destructive effects of the 1930 earthquake on the town of Melfi. References available at [this link](#).

1948 (M_e 5.5) northern Apulia. This seismic sequence struck northern Apulia, in particular the localities of Gargano and Capitanata, in the province of Foggia, and to a lesser extent some centres in the provinces of Bari and Potenza. The earthquake of 22 August 1948 caused considerable damage to Orta Nova and Stornara and some light damage was also reported in some places in the province of Potenza. According to official data communicated in September 1948, the damaged buildings in the province of Foggia were over 2300, of which 335 (14%) were declared uninhabitable, 761 (33%) severely damaged and 1231 (53%) lightly. The tremors were felt in various locations in Abruzzo, Molise, Basilicata and Campania.

1962 (M_e 6.1) Irpinia. The most affected area by the 1962 earthquake was the Campania Apennines on the border between Sannio and Irpinia. The most severely damaged municipalities were Casalbore, Melito Irpino, Molinara, Reino and Sant'Arcangelo Trimonte, where the percentage of damaged buildings was generally greater than 90%, and that of seriously or significantly damaged buildings reached or exceeded 50%. In over 70 inhabited centres, including various locations in the provinces of Benevento, Caserta, Foggia, Napoli and Salerno, there was significant damage.

1980 (M_e 6.7) Irpinia-Basilicata. For this event, in addition to the equivalent magnitude (M_e 6.7), data in local magnitude (M_L 6.5) and moment magnitude (M_w 6.8, CPTI15; M_w 6.9; Global CMT) are also provided, as the 1980 earthquake represents the only instrumental event, for which a M_w estimate from moment tensor exist as well, among those listed so far. Up to 1980, in fact, in the catalogs all earthquakes are considered as historical (therefore, reported in equivalent magnitude M_e), despite the fact that the first instruments were already active. For attenuation models, which will be discussed in the chapter 3, for this event the official instrumental data are used. The Richter or local magnitude (M_L) is obtained from the maximum amplitude of the oscillations recorded by the standard Wood-Anderson seismometer (Richter, 1935); the moment magnitude (M_w) is obtained from conversion laws that are still poorly uniform to date (Castellaro *et al.*, 2006; Gasperini *et al.*, 2015). The destructive earthquake of 1980 had devastating effects in a large area of the southern Apennines, in particular in Irpinia and in the adjacent areas of the provinces of Salerno and Potenza. The area of maximum effects includes the area in the high valleys of Ofanto and Sele; the damage area included almost all of Campania and Basilicata and part of Apulia. The villages of Castelnuovo di Conza, Conza della Campania, Laviano, Lioni, Sant'Angelo dei Lombardi and Santomenna were almost completely destroyed; destructions extended to over 50% of the building were found in Balvano, Calabritto, Caposele, Guardia Lombardi, Pescopagano, San Mango sul Calore, Senerchia, Teora and Torella dei Lombardi. In about 50 other municipalities, collapses and serious injuries were reported, about 450 suffered lighter damage. In Aquilonia Nuova the earthquake caused significant damage.

2.2.1 Macroseismic intensities at locations close to the area of interest

The most commonly used macroseismic intensity scales today are the so called Mercalli – Cànani – Sieberg (MCS; Sieberg, 1930), the Modified Mercalli Intensity scale (MMI; Wood & Neumann, 1931) and the European Macroseismic Scale (EMS; Grünthal, 1998). They describe the effects produced by the shaking of an earthquake on structures and on the environment, according to a scale level from I to XII. Damage to structures begins, by definition (Sieberg, 1930), with degree VI. The ninth degree indicates destruction (damage in more than ½ of the buildings, collapses in ¼). The macroseismic intensity refers to “localities”, understood as residential units of a certain size, regardless of the administrative role they play or have played in history (Locati *et al.*, 2021).

In order to assess the damage levels of the previous earthquakes on the localities surrounding the dams object of this study, the towns of Monteverde and Aquilonia Vecchia were chosen as a reference for the San Pietro dam; the localities of Cerignola and Lavello, as a reference for the Capacciotti dam (Figure 4). The towns of Monteverde and Aquilonia Vecchia are both about 2.5 km

far from the San Pietro dam, while the municipalities of Cerignola and Lavello are both about 13 km far from the Capacciotti dam. For the purposes of this study, descriptions of degrees V to X with reference to the MCS scale (Sieberg, 1930) are here briefly provided.

- **V. Moderate.** The earthquake is felt by many people, on the street or in open space. Inside the houses the shock is felt because of the shaking of the entire building.
- **VI. Strong.** The earthquake is perceived by everyone with panic. In isolated, solidly built houses there is minor damage. More serious, but still not dangerous, damage occurs on poorly constructed buildings.
- **VII. Very strong.** Moderate damage to several solidly built structures: small cracks in the walls, fall of rather large parts of plaster and stucco decorations, collapse of bricks and generally falling tiles. In some cases, badly designed houses collapse.

Table 1. Macroseismic intensities felt in the closest towns to the infrastructures. Data are extracted from the online portals CPTI5 v3.0 (Rovida et al., 2021), DBMI5 v3.0 (Locati et al., 2021) and CFTI5Med (Guidoboni et al., 2018, 2019).

Date	M_e	I_0	I_{max}	Intensity at Monteverde	Intensity at Aquilonia Vecchia	Intensity at Lavello	Intensity at Cerignola
1361	6	IX	X	-	-	-	-
1456	7.1	XI	XI	V	IX?	-	-
1694	6.8	11	X	VII-VIII	VIII	VII-VIII	V
1731	6.5	IX	IX	-	-	-	IX
1732	6.6	X-XI	X-XI	VII-VIII	V – VI	-	VI – VII
1851	6.4	X	X	VII-VIII	VII	VIII	VII
1910	5.7	VIII	IX	VII	VII	-	V
1930	6.7	X	X	VIII- IX	X	VIII	VII
1948	5.5	VII	VII	-	-	-	VII
1962	6.1	IX	IX	-	-	V	VI
1980	6.7	X	X	IV-V	VII (New)	IV-V	VI

- **VIII. Severe.** Solid stone walls are cracked and knocked down. About $\frac{1}{4}$ of the houses are seriously damaged; some of them collapse; many become uninhabitable. Cracks form on slopes and marshy soils; sand and mud come out of the soaked soils. People in driving motor cars are disturbed.
- **IX. Violent.** About $\frac{1}{2}$ of the stone houses are seriously destroyed, many of them collapse, most of them become uninhabitable. Half-timbered houses are torn from their foundations and compressed on themselves, in this way the supporting beams of the rooms are sheared, thus contributing to considerably destroying the houses. Liquefaction occurs. Underground pipes are broken.

- **X. Extreme.** Very serious destruction of about $\frac{3}{4}$ of the buildings; most of the buildings collapse. Cracks form paved and asphalted streets and large wavy corrugations are created by the pressure in the ground. Landslides occur. Wells often vary the water level.

The damage associated to the events described above is summarized in Table 1 for each location. The intensity values follow the MCS Scale (Sieberg, 1930).

Monteverde. The town of Monteverde (Figure 7) reports several collapses and serious injuries to the houses during the earthquakes of 1694, 1731, 1851 and 1910; according to the historical sources, these earthquakes did not cause victims. The earthquake of 1930, on the other hand, caused very serious damage to buildings and casualties. According to available information, the 1930 earthquake is the event with the most destructive impact on the town of Monteverde and it is assigned a macroseismic intensity equal to VIII-IX.

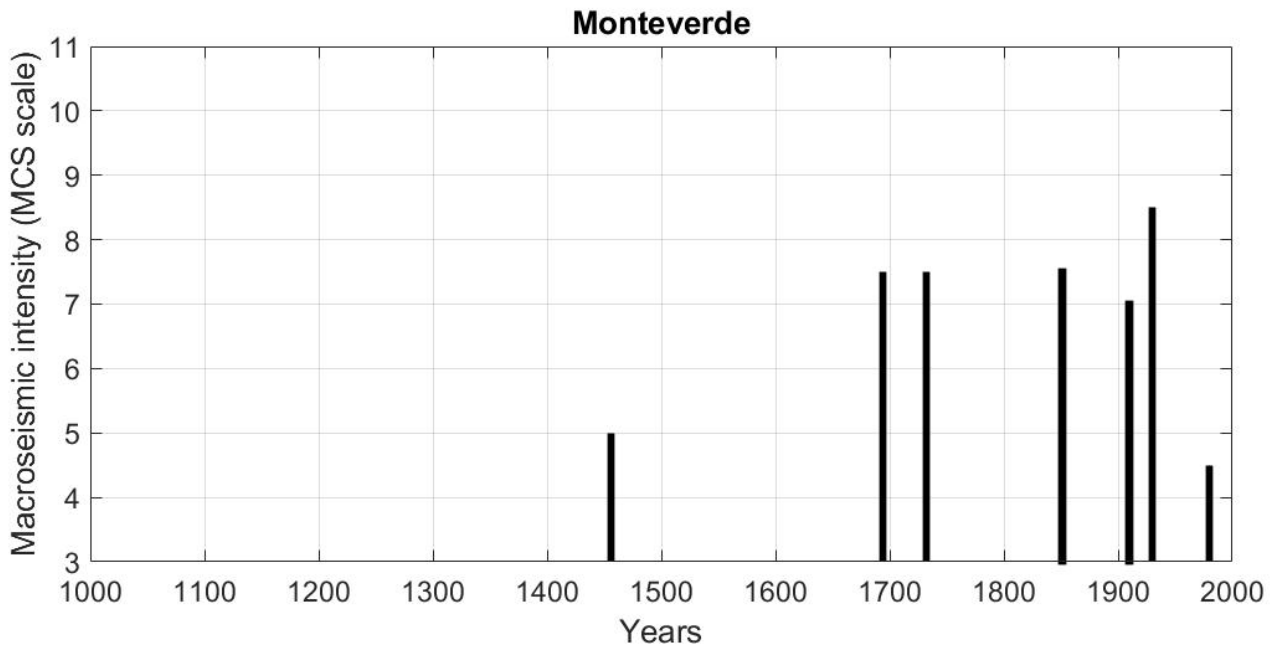


Figure 7. Effects of historical earthquakes on the town of Monteverde: the dates of the earthquakes are shown on the abscissa, the macroseismic intensity values in the MCS scale on the ordinate. The most destructive event for the town of Monteverde is the 1930 earthquake (Guidoboni et al., 2018, 2019).

Aquilonia Vecchia. From the information available (Figure 8), the town of Aquilonia Vecchia (or Carbonara) appears to have been severely damaged by the earthquake of 1456 (macroseismic intensity equal to IX), but there is little information about it. The earthquakes of 1694 and 1851 caused some collapses in the town. The 1930 earthquake totally destroyed the town of Aquilonia Vecchia (maximum intensity for this site equal to X): the town changed location, moving to the current Aquilonia, a little further South.

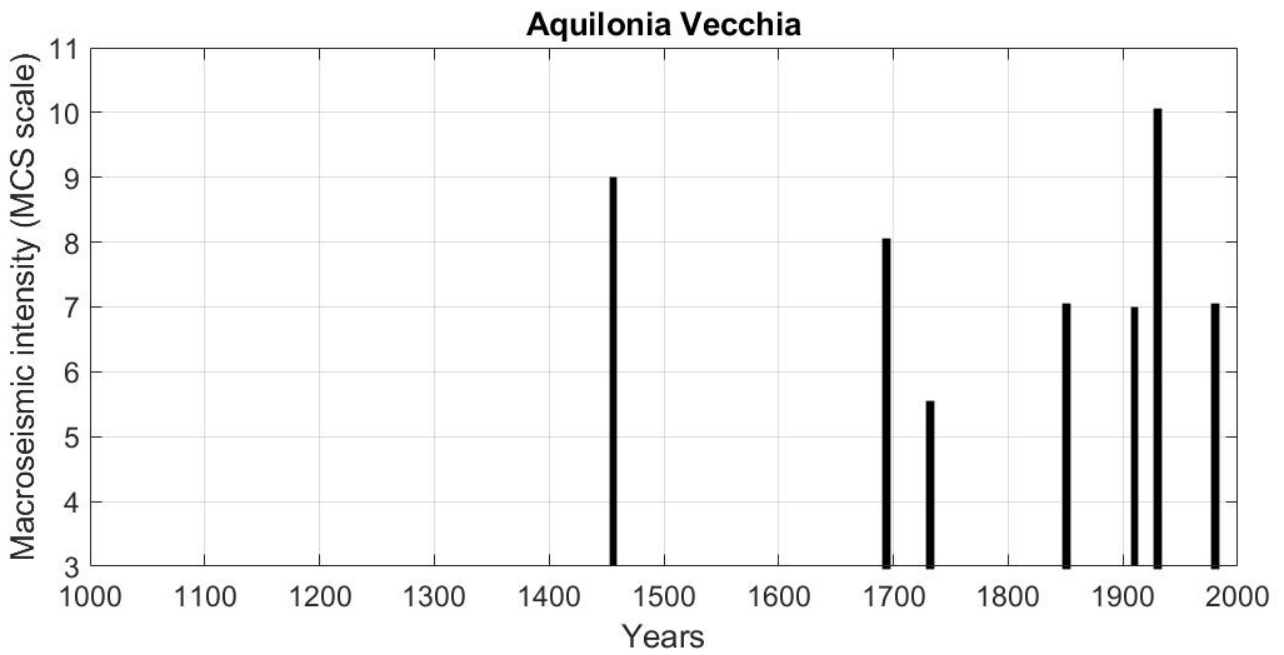


Figure 8. Effects of historical earthquakes on the town of Aquilonia Vecchia: the dates of the earthquakes are shown on the abscissa, the macroseismic intensity values in the MCS scale on the ordinate. The most destructive event for the town of Aquilonia Vecchia is the 1930 earthquake (Guidoboni et al., 2018, 2019).

Lavello. The town of Lavello (Figure 9) was strongly affected by the earthquakes of 1694, 1851 and 1930: in all these events there were collapses and serious damage to the buildings. The 1930 earthquake also caused casualties (MCS intensity equal to VIII).

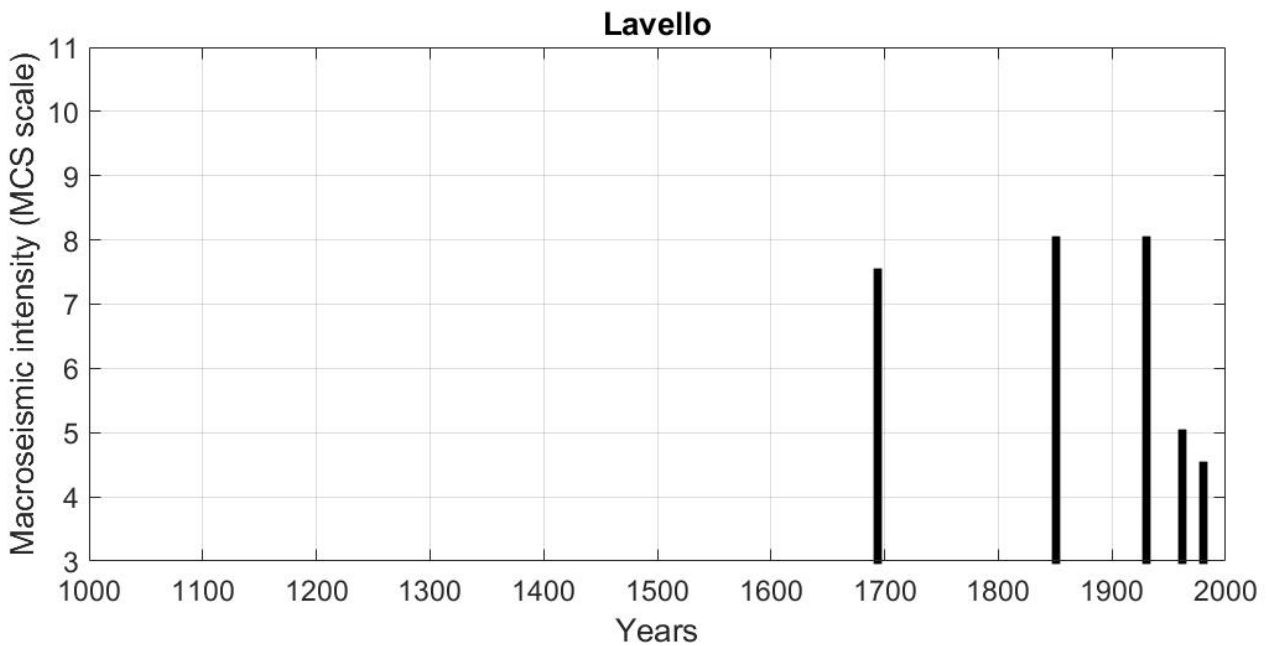


Figure 9. Effects of historical earthquakes on the town of Lavello: the dates of the earthquakes are shown on the abscissa, the macroseismic intensity values in the MCS scale on the ordinate. The most destructive events for the town of Lavello are the earthquakes of 1851 and 1930 (Guidoboni et al., 2018, 2019).

Cerignola. The most destructive earthquake for the city of Cerignola (Figure 10) was the 1731 event: it caused collapses in all sacred buildings and the opening of serious damages in all buildings, also causing deaths. The macroseismic intensity assigned following this event is equal to IX. The events of 1851, 1930 and 1948 did not cause casualties, but serious damage to the buildings is reported, both in the city and in rural homes.

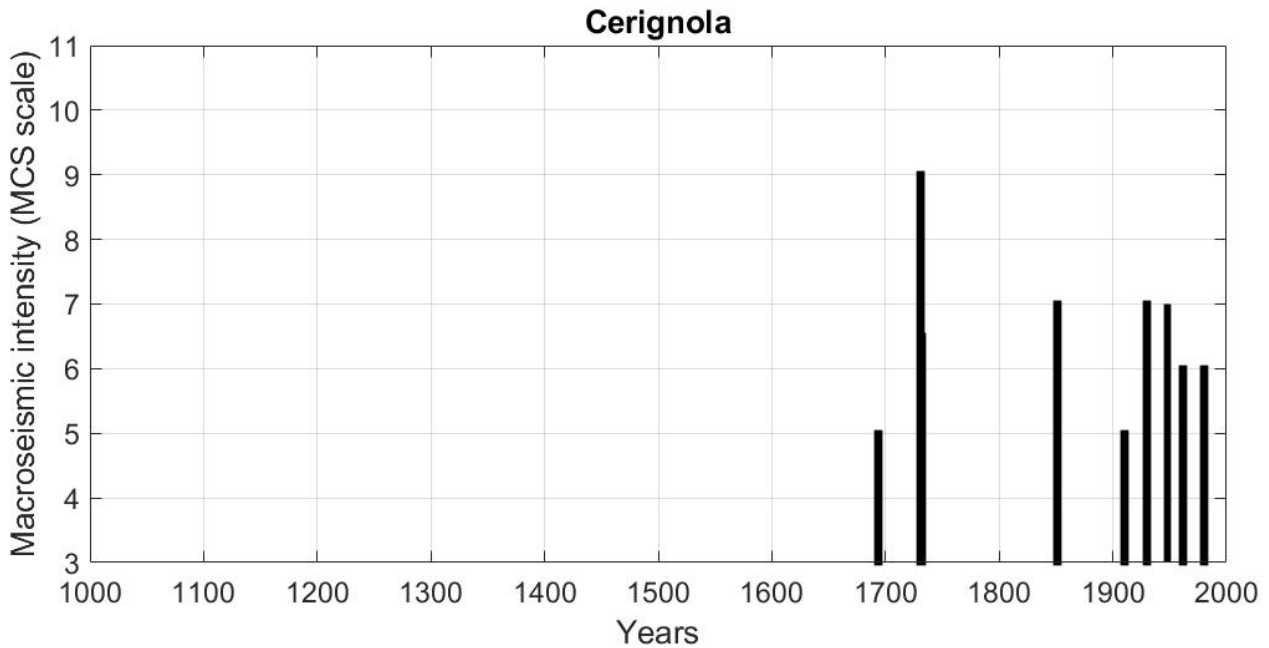


Figure 10. Effects of historical earthquakes on the town of Cerignola: the dates of the earthquakes are shown on the abscissa, the macroseismic intensity values in the MCS scale on the ordinate. The most destructive event for the town of Cerignola is the earthquake of 1731 (Guidoboni *et al.*, 2018, 2019).

The historically documented effects on the natural environment closest to the site are reported in Figure 11 (Martino *et al.*, 2021). In Bisaccia, a town located 10 km from the San Pietro dam, the earthquake of 1694 caused landslides and the opening of cracks in the soil. In this same locality landslides, deformation of the ground and fractures are also reported following the events of 1851, 1930 and 1980. The earthquake of 1851 caused landslides in the locality of Lacedonia, located 8 km from the San Pietro dam, and on the eastern side of the Lavagna hill, in Monteverde. The earthquake that destroyed Aquilonia Vecchia in 1930 caused the formation of many crevasses and various landslides also occurred in neighboring towns, such as Rocchetta Sant'Antonio (10 km from the San Pietro dam). The aqueduct of the source of Monte della Guardia, in Aquilonia Vecchia, varied in size (Guidoboni *et al.*, 2018, 2019). Landslides and mudslides are also reported in the same locality.



Figure 11. Historically documented natural effects in the vicinity of the San Pietro and Capacciotti dams, extracted from the CEDIT online portal (Martino et al., 2021).

2.3 Structural setting

The strongest seismic events in the southern Apennine mostly occurred in a segmented belt of large normal NW–SE striking faults, running along the chain axis (DISS Working Group, 2021). In the foreland, faulting develops along E–W right-lateral strike-slip to oblique-slip faults related to the roll-back of the Adriatic foreland (Di Luccio *et al.*, 2005; Pino *et al.*, 2008). In this region, instrumental earthquakes characterized by transcurrent kinematics generally involve a deeper seismogenic thickness ($\approx 15\text{--}30$ km deep) than earthquakes with extensional kinematics that exclusively characterize the first kilometers of crustal thickness ($\approx 0\text{--}15$ km deep; Vannoli & Burrato, 2018).

In section 2.2 the historical earthquakes that produced damage to the town or effects on the environment near the dams under examination have been shown. Below, the seismogenic sources that produced these events are described. The discussion of the seismogenic sources useful for this study will be dealt within the paragraph 3.1.2. The national reference database for seismotectonic studies is the Database of Individual Seismogenic Sources (DISS Working Group, 2021), a geo-referenced archive of information on the structures that generate earthquakes – the seismogenic sources – and the estimate of their potential (Basili *et al.*, 2008). The seismogenic sources are represented in three dimensions, obtained by parameterizing the geometry and kinematics of large active faults considered capable of generating earthquakes with a magnitude (M_w) greater than 5.5. The sources available in the DISS today are divided into two types: the Individual Seismogenic Sources (ISS), which describe the faults responsible for specific strong earthquakes that have already occurred or which are believed to occur, and the Composite Seismogenic Sources (Composite Seismogenic Sources, CSS) describing extended fault systems with a lower level of detail. Composite seismogenic sources do not have associated instrumental earthquakes, however some scientific papers link them to important earthquakes of the past and to individual seismogenic sources (DISS Working Group, 2021).

Table 2. Individual (ISS) and composite (CSS) seismogenic sources responsible for the historical earthquakes occurred near the San Pietro and Capacciotti dams (DISS Working Group, 2021).

Earthquake	ISS-ID	Name	CSS-ID	Name
1361	ITIS082	Ascoli Satriano	ITCS004	Castelluccio dei Sauri-Trani
1456 - 1962	ITIS092	Ariano Irpino	ITCS057	Pago Veiano-Montaguto
1731	ITIS080	Cerignola	ITCS004	Castelluccio dei Sauri-Trani
1732	ITIS006	Ufita Valley	ITCS084	Mirabella Eclano- Monteverde
1851	ITIS081	Melfi	ITCS089	Rapolla-Spinazzola
1930	ITIS088	Bisaccia	ITCS084	Mirabella Eclano-Monteverde
1980 (1/3)	ITIS077	Colliano	ITCS034	Irpinia-Agri Valley
1980 (2/3)	ITIS078	San Gregorio Magno	ITCS034	Irpinia-Agri Valley
1980 (3/3)	ITIS079	Pescopagano	ITCS087	Conza della Campania-Tolve
1694 – 1910 - 1980	-	-	ITCS063	Andretta-Filano

Table 2 shows the main individual and composite seismogenic sources responsible for the historical earthquakes discussed in paragraph 2.2. The related identification code, the extended name and the location (Figure 4) with respect to the San Pietro and Capacciotti dams are provided for each source.

1361. It is believed that the earthquake of 1361 (M_e 6), associated with the hypothetical individual seismogenic source ITIS082 "Ascoli Satriano", was caused by a deep blind fault (DISS Working Group, 2021; see paragraph 2.3.1): subsoil data of the Apula carbonate platform highlight the presence of numerous EW structures in this area. The related composite source, ITCS004 "Castelluccio dei Sauri-Trani" straddles the southern Capitanata plain, within the lower Ofanto valley, South of the city of Foggia. This source belongs to the right oblique to transverse system that affects the central and southern Adriatic foreland. It is believed to be a deep system of E-W blind faults, a tectonic mechanism that seems to characterize the entire eastern seismogenic domain of the southern Apennine ridge. The western sector of this source may have caused the destructive event of 1361, while the central-eastern one of 1731 (DISS Working Group, 2021).

1456 - 1962. The wide distribution of intensity and the complexity of the damage pattern resulting from the destructive sequence of 1456 (M_e 7.1) led to the hypothesis of the simultaneous activation of multiple seismogenic sources (Meletti *et al.*, 1989). Although no specific source has been recognized (and the epicentre of the event itself is of dubious location), several studies hypothesize the rupture of several normal fault segments in NW-SE trend (DISS Working Group, 2021). Fracassi & Valensise (2007) propose three different seismogenic sources for the sequence of 1456: ITIS092 "Ariano Irpino", represents the southernmost source among the three hypotheticals (the others are located near Campobasso and Chieti). The related composite seismogenic source, ITCS057 "Pago Veiano-Montaguto", is located in the Sannio area, North-East of the city of Benevento, and belongs to the right oblique to transverse system that affects the central and southern Adriatic foreland. Based on its epicentre, the 1962 (M_e 6.1) event could be associated with the same seismogenic structures.

1731. It is believed that the earthquake of 1731 (M_e 6.5) was caused by a very recent normal fault, NW-SE and plunging towards SW, discovered in the subsoil of the Cerignola-Foggia area. The lack of surface evidence in the area still raises doubts as to whether the individual seismogenic source ITIS080 "Cerignola" may or may not be the source of the 1731 earthquake (Scandone, 2004). The related composite source, ITCS004 "Castelluccio dei Sauri-Trani", is the same source that could have caused the destructive event of 1361, in its western sector, and that of 1731, in its central-eastern sector (DISS Working Group, 2021). The 1731 Foggia earthquake can also be connected to a very specific geological structure, represented by a NW-SE oriented fault system, called the "Foggia - Cerignola" system, (see paragraph 2.3.1).

1732. The ITIS006 "Ufita Valley" source is a North dipping fault with normal kinematics and right-sided oblique-to-transcurrent movement. Located near the extinct volcano Vulture, it is believed to be responsible for the 1732 earthquake (M_e 6.6). Historical and instrumental catalogs show a notable concentration of catastrophic earthquakes in this region. From West to East, we recall the events of 29 November 1732 (M_e 6.6), 23 July 1930 (M_e 6.7), 14 August 1851 (M_e 6.4): to date, the structural

relationship between the sources responsible for these earthquakes is still doubtful (DISS Working Group, 2021). The associated composite source, ITCS084 "Mirabella Eclano-Monteverde" is located in eastern Campania, East of the city of Benevento and belongs to the right oblique to transverse system that affects the central and southern Adriatic foreland. This composite source is believed to be a deep WNW-ESE blind fault system. The western sector of this composite source includes the faults responsible for the 1732 earthquake, while the western sector includes the fault responsible for the 1930 earthquake (DISS Working Group, 2021).

1851. This event (M_e 6.4) occurred in a relatively little studied area from a seismotectonic point of view, which is much better known for the presence of the extinct volcanic apparatus of the Vulture. For the 1851 earthquake, the association with the ITIS081 "Melfi" source is assumed. The lack of surface evidence in the area leads to the hypothesis that the 1851 event may have been caused by a deep blind fault (DISS Working Group, 2021). The related composite source, ITCS089 "Rapolla-Spinazzola", is located between the regions of Campania and Apulia, on the northern shoulder of the Vulture, and belongs to the right oblique to transverse system that affects the central and southern Adriatic foreland. This composite source is believed to be a deep E-W blind fault system. The western sector of this source is believed to be responsible for the 1851 earthquake.

1930. The earthquake of 23 July 1930 (M_e 6.7) is one of the strongest events that occurred in the southern Apennines and also one of the best documented, given the wealth of macroseismic information. For this earthquake too, a normal fault has been proposed as a seismogenic source. Pino *et al.* (2008) hypothesize a deep fault associated with the individual seismogenic source ITIS088 "Bisaccia". The composite source, ITCS084 "Mirabella Eclano-Monteverde", is the same as the 1732 earthquake. According to the information contained within the DISS (2021), the San Pietro dam is located within the ITIS088 "Bisaccia", individual seismogenic source, and the ITCS084 "Mirabella Eclano-Monteverde", composite seismogenic source, both related to the destructive earthquake of 1930.

1694 – 1910 – 1980. The seismogenic source responsible for the 1980 (M_e 6.7) earthquake is one of the most studied Italian faults and created the conditions for the start of numerous earthquake geology studies in Italy. The seismic event of 1980 is the result of a multiple rupture process with three sub-events activated within 40 seconds. There is a general consensus regarding the geometric parameters of the three faults activated in 40 seconds, which all have normal kinematics and Apennine direction (NE-SW). The individual source ITIS077 "Colliano" represents the segment responsible for the shock at 0 seconds (1/3), ITIS078 "San Gregorio Magno" at 20 seconds (2/3) and they dip to NE; ITIS079 "Pescopagano" at 40 seconds (3/3) and it dips to SW. The antithetic activated at 40 seconds is a blind fault while the other two structures have allowed the recognition, for the first time in Italy, of surface coseismic faulting. This last characteristic has determined the development of paleoseismology in Italy (Vannoli & Burrato, 2018). The studies by D'Addezio *et al.* (1990, 1991) and (Pantosti *et al.*, 1993a, 1993b) argue that the presence of surface faulting in the localities of Piano di Pecore and Piano di San Gregorio Magno reinforces the idea that the 1980 earthquake can be considered as characteristic for the Irpinia fault system. The earthquake of 1694 (M_e 6.8) was previously believed to be the direct

ancestor of the 1980 event. Currently, the main unsolved problem regarding its source is the lack of a geological record in the trenches at Piano di Pecore and Piano di San Gregorio Magno, as confirmed by the studies by Pantosti *et al.* (1993a, 1993b). To date, it is therefore not possible to state whether the earthquake of 1694 occurred on the Irpinia fault system or not. The same considerations on the uncertainty of the seismogenic source responsible for the 1910 (M_e 5.7) can be done. As regards the composite seismogenic sources, three are identified. The first, ITCS034 "Irpinia-Agri Valley", responsible for the events at 0 seconds (1/3) and 20 seconds (2/3) of 1980, is located between the southern Apennines, between Irpinia and Basilicata. The second, ITCS087 "Conza della Campania-Tolve", responsible for the event at 40 seconds (3/3) of 1980, lies within the entire extensional axis NW-SE of the southern Apennines, forming a sort of SE prolongation of the previous source. The third composite source, ITCS063 "Andretta-Filano", embraces Campania and Basilicata, just South of the Vulture and just North of the two previous sources. This source is considered doubtful and difficult to correlate with individual seismogenic sources (DISS Working Group, 2021).

2.3.1 Focus on active and capable faults

A fault is defined capable when it is considered capable of producing, within a time interval of interest for society, a deformation/dislocation of the ground surface, and/or in the vicinity of it (ITHACA, 2019). The age of the last fault activation event is one of the key elements in evaluating the "capacity" of a fault. The ITHACA Catalog (Italy HAZards from CAPable faults) collects the information available on capable faults affecting the Italian territory on the basis of a critical review of the available literature. In Table 3, the active and capable faults closest to the two hydraulic facilities are listed; the closest ones in terms of space and time of last activity (Figure 12) are then discussed.

Table 3. Capable faults near the San Pietro and the Capacciotti dams (DISS Working Group, 2021; ITHACA, 2019).

Fault name	ID	Last activity
Apricena	ITDS012	-
Castel Baronia	33300	3 000 ÷ 9 000 (prehistory-Neolithic)
Castelluccio – Stornarella	44103	Historical (< 3 000)
Eastern Ofanto Valley	43100	Late Pleistocene
Foggia – Cerignola (Sud)	44101	Historical (< 3 000)
Monte St. Angelo - Mattinata	ITIS020	Before 1273 A.D.
Bella – Casagrande System	30300, 30301, 30302, 30303, 30304, 30305, 30306, 30307, 30308, 30309, 30310	-
Irpinia System	34002, 34003, 34006, 34007, 34008, 34009, 34016, 34017, 34018, 34019, 34020, 34021, 34022, 34023, 34024, 34025	3 000 ÷ 9 000 (prehistory-Neolithic)
Ufita Valley	33400	22 000 ÷ 50 000
Western Ofanto Valley	33500	3 000 ÷ 9 000 (prehistory-Neolithic)

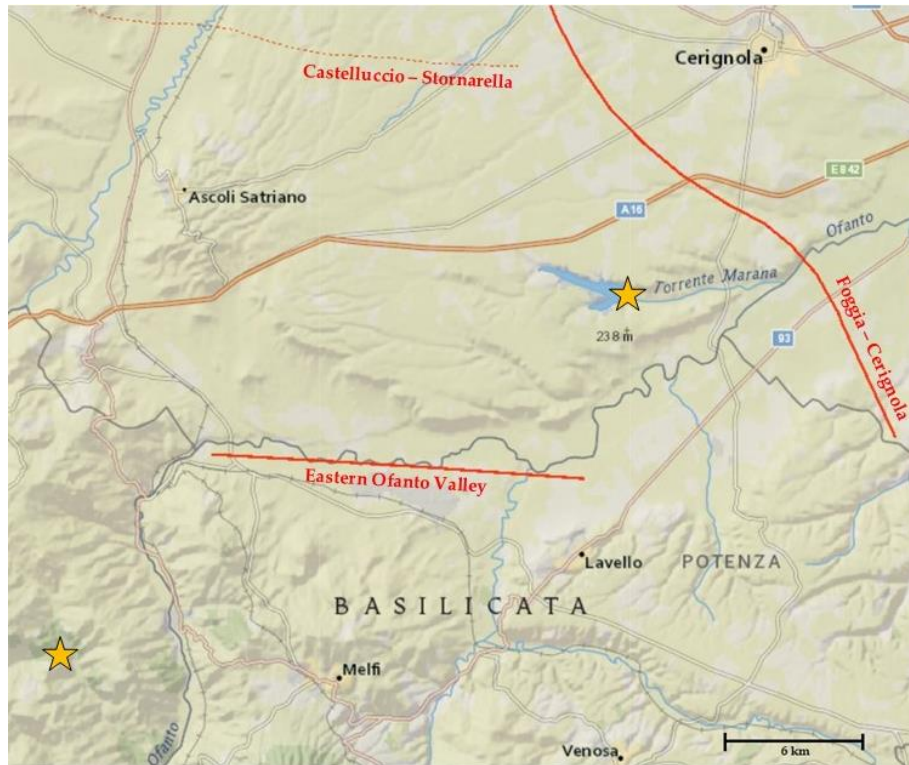


Figure 12. Closest active and capable faults (in red) to the two hydraulic facilities (marked by yellow stars). Dashed line stands for unknown kinematics; solid line stands for normal kinematics.

Castelluccio – Stornarella. Close to the Capacciotti dam (which is located about 30 km NE of the San Pietro dam) two important buried faults are identified, thought to be responsible for the earthquakes of 1361 and 1731 and reported in the ITHACA catalog (ITHACA, 2019). The most important of these is a blind fault with a WNW-ESE direction, which extends for 30 km from Castelluccio dei Sauri to Stornarella. The so-called "Castelluccio dei Sauri-Stornarella" (about 35 km from the Capacciotti dam, see Figure 12) is considered potentially seismogenic. The Castelluccio dei Sauri-Stornarella fault has probably lowered the northern sector, creating a dislocation of the Apulian carbonate roof and a more or less pronounced flexure in the overlying deposits (Scandone, 2004). Nevertheless, its kinematics is reported as "unknown" in the ITHACA database. In any case, the association between this fault and the earthquake of 1361 still remains hypothetical due to the little macroseismic information.

Foggia – Cerignola. The NNW-SSE "Foggia-Cerignola" fault (6 km away from the Capacciotti dam, see Figure 12) is considered to be potentially seismogenic as well. The equivalent magnitude associated with the 1731 earthquake (M_e 6.5) is justified by the rupture of two fault segments (Patacca & Scandone, 2001), of which the southern section is located a few km from the Capacciotti dam. Patacca & Scandone (2001) identify several fault segments showing evidence of recent activity near its north-western and south-eastern extremities. Several segments have lowered towards SW the upper deposits of the Apulian carbonate platform and the Pleistocene regressive deposits. Furthermore, from the CARG "Cerignola" 422 sheet (ISPRA), immediately North of the area of interest, it is possible to observe a SW-NE section that crosses the Foggia-Cerignola fault: in

accordance with the sections reported by Scandone (2004), this feature, to the SW of the city of Cerignola, lowers the upper units of the Avampaese Apulo.

Eastern Ofanto Valley. The "Eastern Ofanto Valley" fault, which is the third closest active fault to the dams (8 km away from the Capacciotti dam, 12 km from the San Pietro dam, see Figure 12) has a normal kinematics, a WNW-ESE direction and its last activity probably occurred during Late Pleistocene. Further information on this fault are not available.

Nevertheless, in order to have a more defined picture about the geotectonics of Capitanata, further geodetic data have been consulted, which do not show any significant tectonic structures in addition to those already mentioned. In fact, geodetic measurements show very low strain-rates in the Capitanata area: the study by Palano *et al.* (2011) provides values below 40 nanostrain/yr. By way of comparison, in the Strait of Messina, where "low" deformation is observed, Serpelloni *et al.* (2010) show values of 65 nanostrain/yr.

3. PROBABILISTIC SEISMIC HAZARD ANALYSIS

3.1 Seismotectonic probabilism (or standard) approach

The most common PSHA approach follows the method developed in theoretical form by Cornell in 1968 (Cornell, 1968). This type of analysis permits the uncertainties related to (i) location, (ii) magnitude, (iii) earthquake recurrence rate and (iv) variation of the characteristics of the ground shaking with the size and the site of the earthquake, to be explicitly considered in the evaluation of seismic hazard (Kramer, 1996). At the same time, however, it is based on the rigid assumption of total independence of events, the sustainability of which the scientific community is still debating. For reasons of continuity and comparison, in this study it was decided to first test the seismotectonic probabilistic approach, which also agrees with the MPS04 Italian seismic hazard map, reference of the current national technical standards for construction (NTC, 2018), built according to this method (Gruppo di Lavoro MPS, 2004).

The seismotectonic probabilistic assessment of seismic hazard follows four steps:

- 1) **Selection of a seismic catalog and identification of the seismogenic sources.** For the purposes of Cornell's (1968) method, which assumes that earthquakes are independent of time, the seismic catalog must first be declustered, i.e. deprived of the foreshock and aftershock. The selected seismicity data are subsequently spatially disaggregated into discrete seismogenic sources, identified as potentially responsible for shaking at site.
- 2) **Time distribution of the recurrence of earthquakes: seismicity rates.** For each seismogenic source, based on the available historical and instrumental data, a magnitude-frequency distribution is defined, i.e. the annual occurrence rate of earthquakes with different magnitudes. This is most often expressed in terms of Gutenberg & Richter law (1944) or through the characteristic earthquake recurrence laws (e.g., Youngs & Coopersmith, 1985).
- 3) **Attenuation relationships.** The way in which the level of ground shaking decays with the distance from the epicentre as a function of the magnitude is described by the attenuation laws. These models are generally estimated with regression analysis on the data collected in the region of interest or through models described in literature.
- 4) **Hazard evaluation.** The exceedance probability, λ_{y^*} , of a particular ground motion parameter, Y , is calculated for one possible earthquake at one possible source location and then multiplied by the probability that that particular magnitude earthquake would occur at that particular location. The process is then repeated for all possible magnitudes and locations with the probabilities of each summed. This probability is computed using the total probability theorem, which can be summarized as follows:

$$\lambda_{y^*} \approx \sum_{i=1}^{N_S} \sum_{j=1}^{N_M} \sum_{k=1}^{N_R} v_i P [Y > y^* | m_j, r_k] P [M = m_j] P [R = r_k] \quad (1)$$

where λ is the occurrence rate of the event in the considered time; N_S , N_M , N_R are respectively the potential earthquake sources, potential magnitudes and potential distances; ν is the occurrence rate of events with $M > m_{min}$.

For this study, the R-CRISIS code (Ordaz & Salgado-Gálvez, 2019) was used, the first version of which was released in 1986. R-CRISIS allows to carry out PSHA analyses using an entirely probabilistic approach through the four steps described above.

3.1.1 Earthquake catalog

The input data are a very delicate aspect for seismotectonic and seismic hazard studies. In line with the MPS04 (Gruppo di Lavoro MPS, 2004), the Parametric Catalog of Italian Earthquakes - CPTI15 v3.0 (Rovida *et al.*, 2021) has been adopted to compile a first input dataset. CPTI is nowadays considered the main tool for seismic hazard models, due to its attempt to homogenize the magnitudes of pre-instrumental (historical) and instrumental events (Valensise *et al.*, 2018). The catalog contains all known Italian earthquakes from year 1000.

For the instrumental period, the catalog makes use of moment magnitude (M_w) estimates defined by various local authorities responsible for this calculation. Where these are readily available (typically for medium to large earthquakes), the data are used directly. Where agencies have provided data in other magnitude scales, these are converted to M_w through regression laws (Rovida *et al.*, 2020).

For pre-instrumental earthquakes, the magnitude is defined starting from the macroseismic intensity data (therefore from the historical earthquake felt reports) through the Boxer code (Gasperini *et al.*, 1999). Boxer is a calculation code that allows to relate the spatial distribution of the intensity data of an earthquake with its location and magnitude and, therefore, to derive the latter. It is evident that the average uncertainty associated with the estimate of the moment magnitude starting from historical data can be significant. For the entire catalog it is estimated, at one standard deviation, in ± 0.46 m.u. (unit of magnitude). Even for the experimentally determined magnitudes, the uncertainty on the estimate remains in the order of ± 0.2 m.u. for numerous problems intrinsic to the definition of magnitude itself, as extensively described in Bormann *et al.*, (2002). To evaluate the overall completeness of the CPTI catalog, Rovida *et al.* (2020) report the cumulative graphs of the numbers of earthquakes above thresholds of different magnitudes at intervals of 0.5 m.u., defining the value of M_w 4 as the magnitude of completeness for the entire catalog. From the CPTI catalog, all the available events have been selected starting from the geographical midpoint between the two dams, within a radius of about 150 km. The resulting selection collects 395 events, spanning a time interval from 1019 to 2017 and having a moment magnitude range of $2.9 \leq M_w \leq 7.2$.

Using this approach, it is assumed that the seismicity of each source has a "Poissonian" behaviour, which means that:

- 1) The number of events in a time interval is independent of the number of any other time interval;

- 2) The probability of an event occurring during a small time interval is proportional to the length of the time interval;
- 3) The probability of more than one event during a small time frame is negligible.

These properties indicate that the events of a Poisson process occur randomly, with no "memory" of the time, size or place of previous events. The seismicity record can therefore be distorted by the presence of dependent events, i.e. events that anticipate (foreshock) or follow (aftershock) the main seismic event. Although these dependent events can cause significant effects, the PSHA according to the Cornell's approach must evaluate the hazard starting from discrete and independent releases of seismic energy, thus requiring the dependent events to be removed from the seismicity database. The success of any attempt to study the randomness of main sequence events depends on the skill with which aftershock are identified and removed from catalog lists. This procedure goes by the name of "declustering".

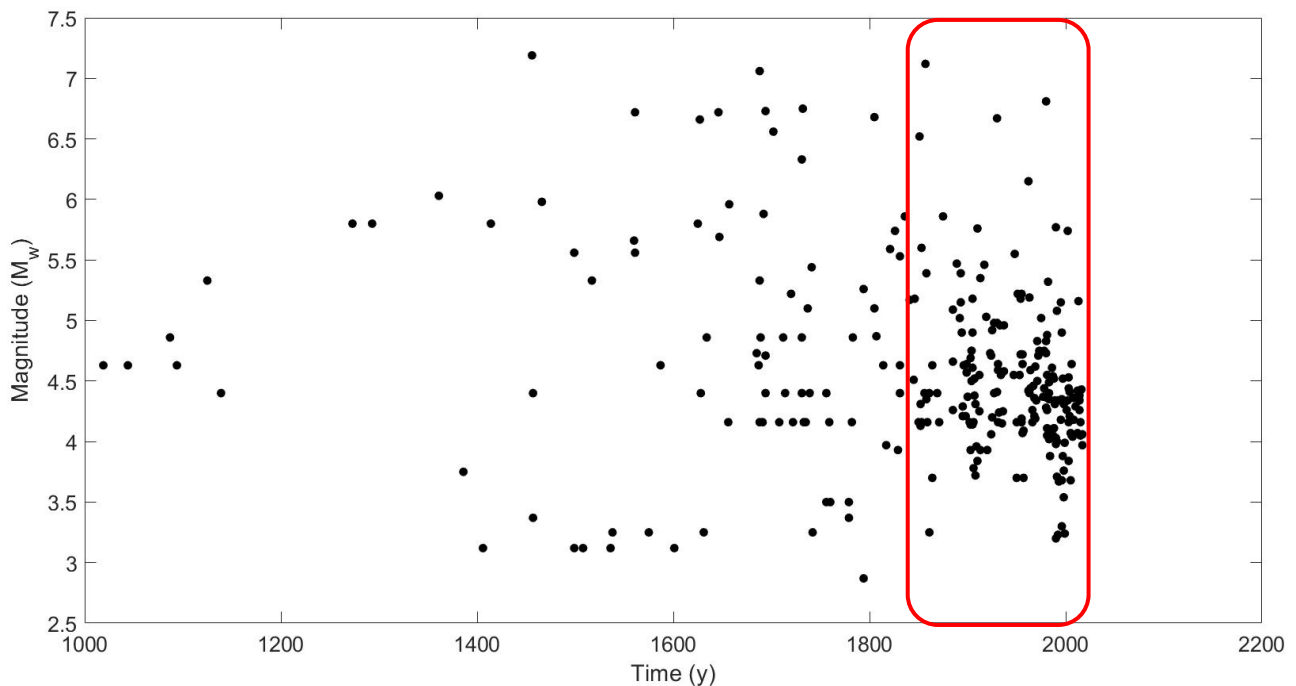


Figure 13. Distribution over time of the declustered database. The size of the earthquakes in the y-axis is given in moment magnitude M_w (estimated and/or converted from other magnitudes or macroseismic intensity data for almost all of the catalog). The area with data refinement is circled in red, used to verify the Poissonian trend of the distribution.

Consistently with MPS04 (Gruppo di Lavoro MPS, 2004), it was decided to consider a spatial window of 30 km and a time window of ± 90 days (centred on the main event), following the Gardner & Knopoff (1974) method. All events within these ranges have therefore been removed from the initial event selection. The declustering reliability was investigated by checking that the distribution of the remaining events was Poissonian, through the statistical goodness of fit Pearson's chi-square test (χ^2 ; Pearson, 1900). The events of the declustered catalog (the quantity of which decreased from

395 to 286) were represented in a time-magnitude graph (Figure 13), in order to investigate the dataset related to the period in which data are more numerous, i.e. from 1850. It was decided to validate the χ^2 test on this temporal portion of data as it is considered more complete, therefore statistically more reliable. The events have been divided into 30-days groups and λ was calculated, that is the average number of events in the considered time interval. A two-tailed hypothesis test was then set up with a significance level of 5%, with null hypothesis (H_0): the distribution of events grouped by months is Poissonian. Table 4 shows the significance test on the data.

Table 4. Calculation of the statistical chi-square (χ^2) and verification by means of a two-tailed hypothesis test with a significance level of 5%.

Mainshock (1850-2017)	Monthly average of events over time	χ^2	p-value for 2015 degrees of freedom
196	0.0972	2087.428571	12% (= 0.12)

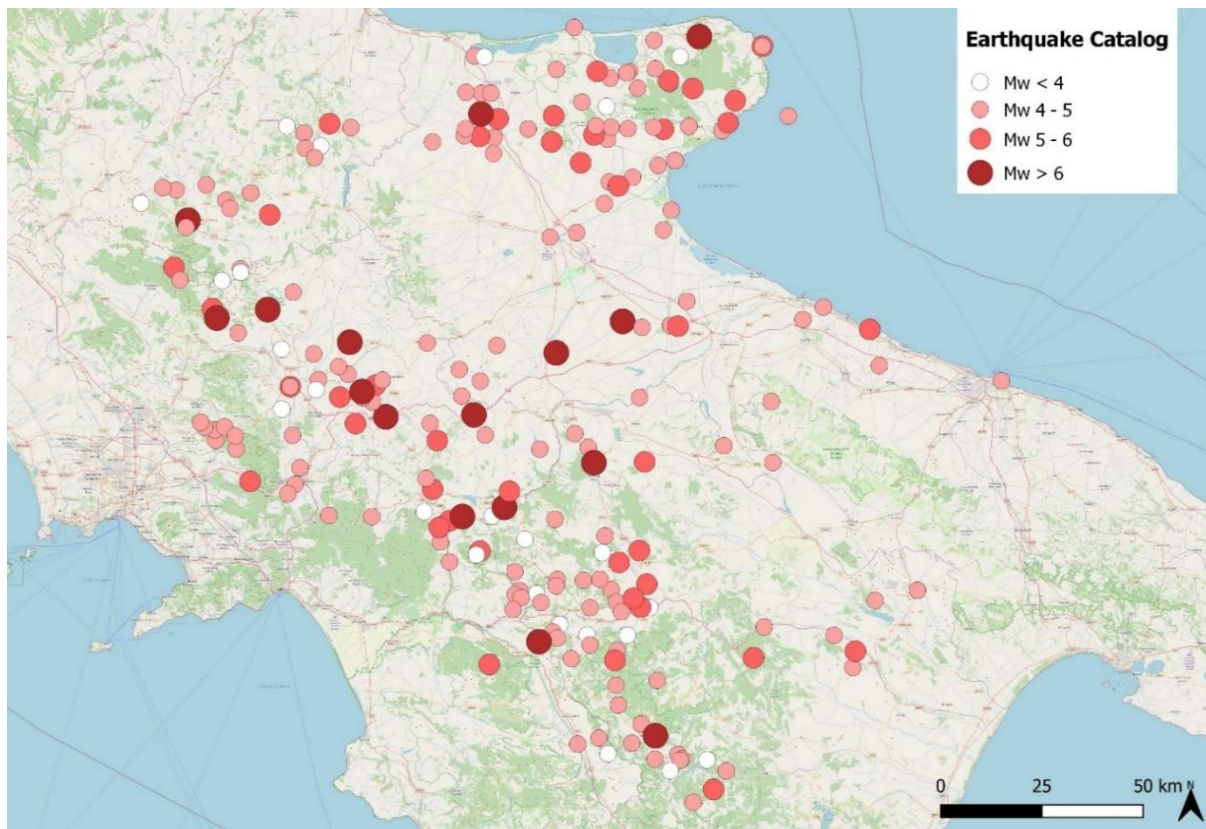


Figure 14. Geographical distribution of the 286 earthquakes of the declustered database, used for the reassessment of the seismic hazard (events occurred between 1019 and 2017, with $3.1 \leq Mw \leq 7.2$). Reference catalog: CPTI15 v3.0 (Rovida et al., 2021).

The p-value of 12% is greater than a significance level of 5% on two tails: it is therefore possible not to reject the null hypothesis, that is that the distribution of events in the declustered catalog is Poissonian. The resulting declustered database, shown in Figure 14, used for the following seismic hazard calculation, collects a total of 286 events, covering a time interval from 1019 to 2017 and ranging a moment magnitude variability of $3.1 \leq Mw \leq 7.2$.

3.1.2 Identification and characterization of seismogenic sources

A seismic hazard model is based primarily on the identification of seismogenic sources that could produce significant ground shaking at the site of interest. Their characterization consists in evaluating the probability that a source could generate a strong earthquake, with potential dislocation on the surface or activation of adjacent/underlying faults (Basili *et al.*, 2007). The characterization of the sources can be operated through two approaches:

- if the amount of local information allows it, by calculating the probability that an earthquake of a given magnitude and with a certain kinematics will cause the faulting of the topographical surface;
- with a more deterministic method, which is based on the known characteristics of the seismogenic sources and of the active faults known for the site of interest. This method was considered more appropriate in the context of this project.

Seismogenic sources can be assumed as point-like, linear, areal or volumetric. The adoption of polygonal areas that enclose a certain number of known structures is one of the expedients used to overcome the uncertainty about the possible incompleteness of information on individual seismogenic sources (Basili *et al.*, 2007). For this study, it was decided to test two types of seismogenic sources: DISS sources (DISS Working Group, 2021) and ZS9 sources (Meletti *et al.*, 2008). The hazard models resulting from the use of one or the other type of source area will be mediated through the use of the logic trees (see paragraph 3.1.5).

To date, the national reference database for seismotectonic studies is the Database of Individual Seismogenic Sources (DISS Working Group, 2021), a geo-referenced archive of information on seismogenic sources and the estimate of their potential (Basili *et al.*, 2008). Many recent seismic hazard studies focused on the prediction of ground shaking have used this database, which represents the first of the two types of seismogenic source chosen for this work. In Appendix A the closest (100 km radius from the facilities) individual (ITIS) and composite (ITCS) seismogenic sources to the Marana Capacciotti and San Pietro sull'Osento dams are listed. For PSHA purposes, the sources were subsequently grouped into six macro-sources (Figure 15), based on the areal distribution of the epicentres useful for this study and the prevailing faulting mechanisms. The choice to group the events into six macro-sources originates from the attempt to try to have a sufficient number of events for each source and to accommodate the different types of faulting. The San Pietro dam is located within the Source 4, which includes the important source of the 1930 earthquake.

For the definition of the MPS04 map officially used at a technical level, a seismogenic zoning of the Italian territory has been defined, the latest version of which is called ZS9 (Meletti *et al.*, 2008). It provides for a subdivision into 36 zones whose limits have been traced on the basis of tectonic or geological-structural information and of different characteristics of seismicity (Figure 16). The seismogenic zones are obtained by drawing a series of polygons on the seismically active territory: they contain areas whose seismicity can be considered homogeneously distributed in space and

stationary over time (Meletti *et al.*, 2008). Since we focus on Southern Apennines and on the Apulian foreland, the source areas 924, 925, 926, 927, 928 were adopted for this study (Figure 16). The Molise earthquakes (October-November 2002) delineate the 924 zone, originating from sources with an E-W direction and right strike-slip kinematics. The same EW direction is shared by the rupture zones 925 (which includes the source of the 1930 earthquake) and 926, based on the events of Potenza in 1990 and 1991. Source 927 encloses the area characterized by the maximum release of energy, linked to the extension of the southern Apennines. Source 928 transfers the minimal, but not negligible, contribution of the Neapolitan volcanic area. The San Pietro and Capacciotti dams are located within the ZS9 - 925 "Ofanto" area (Figure 16).

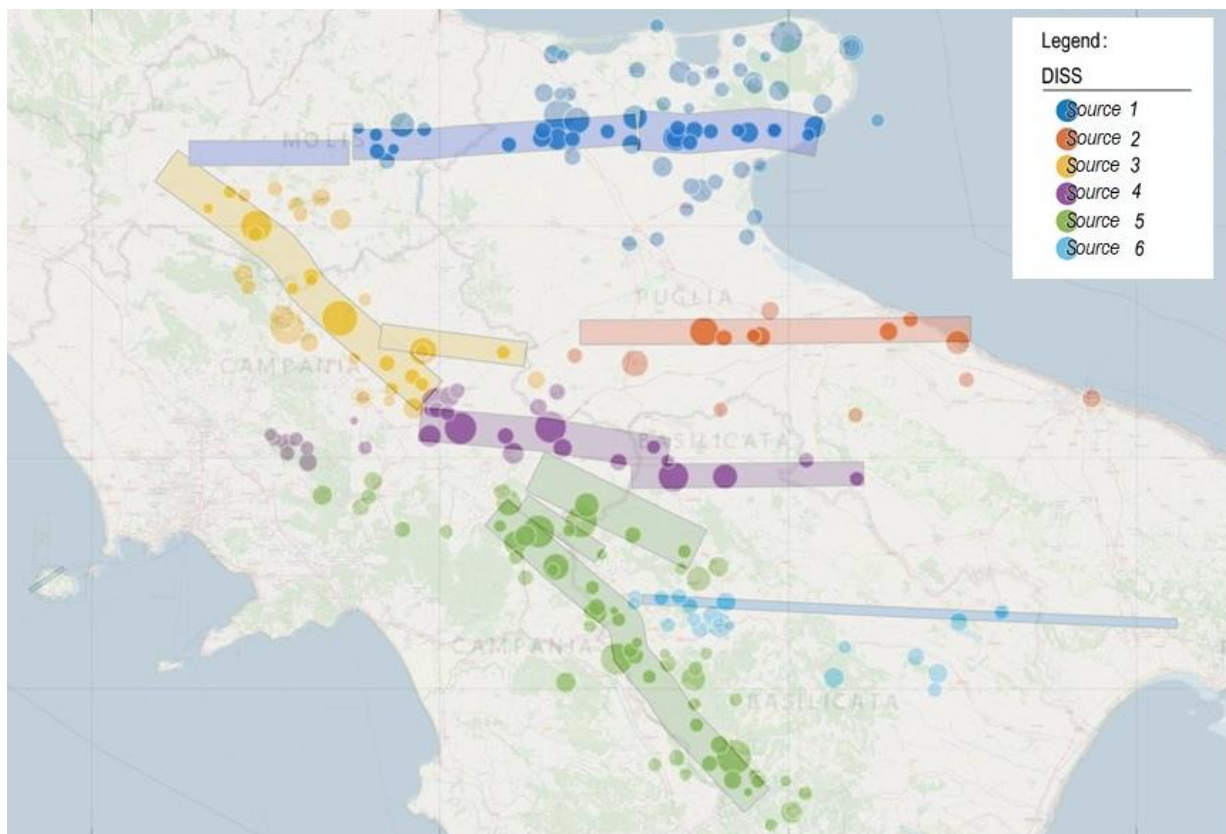


Figure 15. The DISS sources (DISS Working Group, 2021) were grouped into six macro-sources. Each of the six macro-sources brings together individual (ITIS) and composite (ITCS) seismogenic sources, a detailed list of which is provided in Appendix A. The seismic events are associated to the sources based on the areal distribution of the epicentres and the prevailing faulting mechanisms.

For what concerns the geodynamic behaviour of the areas selected from the DISS dataset, in accordance with the classification used by Sadigh *et al.* (1997), the faulting mechanisms have been expressed according to three typologies: normal, inverse, transcurrent. For the DISS sources, the faulting mechanisms of the seismogenic sources were investigated through the parametric information contained in DISS (DISS Working Group, 2021) and in specific studies available for some sources.

- **Source 1.** Located near the Gargano promontory, it is the northernmost of the sources useful for this study. It develops in the W-E direction and it is characterized by individual and composite sources with almost vertical planes, slightly north-dipping. The epicentres of the San Giuliano di Puglia sequence are recognized in this area with a dominant transcurrent kinematics (Di Luccio *et al.*, 2005; Fracassi & Valensise, 2007; Vannoli *et al.*, 2016).
- **Source 2.** It crosses the town of Cerignola (Foggia) and it is about 10 km far from the Marana Capacciotti dam. It develops in the W-E direction and it is characterized by individual and composite sources with almost vertical planes, slightly north-dipping. The study by Vannoli *et al.* (2016) and the focal mechanisms provided by the national seismic network managed by INGV (<http://terremoti.ingv.it/>) recognize the same transcurrent mechanism.

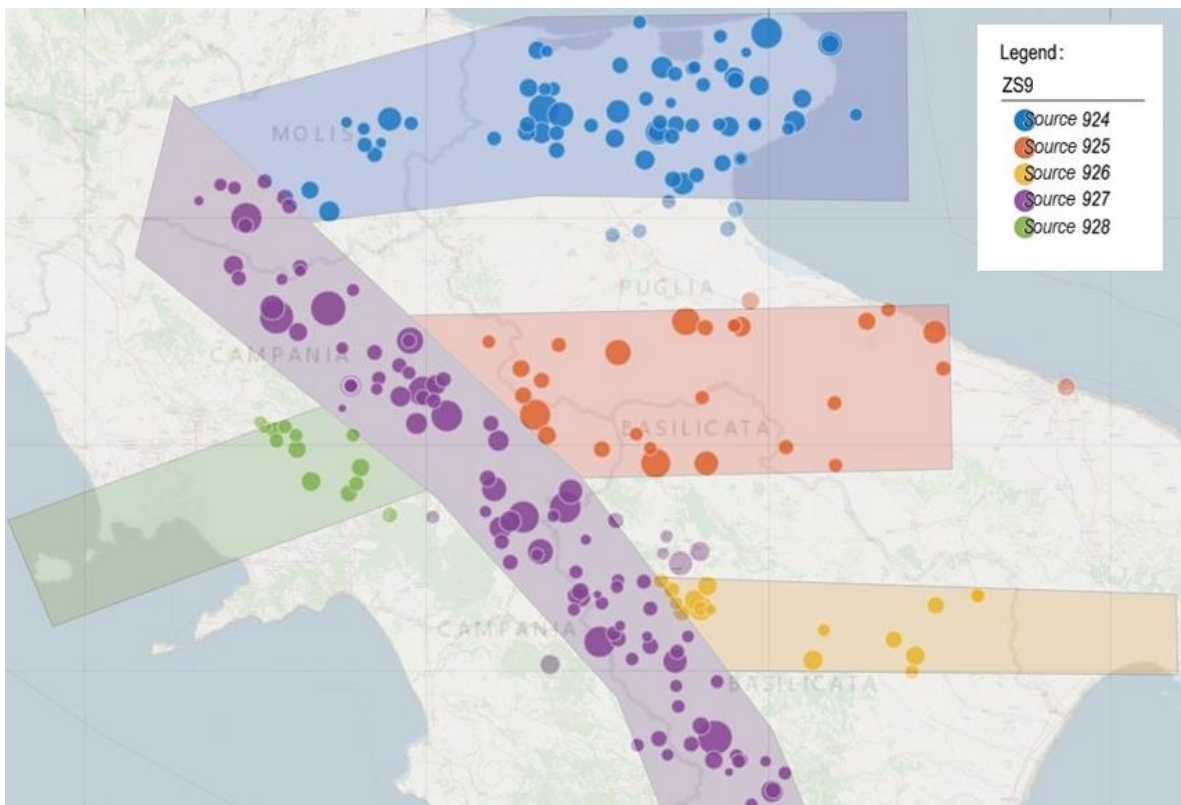


Figure 16. The ZS9 sources. The San Pietro and Capacciotti dams lie within zone 925. The seismic events are associated to the sources based on the areal distribution of the epicentres and the prevailing faulting mechanisms.

- **Source 3.** It is the northernmost sector of the large NE dip high-angle normal fault system of the southern Apennines (Vannoli *et al.*, 2016; DISS Working Group, 2021). This source is associated with the highest (estimated) magnitude event present in the database used for this study, the 1456 Mw 7.2 earthquake, whose epicentre is still debated (Guidoboni & Ferrari, 2004; Fracassi & Valensise, 2007).

- **Source 4.** This fault system is located between Sources 3 and 5, breaking the Apennine ridge, east of the city of Benevento and towards the northern slope of the Vulture volcano. Inside the source, in its central portion, is the San Pietro sull'Ossento dam. It includes individual and composite seismogenic sources in W-E direction which generally dip to the North. Several studies (e.g., Fracassi & Valensise, 2007; Vannoli *et al.*, 2016) recognize an oblique transcurrent mechanism.
- **Source 5.** It develops along the axial zone of the Apennine chain, as a southern continuation of Source 3, and it is characterized by a normal faulting with NE-SW oriented axes (Fracassi & Valensise, 2007; Vannoli *et al.*, 2016). This source is associated with the M_w 6.8¹ 1980 Irpinia event.
- **Source 6.** It develops in the W-E direction, East of the main extensional axis of the southern Apennines. It straddles the area between Basilicata and Puglia, from the city of Potenza (West) to the North of the city of Taranto (East). It is characterized by an oblique strike-slip mechanism and by almost vertical plans, slightly dipping towards the South (DISS Working Group, 2021).

As regards the prevailing faulting mechanisms associated with the source zones ZS9, Sources 924, 925, 926 have been modelled with a prevalent transcurrent faulting mechanism, while zones 927 and 928 according to normal mechanism (Meletti *et al.*, 2008).

Seismogenic sources have traditionally been modelled in different ways: from simple plans to circular ones (e.g., Brune, 1970). In Figure 17 simplified representations of the two different seismogenic zonings are shown. For areal seismic sources, we initially assume a circular rupture behaviour (Ordaz & Salgado-Gálvez, 2019) whose radius R (in km) is correlated to the magnitude M through coefficients, K_1 and K_2 according to the relationship:

$$R = K_1 * e^{K_2 M} \quad (2)$$

There exist several regression analyses to study the relationship between magnitude and rupture area; for this study, the Wells & Coppersmith (1994) empirical law was chosen as a reference, in which the coefficients K_1 and K_2 assume different values based on the faulting mechanisms (normal, inverse, transcurrent). The seismicity within each zone is assumed to be uniform (this is the basic requirement of the Cornell method, 1968): earthquakes have the same probability of occurrence over the entire source and they follow the same law of recurrence, which will be discussed in the following paragraph.

¹ Moment magnitude classification according to the CPTI3 v3.0 catalog (Rovida *et al.*, 2021).

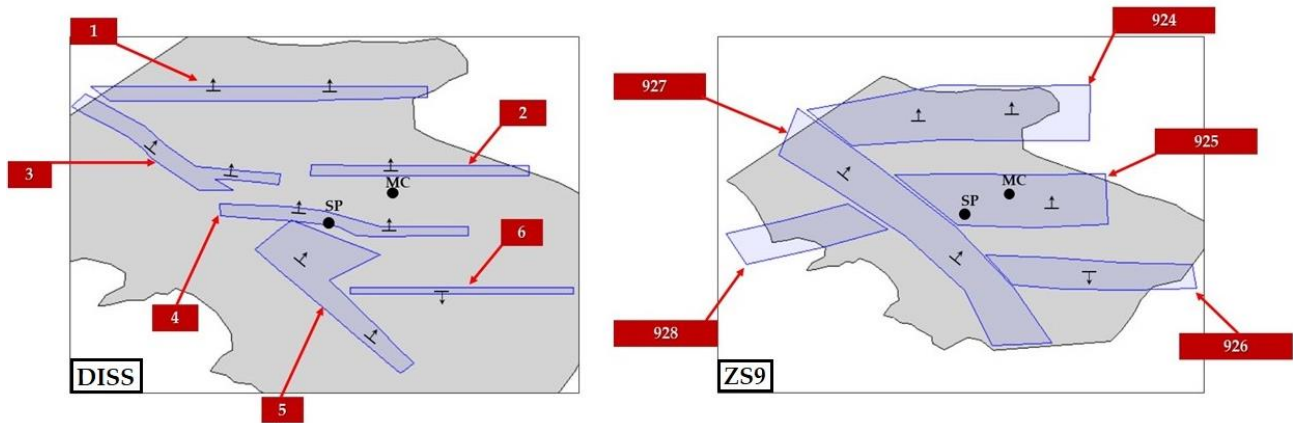


Figure 17. Representation on R-CRISIS of the two seismogenic zonings proposed in this study. The position of the facilities is highlighted by the black dots: in the DISS zoning (left panel) the Marana Capacciotti dam (MC) is located between Source 2 and Source 4, while the San Pietro sull'Osento dam (SP) it is placed within the latter; in the ZS9 zoning (right panel) both the Marana Capacciotti dam (MC) and the San Pietro sull'Osento dam (SP) are located within the 925 seismogenic zone. Arrows show dip angles.

3.1.3 Seismicity rates and maximum expected magnitude

The seismic hazard analysis requires that a distribution of the seismicity rates is defined, i.e. that the annual occurrence rate of earthquakes of different magnitudes is defined. This distribution is described by earthquake recurrence laws. A basic assumption of the PSHA is that these laws, obtained from past seismicity, are appropriate for the prediction of future seismicity. Since the 1940s Gutenberg and Richter, after defining the first magnitude scales (local magnitude M_L and surface wave magnitude M_s) focused their studies on the magnitude-frequency distributions of seismic events. They observed that the number of earthquakes per magnitude class decreased by roughly a factor of 10, i.e. that earthquakes with a magnitude, for example, < 7 were 10 times less frequent than those of magnitude < 6 , 100 times less frequent than those of magnitude < 5 and so on. The empirical law that relates the number of earthquakes to the magnitude takes the name of "Gutenberg & Richter Law" (1944), hereinafter referred to as "G-R", and is expressed in general form as:

$$\log(N) = a - bM \quad (3)$$

where N is the number of earthquakes with magnitude greater than or equal to M , a is the intercept of the G-R curve and corresponds to the number of earthquakes that occur for a certain time interval (usually normalized to one year) for the completeness magnitude, b (or b -value) is the slope of the G-R and defines the abundance of small versus large earthquakes. Among these variables, the parameter b has received much more attention in recent decades and it has undergone many statistical and evaluative analyses. In fact, experimental data show a certain variability of the b -value of G-R in space and time: its long-term average value for the entire globe varies in the range 1.02 ± 0.03 (El-Isa & Eaton, 2014). On a local scale, however, the b -value has been reported to show a relatively large range of variation, from 0.3 to 2.5 or more (El-Isa & Eaton, 2014). Some studies suggest that the temporal and spatial variations of b may be caused by a number of factors, including

calculation method, tectonic stress, volcanic activity, clustering and background seismicity, petrological characteristics, completeness and homogeneity of seismicity data.

As for the magnitude of completeness (M_c), by definition, no catalog is ever complete, since it does not report all the earthquakes that actually occurred in the area of interest and in the period of reference. The magnitude of completeness, i.e. the magnitude threshold below which data are probably missing in the catalog, is the point at which the experimental curve deviates from the theoretical trend, calculated as the maximum curvature on the number of events (Wiemer & Wyss, 2000). Although completeness problems generally concern small earthquakes, the importance of determining the completeness of a catalog lies in the fact that, in order to obtain the seismicity rates, the number of earthquakes must be normalized with respect to time, therefore with respect to the period in which the catalog it is considered complete (Basili *et al.*, 2007). The completeness of the entire CPTI catalog, as already mentioned in paragraph 3.1.1., is reached from 1975 onwards for earthquakes of magnitude $M_w \geq 4.0$ (Rovida *et al.*, 2021). Having used a selected portion of the entire catalog for this study, it was decided to verify the magnitude of completeness of the data available in the selected geographical area, starting from 1975, both through the method of Wiemer & Wyss (2000), and through the method of Cao & Gao (2002). In this case, M_c is estimated using the stability of the b -value as a function of the cut-off magnitude (M_{co}). The procedure consists in calculating the b -value for progressive cut-off magnitudes: this assumes that the values of b increase for $M_{co} < M_c$, until $M_{co} = M_c$. At this value, b reaches its real value and the trend stabilizes, so it is possible to identify the most likely magnitude of completeness, in this case equal to $M_c = 4.2$ (Figure 18). The method returns the same result obtained with the maximum curvature method (Figure 19). Not surprisingly, this value is only slightly different from the magnitude of completeness considered in the CPTI catalog as a whole.

The declustered catalog has been subsequently spatially disaggregated into the six seismogenic sources relating to the DISS catalog and into the five source zones relating to the ZS9 zoning, neglecting the distribution with the depth of seismicity (due to the enormous uncertainties of this parameter, not only relating to historical data but also often instrumental ones). Where bibliographic sources were present (DISS Working Group, 2021), the events were easily associated with the corresponding source. In the absence of information, the epicentres were associated with the sources by proximity (see also Figure 15 and Figure 16).

The maximum expected magnitude determines, together with the seismicity rates, the expected shaking for various return periods and its role is to truncate this distribution upwards. The maximum expected magnitude is traditionally set equal to the magnitude of the strongest event reported in the catalog of earthquakes associated with a given source (in this case, by the CPTI5 v3.0; Rovida *et al.*, 2021). However, since believing this value would imply being certain of the absolute correctness and completeness of the reference catalog, it was considered appropriate to compare with the maximum magnitude potentially associated to the seismogenic sources identified in the reference databases for faults (DISS Working Group, 2021). In this case, the value is defined on the basis of geological, geometric and paleoseismological evidence of the structure itself. There are

various methods in literature (e.g., Kanamori & Anderson, 1975; Scholz *et al.*, 1986) which allow to estimate the expected magnitude for a source from its area or fault length. Typically, such empirical laws are based on the observed relationship between geometric data and the seismic moment for large inter- and intra-plate earthquakes.

Table 5. Distribution of the 286 seismic events divided by source. For each seismogenic source, the number of events and the associated maximum magnitude are listed.

		Number of events	Maximum Magnitude
DISS ZONATION	SOURCE 1	68	$M_w = 6.7$
	SOURCE 2	15	$M_w = 6.3$
	SOURCE 3	41	$M_w = 7.2$
	SOURCE 4	78	$M_w = 6.7$
	SOURCE 5	62	$M_w = 7.1$
	SOURCE 6	22	$M_w = 5.8$
ZS9 ZONATION	SOURCE 924	68	$M_w = 6.7$
	SOURCE 925	44	$M_w = 6.7$
	SOURCE 926	22	$M_w = 5.8$
	SOURCE 927	90	$M_w = 7.1$
	SOURCE 928	62	$M_w = 5.9$

The common practice is to use the highest magnitude between the two databases as a precaution. In the case of DISS sources, the maximum expected magnitude provided by the two sources coincides for Sources 2, 4 and 6; it is underestimated in Sources 3 and 5 in the paleoseismological studies with respect to the catalog (for which the highest value, provided by the CPTI, is taken as a reference); it is overestimated in Source 1 in paleoseismological studies compared to data. In this case, in fact, the bibliography proposes a higher maximum expected magnitude (M_w 7, referring to the 1456 earthquake) compared to the strongest event associated with Source 1 (M_w 6.7). As previously discussed, for this historical earthquake various hypotheses have been proposed regarding the location of the seismogenic sources (e.g., Guidoboni & Ferrari, 2004), for which its epicentre in the CPTI was located in a point that lies within the immediately adjacent source, that is in Source 3. However, as a precaution, for Source 1 we have chosen to consider as the maximum expected magnitude the one reported by the reference catalog for faults (DISS Working Group, 2021). The maximum magnitudes of the ZS9 rupture zones agree with what is reported in the DISS zones.

Earthquake data were then organized in a magnitude-frequency distribution and, by applying the method of Aki (1965), the G-R laws for each of the different seismogenic sources were calculated. Aki's formula (1965) uses the maximum likelihood method to calculate the b -value and can be expressed as follows:

$$b = \frac{1}{\ln(10)(\mu - M_{\text{thresh}})} \quad (4)$$

where μ is the sample mean of the magnitudes, M_{thresh} is the threshold magnitude of completeness. The uncertainty σ_b is estimated by Aki (1965) as

$$\sigma_b = \frac{b}{\sqrt{N}} \quad (5)$$

where N corresponds to the number of earthquakes. Having a limited dataset available for the study area, we have cautiously chosen to use the G-R law for the overall dataset and to extend its slope to all sources, modulating instead the parameter a , source by source.

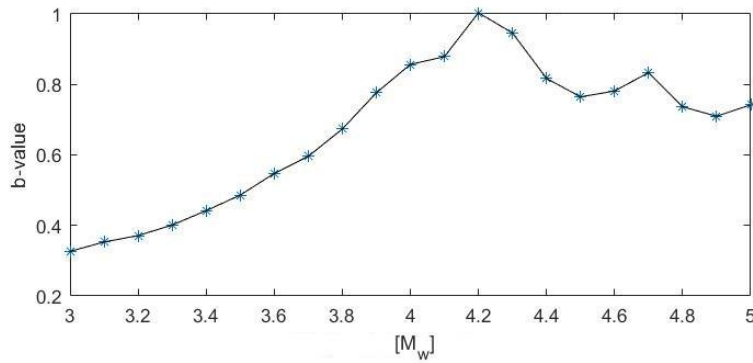


Figure 18. Identification of the magnitude of completeness ($M_c=4.2$) through the method of Cao & Gao (2002).

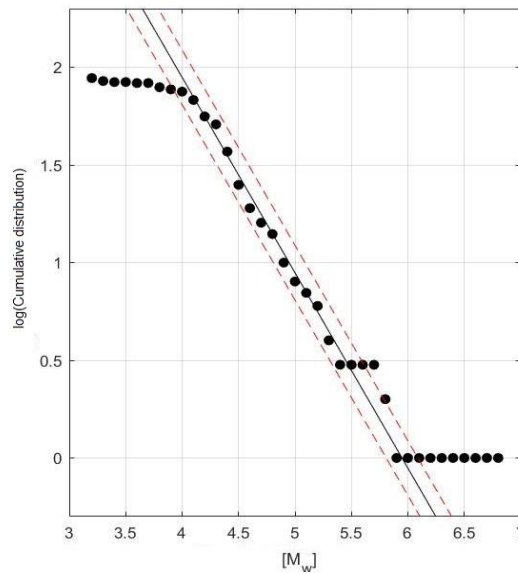


Figure 19. Gutenberg-Richter distribution for the overall dataset. The magnitude of completeness ($M_c = 4.2$) is also confirmed by the method of maximum curvature of Wiemer & Wyss (2000). In black, the regression line; the uncertainty range is dashed in red. The b -value $b = 1.00 \pm 0.14$ was taken as a reference for all the sources used.

The b -value 1.00 ± 0.14 was assumed to be representative of all sources. The data obtained in terms of threshold magnitude, annual frequency of the threshold magnitude, b -value, maximum expected magnitude have been the input for the seismic hazard calculation.

3.1.4 Ground Motion Models (GMMs)

After determining the seismogenic potential of the sources, the seismic hazard was assessed by transferring the contribution of each zone to the site through appropriate Ground Motion Models (GMMs). In general, the functional form of the GMMs includes a linear term (which describes the dependence of the shaking on the magnitude) and a non-linear term (which represents the dependence on the distance). The most recent attenuation laws also include a site coefficient, a factor by which the amplifications related to non-rocky sites can be taken into account. The choice of the models to be used for the PSHA is often difficult, because the number of equations available in literature is very high and the difference between them is extremely large, since the dispersion of data is very large. The commonly used criterion is to choose relationships derived from data sets registered in the region of interest and, possibly, to combine them in a logic tree. This should allow to obtain an average result, but with no guarantee that this is a more correct approach (see paragraph 3.1.5). The GMMs deemed more appropriate in the context of this project are the following:

- **Sabetta & Pugliese (1996)**. Also employed in MPS04 (Gruppo di Lavoro MPS, 2004), it is one of the first and most important attenuation relationships for Peak Ground Acceleration (PGA) built on an Italian database. It is valid over an integration distance from 1 to 100 km, for a moment magnitude range from 4.6 to 6.8 (therefore it does not completely cover the range of our input data). To compute the seismic hazard in the two sites taking into account the amplifications related to non-rocky sites, this law distinguishes two categories: shallow alluvium ($H = < 20$ m) and deep alluvium ($H > 20$ m), where H is the thickness of the soil layer. Based on our geophysical characterization (see chapter 5), the San Pietro dam can be modelled as a shallow alluvium category; the Marana Capacciotti dam as a deep alluvium.
- **Ambraseys *et al.* (1996)**. Also used as an attenuation model in MPS04 (Gruppo di Lavoro MPS, 2004), it was developed using European strong-ground motion data. Its spectral period range goes from 0.01 to 2 s, it is valid over an integration distance from 1 to 100 km, for a moment magnitude range from 4.6 to 6.8 (therefore, even in this case it does not completely cover the full range of our input data). The classes of site geology for the non-rocky site computation are defined by the following ranges of average V_s : stiff soil (A) 360-750 m/s; soft soil (S) 180-360 m/s, and very soft soil (L) < 180 m/s. Based on our geophysical characterization (see chapter 5) the San Pietro dam can be modelled as a stiff soil; the Marana Capacciotti dam as a soft soil.
- **Bindi *et al.* (2011)**. Also used among the attenuation laws in the most recent Italian seismic hazard model MPS19 (Lanzano *et al.*, 2020; Meletti *et al.*, 2021), this GMM has been derived for the geometrical mean of the horizontal and vertical components, from the Italian strong motion database. It is valid over an integration distance from 1 to 200 km, for a moment magnitude range from 4.6 to 6.9 (therefore, in this case too, it does not fully cover the range of our input data). In this case the model contemplates the choice of site classes based on V_{S30} , so the models have been computed for site class C for both facilities.

- **Cauzzi *et al.* (2015)**. Also used among the attenuation laws in the most recent Italian seismic hazard model MPS19 (Lanzano *et al.*, 2020; Meletti *et al.*, 2021), this GMM is an empirical model based on a global dataset of digital acceleration records, with a valid distance ranging from 0 to 150 km and with a moment magnitude range from 4.5 to 7.9. In this case the model contemplates the choice of site classes based on V_{s30} , so the models have been computed for site class C for both facilities.

Figure 20 provides a graphical comparison of the four attenuation laws used for the seismic hazard assessment, modulated according to magnitude classes. In all cases, the Sabetta & Pugliese (1996) and Ambraseys *et al.* (1996) models are the laws that attenuate less the shaking parameter (in this case, the acceleration expressed in cm/s^2) with distance, so they are to be considered more precautionary among the four.

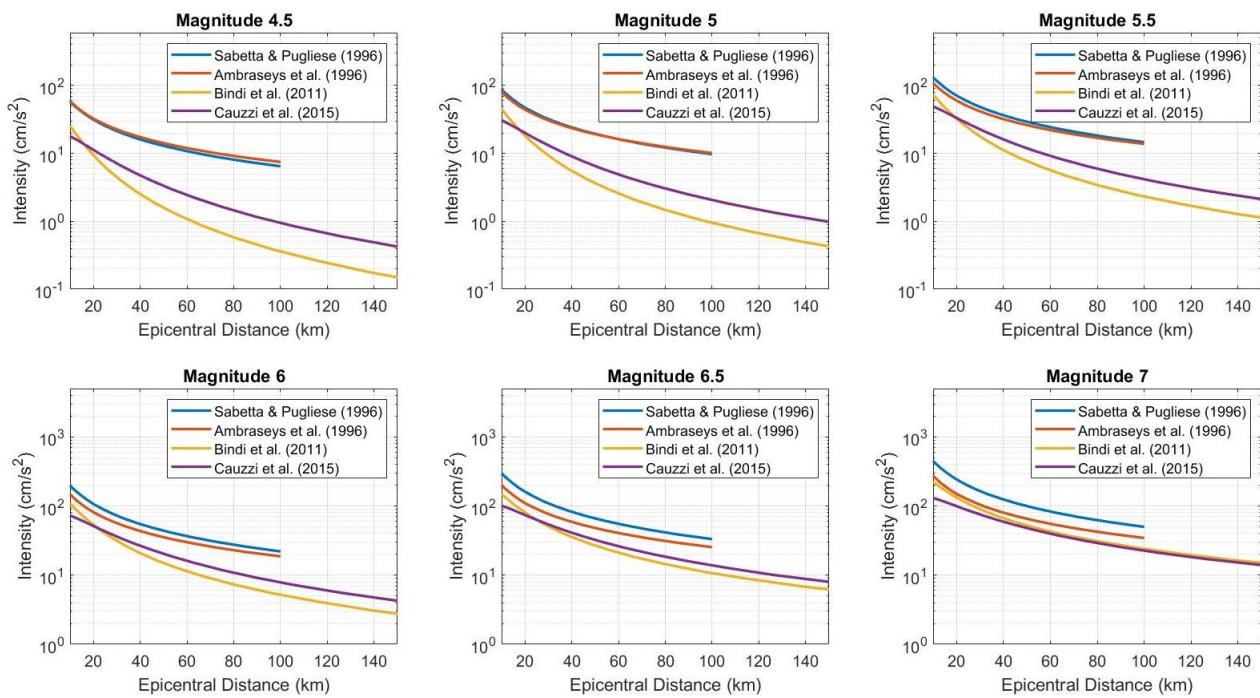


Figure 20. Comparison between the selected GMMs, modulated according to magnitude classes.

3.1.5 Discussion of the uncertainties

In order to explore the uncertainties in our models, the use of logic trees was adopted, nowadays widely used as a tool for considering the epistemic uncertainty. In PSHA, the procedure is to incorporate the epistemic uncertainty in the calculations by building separate branches for each of the choices made during the creation of the hazard model. Each of these choices is assigned a normalized weight that reflects its confidence. The hazard calculations are then carried out following all the possible branches of the logic tree. The final weight of each hazard model is determined by multiplying the weights along all the branches. Despite the extensive use of this methodology, there

are obvious gaps in literature on the guidelines for building logic trees and for assigning weights to branches (Mulargia *et al.*, 2017). For this reason, it was decided to follow the choices made for the realization of MPS04 and MPS19.

The earthquake catalog used for MPS04 and for MPS19 is, as for this work, the parametric catalog of Italian earthquakes - CPTI (paragraph 3.1.1). While in MPS04 a single seismogenic zoning (ZS9) was used and in MPS19 different zonings based on the DISS catalog were chosen, for this work it was decided to consider them both (paragraph 3.1.2). For what concerns the Earthquake Rate Models (ERMs), in MPS04 it is possible to distinguish rates deriving from Gutenberg-Richter laws and individual seismicity rates. In MPS19, 11 independent ERMs are proposed. Due to the limited number of events available in the study area, it was considered appropriate to use only one G-R regression law and its associated b -value (paragraph 3.1.3). The attenuation laws used in MPS04 are four, among which the Ambraseys *et al.* (1996) and the Sabetta & Pugliese (1996) are present. The attenuation laws used in MPS19 are numerous and among them we can also find the Bindi *et al.* (2011) and the Cauzzi *et al.* (2015) models, used for this study. The branches of the logic tree were created taking a cue from MPS04 and MPS19, trying to adopt a similar general structure. As for the weight to be assigned to each branch, first of all several models were run, weighing every choice differently and observing the different results in the final models. Thanks to these sensitivity analyses through the R-CRISIS code (i.e., Aguilar Meléndez *et al.*, 2018), we understood which factor caused a greater difference in the result, therefore substantially the ones that had the most influence on the final data. Thanks to this we realized the influence of each factor on the final result and we weighed each branch accordingly.

3.1.5.1 San Pietro sull'Osento dam

The results presented in paragraph 3.1.6.1 come from the choices described below on the treatment of uncertainties, i.e. of the logic trees that we are about to describe. Generally speaking, the importance of the weights attributed to the branches of a logic tree decreases as the number of branches increases (Bommer *et al.*, 2005), which is why, also in the light of the available data, it was chosen not to include an excessive number of branches. The logic tree built for the San Pietro dam is shown in Figure 21 and discussed below. As discussed extensively in paragraph 3.1.2, it was decided to use two types of seismogenic zones, to test the impacts of the different geometries and, consequently, of a different areal distribution of seismicity. In the case of the San Pietro sull'Osento dam, it was considered appropriate to assign a greater weight to the DISS zoning, due to the greater detail with which it was built.

From our sensitivity analysis, but also widely known in the literature (i.e., Bommer *et al.*, 2005), the attenuation laws are the component of the hazard analysis that has the greatest influence on the final results. As discussed in paragraph 3.1.4, the laws of Sabetta & Pugliese (1996), Ambraseys *et al.*, (1996), Bindi *et al.* (2011) and Cauzzi *et al.* (2015) were considered. Although we are aware that modern laws are calibrated on more recent data, their use would take us too far, downwards, from the values of the current national technical regulations. Given the strategic nature of the surveyed facilities, it was decided to assign greater weight to the oldest laws, which were adopted as well in

MPS04, as they are more precautionary for all ranges of magnitude of interest. The choice differs from the newest MPS19 model, which purposely does not evaluate the impact on the risk, and/or introduces any additional subjective "precautionary" choices.

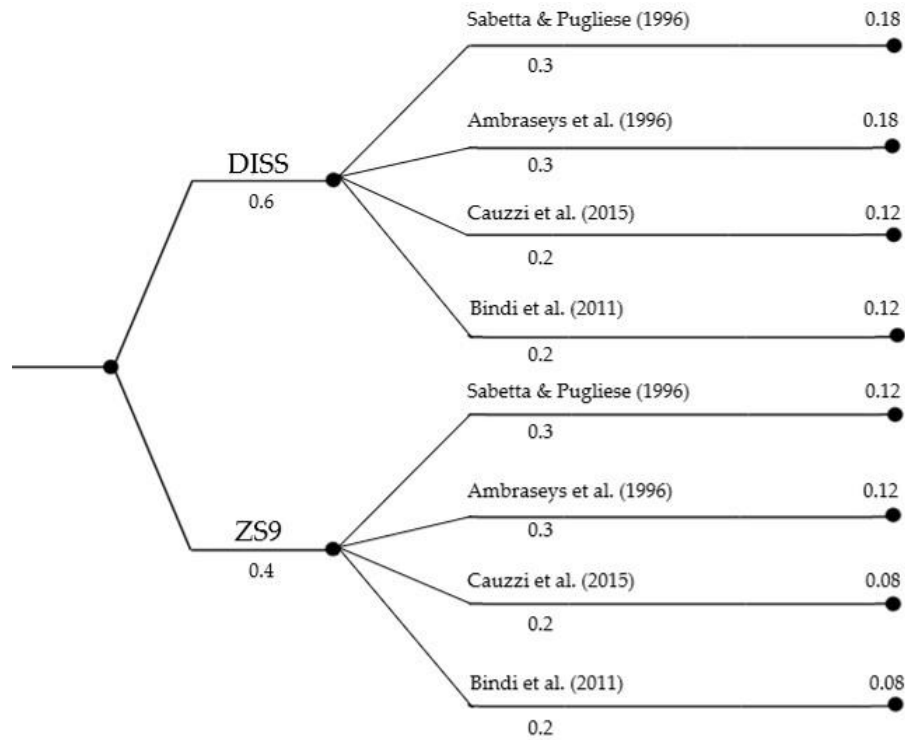


Figure 21. Logic tree and relative weights used for the construction of the seismic hazard model of the San Pietro sull'Ossento dam.

In light of the choices made, the logic tree for the San Pietro sull'Ossento dam has eight total branches, each averaged according to its normalized weight (Figure 21). The eight partial models are shown in Appendix B: the partial models are the same for both sites of interest; the difference lies in the weights with which they have been averaged to obtain the final models. The final model averaged according to the weights of Figure 21 is the result presented in paragraph 3.1.6.1.

3.1.5.2 Marana Capacciotti dam

The logic tree built for the Marana Capacciotti dam is shown in Figure 22 and discussed below. As discussed extensively in paragraph 3.1.2, it was decided to use two types of seismogenic zones. In the case of the Capacciotti dam, it was considered appropriate to give greater weight to the ZS9 zoning, as the DISS zoning does not allow an adequate contribution in terms of seismicity rates to be transferred to this area. As for the attenuation laws, we refer to the considerations of the San Pietro dam. In light of the choices made, the logic tree for the Capacciotti dam appears to have eight total branches, each averaged according to its normalized weight. The eight partial models are shown in the Appendix B: the partial models are the same for both sites of interest, what changes are the weights with which they were averaged to obtain the final models. The final model averaged according to the weights of Figure 22 is the result presented in paragraph 3.1.6.2.

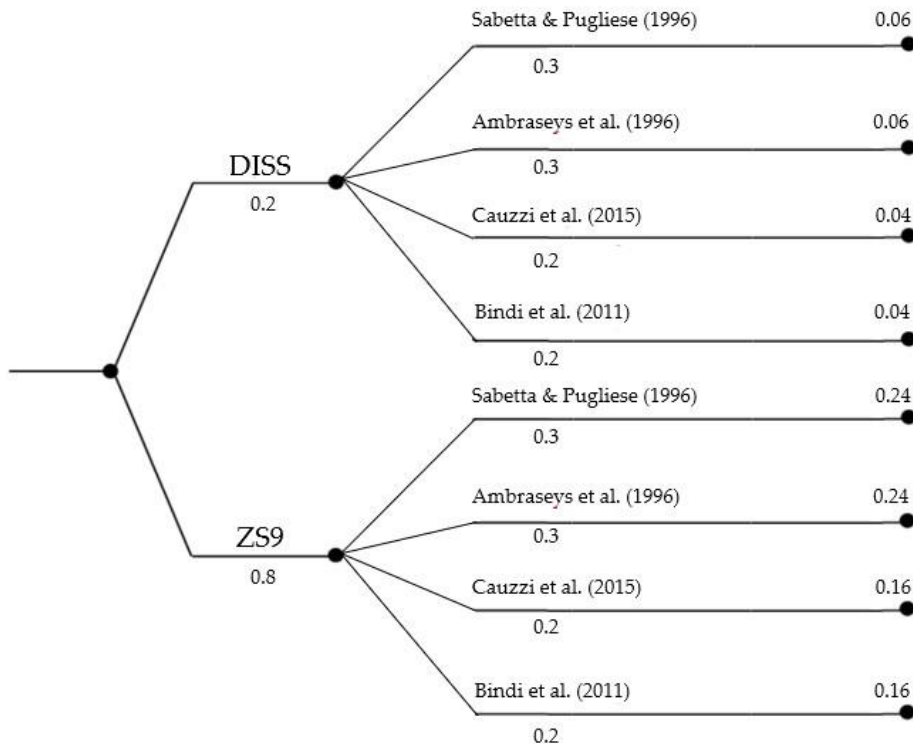


Figure 22. Logic tree and relative weights used for the construction of the seismic hazard model of the Marana Capacciotti dam.

3.1.6 Seismic hazard results

One of the most common ways to represent PSHA results are seismic hazard maps, which usually show values of PGA in a region for a specific return period (T_R). These types of maps are frequently incorporated in seismic codes, which include the minimum requirements to design new buildings and for seismic safety verification of large facilities. To establish T_R , it is necessary to define the reference time period V_R of a construction,

$$V_R = V_N C_U \quad (6)$$

given by the product of nominal life V_N and the class of use C_U . The reference time period V_R represents the time in which it is intended that the ground shaking has a certain probability to be exceeded. The nominal life V_N is intended as the number of years for which the structure can be used with the purpose for which it was built. The four classes of use C_U correspond to a coefficient of use. The V_N and C_U parameters are listed in detail in Table 6: both dams can be considered having a $V_N = 50$ and a $C_U = 2.0$; consequently $V_R = V_N C_U = 50 \times 2.0 = 100$ years. The seismic actions are put in relation to the limit states of the building, which correspond to increasing values of shaking based on the values of the exceedance probability (p): limit state of operation (SLO – 81%), limit state of damage (SLD – 63%), limit state of safety of life (SLV – 10%), limit state of collapse prevention (SLC – 5%). For the purposes of this study, we will refer to the last three limit states just mentioned. For each limit state, the return period (T_R) is therefore calculated:

$$T_R = \frac{V_R}{\ln(1-p)} \quad (7)$$

Table 6. Description of the nominal life V_N parameters and the class of use C_U parameters (NTC, 2008, 2018). Features associated with the San Pietro sull'Ossento and Marana Capacciotti dams are highlighted in green.

	Construction types	V_N (years)
1	Temporary buildings or in construction phase	≤ 10
2	Ordinary buildings: small bridges, infrastructures and dams	≥ 50
3	Great buildings: large bridges, infrastructures and dams or with strategic importance	≥ 100
	Class of use	C_U
I	Buildings with occasional presence of people and agricultural	0.7
II	Buildings with normal crowding, with no dangerous content or public and social essential functions. Not dangerous industries. Infrastructures whose disruption or injury does not cause emergency.	1.0
III	Buildings with significant crowding. Industries with hazardous works. Infrastructures whose disruption may cause emergency. Dams relevant to the consequences of their collapse.	1.5
IV	Buildings with important public functions also in relation to the management of civil protection in case of disasters. Industries with particularly dangerous activities. Roads of type A and B or C connecting exclusively main towns and strategic for the communication after a seismic event. Dams for production of electrical energy or related to the operation of aqueducts.	2.0

The results are shown as follows. The distributions of the PGA values at the sites of interest, with exceedance probability 63% in 100 years ($T_R = 101$ years), 10% in 100 years ($T_R = 949$ years) and 5% in 100 years ($T_R = 1950$ years), respectively for the limit state of damage (SLD), life protection (SLV) and collapse prevention (SLC), were evaluated on the basis of the probabilistic method theorized by Cornell (1968), using all the data, the procedures and choices illustrated in the previous sections, in accordance with the procedures established by the NTC (2008, 2018). The calculations were performed on a grid of points with a step of 0.05° . The seismic hazard models, presented below both in the form of maps (Figure 24, Figure 25, Figure 27, Figure 28), and in numerical values (Table 7, Table 9), were obtained as weighted averages of eight models for each limit state, corresponding to as many branches of a logic tree, which are dealt with separately in the paragraph 3.1.5.

3.1.6.1 San Pietro sull'Ossento dam

The PGA values for the San Pietro sull'Ossento site are slightly higher if compared to the current national technical regulation ones (Table 7), therefore more precautionary, except for the SLD limit state.

Table 7. Results of the seismic hazard models. The table shows the PGA values with exceedance probability of 63%, 10% and 5% in 100 years, according to the method applied in this study and these are compared with the corresponding values reported in the national technical regulation (NTC, 2008, 2018).

REFERRED TO BEDROCK				
	Exceedance probability	Dam	PGA This study	PGA NTC (2008, 2018)
SLD	63% $T_R = 101$ years	San Pietro sull'Osento	0.1 g	0.1 g
SLV	10% $T_R = 949$ years	San Pietro sull'Osento	0.35 g	0.28 g
SLC	5% $T_R = 1950$ years	San Pietro sull'Osento	0.48 g	0.39 g

A comparison was also performed in terms of response spectra, (i) representing the simplified regulatory response spectra at the San Pietro sull'Osento dam site according to the various models for category A (rock) and for the site category C (Figure 23) and (ii) by calculating the Housner intensity (Housner, 1952). The Housner intensity was calculated as the ratio between the integral of the response spectrum of category C and A, in the period bands of major interest for the dams (0.1 - 0.5 s; 0.5 - 1 s); values were then compared to the NTC standard ones. The values of the Housner intensities are provided in Table 8 for the San Pietro sull'Osento dam.

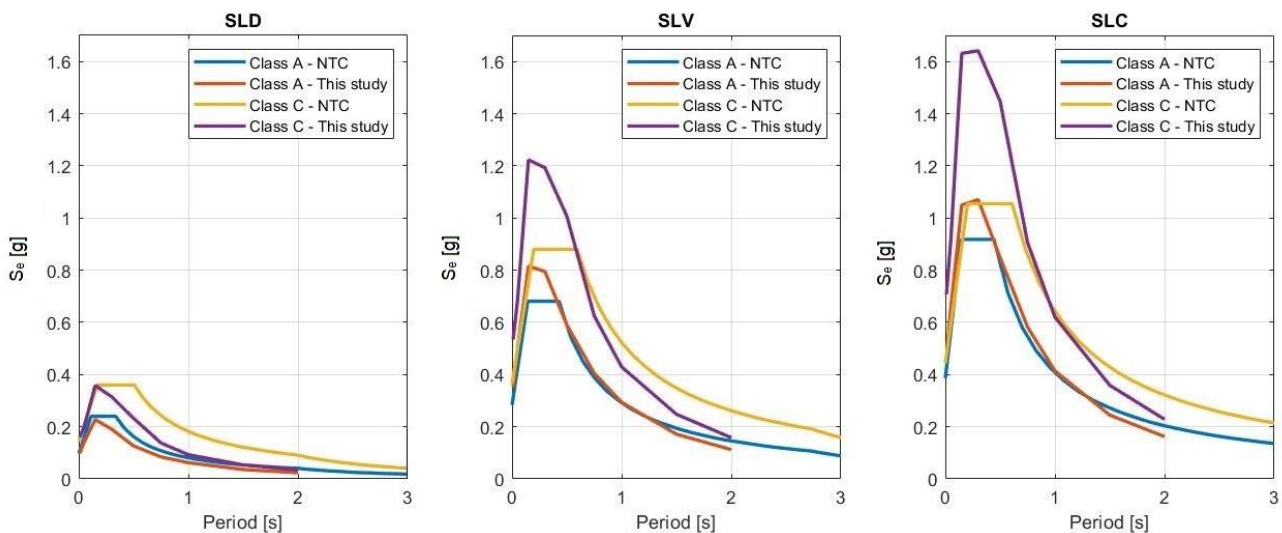


Figure 23. Response spectra for different soil classes at the San Pietro sull'Osento dam.

Table 8. Housner intensity values for the San Pietro sull'Osento dam. The values calculated for the different limit states (SLD, SLV, SLC), for two different period bands (0.1 - 0.5 s; 0.5 - 1 s), are provided, comparing the values relating to this study with those of the standard technical regulations (NTC, 2018).

	Exceedance probability	Model	Housner Intensity (0.1 – 0.5 s)	Housner Intensity (0.5 – 1 s)
SLD	63% $T_R = 101$ years	This study	1.67	1.68
		NTC	2.05	1.58
SLV	10% $T_R = 949$ years	This study	1.55	1.59
		NTC	1.66	1.38
SLC	5% $T_R = 1950$ years	This study	1.58	1.60
		NTC	1.45	1.25

In order to facilitate the understanding of the different PGA values at the site for the different limit states, and to better appreciate the differences, two sets of figures are shown below containing the same information, but with different chromatic scales. In Figure 24, the hazard models are shown according to variable colour scales in the range of values covered by each limit state, while in Figure 25 according to a colour scale that is the same for all limit states.

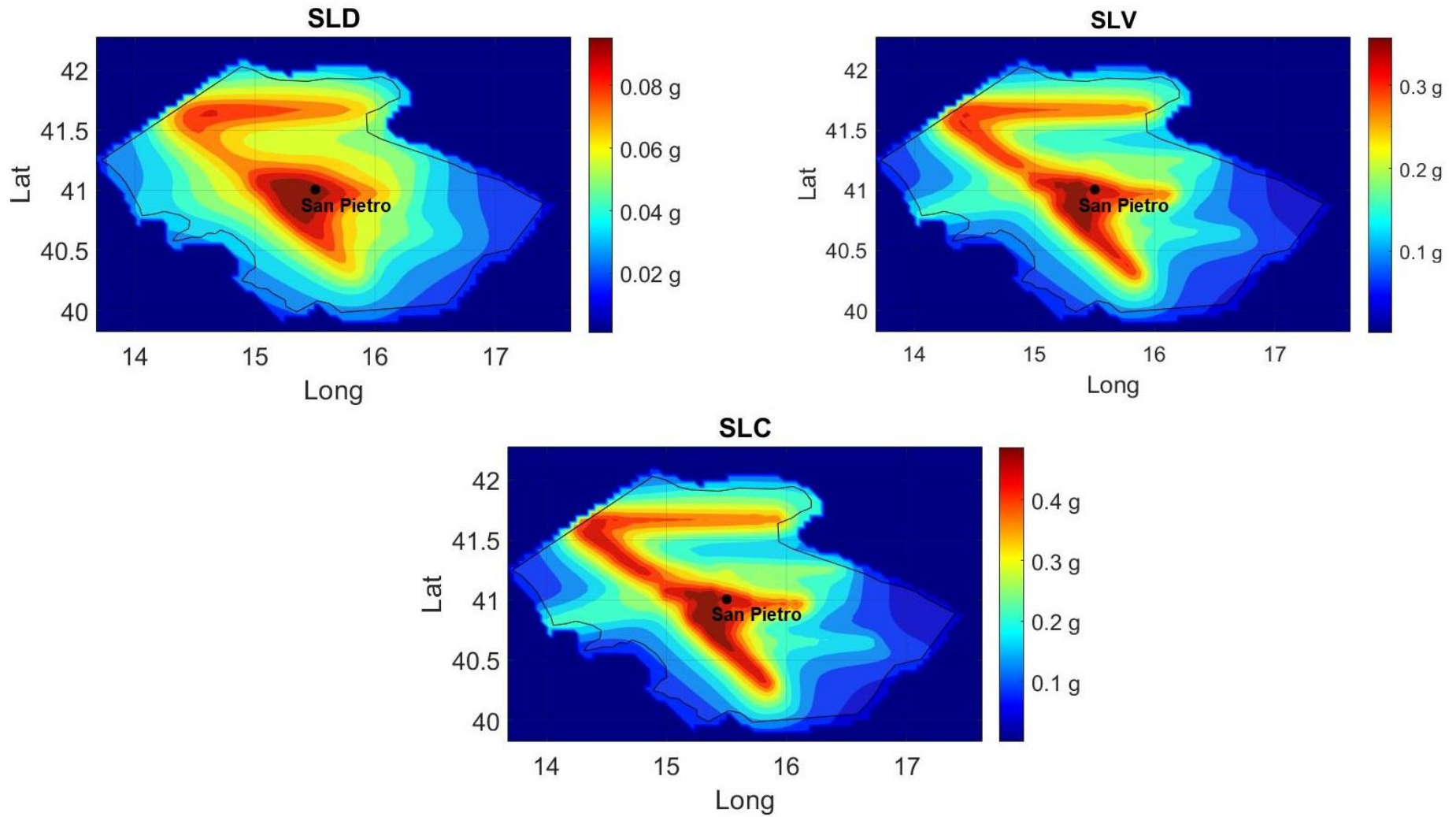


Figure 24. Seismic hazard models for the San Pietro sull'Osento dam. The PGA values are expressed in g (using a colour palette that covers the range of values necessary for each limit state), with an exceedance probability of respectively 63%, 10% and 5% in 100 years at $T = 0.01$ s. For the numerical values in the sites of interest see Table 7.

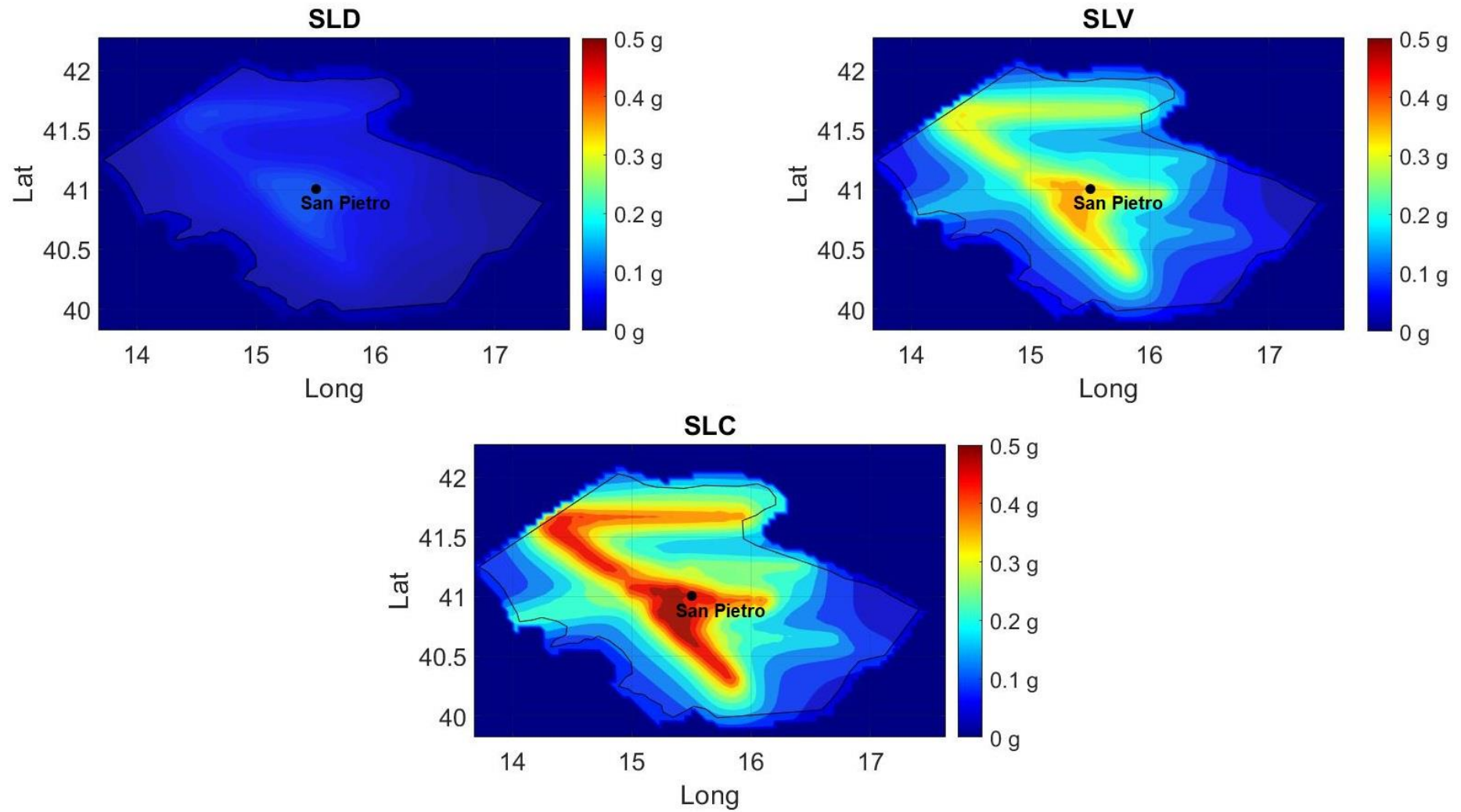


Figure 25. Seismic hazard models for the San Pietro sull'Osento dam. The PGA values are expressed in g (using a colour palette that is the same for all three limit states), with an exceedance probability of respectively 63%, 10% and 5% in 100 years at $T = 0.01$ s. For the numerical values in the sites of interest see Table 7.

3.1.6.2 Marana Capacciotti dam

The PGA values computed for the Marana Capacciotti site are generally lower than the standard ones (Table 9), for all the investigated limit states (SLD, SLV and SLC).

Table 9. Results of the seismic hazard models. The table shows the PGA, with exceedance probability of 63%, 10% and 5% in 100 years, according to the method applied in this study. These are compared with the corresponding values reported in the national technical regulation (NTC 2008, 2018).

REFERRED TO BEDROCK				
	Exceedance probability	Dam	PGA This study	PGA NTC (2008, 2018)
SLD	63% $T_R = 101$ years	Capacciotti	0.06 g	0.08 g
SLV	10% $T_R = 949$ years	Capacciotti	0.20 g	0.23 g
SLC	5% $T_R = 1950$ years	Capacciotti	0.28 g	0.33 g

As for the San Pietro dam, a comparison was also performed in terms of response spectra (i) representing the simplified regulatory response spectra at the Marana Capacciotti dam site according to the various models for category A (rock) and for site category C (Figure 26, Table 10) and (ii) by calculating the Housner intensity (Housner, 1952). The Housner intensity was calculated as the ratio between the integral of the response spectrum of category C and A, in the period bands of major interest for the dams (0.1 - 0.5 s; 0.5 - 1 s), by comparing the values obtained in this work with the values of the NTC standard. The values of the Housner intensities are provided in Table 10 for the Marana Capacciotti dam.

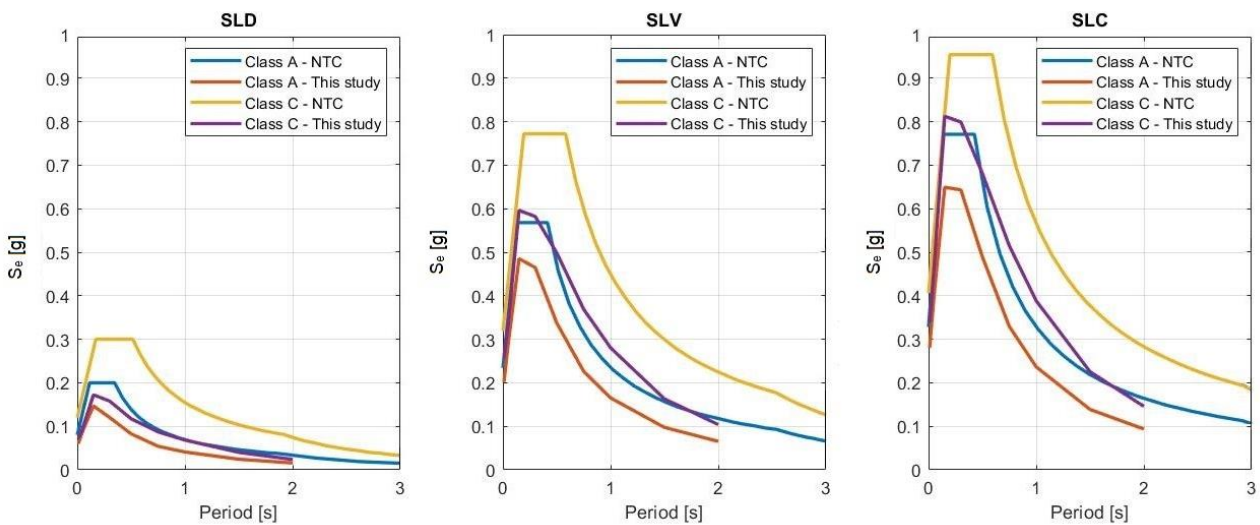


Figure 26. Response spectra for different soil classes at the Marana Capacciotti dam.

Table 10. Housner intensity values for the Marana Capacciotti dam. The values calculated for the different limit states (SLD, SLV, SLC), for two different period bands (0.1 - 0.5 s; 0.5 - 1 s), are provided, comparing the values relating to this study with those of the standard technical regulations (NTC, 2018).

	Exceedance probability	Model	Housner Intensity (0.1 – 0.5 s)	Housner Intensity (0.5 – 1 s)
SLD	63% $T_R = 101$ years	This study	1.30	1.55
		NTC	2.04	1.56
SLV	10% $T_R = 949$ years	This study	1.30	1.59
		NTC	1.76	1.44
SLC	5% $T_R = 1950$ years	This study	1.28	1.52
		NTC	1.58	1.34

As for the San Pietro dam, in order to facilitate the understanding of the different PGA values at the site for the different limit states and to better appreciate the differences, two sets of figures are shown below containing the same information, but with different chromatic scales. In Figure 27, the hazard models are shown according to varying chromatic scales in the range of values covered by each limit state, while in Figure 28 according to a chromatic scale that is the same for all limit states.

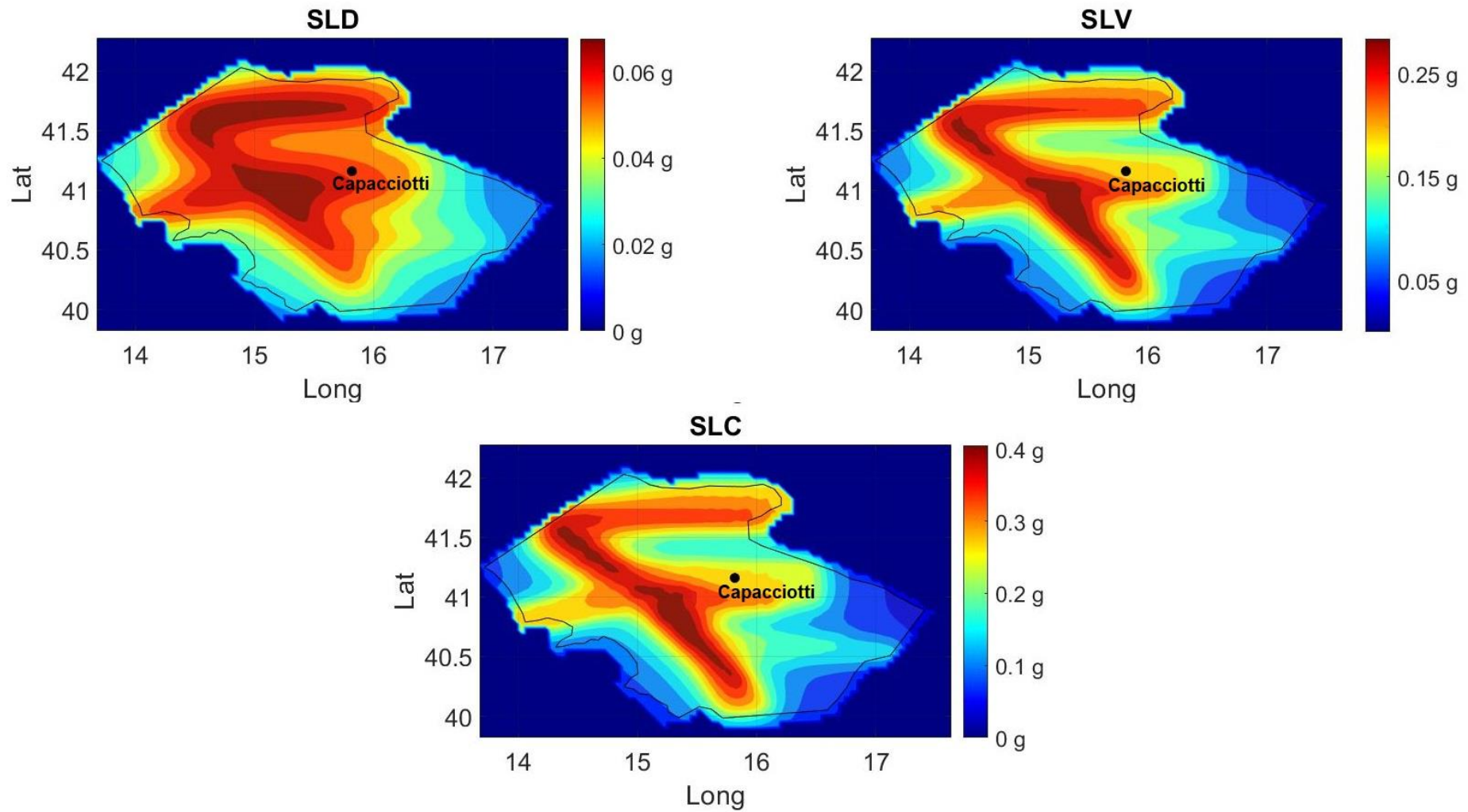


Figure 27. Seismic hazard models for the Marana Capacciotti dam. The PGA values are expressed in g (using a colour palette that covers the range of values necessary for each limit state), with an exceedance probability respectively 63%, 10% and 5% in 100 years at $T = 0.01$ s. For the numerical values in the sites of interest see Table 9.

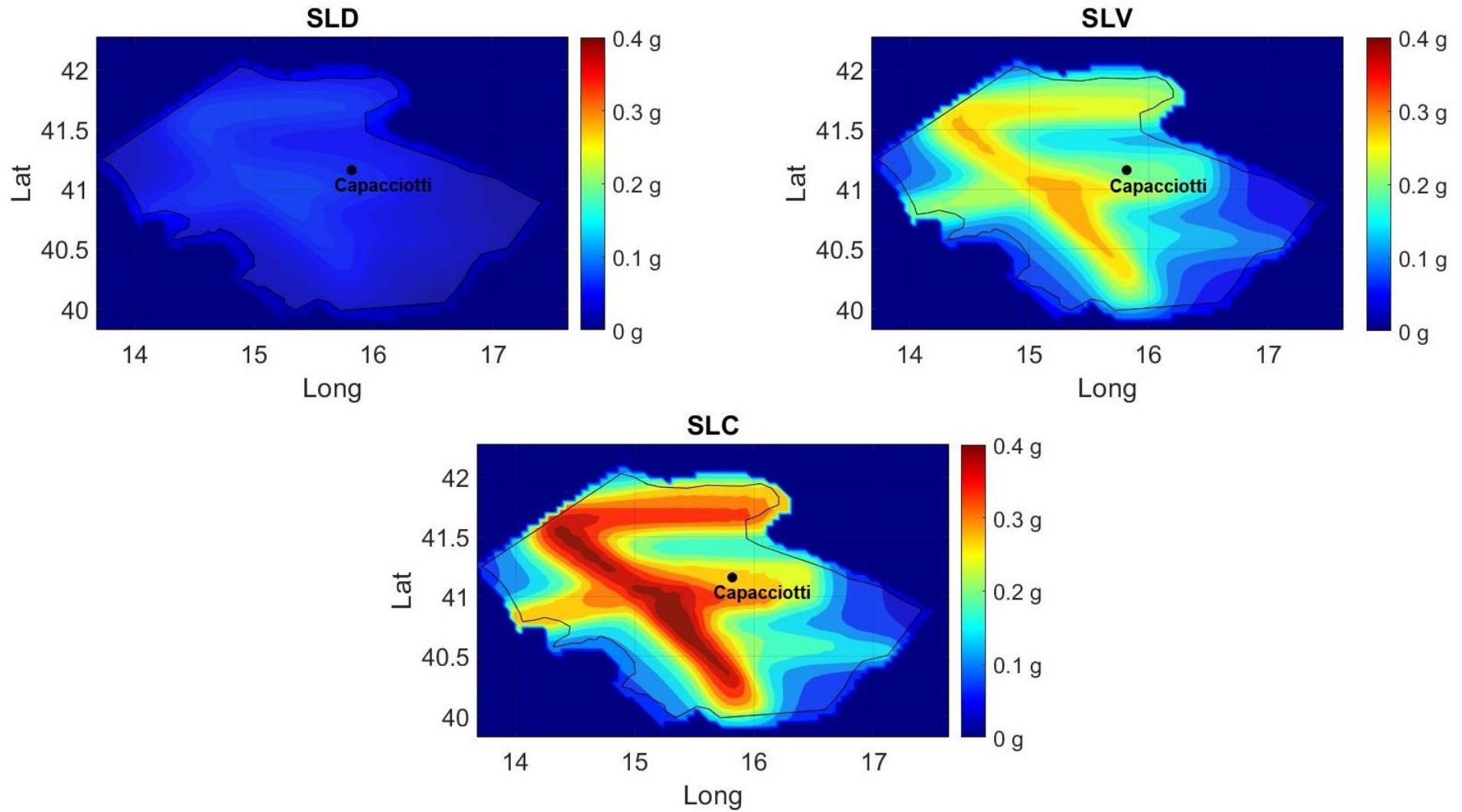


Figure 28. Seismic hazard models for the Marana Capacciotti dam. The PGA values are expressed in g (using a colour palette that is the same for all three limit states), with an exceedance probability respectively 63%, 10% and 5% in 100 years at $T = 0.01$ s. For the numerical values in the sites of interest see Table 9.

3.2 Fault-based approach

In recent years, fault-based and time-dependent approaches to seismic hazard assessment have been proposed all over the world. These methods require the transition from catalogue-based probabilistic seismic hazard estimates to geology-based time-dependent PSHA. The use of active faults as an input for seismic hazard analysis is becoming a consolidated approach in regions with either high strain rates, e.g., in California (Field *et al.*, 2015) and in New Zealand (Stirling *et al.*, 2012), and in regions characterized by moderate-to-low strain rates, such as France (Scotti *et al.*, 2014), SE Spain (García-Mayordomo *et al.*, 2007; Gómez-Novell *et al.*, 2020b) and central Italy (Peruzza *et al.*, 2011; Valentini *et al.*, 2017, 2018, 2019; Valentini, 2020). Linking faults to seismic hazard assessment in Europe is a goal that has been set in last years. A working group of the European Seismological Commission, named Fault2SHA, is promoting the debate about the best use of active faults in seismic hazard analyses. In this framework, Pace *et al.* (2018) give an overview of European projects where efforts to create a working group of field geologists, fault modellers, and data modellers to improve knowledge and practice of fault-based seismic hazard assessment are being made.

Zone-based approaches with seismicity rates derived from earthquake catalogs are commonly used in many countries as the standard for national seismic hazard models. In Italy, a single zone-based Earthquake Rupture Forecast (ERF) is the basis for the official seismic hazard model currently used as reference by the Italian Building Code (NTC, 2018; see section 3.1). Fault-based approaches with seismicity rates derived from active faults are now being proposed to be used as an input for probabilistic seismic hazard assessment. In the newest MPS19 Seismic Hazard Model of Italy, between the eleven new ERFs, two fault-based have been actually employed (Visini *et al.*, 2021). The use of active faults in seismic hazard models allows to capture the recurrence of large-magnitude events (e.g., Valentini *et al.*, 2018; Valentini, 2020; Visini *et al.*, 2020), usually not represented in the earthquake catalogs, which is a key aspect for the seismic verifications of large infrastructures. In this sense, fault-based and time-dependent approaches can give a complementary view of PSHA. Moreover, as highlighted by the 2016–2017 seismic sequences in central Italy, fault-based models can provide better insights for local spatial variations in ground motion with respect to the standard approaches (Peruzza *et al.*, 2016).

Another difference between standard and fault-based approaches lies in the fact that the formers consider each fault independently as an individual seismogenic source and do not contemplate the occurrence of multi-fault earthquakes. However, seismological, geological and paleoseismological data show that earthquake rupture surfaces can be very complex. Recent complex coseismic ruptures (e.g., Mw 8.6 Sumatra in 2012; Mw 6.5 central Italy in 2016) highlighted the need to include the multi-fault earthquakes in PSHA, going thus beyond strict fault segmentation assumptions (e.g., Valentini, 2020). Incorporating this widely observed behaviour in nature is a step towards more realistic approximations of fault modelling in PSHA.

In recent years, new approaches for modelling faults as complex and interacting sources in seismic hazard have been developed. Among the emerging methodologies, the UCERF3 (Third Uniform

California Earthquake Rupture Forecast) approach (Field *et al.*, 2014) is probably the most advanced model developed to date. Similarly to UCERF3, Chartier *et al.* (2019) proposed an innovative approach called SHERIFS (Seismic Hazard and Earthquake Rate In Fault Systems) where ruptures can be limited to one fault or involve several faults allowing multi-fault earthquakes. Recently, Visini *et al.* (2020) presented other two new methodologies that model rupture rates along complex fault systems, one based on a floating rupture approach (FRESH) and another one based on assumed rupture scenarios (SUNFISH), which represent alternatives to the SHERIFS approach. For this study, it was decided to test the SHERIFS approach on the Irpinia region.

3.2.1 SHERIFS approach

SHERIFS is an approach implemented and distributed by Chartier *et al.* (2019) in the form of a computer code, born in order to achieve more realistic models that treat fault systems as a whole, by modelling seismicity rates of complex multi-fault ruptures. So far, it has been tested in several locations worldwide (e.g., Gómez-Novell *et al.*, 2020a, 2020b, in SE Spain; Chartier *et al.*, 2021, in the Marmara Region; Cheng *et al.*, 2021, in the Tibetan Plateau). SHERIFS approach requires as input data the geometry and the geologic/geodetic slip rates of the faults, the set of different multi-fault rupture scenarios that can be expected in the fault system, and the imposed shape of a Magnitude-Frequency Distribution (MFD) defined at the fault system level.

After defining all the input data, the iterative method of SHERIFS converts the slip-rate budget of each fault into earthquake rates until the MFD target is reached and the slip-rate budgets are exhausted. In some cases, the target is achieved before the budget of all faults is exhausted. The remaining slip-rate budget is then considered as Non-Mainshock Slip (NMS) and it is not converted into seismicity rates. A NMS of more than 30% is most likely an indication that the combination of input hypotheses used does not agree with the fault parameters in the SHERIFS framework and that they should be reconsidered (Chartier *et al.*, 2019).

The modelled seismicity rates can then be compared with historical and instrumental data, to assess the effects of the different input hypotheses. The adequacy of the model is assessed in terms of accordance with the regional seismic catalog and with paleoseismic data.

3.2.2 Case study: the Irpinia region

So far there are no studies available in the Irpinia region using a fault-based approach, so this represents the first attempt using this methodology. The goal of this exercise is to compare the synthetic MFDs with respect to the earthquake rates coming from the CPTI v3.0 seismic catalog (Rovida *et al.*, 2021).

The fault segments employed for this analysis are the merge of the Individual Seismogenic Sources (ISS) provided by the DISS database (DISS Working Group, 2021) and some additional active faults reported by Valentini *et al.* (2017), which proposed an integration of active faults and seismological data for seismic hazard purposes. The fault IDs and their characteristics (upper and lower seismogenic depth, slip rates, kinematics) are listed in Appendix C and their geometry is shown in

Figure 29. To give a plane view representation of the master faults, they are here symbolized as 'seismogenic boxes' (Boncio *et al.*, 2004), that are the surface projections of the fault planes capable of major earthquakes.

An important issue in the definition of fault source inputs is the formulation of segmentation rules. In fact, the question of whether structural segment boundaries along multi-segment active faults act as persistent barriers to a single rupture is critical to define the maximum seismogenic potential of fault sources. Following the approaches of Boncio *et al.* (2004), Field *et al.* (2014), Gómez-Novell *et al.* (2020a), four possible fault and multi-fault rupture scenarios were defined (Table 11). In Hypothesis 1, only single fault section ruptures are allowed. This means that the length of the segments proposed for each fault in literature sets the maximum length of the ruptures; multi-segments ruptures with neighbouring faults are not allowed. In Hypotheses 2, 3, 4 incremental multi-fault ruptures are allowed. The criteria used to define the segments that could break together rely on the geometry (strike, dip, rake), lower and upper seismogenic depth, proximity between fault segments and average slip rate. The maximum magnitude (M_{max}) is then set by the empirical scaling relationship of Wells & Coppersmith (1994).

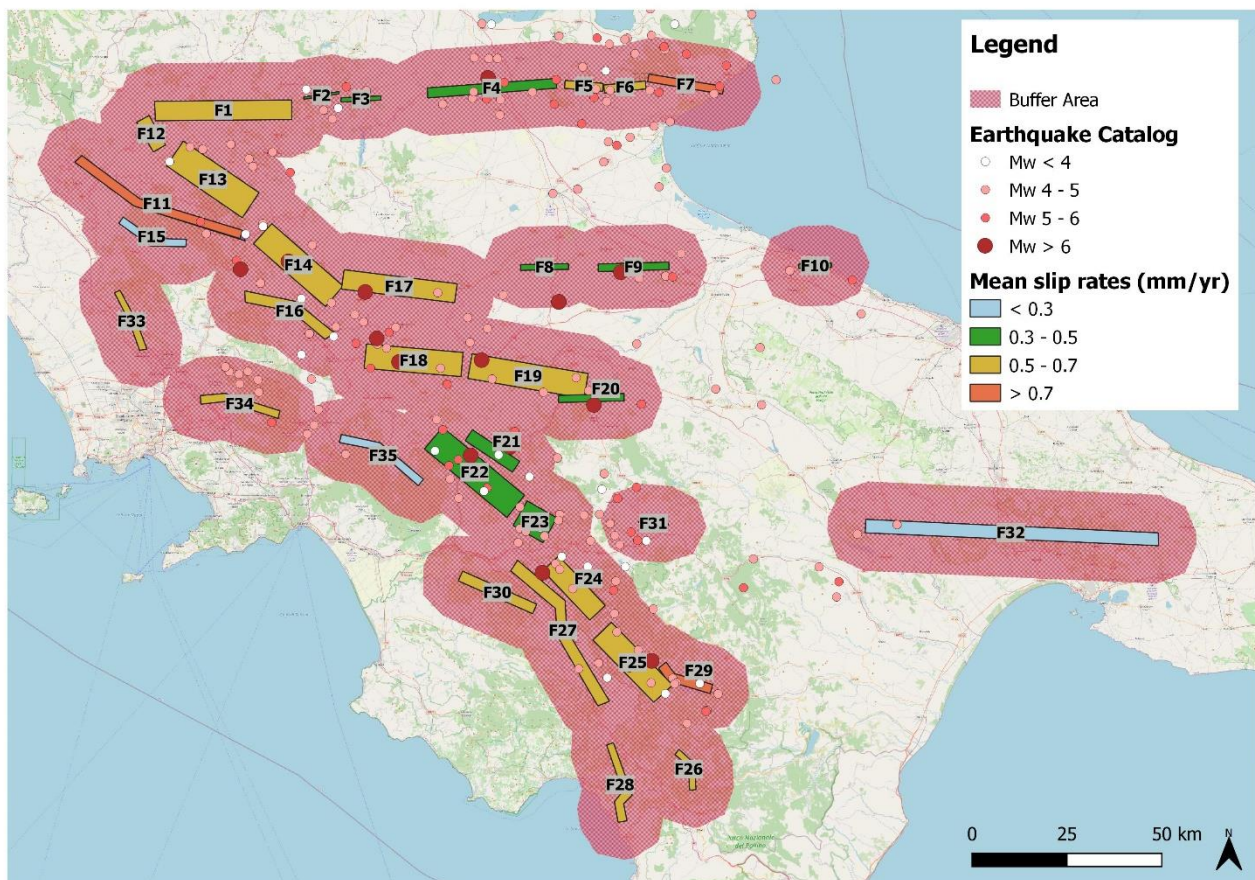


Figure 29. Representation of the fault sections (from F1 to F35) surrounded by a 10 km buffer area. All faults NW-SE oriented have a normal kinematics, while all the structures W-E oriented have a strike-slip mechanism. The faults are here also distinguished by different mean slip rates. Circles represent all earthquakes occurred between 1019 and 2017 (reference catalog: CPTI15 v3.0; Rovida *et al.*, 2021). All earthquakes outside the buffer area represent the ratio of background seismicity.

The b -value of 1.00 ± 0.14 was set in accordance with the one calculated and used in our standard approach model (see paragraph 3.1.3) and a GR-type shape of the magnitude-frequency distribution was imposed. A buffer area of 10 km away from the faults was drawn (Figure 29), which was used in order to define the background seismicity. The background seismicity is a parameter that allows to share a small fraction of the seismicity rate of a given magnitude between the faults and the background of the area directly surrounding the faults. Chartier *et al.* (2019) suggest to use the distance between the epicentres of the earthquakes and the faults as a possible criterion to define this parameter. Being the ratio of seismicity occurring on the modelled faults for different ranges of magnitude, the background seismicity typically coincides with 1 for high magnitudes, while it decreases for lower magnitude earthquakes.

Table 11. List of the four fault rupture scenarios, characterized by incremental multi-fault ruptures. Fault sections (from F1 to F35) are shown in Figure 29.

Fault rupture scenario	Maximum expected multi-fault ruptures
Hyp. 1	Only single fault section ruptures allowed
Hyp. 2	F2 + F3
	F5 + F6
	F13 + F14
	F22 + F23
Hyp. 3	F2 + F3 + F4
	F5 + F6 + F7
	F8 + F9 + F10
	F11 + F12 + F13 + F14
	F18 + 19
	F21 + F22 + F23
Hyp. 4	F24 + F25 + F26 + F27 + F28
	F1 + F2 + F3 + F4 + F5 + F6 + F7
	F8 + F9 + F10
	F11 + F12 + F13 + F14 + F15 + F16 + F17
	F18 + F19 + F20
	F21 + F22 + F23 + F24 + F25 + F26 + F27 + F28 + F29 + F30
	F31 + F32
F33 + F34 + F35	

3.2.3 Model performance and final remarks

The iterative method of SHERIFS spends the slip rate budget of each fault until the MFD target is reached and the slip rate budgets are exhausted. As mentioned before, in some cases, the target is reached before the budget of all faults is exhausted: the remaining slip rate budget is then considered as Non Mainshock Slip (NMS) and is not converted into seismicity rates. This is the first parameter to look for in order to discuss the model performance. In fact, the configuration influences how the slip rate budget is consumed in the different iterations. Chartier *et al.* (2019) believe that too high NMS values are to be interpreted as a mistake, or rather, that the input slip rate for the fault section is not compatible with the scenario set. Considering the 30-40% threshold, the models resulting from

Hypotheses 1 and 2 (Figure 30) should be reconsidered in detail, while Hypotheses 3 and 4 show low NMS on the modelled fault and can be considered more suitable.

To assess the performance of the SHERIFS hypotheses, we compare the four synthetic MFDs with the seismicity rates from the historical and instrumental regional catalogs (Figure 31). The fit between the resulting MFDs appear to be poor for Hypotheses 1, 2, 4, while more acceptable for Hypothesis 3.

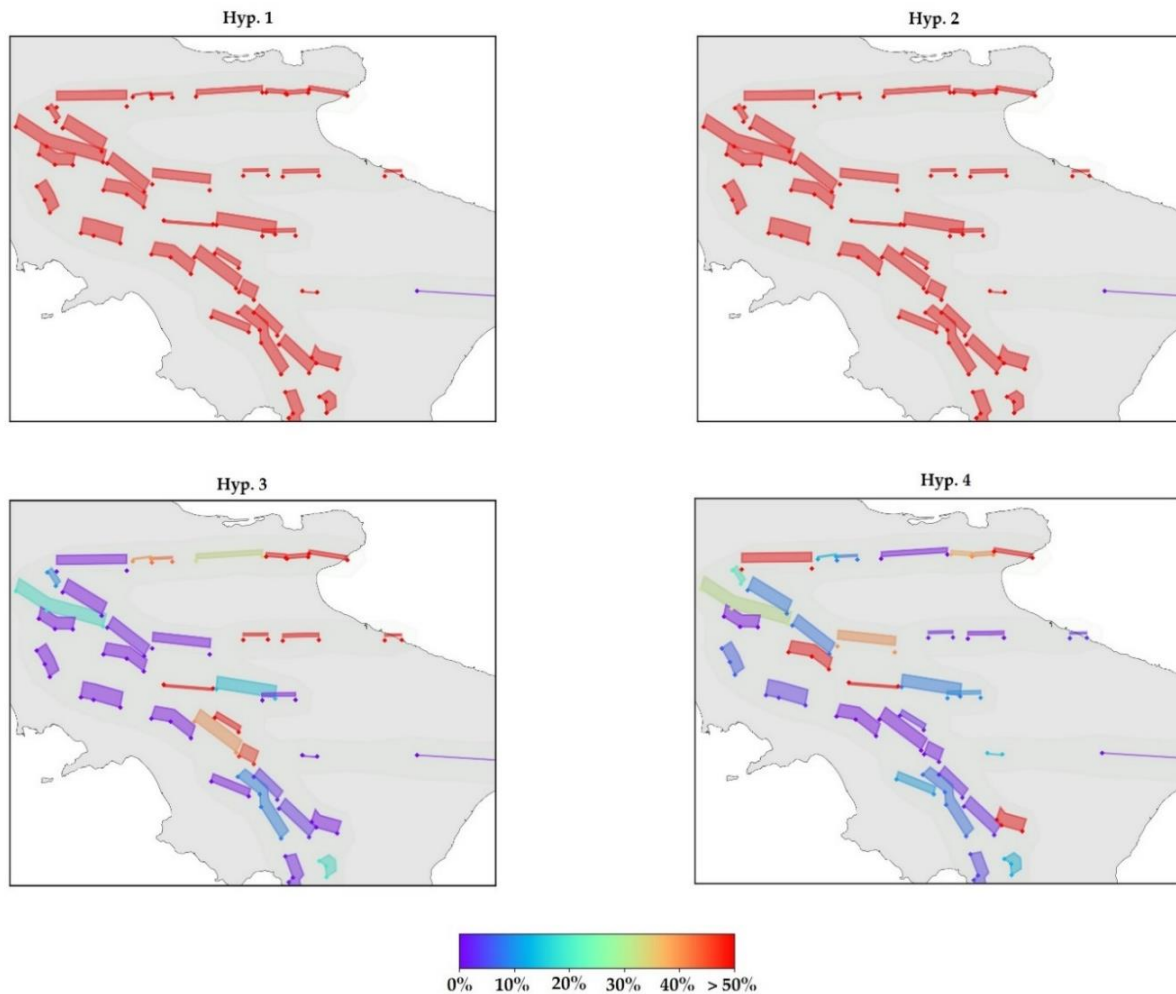


Figure 30. Map of the NMS slip ratio for each fault segment of the four hypotheses.

In light of these results, the rupture scenario that seems to best describe the behaviour of the study area appears to be Hypothesis 3. Nevertheless, some further considerations on these results have to be made. The fact that the synthetic seismicity rates underestimate the seismic catalog ones, may be due to different reasons. The most relevant and important is, unfortunately, the lack of quality data in the study area. Knowledge of seismogenic sources and their slip rates have a dominant role in the SHERIFS approach and they can have an important impact on the final results. Since several faults in Southern Italy have no measured slip rate, some of these parameters used in this study come from

the statistically derived approach proposed by Valentini *et al.* (2017). Else, we could be ignoring the contribution of other fault sources or, perhaps, in that area this approach does not bring benefits because the nature of the faults does not allow it.

A big challenge for the fault-based approaches is actually to rely on a complete and trustworthy dataset of active faults and related parameters. Updating paleoseismic and geodetic data on faults and the inclusion of multiple faults as sources is therefore necessary for the reassessment of source modelling.

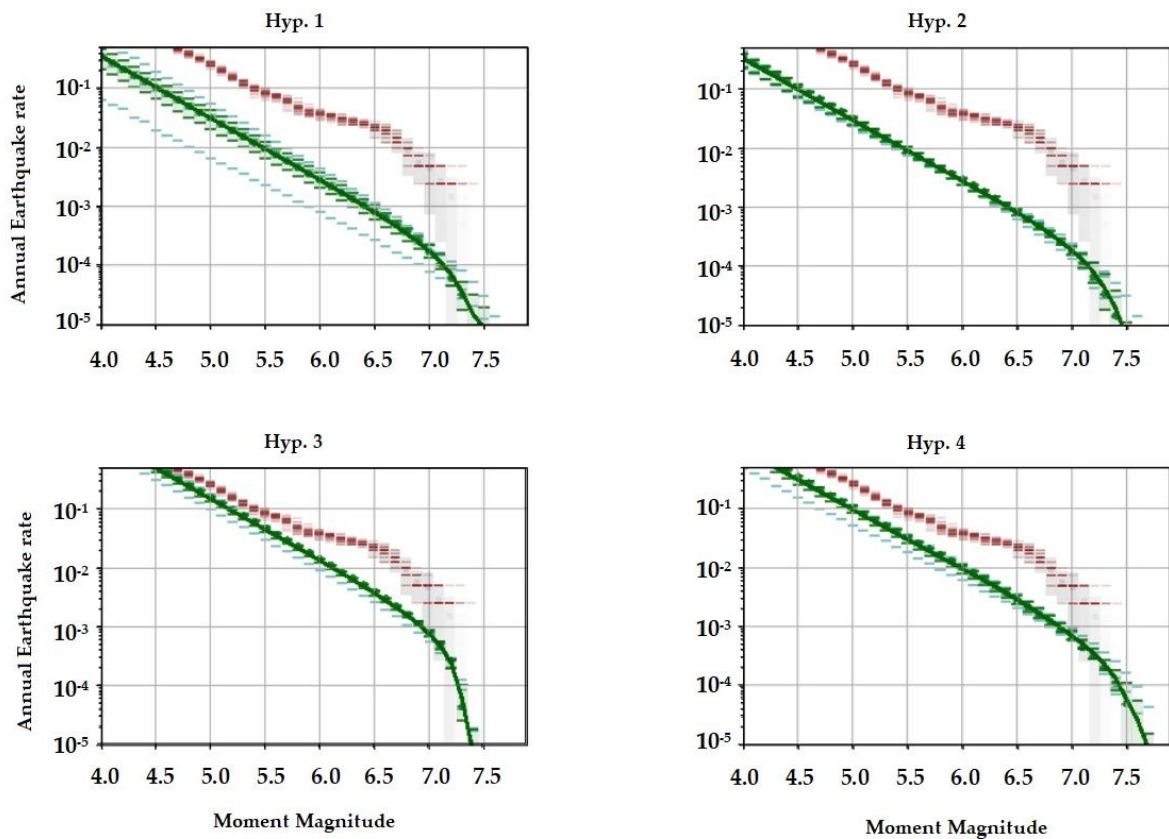


Figure 31. For each rupture scenario, comparison between the modelled MFD (green) and the earthquake rate calculated from the catalog (red). Solid green line is the mean MFD and green patches represent the uncertainty (16–84 percentiles).

4. SEISMIC STATIONS AND SEISMIC HAZARD

As we highlighted during our sensitivity analyses (section 3.1.5), one of the most important steps in PSHA is the definition of the attenuation models used to predict the ground motion at a site of interest. In the last few years it has been recognized that some of the uncertainty in the PSHA results may have been introduced by the derivation of GMMs used in all hazard studies (Barani *et al.*, 2014). The data used to calibrate the GMMs come from accelerometric stations that record a "pure" signal, if they are placed directly on outcropping bedrock, or a modified signal, if placed in a non-rocky site. In fact, when local soil deposits are located above the seismic bedrock, the amplification of seismic waves can take place. It is also known that seismic installations within buildings or structures lead to a further alteration of the recorded motion and these limits go under the generic name of "soil-structure interaction". Can we trust what seismic stations record at any frequency interval? Are these data appropriate for building GMMs? During this PhD project we have been trying to answer these questions by investigating these phenomena closely related to hazard studies; we show our results in the following paragraphs.

4.1 Seismic soil classification

Since the first attempts in defining the attenuation laws of the seismic motion as a function of distance and magnitude (e.g., Ambraseys *et al.*, 1996; Sabetta & Pugliese, 1996), the scientific community has been trying to take into account the site effects. In early studies, 2 or 3 site classes were considered (stiff, deep soil, shallow soil). At present, the most universally used (albeit debated) seismic classification is based on the average seismic shear-wave velocity from the surface to a depth of 30 meters, a parameter known as V_{S30} and described by equation (8).

$$V_{S30} = \frac{30}{\sum_{i=1}^N \frac{h_i}{V_{Si}}} \quad (8)$$

Nowadays, most GMMs refer to V_{S30} either (i) by directly considering the V_{S30} value in the functional form or (ii) by classifying the soil characteristics in terms of mechanical properties (e.g., stiff or soft soil) according to V_{S30} intervals, and defining variables associated to each category (Forte *et al.*, 2019). V_{S30} is also adopted by several seismic codes to identify the appropriate site-dependent design spectrum for structures; some examples are Eurocode 8 in Europe (CEN, 2003), the National Earthquake Hazard Reduction Program in USA (BSSC, 2003), and the Norme Tecniche sulle Costruzioni in Italy (NTC, 2008, 2018).

Since 2018, in Italy the NTC have introduced the V_{Seq} parameter which coincides with V_{S30} when the seismic bedrock is over 30 m deep, and it is instead the average seismic shear-wave velocity of the equivalent homogeneous layer within the depth of the bedrock, in the other cases, described by equation (9).

$$V_{Seq} = \frac{H}{\sum_{i=1}^N \frac{h_i}{V_{Si}}} \quad (9)$$

To date, seismic soil classifications provide 5 site classes based on V_{S30} (today V_{Seq} , in Italy), which are shown in Table 12. These categories are identified by decreasing V_{Seq} values, i.e., by decreasing mechanical properties of the soil with depth.

Table 12. Description of the 5 soil classes based on the NTC2018 classification.

Soil class	Description of stratigraphic profile	V_{Seq} [m/s]
A	Rock or other rock-like geological formation, including at most 3 m of weaker material at the surface.	> 800
B	Deposits of very dense sand, gravel, or very stiff clay, at least several tens of meters in thickness, characterized by a gradual increase of mechanical properties with depth.	800 – 360
C	Deep deposits of dense or medium-dense sand, gravel or stiff clay with thickness greater than 30 m and characterized by a gradual increase of mechanical properties with depth.	360 – 180
D	Deposits of loose-to-medium cohesion soil with thickness higher than 30 m and characterized by a gradual increase of mechanical properties with depth.	180 – 100
E	Soils with characteristics and equivalent shear velocity analogous to those defined for classes C and D but with a deposits thickness not greater than 30 m.	-

These parameters should preferably be measured by one of the many available geophysical techniques, rather than estimated from relations with other (e.g., geotechnical) parameters. However, the unavailability of these measurements, which are often expensive and require some fieldwork, has led researchers to look for a number of estimators, more or less justified, of V_{S30} (or V_{Seq}) by non-geophysical methods. For example, many of the Italian accelerometric stations are located on sites whose classification is made by assessing V_{S30} (or V_{Seq}) from surface geology, so from large scale geological maps. Basically, this method correlates sites with similar lithology, geomorphology and facies with site-specific investigations. This classification is also reported in the official accelerograms database (e.g., for Italy, the ITalian ACcelerometric Archive v3.1 - ITACA; D’Amico *et al.*, 2020) as "Site category from surface geology". This type of classification is usually marked by a star, meaning that the site category is estimated and not geophysically-assessed. Another common method uses the topographic slope at each site as a proxy to V_{S30} (Wald & Allen, 2007). Even though Lemoine *et al.* (2012) and other studies showed that V_{S30} -slope correlations are not sufficiently accurate to replace actual field measurements, this estimate is still reported in the official accelerograms databases as "Site class from topography". Both these non-geophysical methods assign soil categories that are often different from those estimated subsequently by

geophysical methods, mostly by overestimating the site category and therefore erroneously indicating stiffer soil characteristics.

The database we used in our seismotectonic study is the result of the data recorded by 142 seismic stations belonging to the following seismic networks: BA (UniBAS), E (Rete ENEA), IT (Italian Strong Motion Network - RAN), IV (Italian National Seismic Network), IX (Irpinia Seismic Network). Among these stations, only 33 were provided with a geophysical site classification at the time of selection (corresponding to the 23% of the stations useful for this study; Figure 32). The fact that only few stations have a geophysically-assessed V_{s30} could have relevant consequences on modern GMMs, which all take site effects into account (e.g., Bindi *et al.*, 2011; Cauzzi *et al.*, 2015). For this reason, based on the abundance of recorded seismic history (number of recorded events), 10 significant seismic stations have been chosen (Figure 32). These stations have been surveyed during an *ad hoc* fieldwork conducted in October 2019. The results (paragraph 4.1.1) have been received by the Istituto Nazionale di Geofisica e Vulcanologia (INGV), published, and now available online at the ITACA database (D'Amico *et al.*, 2020). The complete reports of these stations (Alessandrini *et al.*, 2019) are also attached at the end of this thesis, in the "Additional Material" section (page 115).

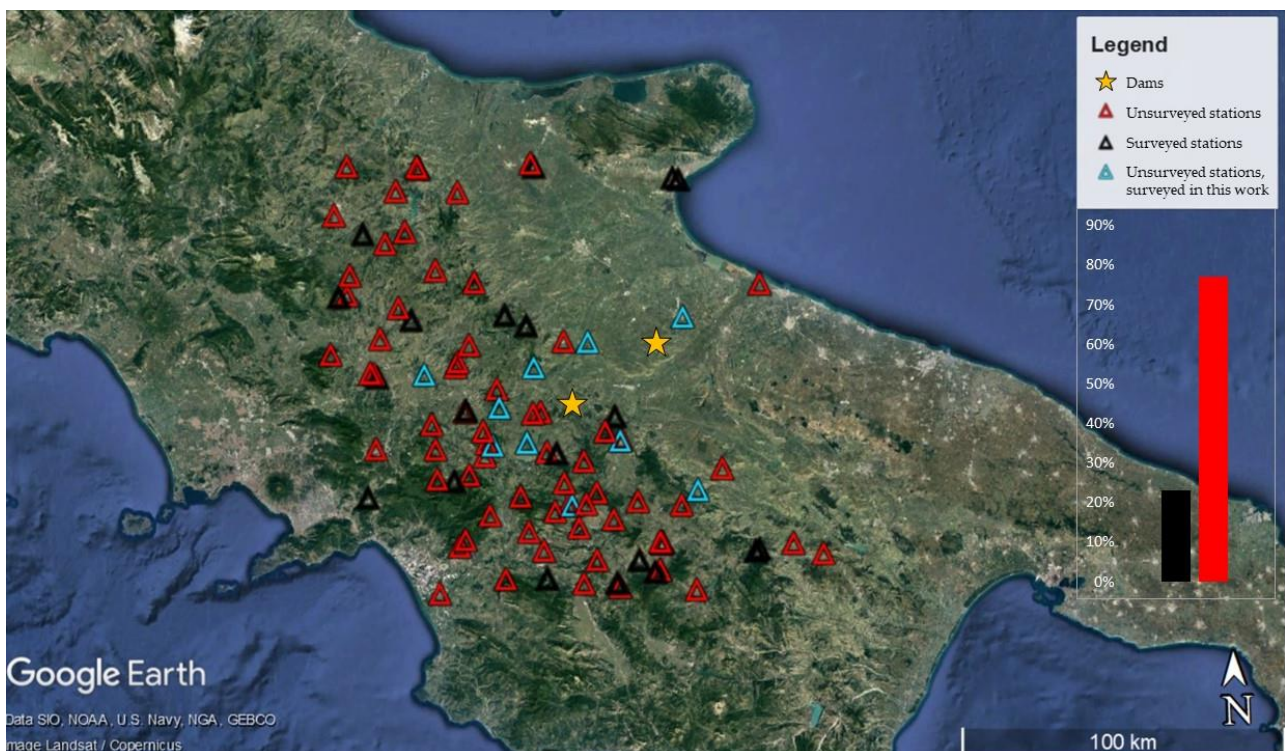


Figure 32. Geographical distribution of the 142 seismic stations used for this PSHA study. Unsurveyed stations (whose site category is therefore assessed by surface geology or topography) are highlighted by red triangles; surveyed stations (whose site category is assessed by geophysical measurements) are represented by black triangles; the 10 significant seismic stations that have been surveyed and classified by means of geophysical methods (results are shown in Table 13) are highlighted by light blue triangles.

4.1.1 Surveyed seismic stations

The 10 seismic stations (Figure 32) were selected following some scrupulous criteria. As anticipated, among the stations without a geophysical characterization, priority was given according to the duration of the seismic history, by ordering in descending order with respect to the total number of records. Among these, priority was given to the stations with the highest number of useful events, i.e., the stations with records relating to seismic events used for our study. Priority has also been assigned based on the housing: the sensors can in fact be positioned in a free field or in stations close to structures: priority has been given to the latter. The choice was also made for the type of terrain: using site categories coming from surface geology or topography there is a tendency to overestimate subsoil classes, so precedence has been given to stations on presumed higher site classes.

Table 13. Results of the surveyed accelerometric stations. For each of them, site classifications estimated by topography, surface geology (marked by a star) and geophysical surveys are provided. Stations where there is no match between assumed and verified categories are marked with an exclamation mark. The V_{S30} (NTC, 2008) and V_{Seq} (NTC, 2018) values are also provided. The V_{S30} value is given as it is still a reference in the official national seismic databases.

Accelerometric station name	Site name	SITE CLASSIFICATION			V_{Seq} (m/s)	V_{S30} (m/s)
		Topography	Surface Geology	Geophysical characterization		
ACER	Acerenza	A*!	B*	B	520	520
AND3	Andretta	B*!	A*!	C	300	300
ASR	Ascoli Satriano	B*!	A*!	C	280	280
CAFE	Carife	B*	A*!	B	620	620
CER	Cerignola	B*	B*	B	400	400
MRB1	Monte Rocchetta	A*!	B*	B	450	450
MRLC	Muro Lucano	A*!	B*	B ²	600	860
RNV2	Rionero in Vulture	B*	C*!	B	380	380
SGTA	Sant'Agata di Puglia	B*	B*	B	400	400
SNAL	Sant'Angelo dei Lombardi	A*!	A*!	B	600	730

The geophysical method we carried out consists in the joint fit of two types of measurements: soil active and passive multichannel surveys (MASW, Park *et al.*, 1999; ReMi, Louie, 2001) and passive single-station surveys (H/V, Nakamura, 1989; SESAME, 2004) (see also chapter 5 for further details). These surveys allowed us to reconstruct the local seismic stratigraphy and to assess the V_{S30} (or V_{Seq}). The result of the geophysical characterization of the investigated stations is summarized in Table 13.

² The MRLC station has been classified as category B according to the new technical standards (NTC, 2018), as it is characterized by V_{Seq} higher than 800 m/s, with superficial soil of thickness greater than 3 m (10 m).

If we compare the geological method with the geophysical one, we can observe that 60% of the surveyed seismic stations result in a subsoil class different from what expected from the geological evidence. In all cases, the geological approach results in stiffer subsoil classes. If we compare the topographic and geophysical method, 50% of the stations are located in a different site category. In all cases, except for the RNV2 station only, the topographical approach results once again in stiffer subsoil classes. Also, 70% of the topographical classes differ from the geological evidences.

The discrepancy between estimated and measured site classes is evident: the surface geology and the topographic methods are not sufficiently accurate to replace actual field measurements. Furthermore, they show evident inconsistencies between them. By updating the database with our results, the surveyed seismic stations still represent a minor part (only 30%) of the selected seismic stations used for our hazard models. It is therefore necessary to invest in the geophysical characterization of seismic stations, since the recorded data have direct consequences on the estimation of the site effects, of the PGA and on the calculation of the attenuation laws. Moreover, a further ambiguity arises, since the regulations have changed from 2018 in Italy. The V_{seq} "A" class is now different from the V_{S30} "A" class. In the Italian reference databases, we found that the locations of the seismic stations are still classified according to V_{S30} : an update is therefore necessary.

4.2 Soil-structure interaction

At the early stages of seismology, seismic stations were installed directly on rock to minimize the effects of the fine sediments/weathering on the recorded seismic waves. The bulky size of permanent installation seismometers, their need for external batteries, cables and levelling, led to place seismic stations on artificial ground, such as *ad hoc* concrete platforms. In addition, to ensure protection from environmental conditions, vandalism and to facilitate maintenance, many seismic stations were placed inside structures. A common installation in Italy, as an example, is at the base of the (5-8 m tall) towers of the electrical national service.

The presence of a structure around the instrument perturbs the recorded motion. This phenomenon, generally referred to as soil-structure interaction, can be summarized into three main effects. The first one is the transmission of the structure own motion to the surrounding ground. When seismic waves hit a building, the building enters forced oscillation and this vibration is re-transmitted to the ground. Sensors placed inside the building record, therefore, a composite signal, made of seismic waves and the response of the structure to them. This affects the sensors also when they are isolated from the building foundations by means of cuts around the sensor pillars, because the ground under the pillar and the ground under the structure is the same and is continuous. The second effect lays in the fact that a foundation, typically made of reinforced concrete, acts as a layer with seismic impedance much higher than any natural soil. Seismic waves travelling upwards will be reflected downwards as they hit the foundation. On one side they shake the structure (effect 1), but on the other only a small fraction of them crosses the foundation (effect 2) and can be recorded by the instruments installed on the foundation. The same applies to the concrete pillars where seismic sensors are installed. These installations violate the basic principle of any physical measurements according to which when an interface is needed between the instrument and the object of

measurement (the ground) then the interface must have an impedance as close as possible to the object of measurement, in order to minimize the perturbation of the wavefield. Clearly concrete platforms/pillars do not have this property, unless when installed on very stiff rocks. The third main effect (effect 3) concerns the back reflection of the surface waves reaching the foundation. Similarly to effect 2, when surface waves strike an extended rigid layer, such as the foundations of a building, they are mainly reflected back along the Earth's surface. This implies that, in seismic tremor recordings (or seismic events) carried out inside a structure, a fraction of surface waves will be missing.

In our manuscript (Castellaro *et al.*, 2022), which is attached at the end of this thesis (see the "Additional Material" section, page 115), we show these effects in a number of real cases and we show the consequences that this can have in the assessment of seismic site effects, of PGA, and on the computation of attenuation laws.

5. ADDITIONAL SURVEYS

An additional geophysical survey was conducted in July and October 2019 to characterize the dynamic properties of the soils of foundation of the dams, of the soils surrounding the dams and the dams themselves. This survey was meant to collect the parameters required for the geotechnical finite element models meant at studying the seismic resistance to collapse of the earth dam.

To this aim, on the soil active and passive multichannel surveys (MASW, Park *et al.*, 1999; ReMi, Louie, 2001) and passive single-station surveys (H/V, Nakamura, 1989; SESAME, 2004) were collected, as per Table 14. For what concerns the microtremor H/V surveys, the average amplitude spectra in velocity and their standard deviation are computed for each measurement point by splitting the recorded signal into 30 second non-overlapping windows. On average, 32 to 40 signal windows are retained to compute the average H/V curve and its standard deviation. Each window is detrended, tapered with a Bartlett window, zero-padded and FF-transformed. The Fourier spectra are smoothed according to triangular windows with width equal to 10% of the central frequency, in order to keep only the significant peaks. For what concerns the active/passive 1D array surveys, the vertical-component Rayleigh-wave phase-velocity dispersion curves obtained by averaging several active and passive surveys are illustrated. Only the windows showing the lowest phase velocities (with the exclusion of the alias) are retained, for their being closer to the fundamental mode dispersion curve. The phase-velocity spectra are obtained by slant-stacking the seismograms and by applying a FFT. These kinds of surveys provided the shear wave velocity profiles and the resonance frequencies at the inspected sites that, combined with direct information from boreholes, allowed us to reconstruct the local seismic stratigraphy. As anticipated, the data were collected both on the embankments and on the foundation soil of the San Pietro sull'Osesto (paragraph 5.1.2) and Marana Capacciotti (paragraph 5.2.2) dams. On the structures of interest, passive recordings were also acquired to get the natural frequencies and damping.

Table 14. Details geophysical surveys performed at the sites.

Survey type	Acquisition length	Sampling rate [Hz]	Notes	Instrument used
Microtremor H/V	20' each	512	Two Tromino® were arranged asynchronously	Tromino® - MoHo srl
Active/passive 1D array	Active: MASW Passive: ReMi (7' recording)	512	16 geophones, 3 m inter-receiver distance	Seismograph: SoilSpy – MoHo srl Geophones: OYO – Geospace 4.5 Hz (vertical)

In the following pages we present the average V_s models for each inspected site, obtained from the joint fit of all the acquired surface-wave dispersion and H/V curves. Since the H/V curves are more sensitive to local geological features compared to the array dispersion curves, the average V_s model might not faithfully reproduce the H/V features at high frequency. The theoretical H/V curve

overlapped to the experimental H/V curve could be computed on a slightly different model. Since the theory and practice behind dispersion curves and H/V has extensively been described in the literature (see respectively Foti *et al.*, 2018 and Molnar *et al.*, 2018 for a review); we will not discuss these and we will refer to the cited authors and to the references therein.

Moreover, the soils and structures analysis that we are going to show allowed the selection of accelerograms referring to the identified seismic bedrocks, the definition of which is necessary for the geotechnical modelling with finite elements of the dam and associated structures.

5.1 San Pietro sull'Osento dam

5.1.1 Existent surveys

The first geological surveys have been performed by Cotecchia (1959) during the construction of the San Pietro sull'Osento dam. In that study, a tectonic discontinuity between the geological formations of the hydrographic left side and those of the hydrographic right side was supposed. As anticipated in chapter 2, different lithologies have been observed on the two sides of the riverbed; the geological-structural maps are shown in Figure 34, whose location is shown in Figure 33.

In 2003, seismic verifications on the dam have been carried out (SolGeo, 2003). As part of the assignment, cross-hole tests were performed in five pairs of holes named from CH1-S1 to CH5-S5. The tests were aimed at determining the P-waves and S-waves velocity on the dam crest, on the embankment and on natural ground. A summary of these surveys is shown in Figure 35.

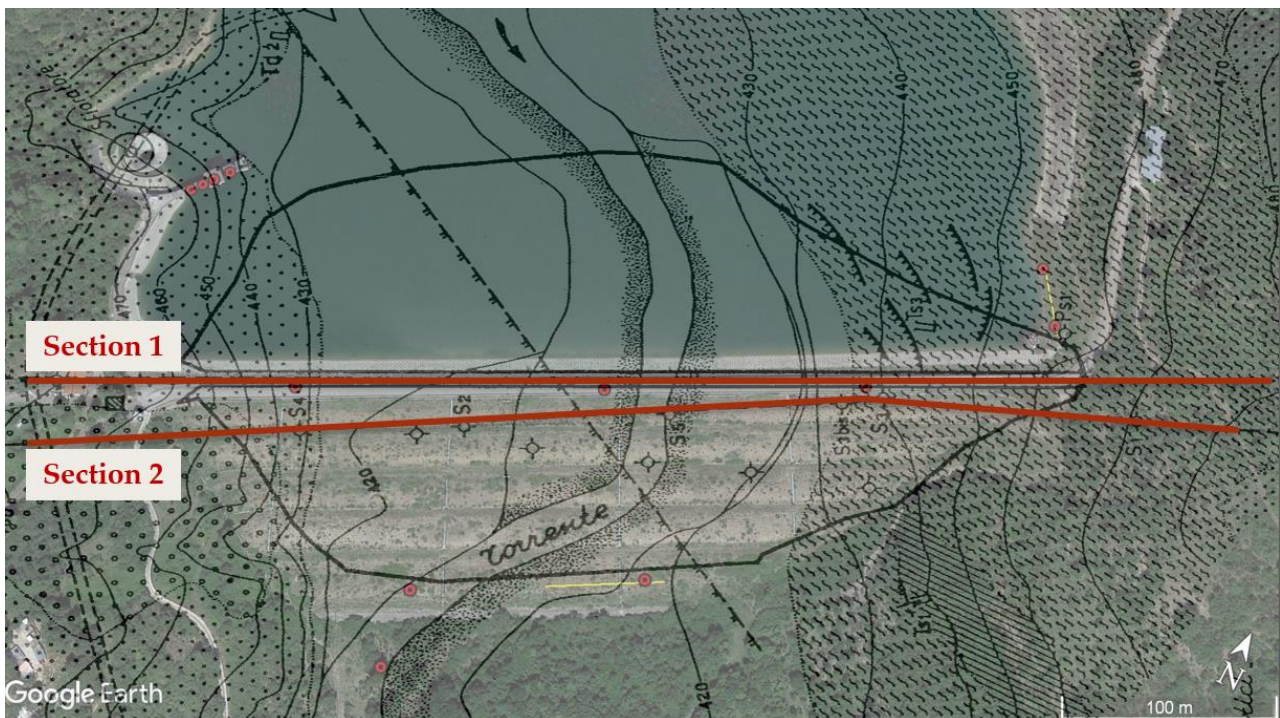
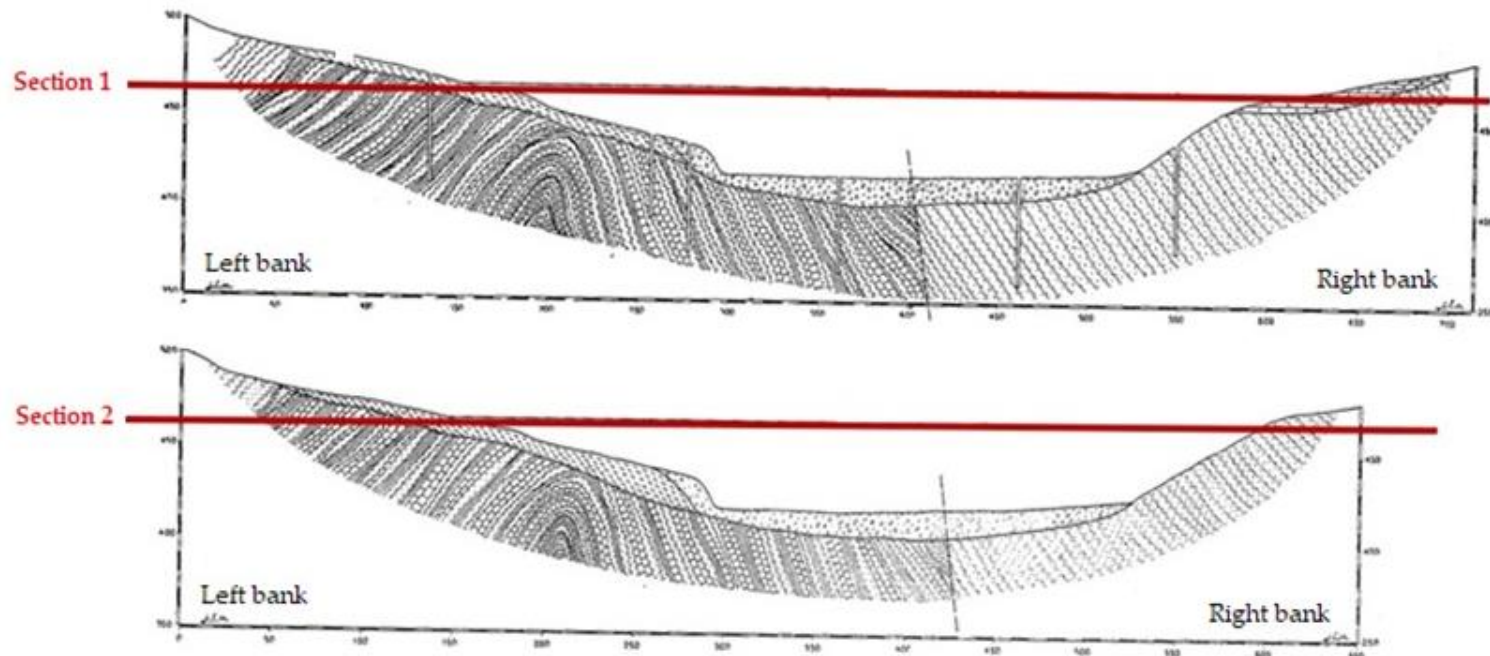


Figure 33. Map of the stratigraphic sections 1 and 2 made by Cotecchia (1959), superimposed on a satellite photo (Google Earth). Section 1 is located longitudinal to the dam crest; section 2 is almost parallel and located further downstream, on the embankment. The map also shows the trace of the NW-SE tectonic discontinuity.



	Geological formation	Average thickness
	Alluvial deposits (right bank)	$\bar{H} = 15 \text{ m}$
	Oligocene Varicolored Clays (left bank)	$H = 8 \text{ m}$
	Miocene yellowish sandbanks (right bank)	$\bar{H} = 100 \text{ m}$
	Miocene marly-arenaceous Flysch (left bank)	$H = 100 \text{ m}$

Figure 34. Geological interpretation made by Cotecchia (1959), preliminary to the construction of the dam. The average thicknesses of the mapped surface deposits are not to be considered realistic anymore, since part of the material was removed before the construction of the work.

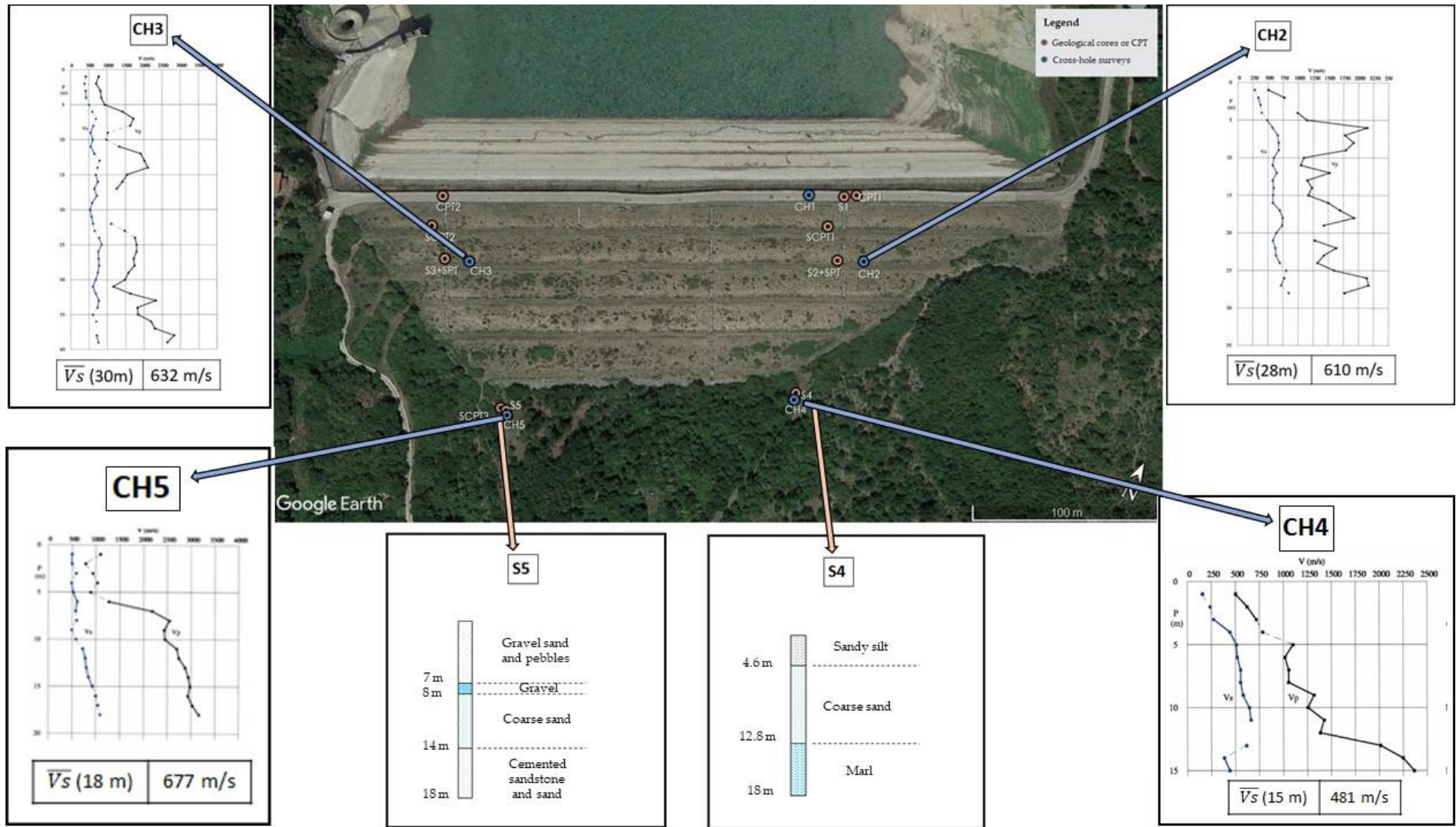


Figure 35. Summary diagram of the average velocities and the stratigraphy related to the embankment and to the natural ground of the San Pietro sull'Ossento dam. The cross-hole measurements (CH2, CH3, CH4, CH5) and the geological cores (S4 and S5) date back to the seismic verifications carried out in 2003 (SolGeo, 2003).

5.1.2 New surveys

During the surveys that we carried out in July and October 2019, a total of 24 environmental vibration measurements were acquired on the San Pietro sull'Osento dam (7 on structure and 17 on natural ground) and 5 measurements of surface wave dispersion (1 on the dam embankment and 4 on natural ground), whose location is given in Figure 37.

5.1.2.1 Ground – Left bank

On the left bank, multi-channel and single-station passive seismic data were acquired:

- upstream of the dam, close to sections 1 and 2 of the geological study made by Cotecchia (1959; Figure 33);
- downstream of the dam, at the same location as the surveys carried out for the previous seismic verifications (SolGeo, 2003; Figure 35).

The joint modelling of the multichannel and single station data suggests the V_s profile illustrated in Figure 39, characterized by a 8 m-thick layer with an average shear wave velocity of 230 m/s, in agreement with the thickness of 6 ÷ 10 m identified by Cotecchia (1959). At this depth, an increase in the shear waves velocity is observed, from 230 m/s to 400 m/s, probably due to the Varicolored Clays – Flysch transition. The dam foundation is located in the Flysch lithology. The H/V curves acquired downstream (Figure 38) show peaks at 1.5 Hz, 3 Hz and 12 Hz. At a depth of 40 m, velocity values referable to the seismic bedrock are observed, although the seismological bedrock *sensu stricto* of the left bank can be set around 90-100 m depth (1.5 Hz). However, the one starting at a depth of 40 m can already be considered as a bedrock-like layer, as the effect of impedance contrasts at greater depths is modest.

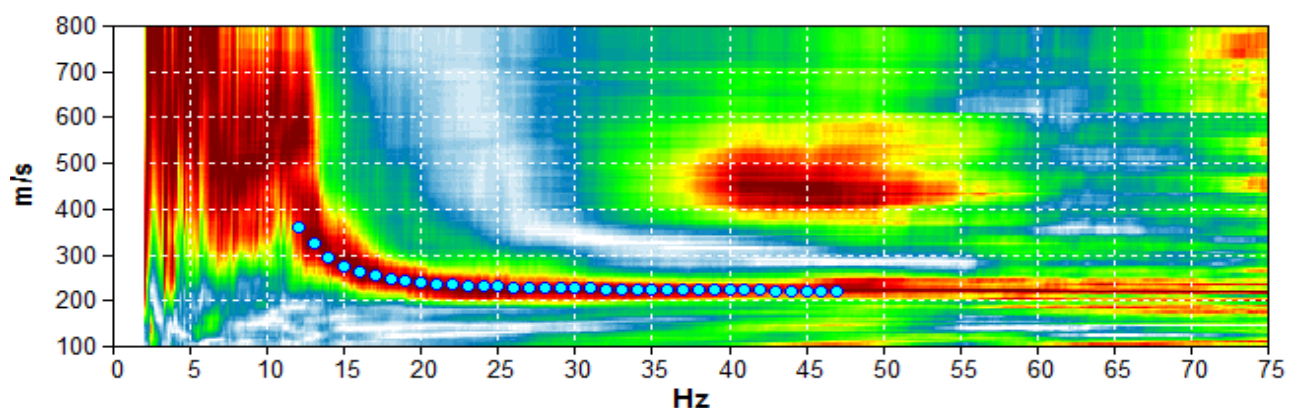


Figure 36. Dispersion curve A01 (Figure 37). Left bank upstream, natural soil. In the vertical axis there are the phase velocities of the Rayleigh waves, vertical component. The blue dots indicate the theoretical dispersion curve obtained for the soil model of Table 15.

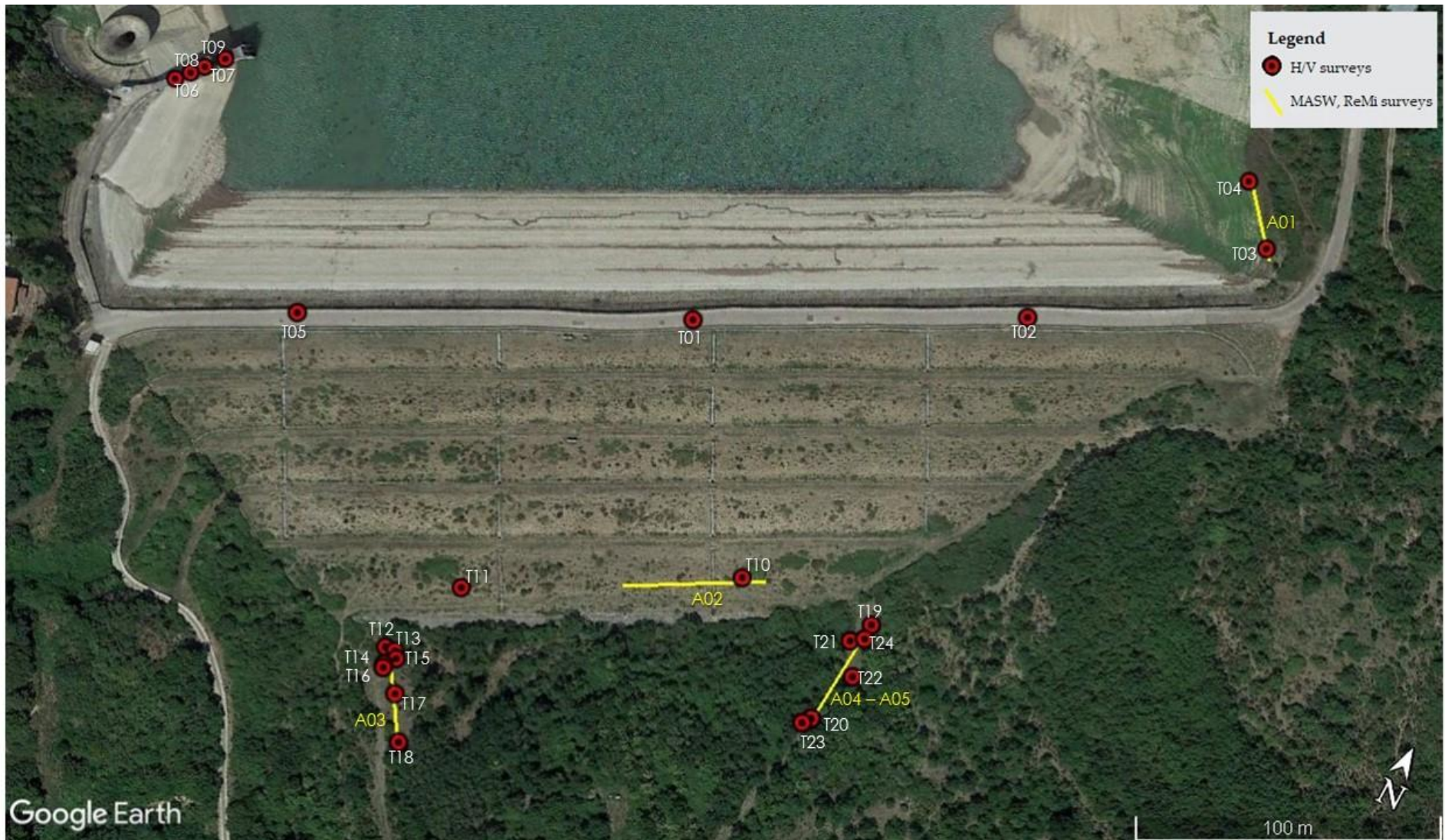


Figure 37. Location of the H/V measurements (red dots) and of the MASW-ReMi measurements (yellow lines) acquired during the July-October fieldwork carried out at the San Pietro sull'Ossento dam.

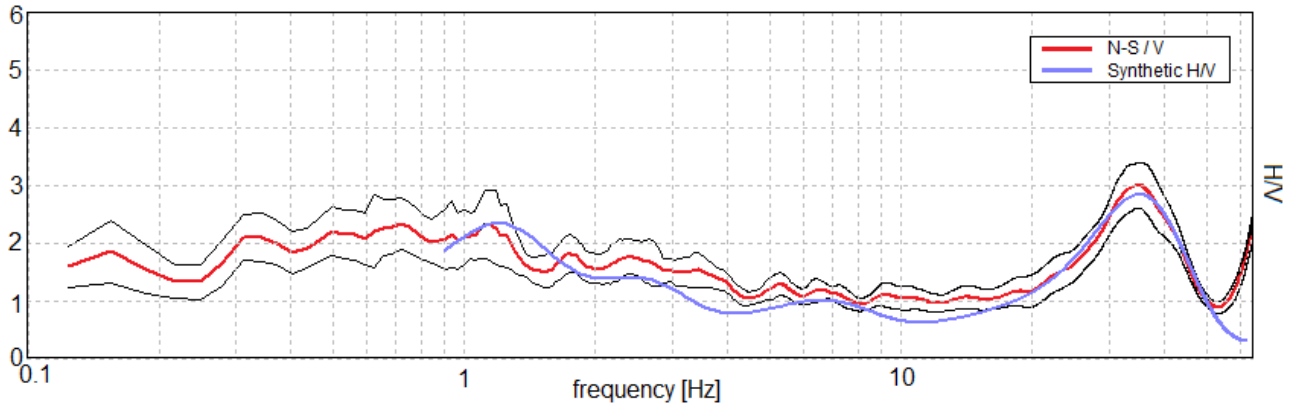


Figure 38. H/V T04 (Figure 37), left bank upstream, natural soil (mean in red, standard deviation in black, synthetic curve in blue). The synthetic H/V curve refers to the subsoil model of Table 15.

Table 15. Subsoil shear wave velocity model, obtained from the joint fit of single station and array measurements A01 and T04 (Figure 37). Left bank, natural terrain.

Depth at the bottom of the layer [m]	Thickness [m]	V _s [m/s]	Poisson Ratio
0.90	0.90	130	0.48
9.90	9.00	250	0.46
39.90	30.00	370	0.42
129.90	90.00	600	0.4
inf.	inf.	880	0.39

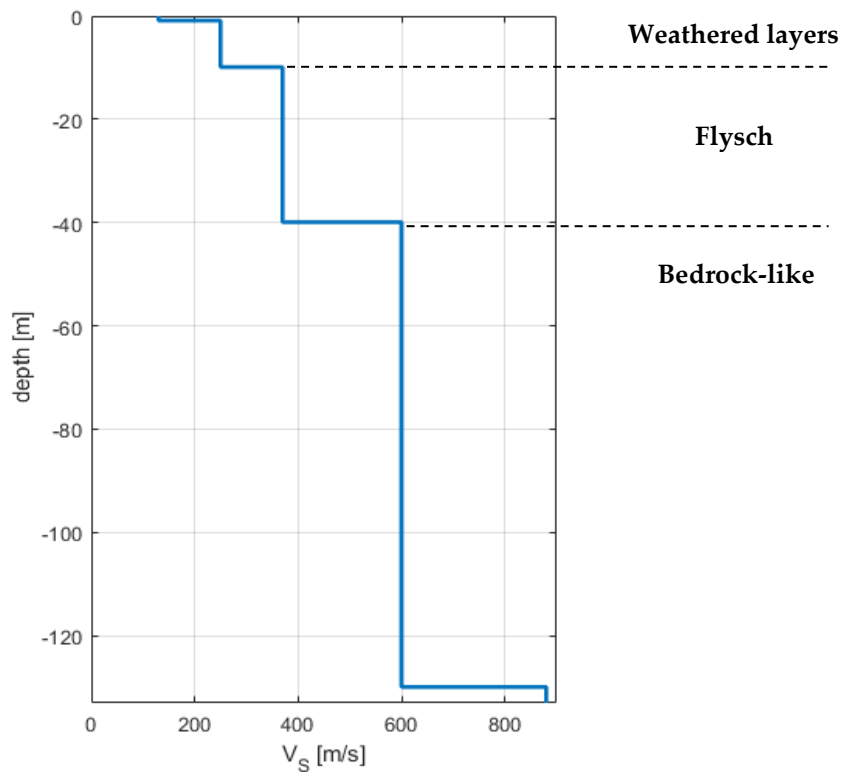


Figure 39. Shear wave velocity model and possible stratigraphic model, from the joint fit of A01 and T04. Left bank, natural terrain.

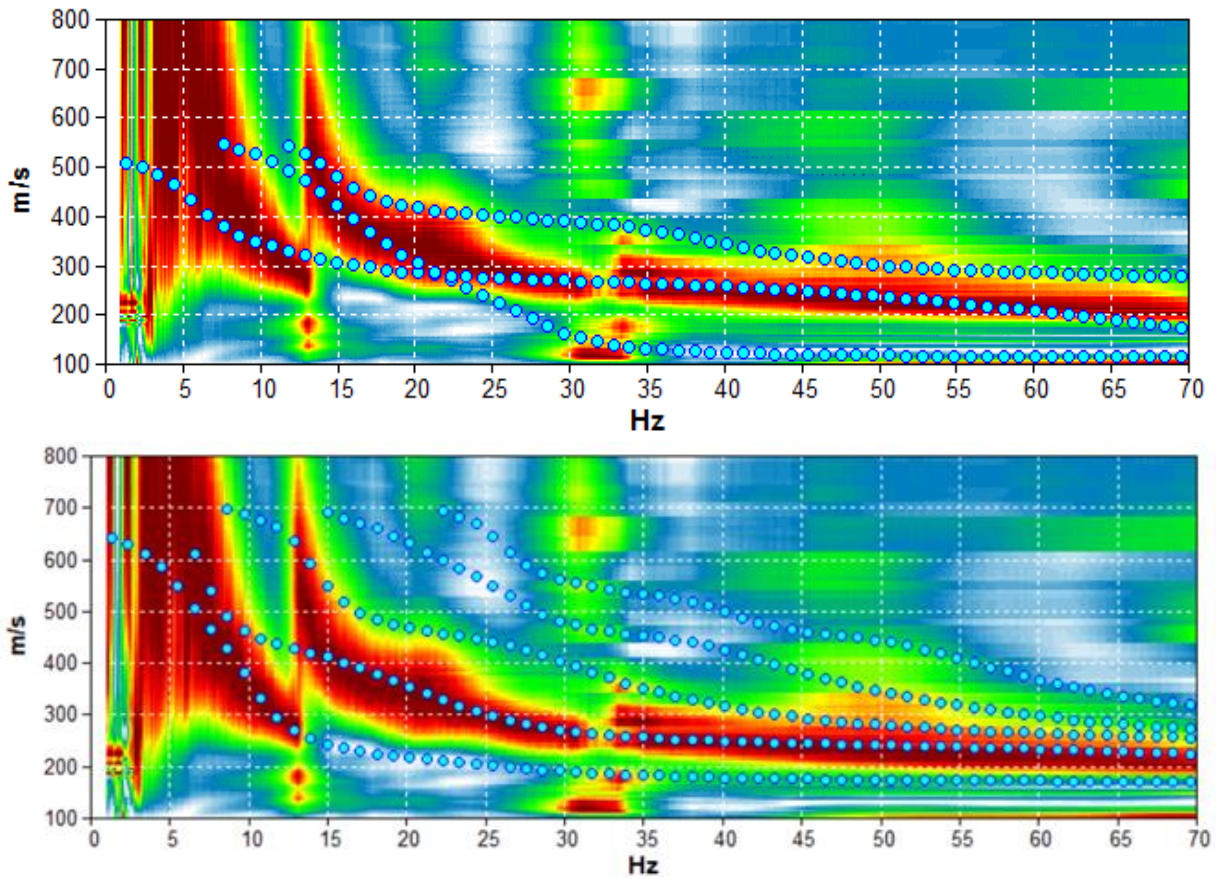


Figure 40. Dispersion curve A05 (Figure 37). Left bank downstream, natural soil. In the vertical axis there are the phase velocities of the Rayleigh waves, vertical component. The blue dots indicate the first 5 modes of the theoretical dispersion curve related to the subsurface model of Table 16.

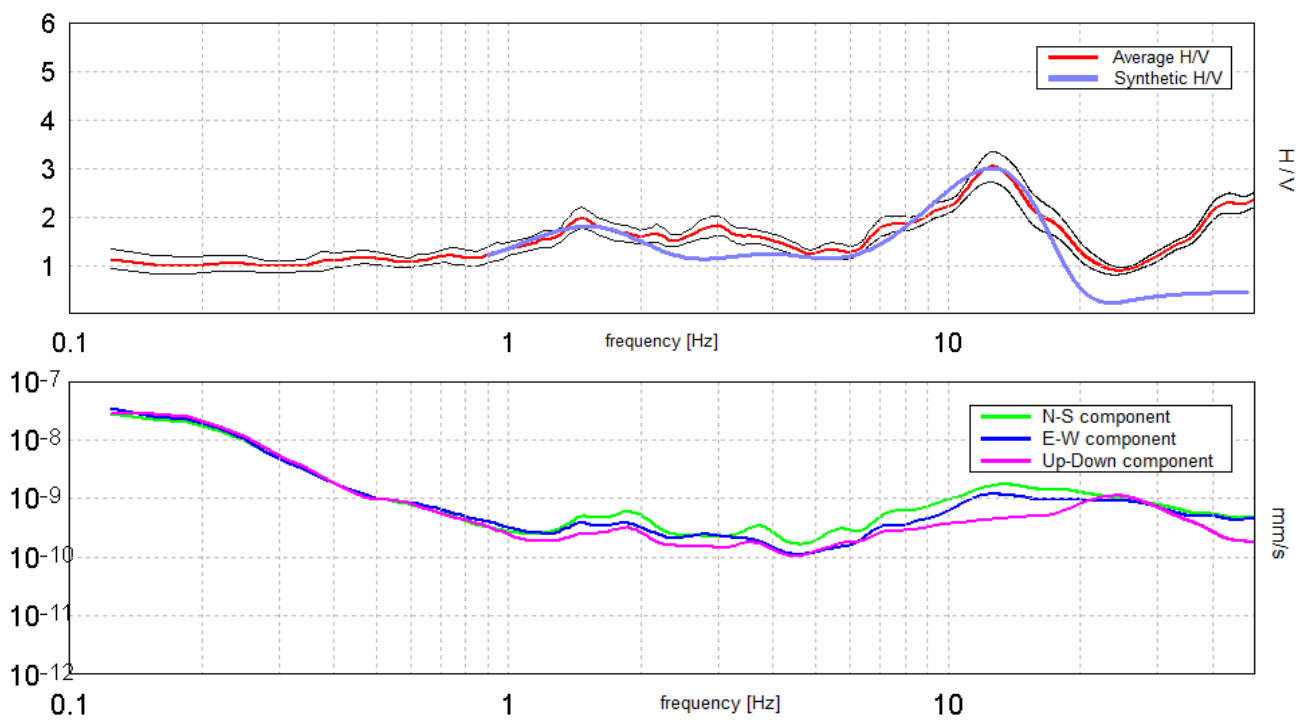


Figure 41. H/V T22 (Figure 37): mean curve in red, standard deviation in black, synthetic curve in blue (above) related to the subsoil model of Table 16. Amplitude velocity spectra of the seismic microtremor (below). Left bank downstream, natural terrain.

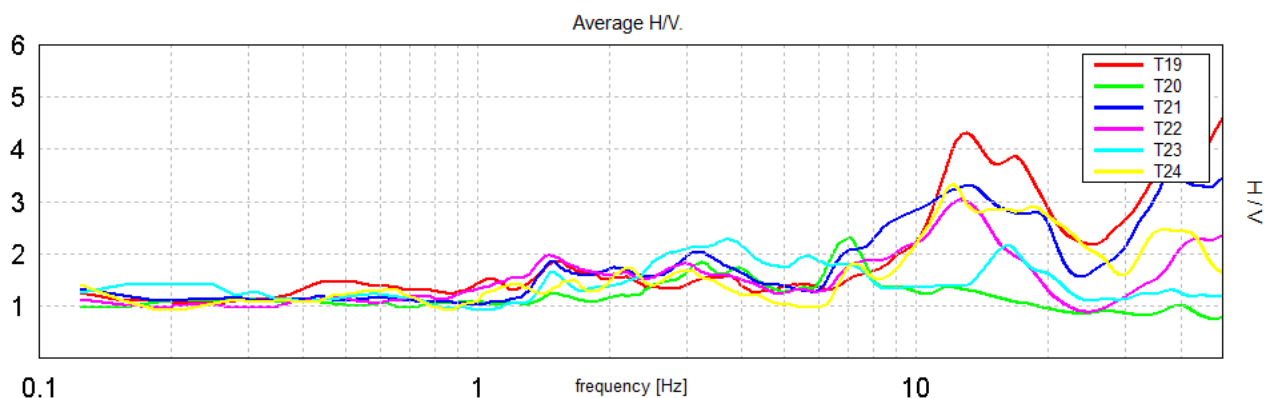


Figure 42. H/V curves acquired downstream of the dam at the sites listed in the legend (Figure 37)

Table 16. Subsoil shear wave velocity model, obtained from the joint fit of single station and array measurements A05 and T22 (Figure 37). Left bank, natural terrain.

Depth at the bottom of the layer [m]	Thickness [m]	V _s [m/s]	Poisson Ratio
2.80	2.80	150	0.48
10.80	8.00	320	0.48
30.80	20.00	400	0.48
90.80	60.00	550	0.47
Inf.	Inf.	750	0.46

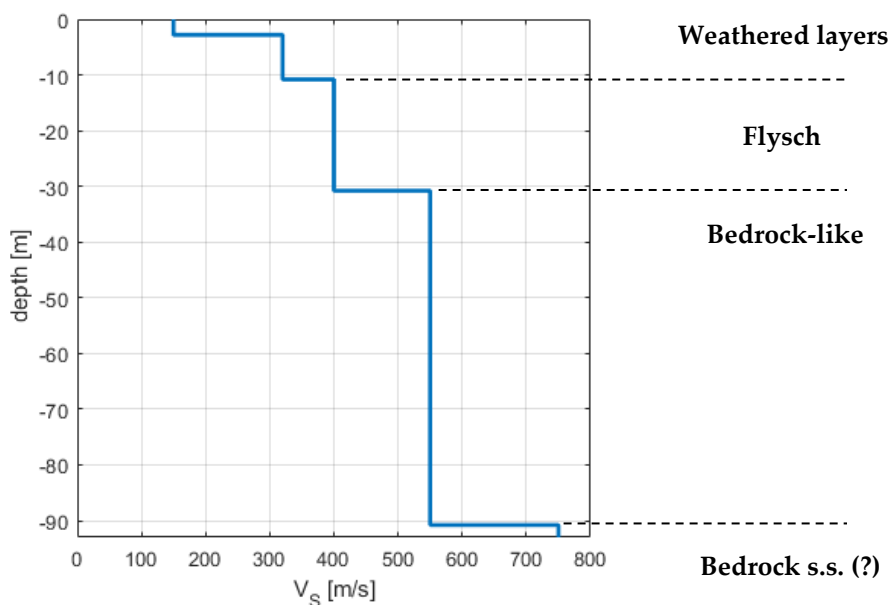


Figure 43. Shear wave velocity model and possible stratigraphic model, obtained from the joint fit of measurements A05 and T22 (Figure 37). Left bank, natural terrain.

The surveys carried out on the occasion of the seismic verification of the San Pietro dam in 2003 (SolGeo, 2003) are located downstream of the dam body. The survey S4 (Figure 35), carried out on

the left bank, confirms the presence of clays in the first 10 m, above marls (probably attributable to the Miocene Flysch). The CH4 cross-hole test (Figure 35) estimates an average velocity of the S-waves in the first 15 m of 480 m/s, which is actually greater than the $V_{seq} = V_{s30}$ value calculated in this study, equal to 330 m/s.

Table 17. Summary of the main geological formations on the right and left banks of the San Pietro sull'Osento dam.

	Geological formation	Depth interval	Average thickness	Average velocity
Left bank	Varicoloured Clays	0 - 8 m	$\bar{H} = 8$ m	$\bar{V}_s = 230$ m/s
	Flysch	8 - 108 m	$\bar{H} = 100$ m	$\bar{V}_s = 400$ m/s
Right bank	Alluvial deposits	0 - 15 m	$\bar{H} = 15$ m	$\bar{V}_s = 400$ m/s
	Yellow sandstone	15 - 115 m	$\bar{H} = 100$ m	$\bar{V}_s = 700$ m/s

Left bank: $V_{seq} \equiv V_{s30} = 330$ m/s \rightarrow Soil category C (NTC, 2018)

Right bank: $V_{seq} [0 - 15] m = 400$ m/s \rightarrow Soil category B (NTC, 2018)

For modelling purposes, we consider the more conservative soil category, that is the C one.

5.1.2.2 Ground - Right bank

The multi-channel and single-station seismic data acquired on the right bank show a single H/V peak at 6 Hz (Figure 45), which can be interpreted as the Alluvial deposits - Yellow Sandstone transition at about 15 m, depth at which the seismic bedrock was estimated, according to the description provided by Cotecchia (1959). This value is also attributable to the transition between alluvial deposits and sandstones indicated in the S5 survey (Figure 35), carried out during the seismic verifications of 2003 (SolGeo, 2003). The average velocity of the S-waves obtained from the cross-hole test CH5 (Figure 35), in the first 15 m was 580 m/s, higher than the 400 m/s estimated in this study. The discrepancy in the velocity values of the seismic waves measured between hole tests and multi-channel surface tests is not surprising, considering that the volume of the material investigated by the surface tests is much greater than the volume investigated by the hole tests and, therefore, includes a much greater number of inhomogeneities and anisotropies. However, the seismic response of the structures under examination, whose natural period is of 0.5-1 s, are governed by the wavelengths typically observed in surface tests, not in those in hole. The formers are therefore more representative than the latter, for the seismic response study object of this work.

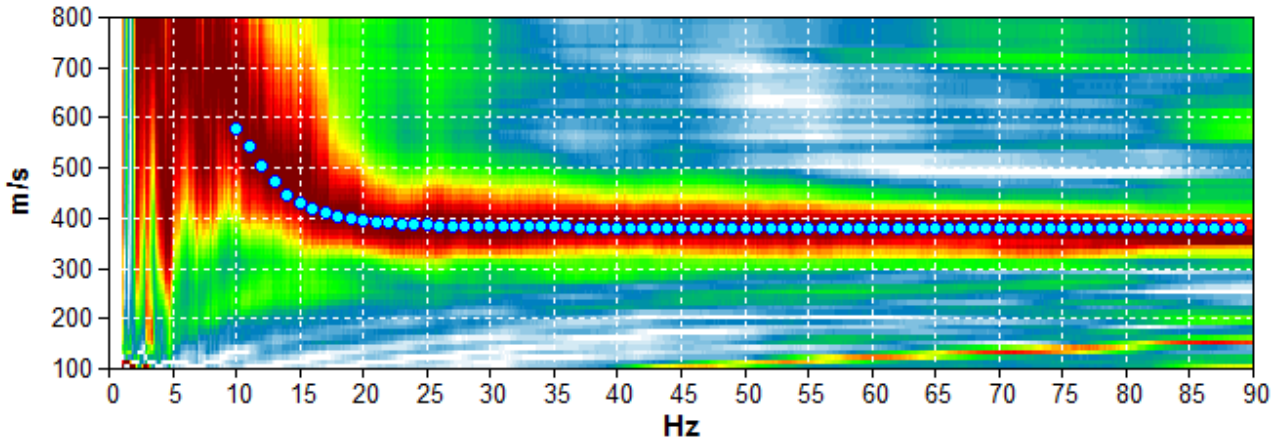


Figure 44. Dispersion curve A03 (Figure 37). Right bank downstream, natural soil. In the vertical axis there are the phase velocities of the Rayleigh waves, vertical component. The blue dots indicate the theoretical dispersion curve obtained for the subsoil model of Table 18.

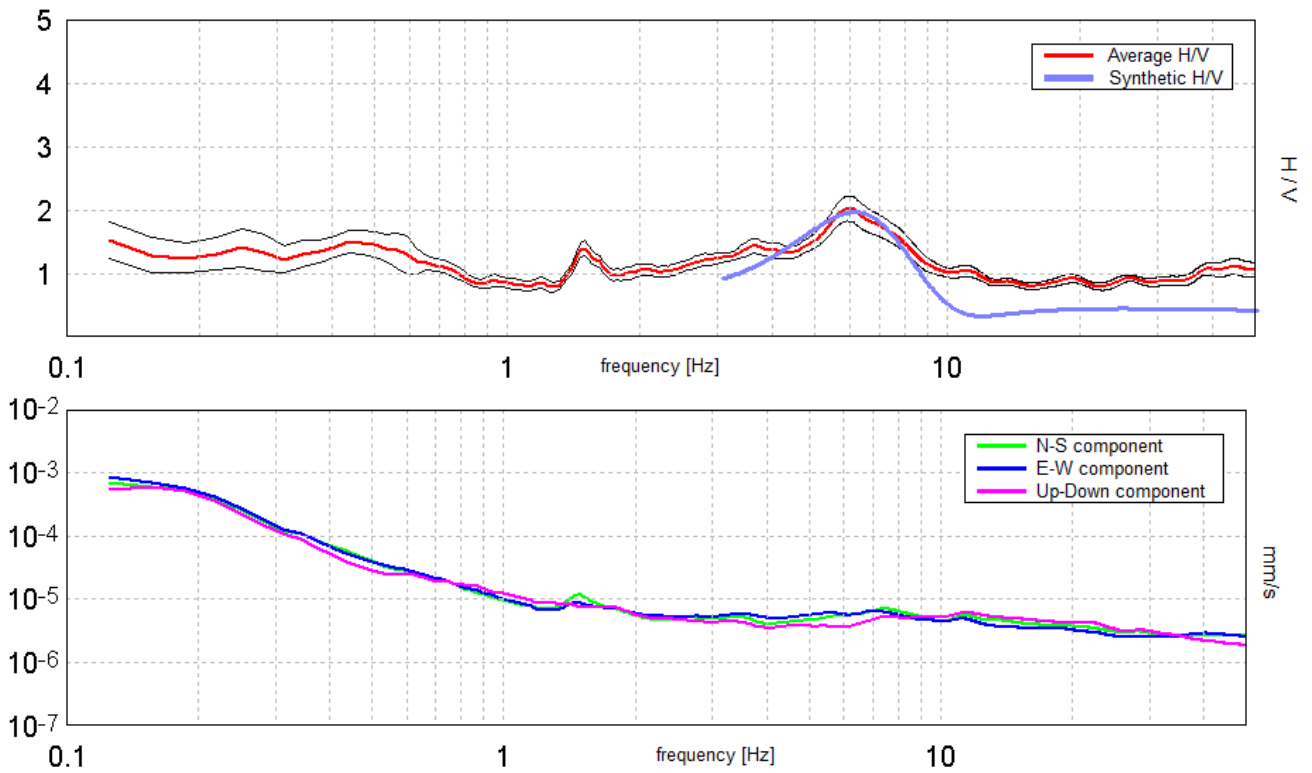


Figure 45. H/V T18: mean curve in red, standard deviation in black, synthetic curve in blue (above) relative to the terrain model of Table 18. Amplitude spectra in velocity of the seismic microtremor (below). Right bank, natural soil.

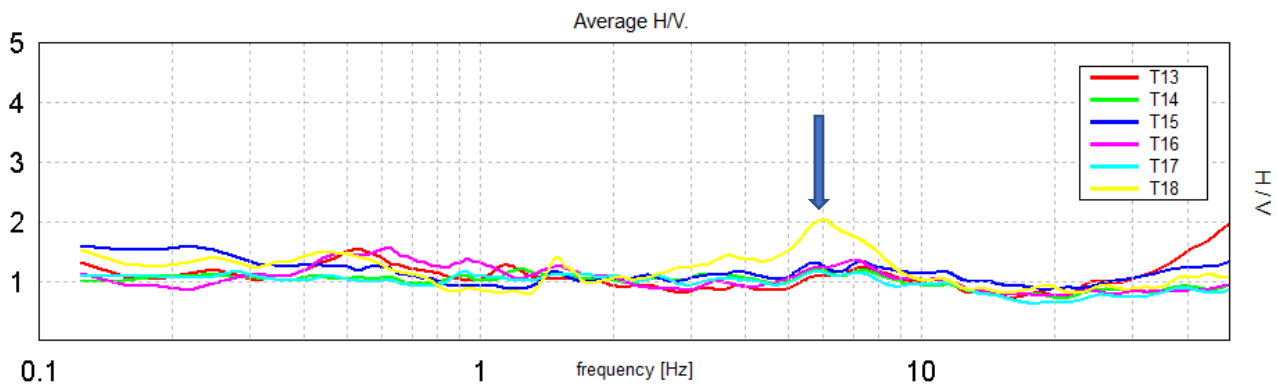


Figure 46. The H/V curves acquired on the right bank show a very low to medium marked peak at 6 Hz (see also Figure 37).

Table 18. Subsoil shear wave velocity model, obtained from the joint fit of single station and array measurements A03 and T18. Right bank, natural soil.

Depth at the bottom of the layer [m]	Thickness [m]	V _s [m/s]	Poisson Ratio
15	15	400	0.48
Inf.	Inf.	700	0.48

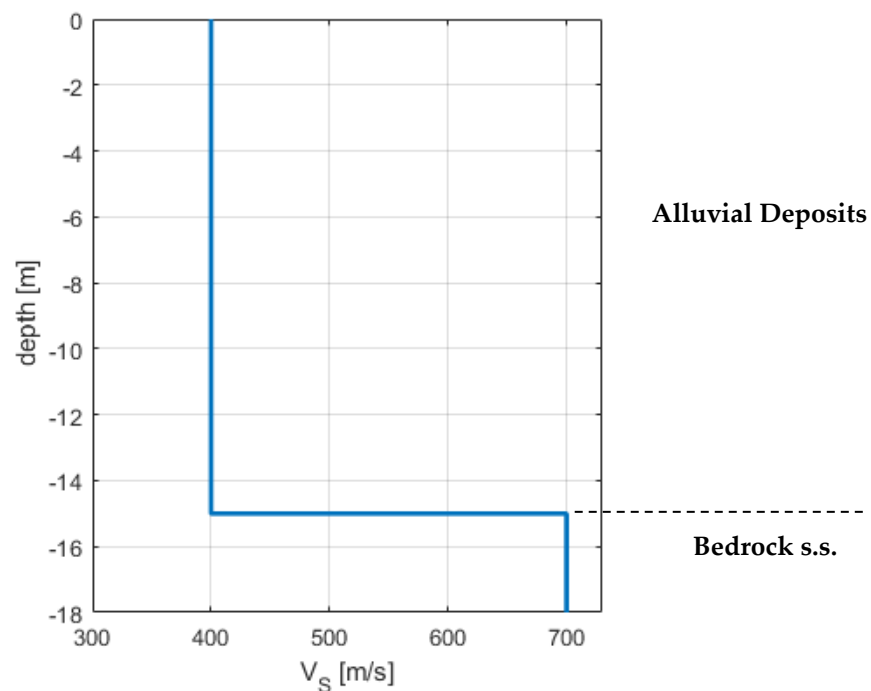


Figure 47. Shear wave velocity model and possible stratigraphic model, obtained from the joint fit of measurements A03 and T18. Right bank, natural soil.

5.1.2.3 Embankment

On the same occasion as the seismic verifications made in 2003, measurements were also carried out on the embankment of the San Pietro dam. In the embankment area adjacent to the left bank, the

cross-hole measurements CH2 (Figure 35) revealed an average velocity of the shear waves of 610 m/s in the first 28 m. The stratigraphy of the S2 survey (Figure 35) reports 37 m of silty sand and pebbles. In the embankment area adjacent to the right bank, the measurements in cross-hole CH3 (Figure 35) revealed an average velocity of the shear waves of 630 m/s in the first 30 m. The stratigraphy of the S2 survey shows 40 m of silty sand and pebbles, overlying silty clayey sand. The model carried out in the present study shows average velocities typically lower, equal to 390 m/s in the first 14 m (Figure 49). The same considerations as on page 74 apply here.

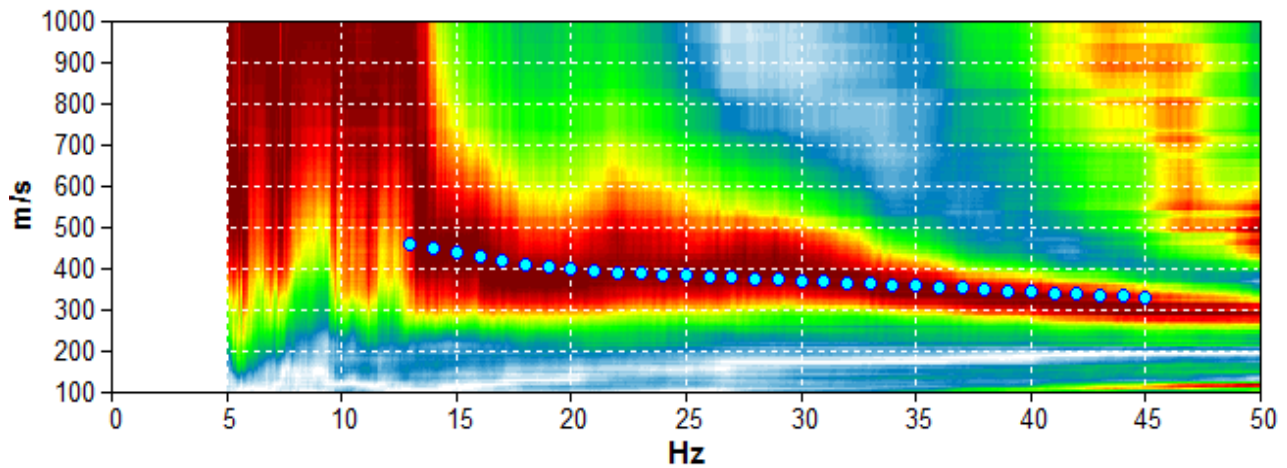


Figure 48. Dispersion curve A02. Embankment of the dam body. The blue dots indicate the theoretical dispersion curve obtained for the subsoil model of Table 19.

Table 19. Velocity model of the shear waves in the embankment of the dam body, obtained from the dispersion curve A02.

Depth at the bottom of the layer [m]	Thickness [m]	Vs [m/s]	Poisson Ratio
4.00	4.00	320	0.47
14.00	10.00	420	0.47
inf.	inf.	600	0.47

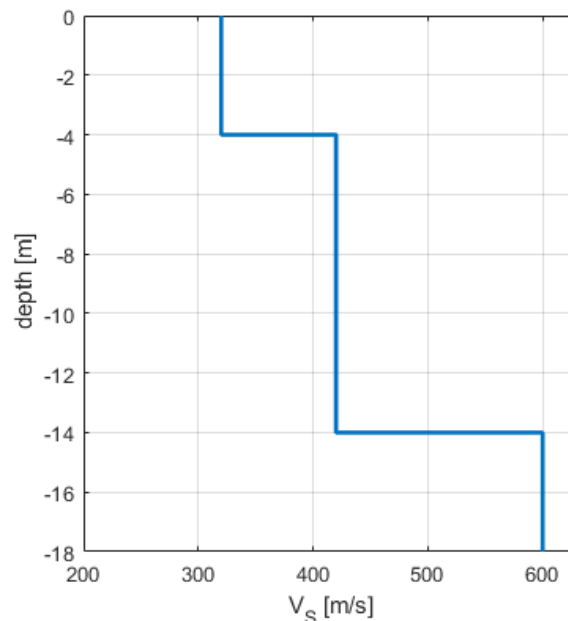


Figure 49. Velocity model of the shear waves in the embankment of the dam body, obtained from the dispersion curve A02.

5.1.2.4 Dam

With reference to the symbols and positions of Figure 37 and Figure 50, 3 measurements were carried out on the body of the San Pietro dam (quarter, middle and three-quarters of the longitudinal extension), whose average amplitude spectra, in displacement, are given in Figure 51. The ordinate scale is the same for all three graphs, emphasizing that the maximum displacement occurs in the transverse direction, around 2.25 Hz and it is the first flexural mode of the dam in this direction. It should be noted that this way of vibrating is naturally affected by the level of the reservoir in the instant of measurement.



Figure 50. H/V measurements on the dam crest (T01), on the access bridge to the well (T07) and on the well (T09) on the San Pietro sull'Osento dam.

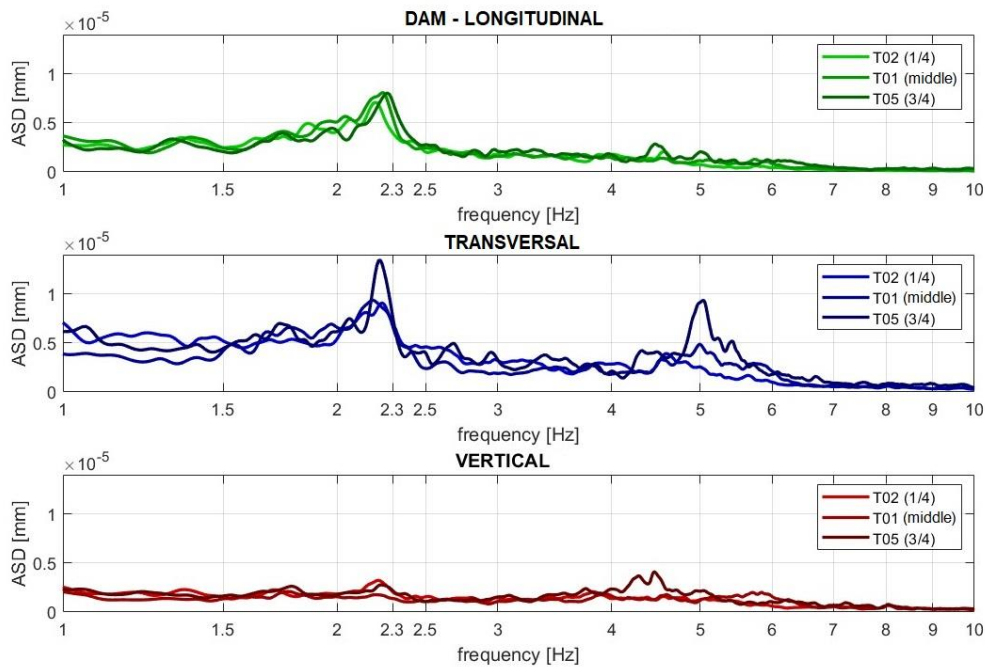


Figure 51. Amplitude spectra in displacement collected on the earth dam as indicated in Figure 37 and Figure 50, along the 3 principal directions.

5.1.2.5 Access bridge to the well

With reference to the symbols and positions of Figure 37 and Figure 50, 2 measurements were carried out on the access bridge to the well of the San Pietro dam, in a central position (points T06 and T07). The resulting average amplitude spectra, in displacement, are given in Figure 52. The ordinate scale is the same for all three graphs, emphasizing that the maximum displacement occurs in the transverse direction, around 2.7 Hz and subsequently at 4.7 Hz. As we will see, these frequencies are also dominant within the body of the well (positions T08 and T09) and are therefore not attributable to the proper transverse bending modes of the bridge alone but of the entire well + bridge structure.

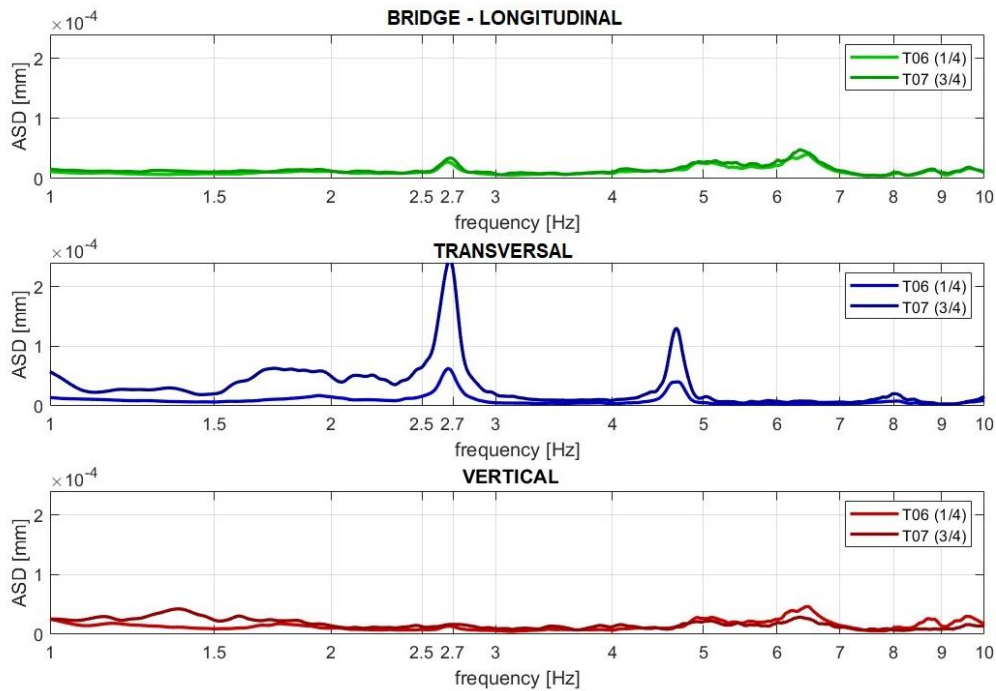


Figure 52. Average amplitude spectra in displacement as indicated in Figure 37 and Figure 50, along the 3 principal directions of motion recorded along the access bridge to the well.

5.1.2.6 Well

With reference to the symbols and positions of Figure 37 and Figure 50, 2 measurements were carried out on the well of the San Pietro dam. The resulting average amplitude spectra, in displacement, are given in Figure 53. The scale of the ordinates in the transverse direction is one order of magnitude greater than in the other two directions, indicating that the motion is mainly in the transverse direction and it has a main frequency of 2.7 Hz and 4.7 Hz, as already found on the access bridge to the well. The amplitudes of these harmonics here are one order of magnitude higher than in the previous case. It is noted that the active machines inside the well cause vibrations higher than 2 mm/s² in acceleration, at frequencies higher than 10 Hz.

Table 20. Main frequencies of the vibration modes of the San Pietro dam.

	I Mode Longitudinal [Hz]	I Mode Transversal [Hz]
Dam	2.25	-
Access bridge to the well	6.5	2.7
Well	2.7	-

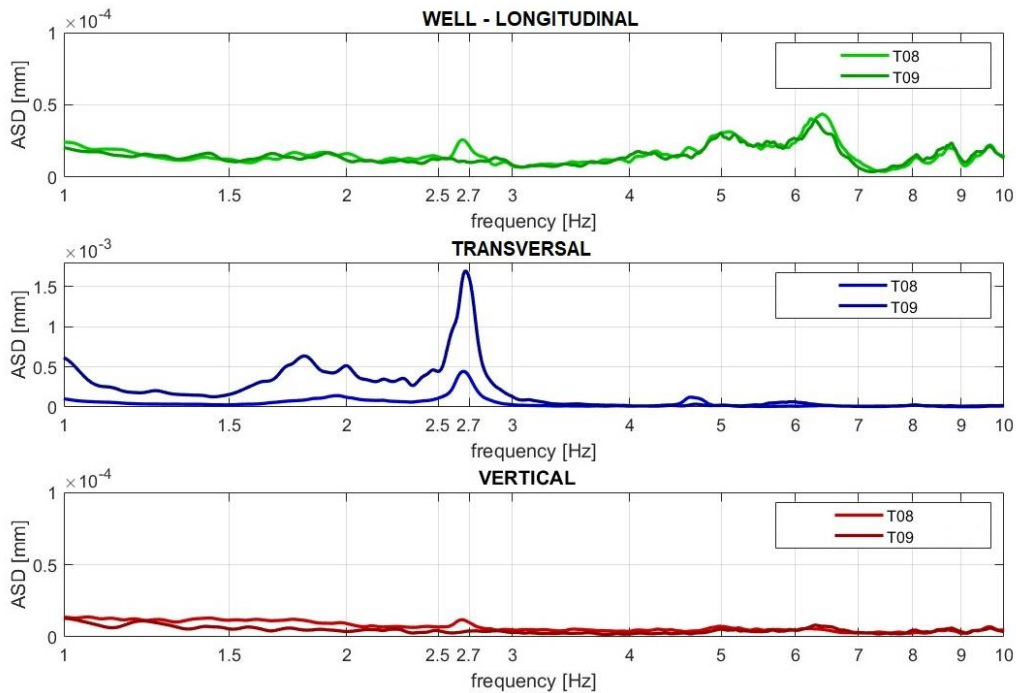


Figure 53. Average amplitude spectra in displacement as indicated in Figure 37 and Figure 50, along the 3 main directions of motion recorded at the well of the San Pietro dam.

5.1.2.7 Accelerograms for SSR (Site Seismic Response) studies referring to stiff ground

The soils and structures analysis presented above is necessary, as already anticipated, for the geotechnical modelling with finite elements of the dam and the related structures. For that analysis it is necessary to define the seismic bedrock and the periods of interest of the buildings. Lastly, in order to be carried out, the analysis also requires a set of accelerograms referring to the identified seismic bedrock. In this paragraph we illustrate how they were identified.

The European (European Strong Motion Database, ESD) and Italian (Italian Accelerometric Archive, ITACA) databases were accessed in order to find combinations of natural accelerograms compatible with the simplified acceleration spectra provided by the Italian Building Code (NTC, 2018) for specific return periods. The nominal life of the facilities under investigation is $V_N = 50$ years, the class of use is $C_U = IV$ and this corresponds to return times $T_R = 950$ and $T_R = 1950$ years respectively for the limit state of safety of life (SLV) and the limit state of collapse prevention (SLC). For the SLV state, 17 horizontal accelerograms were found (Figure 54), while 12 horizontal accelerograms were found for the SLC state (Figure 55). The accelerograms refer to rigid ground. By spectral-compatibility we mean a 10% average tolerance in the 0.15-2 s band and a 30% average tolerance in excess in the same period band. The range of magnitude covered by the accelerograms found goes from $M_w 5.6$ to $M_w 6.9$. The events found are listed in Table 21 and Table 22. The response spectra of the selected earthquakes are superimposed on the simplified regulatory spectra for the sites related to the dams (for soil category A and, by way of reference, for the soil category C, which is the one associated with the dams) in Figure 56 and Figure 57.

Table 21. Earthquakes selected for the limit state of safety of life (SLV), related to the San Pietro dam.

ID waveform	ID earthquake	Date	M_w	Database	PGA [m/s²]
007187xa	Avej (Iran)	22/06/2002	6.5	European	4.374
007142ya	Bingol (Turkey)	01/05/2003	6.3	European	2.9178
006349ya	Southern Iceland (aftershock)	21/06/2000	6.4	European	7.2947
006349xa	Southern Iceland (aftershock)	21/06/2000	6.4	European	8.218
004675ya	Southern Iceland	17/06/2000	6.5	European	1.5325
004675xa	Southern Iceland	17/06/2000	6.5	European	1.2916
004674ya	Southern Iceland	17/06/2000	6.5	European	3.3109
004674xa	Southern Iceland	17/06/2000	6.5	European	3.1176
000766ya	Umbria Marche (aftershock)	14/10/1997	5.6	Italian	3.3014
000290ya	Campano Lucano	23/11/1980	6.9	Italian	3.1662
000290xa	Campano Lucano	23/11/1980	6.9	Italian	2.1206
000287ya	Campano Lucano	23/11/1980	6.9	Italian	1.7756
000287xa	Campano Lucano	23/11/1980	6.9	Italian	1.3633
000198ya	Montenegro	15/04/1979	6.9	European	2.1985
000198xa	Montenegro	15/04/1979	6.9	European	1.7743
000055ya	Friuli	06/05/1976	6.5	Italian	3.0968
000055xa	Friuli	06/05/1976	6.5	Italian	3.4985

Table 22. Earthquakes selected for the limit state of collapse prevention (SLC), related to the San Pietro dam.

ID waveform	ID earthquake	Date	M_w	Database	PGA [m/s²]
007329ya	Faial (Azores)	09/07/1998	6.1	European	3.749
007142xa	Bingol (Turkey)	01/05/2003	6.3	European	5.0514
006349ya	Southern Iceland (aftershock)	21/06/2000	6.4	European	7.2947
006349xa	Southern Iceland (aftershock)	21/06/2000	6.4	European	8.218
006332ya	Southern Iceland (aftershock)	21/06/2000	6.4	European	5.5698
006263ya	Southern Iceland	17/06/2000	6.5	European	5.018
004674ya	Southern Iceland	17/06/2000	6.5	European	3.3109
004674xa	Southern Iceland	17/06/2000	6.5	European	3.1176
004673ya	Southern Iceland	17/06/2000	6.5	European	4.6775
000879xa	Dinar (Turkey)	01/10/1995	6.4	European	2.6739
000198ya	Montenegro	15/04/1979	6.9	European	2.1985
000055ya	Friuli	06/05/1976	6.5	Italian	3.0968

Table 23. Values of the parameters a_g (maximum horizontal acceleration at the site), F_0 (maximum value of the amplification factor of the spectrum in horizontal acceleration), T_c^* (starting period of the constant velocity segment of the spectrum in horizontal acceleration) for the return periods T_R associated with each border state, relating to the San Pietro dam (according to NTC, 2018).

Limit state	T_R [years]	a_g [g]	F_0 [-]	T_c^* [s]
SLV	949	0.290	2.398	0.428
SLC	1950	0.396	2.372	0.445

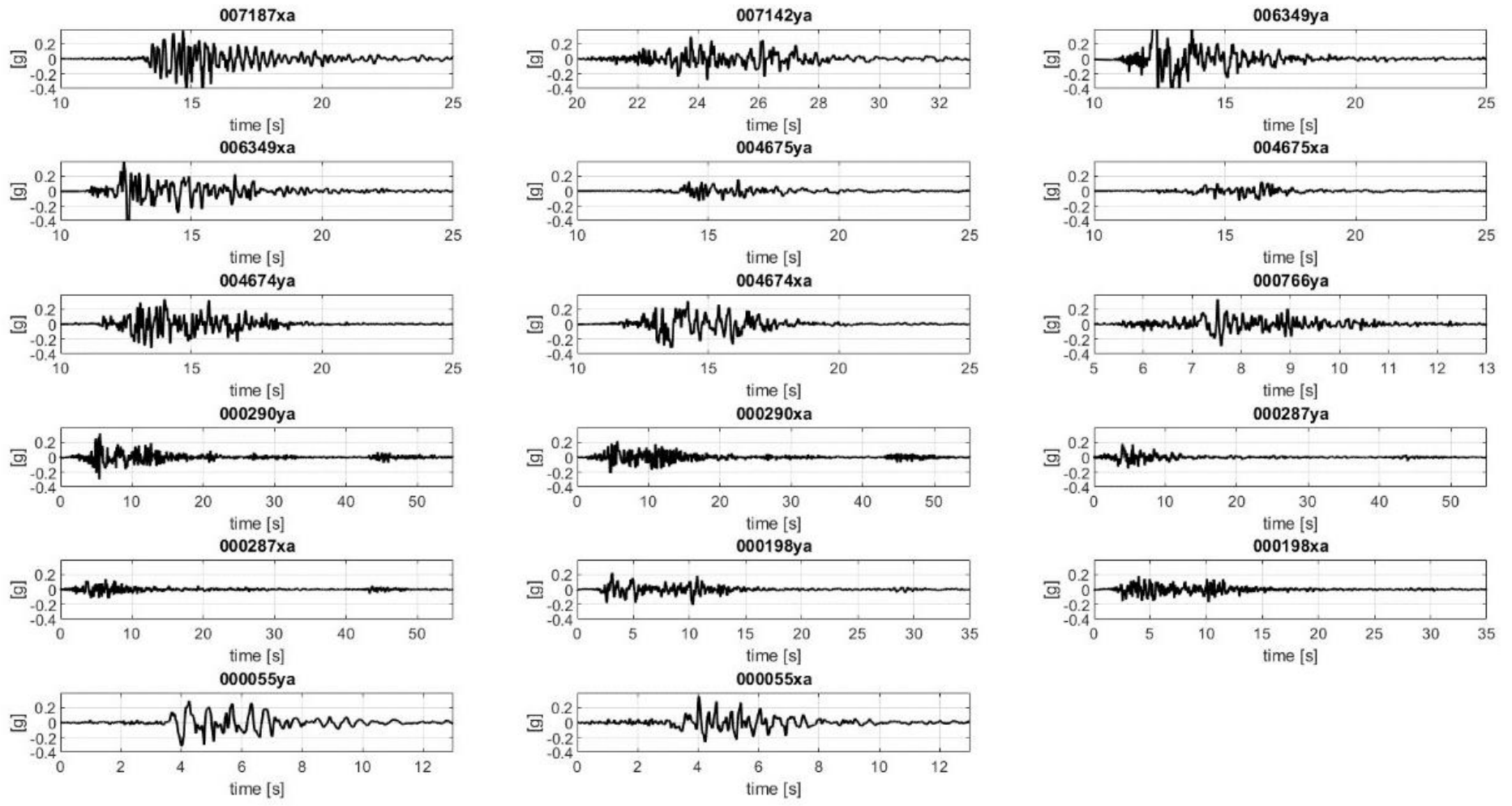


Figure 54. Accelerograms of earthquakes selected for the SLV state, related to the San Pietro dam compatible with the target spectra provided by NTC2018.

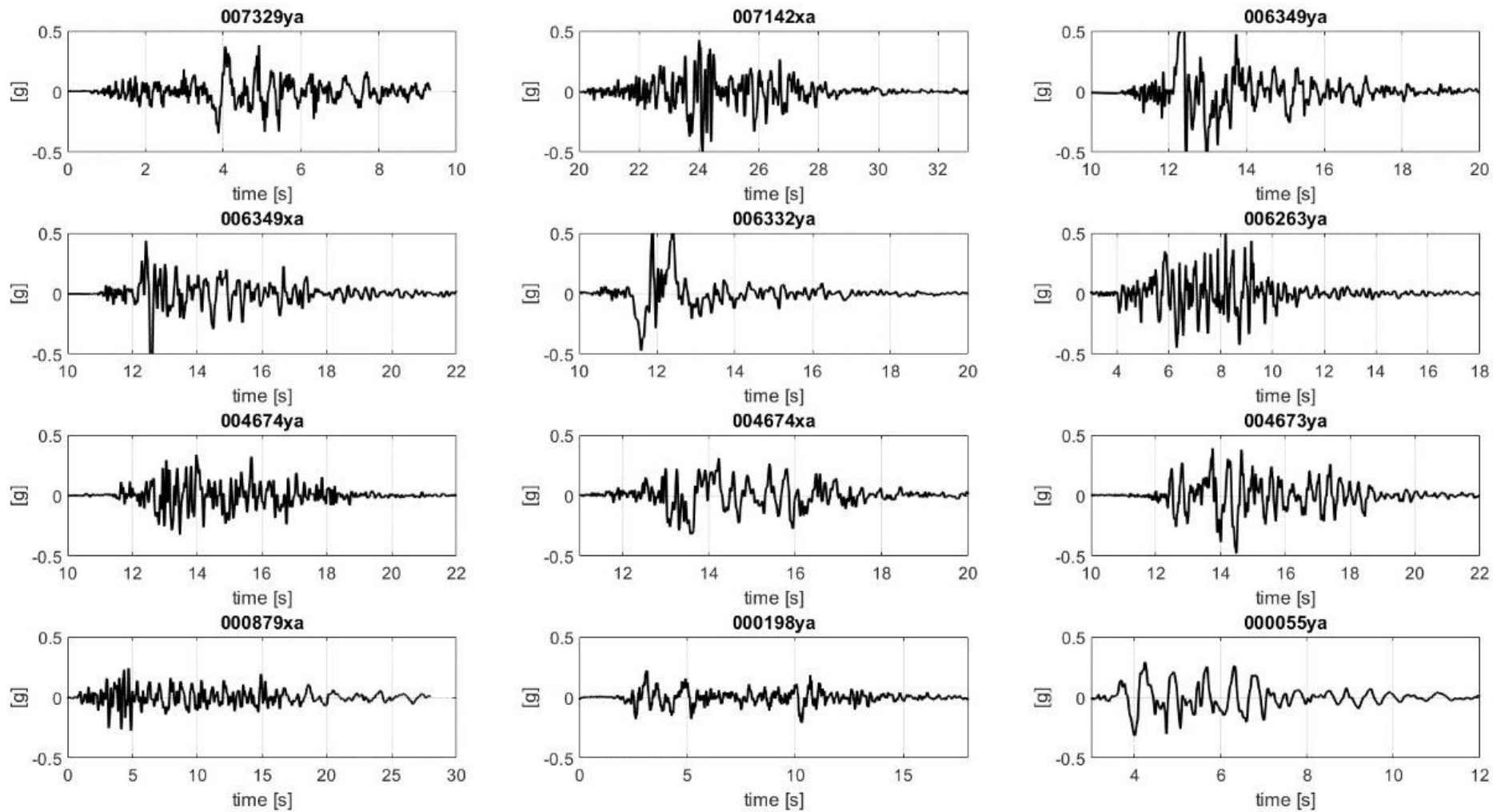


Figure 55. Accelerograms of earthquakes selected for the SLC state, related to the San Pietro dam compatible with the target spectra provided by NTC2018.

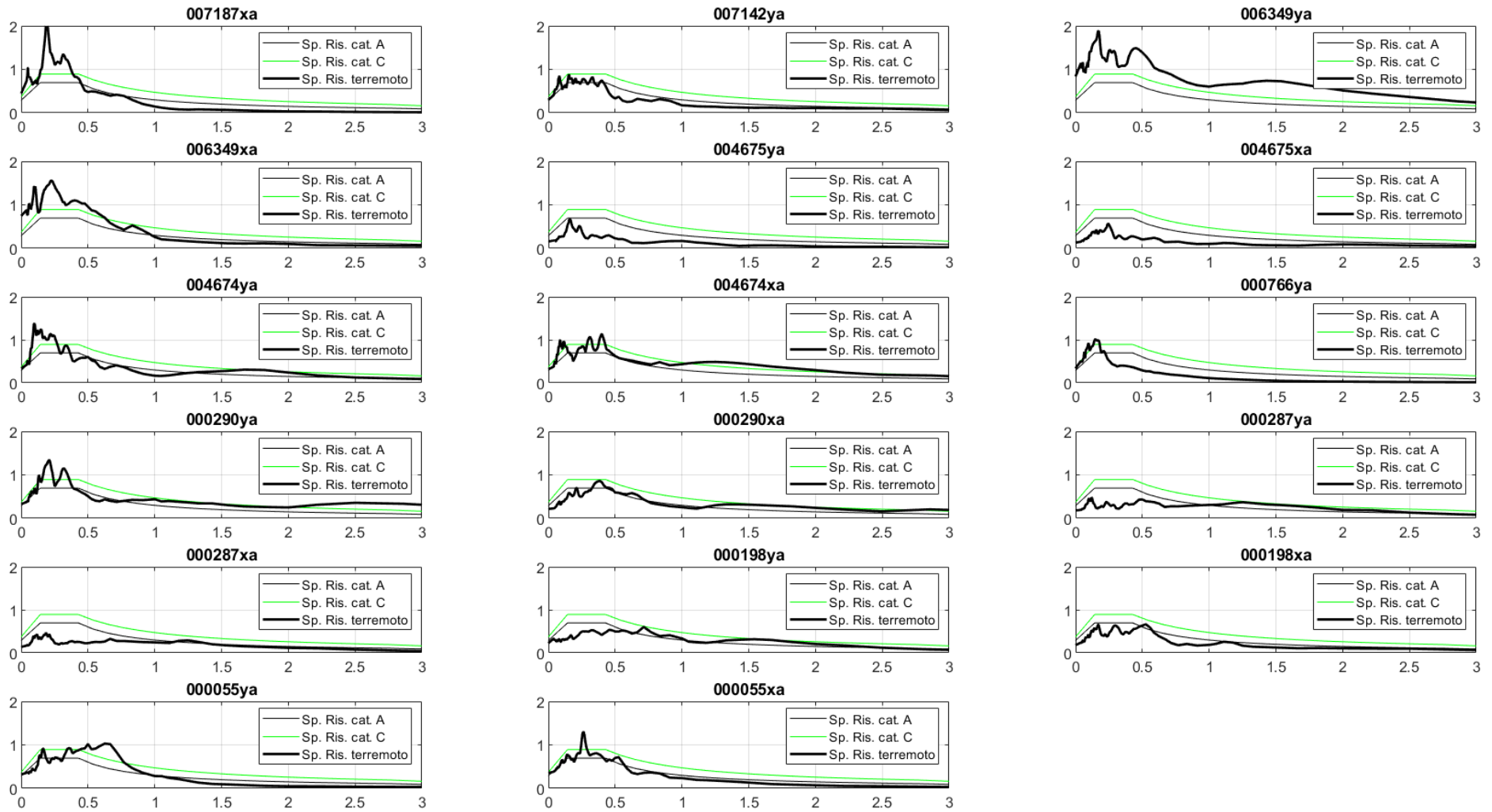


Figure 56. Response spectra of selected earthquakes (bold black) and simplified regulatory response spectra for site category A (thin black) and C (green) for the SLV state, related to the San Pietro dam.

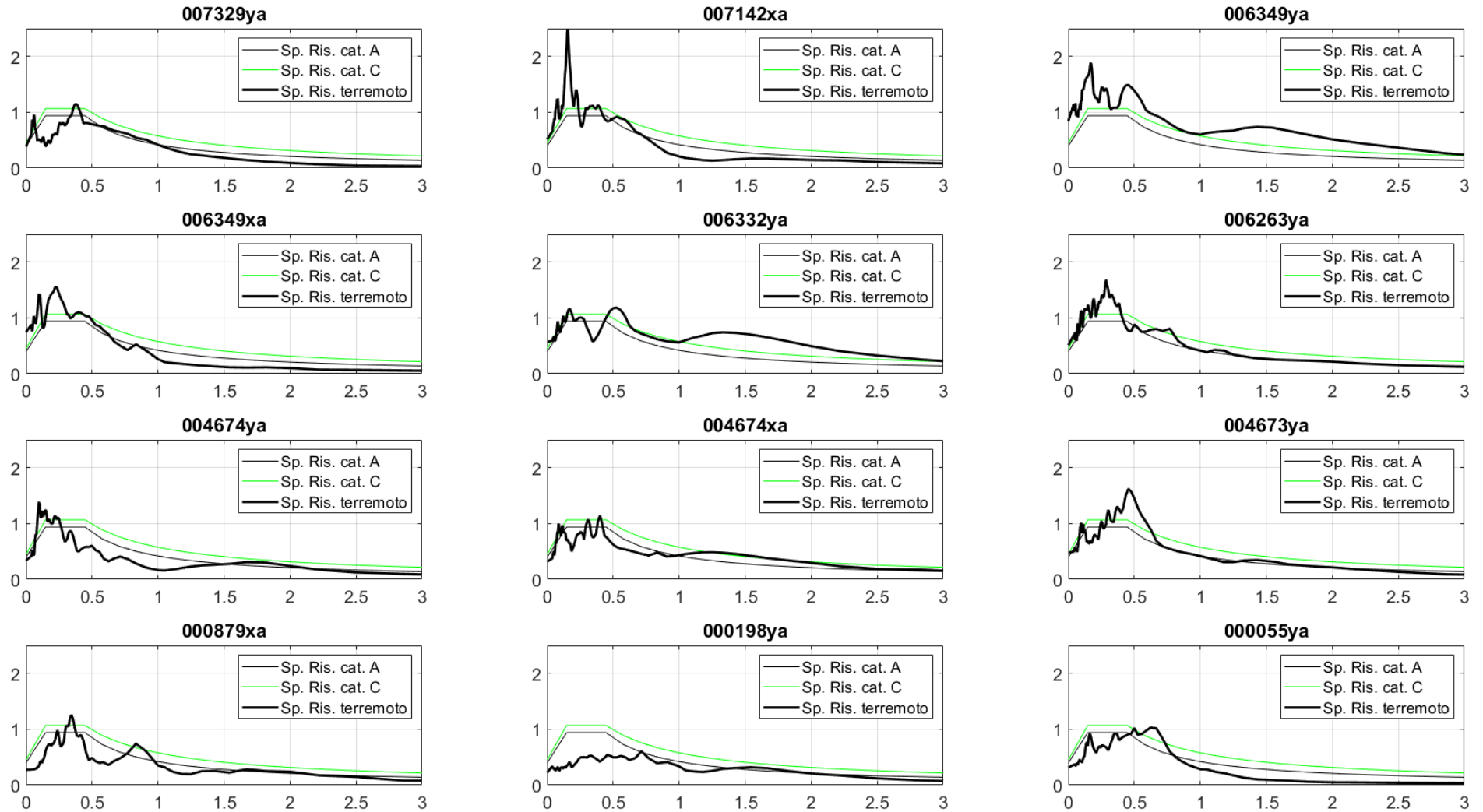


Figure 57. Response spectra of the selected earthquakes (bold black) and simplified regulatory response spectra for site category A (thin black) and C (green) for the SLC state, related to the San Pietro dam.

5.2 Marana Capacciotti dam

5.2.1 Existent surveys

From the ISPRA national archive of subsoil surveys (ISPRA), the presence of useful analysis for checking the stratigraphy modelled in this work was investigated. The only data available is the water well 155780, which is about 2 km away from the Marana Capacciotti dam. The transition from yellow clay to cemented sand in the first meters (Table 24) suggests that the stratigraphic succession on the surface may be the same as that hypothesized for the Capacciotti dam.

Table 24. Superficial stratigraphic succession of well 155780, located about 2 km from the Capacciotti dam (ISPRA).

Depth Interval	Lithological Description
0 – 2 m	Soil
2 – 9 m	Breccia
9 – 12 m	Yellow clay
12 – 29 m	Sandstone

5.2.2 New surveys

During the surveys that we carried out in July and October 2019, a total of 15 environmental vibration measurements (13 on structure and 2 on natural soil) and 3 dispersion measurements of surface waves (2 on structure and 1 on natural soil) were acquired on the Marana Capacciotti dam, whose location is shown in (Figure 59).

5.2.2.1 Ground

The measurements for the subsoil model were carried out on the gray-blue clays downstream of the embankment of the Capacciotti dam. The velocity model obtained from the joint analysis of the measurements is shown in Table 25 and Figure 62. It proposes a shallow layer of about 10 m thickness with $V_s \approx 190\text{-}200$ m/s and two strong impedance contrasts in depth, at about 80 m ($V_s \approx 320$ m/s) and 400 m ($V_s \approx 550$ m/s). The seismic bedrock *sensu stricto* is estimated to be 400 m deep. All the H/V measurements acquired both on natural soils and on embankments show repeated peaks at 0.9 Hz and 0.33 Hz (Figure 60).

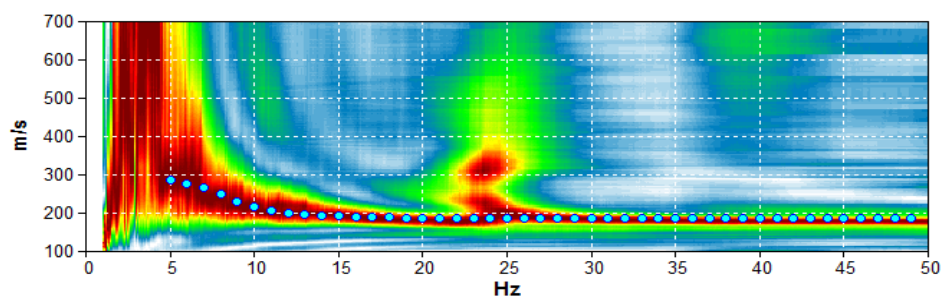


Figure 58. Dispersion curve A03 (Figure 59). Natural soil. In the vertical axis there are the phase velocities of the Rayleigh waves, vertical component. The blue dots indicate the theoretical dispersion curve obtained for the subsoil model of Table 25.



Figure 59. Location of the H/V measurements (red and white dots) and of the MASW-ReMi measurements (yellow lines) acquired during the July-October fieldwork carried out at the Marana Capacciotti dam.

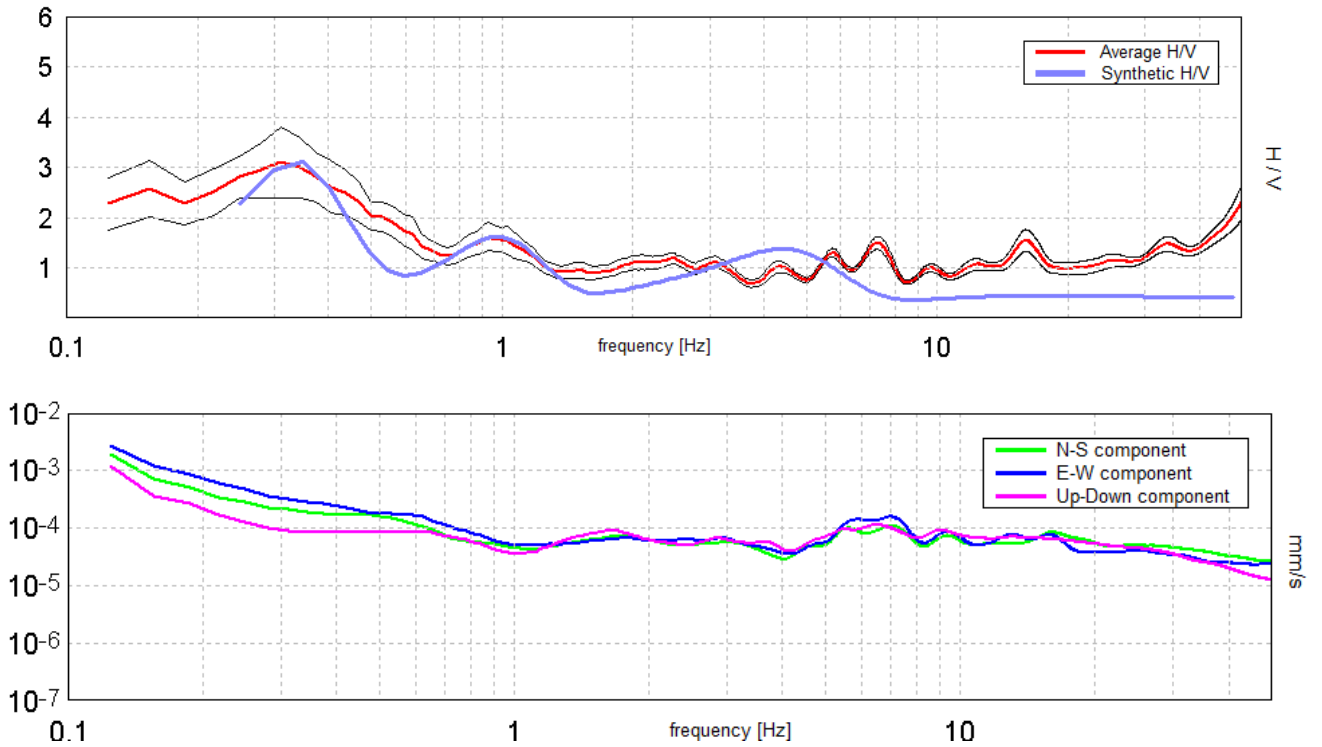


Figure 60. H/V T14 (Figure 59): mean curve in red, standard deviation in black, synthetic curve in blue (above) related to the subsoil model of Table 25. Amplitude spectra in velocity of the seismic microtremor (below).

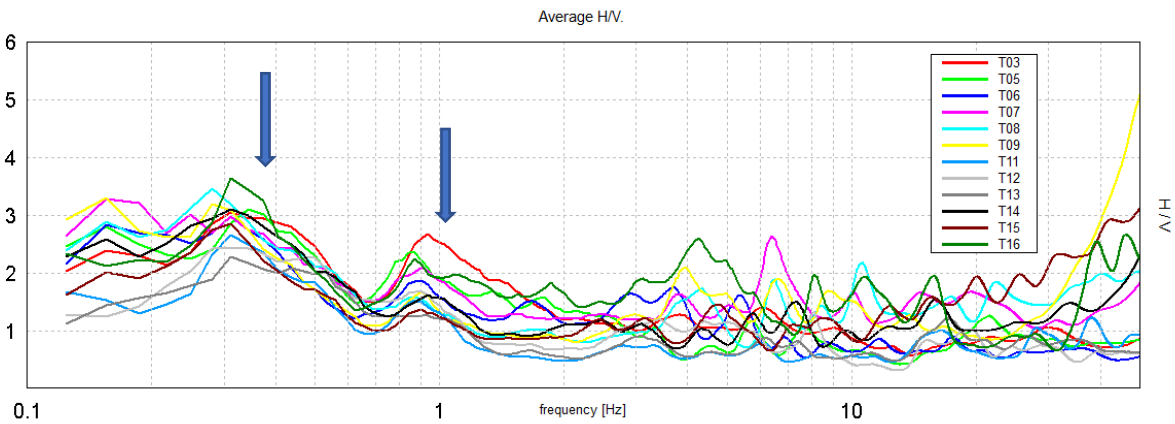


Figure 61. The H/V curves acquired on natural soil (Figure 59) show repeated peaks at 0.33 Hz and 0.9 Hz.

Table 25. Shear wave velocity model, obtained from the joint fit of single station and array measurements A03 and T14, natural soil.

Depth at the bottom of the layer [m]	Thickness [m]	Vs [m/s]	Poisson Ratio
10.00	10.00	195	0.48
85.00	75.00	320	0.48
405.00	320.00	550	0.48
inf.	inf.	920	0.46

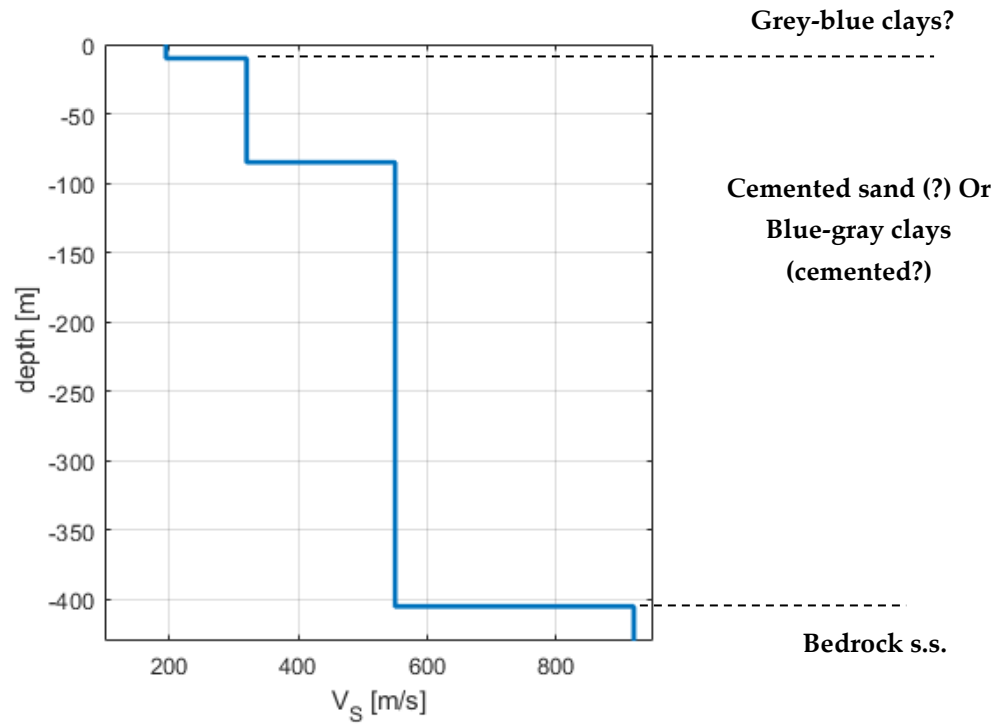


Figure 62. Shear wave velocity model and possible stratigraphic model, obtained from the joint fit of measurements A03 and T14 (Figure 59). Natural soil.

$$V_{seq} \equiv V_{s30} = 260 \text{ m/s} \rightarrow \text{Soil category C (NTC, 2018)}$$

5.2.2.2 Embankment

The V_s model derived from the joint modelling of the measurements carried out on the embankment of the Marana Capacciotti dam shows an equivalent velocity in the first 30 m of about 300 m/s.

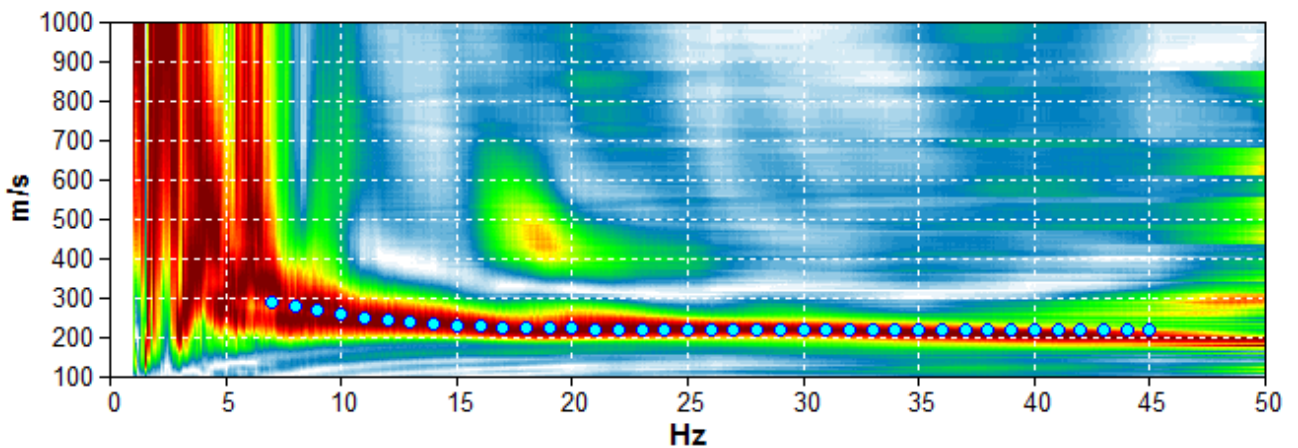


Figure 63. Dispersion curve A01 (Figure 59). Embankment of the dam body. The blue dots indicate the theoretical dispersion curve obtained for the subsoil model of Table 26.

Table 26. Shear wave velocity model in the embankment of the dam body, obtained from measurements A01 and A02.

Depth at the bottom of the layer [m]	Thickness [m]	V _s [m/s]	Poisson Ratio
10.00	10.00	230	0.48
inf.	inf.	340	0.48

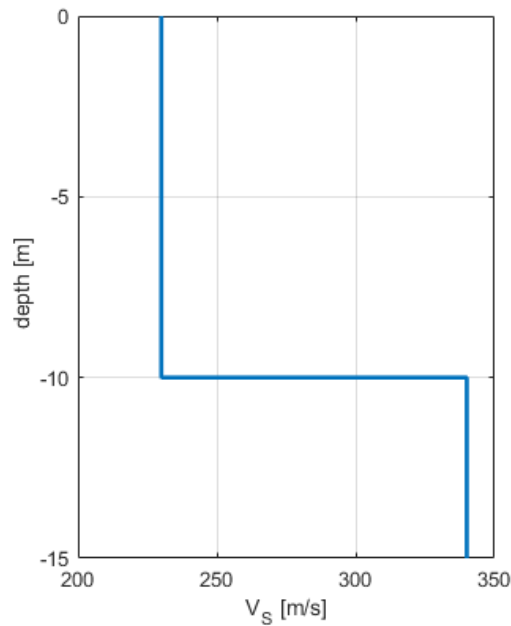


Figure 64. Shear wave velocity model in the embankment of the dam body, obtained from measurements A01 and A02 (Figure 59).

5.2.2.3 Dam

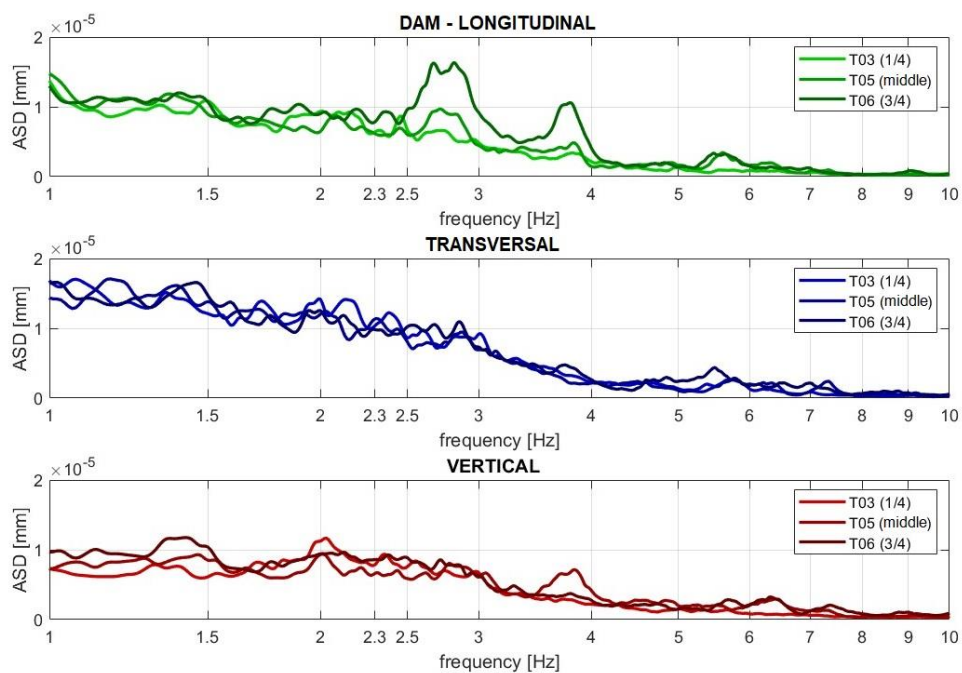


Figure 65. Average amplitude spectra modes in the 3 main directions of motion recorded along the body of the Marana Capacciotti dam.



Figure 66. H/V T06 (Figure 59) measurement, carried out on the dam crest.

With reference to the symbols and positions of (Figure 59 and Figure 66), 3 measurements were carried out on the body of the Marana Capacciotti dam (quarter, middle and three-quarter positions), whose average amplitude spectra, in displacement, are given in Figure 65. The ordinate scale is the same for all three graphs, emphasizing that the maximum displacement occurs in the longitudinal direction, around 2.7 Hz, 3.8 Hz and 5.6 Hz. The most visible vibration mode is in the the longitudinal direction. No other modes are evident in the other directions.

Table 27. Main frequencies of the vibration modes of the Marana Capacciotti dam.

	I Mode Longitudinal [Hz]	I Mode Transversal [Hz]	I Mode Vertical [Hz]
Dam	2.7	-	-

5.2.2.4 Accelerograms for SSR (Site Seismic Response) studies referring to stiff ground

The soils and structures analysis presented above is necessary, as already anticipated, for the geotechnical modelling with finite elements of the dam and the related structures. For that analysis it is necessary to define the seismic bedrock and the periods of interest of the buildings. Lastly, in order to be carried out, the analysis also requires a set of accelerograms referring to the identified seismic bedrock. In this paragraph we illustrate how they were identified.

For the SLV state 10 horizontal accelerograms were found (Figure 67) and for the SLC state 11 accelerograms were found (Figure 68). The accelerograms refer to stiff ground. By spectral compatibility we mean a 10% average tolerance in the 0.15-2 second band and a 30% average tolerance in excess in the same period band. The range of magnitude covered by the accelerograms found ranges from Mw 5.6 to Mw 6.9. The events found are listed in Table 28 and Table 29. The response spectra of the selected earthquakes are superimposed on the simplified regulatory spectra for the sites related to the dams (for the soil category A and, by way of reference for the soil category C, which is the one associated with the dams) in Figure 69 and Figure 70.

Table 28. Earthquakes selected for the SLV state, related to the Marana Capacciotti dam.

ID waveform	ID earthquake	Date	M _w	Database	PGA [m/s ²]
000055xa	Friuli	06/05/1976	6.5	Italian	3.4985
000198xa	Montenegro	15/04/1979	6.9	European	1.7743
000198ya	Montenegro	15/04/1979	6.9	European	2.1985
000287xa	Campano Lucano	23/11/1980	6.9	Italian	1.3633
000290xa	Campano Lucano	23/11/1980	6.9	Italian	2.1206
000290ya	Campano Lucano	23/11/1980	6.9	Italian	3.1662
000766ya	Umbria Marche (aftershock)	14/10/1997	5.6	Italian	3.3014
004674xa	Southern Iceland	17/06/2000	6.5	European	3.1176
006349xa	Southern Iceland (aftershock)	21/06/2000	6.4	European	7.2947
007142ya	Bingol (Turkey)	01/05/2003	6.3	European	2.9178

Table 29. Earthquakes selected by Rexel for the SLC state, related to the Marana Capacciotti dam.

ID waveform	ID earthquake	Date	M _w	Database	PGA [m/s ²]
000055xa	Friuli	06/05/1976	6.5	Italian	3.4985
000055ya	Friuli	06/05/1976	6.5	Italian	3.0968
000198ya	Montenegro	15/04/1979	6.9	European	2.1985
000290xa	Campano Lucano	23/11/1980	6.9	Italian	2.1206
000290ya	Campano Lucano	23/11/1980	6.9	Italian	3.1662
004674xa	Southern Iceland	17/06/2000	6.5	European	3.1176
004674ya	Southern Iceland	17/06/2000	6.5	European	3.3109
006332xa	Southern Iceland (aftershock)	21/06/2000	6.4	European	5.1881
006349xa	Southern Iceland (aftershock)	21/06/2000	6.4	European	7.2947
006349ya	Southern Iceland (aftershock)	21/06/2000	6.4	European	8.218
007142ya	Bingol (Turkey)	01/05/2003	6.3	European	2.9178

Table 30. Values of the parameters a_g (maximum horizontal acceleration at the site), F_0 (maximum value of the amplification factor of the spectrum in horizontal acceleration), T_c^* (starting period of the constant velocity segment of the spectrum in horizontal acceleration) for the return periods T_R associated with each limit state, related to the Capacciotti dam (according to NTC, 2018).

Limit state	T_R [years]	a_g [g]	F_0 [-]	T_c^* [s]
SLV	949	0.271	2.363	0.408
SLC	1950	0.380	2.306	0.427

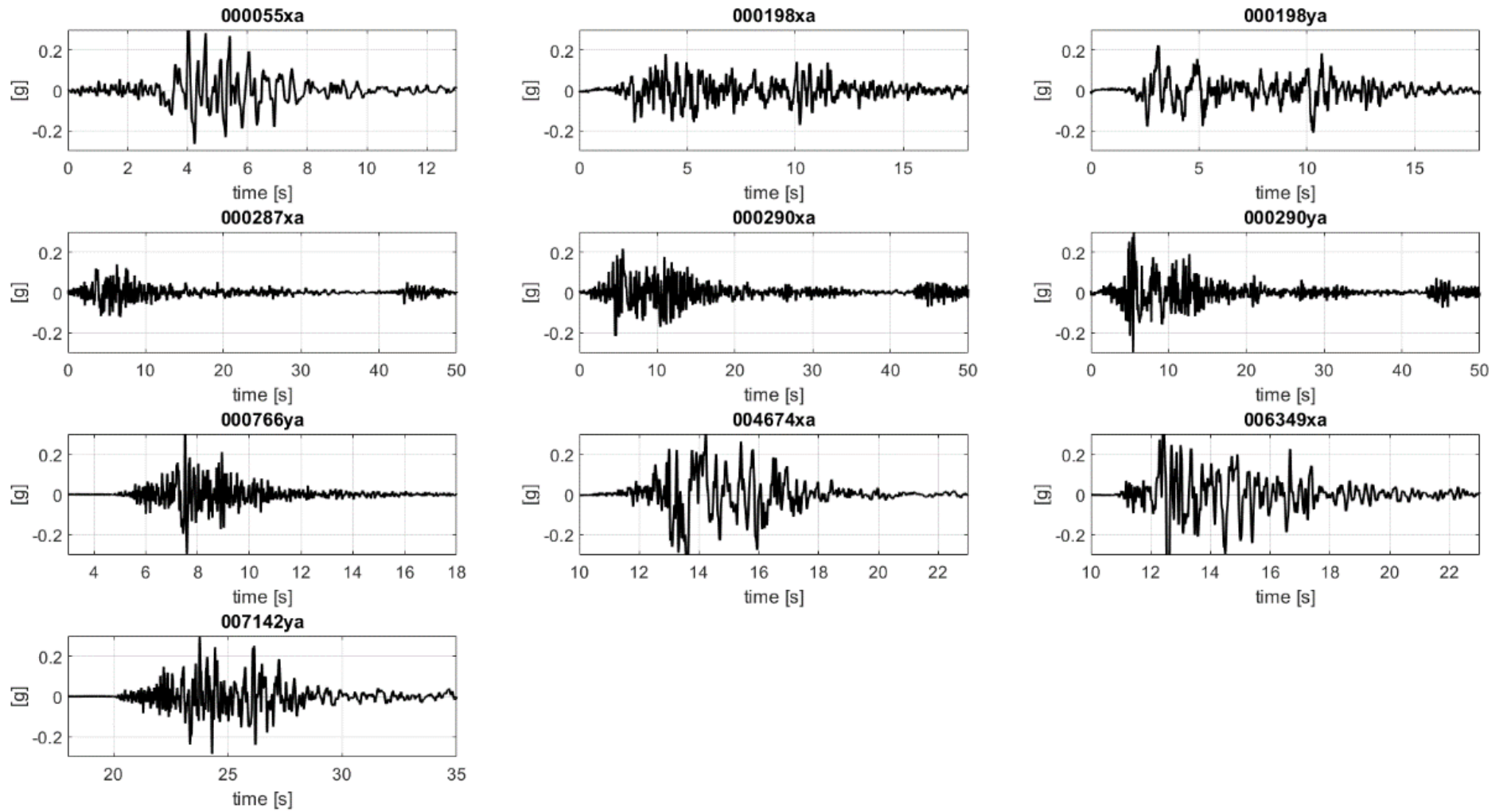


Figure 67. Accelerograms of the earthquakes selected for the SLV state, related to the Marana Capacciotti dam compatible with the target spectra provided by NTC2018.

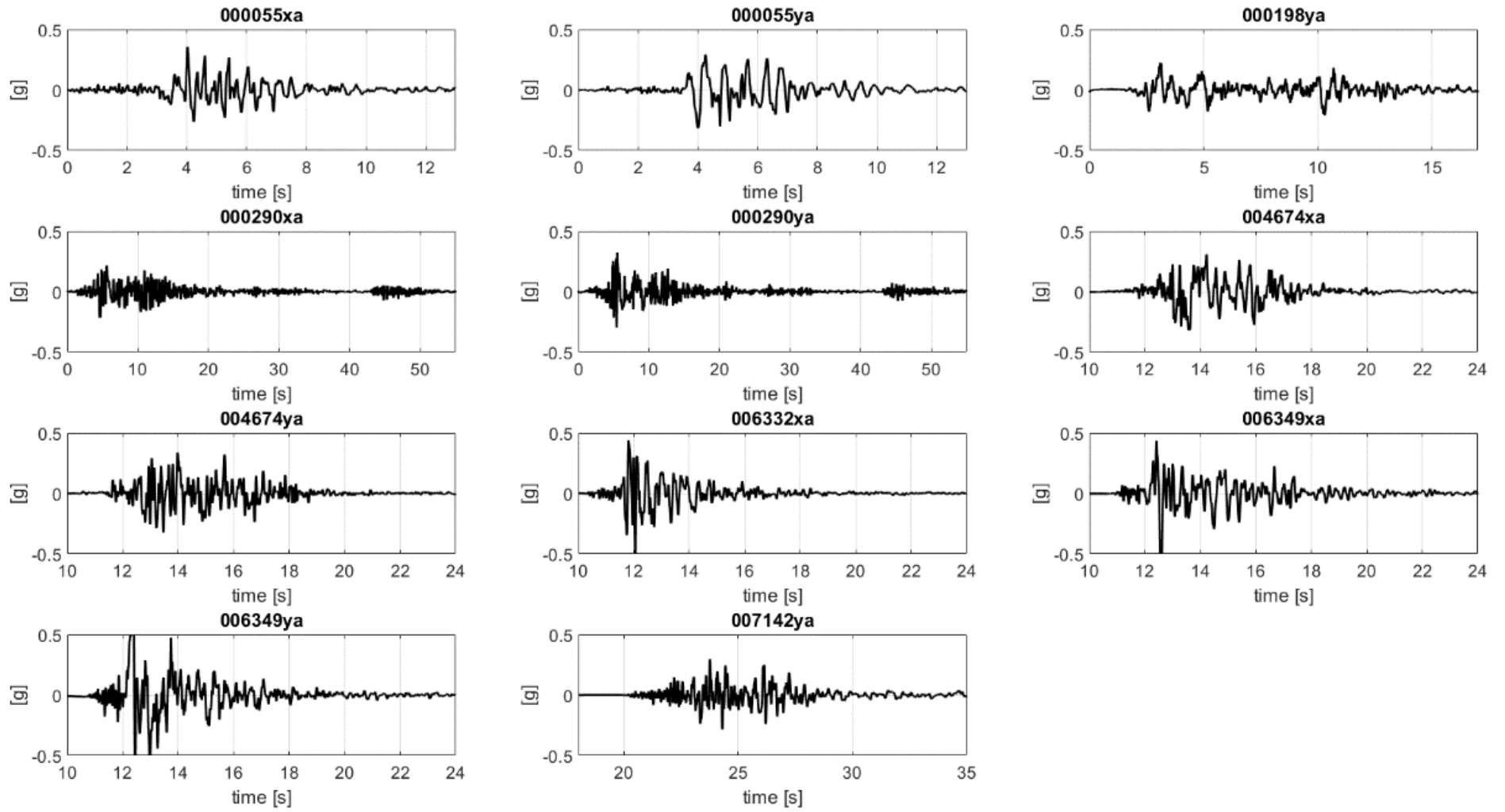


Figure 68. Accelerograms of the earthquakes selected for the SLC state, related to the Marana Capacciotti dam compatible with the target spectra provided by NTC2018.

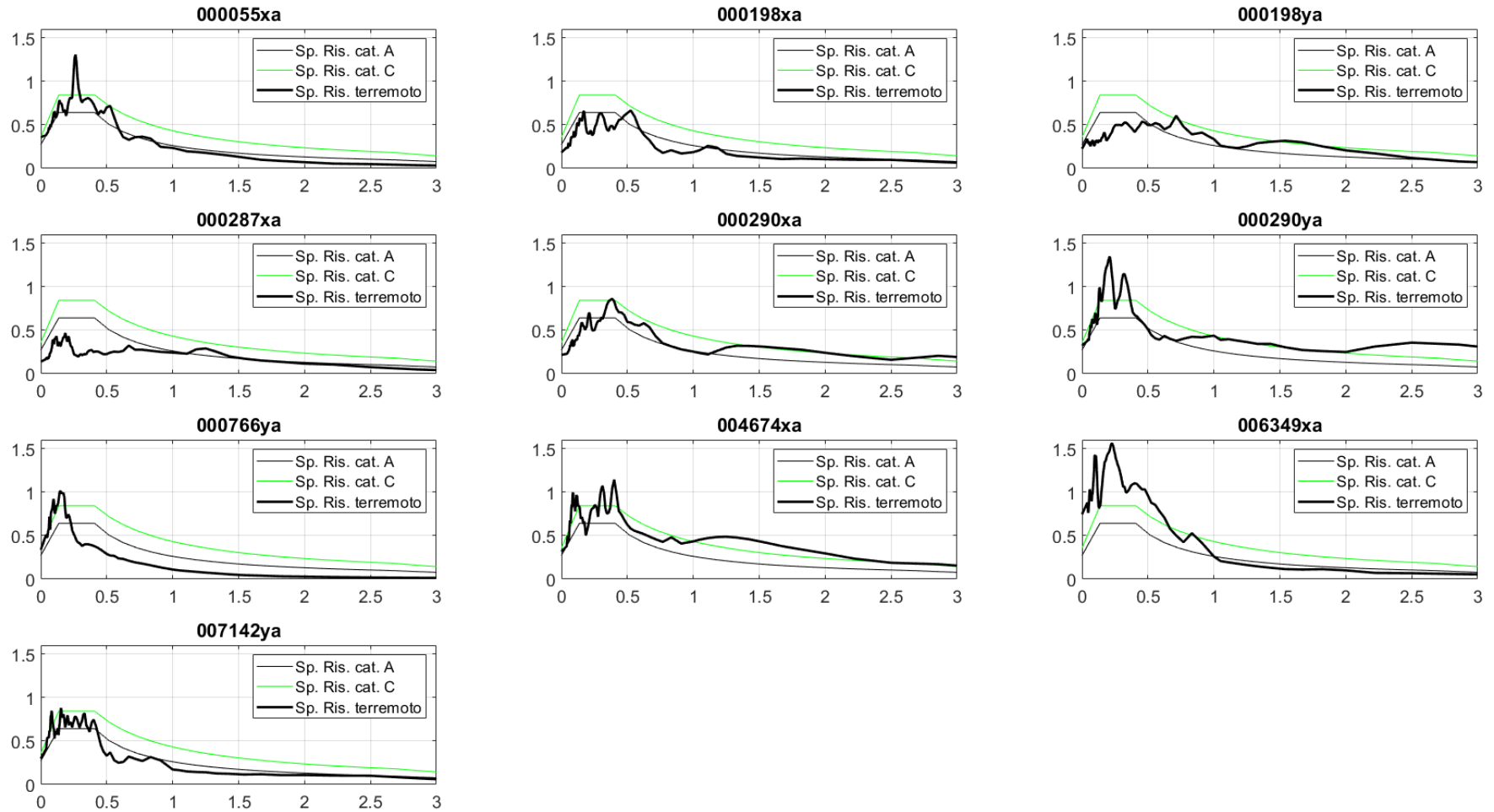


Figure 69. Response spectra of the selected earthquakes (bold black) and simplified regulatory spectra for site category A (thin black) and C (green) for the SLV state, related to the Marana Capacciotti dam.

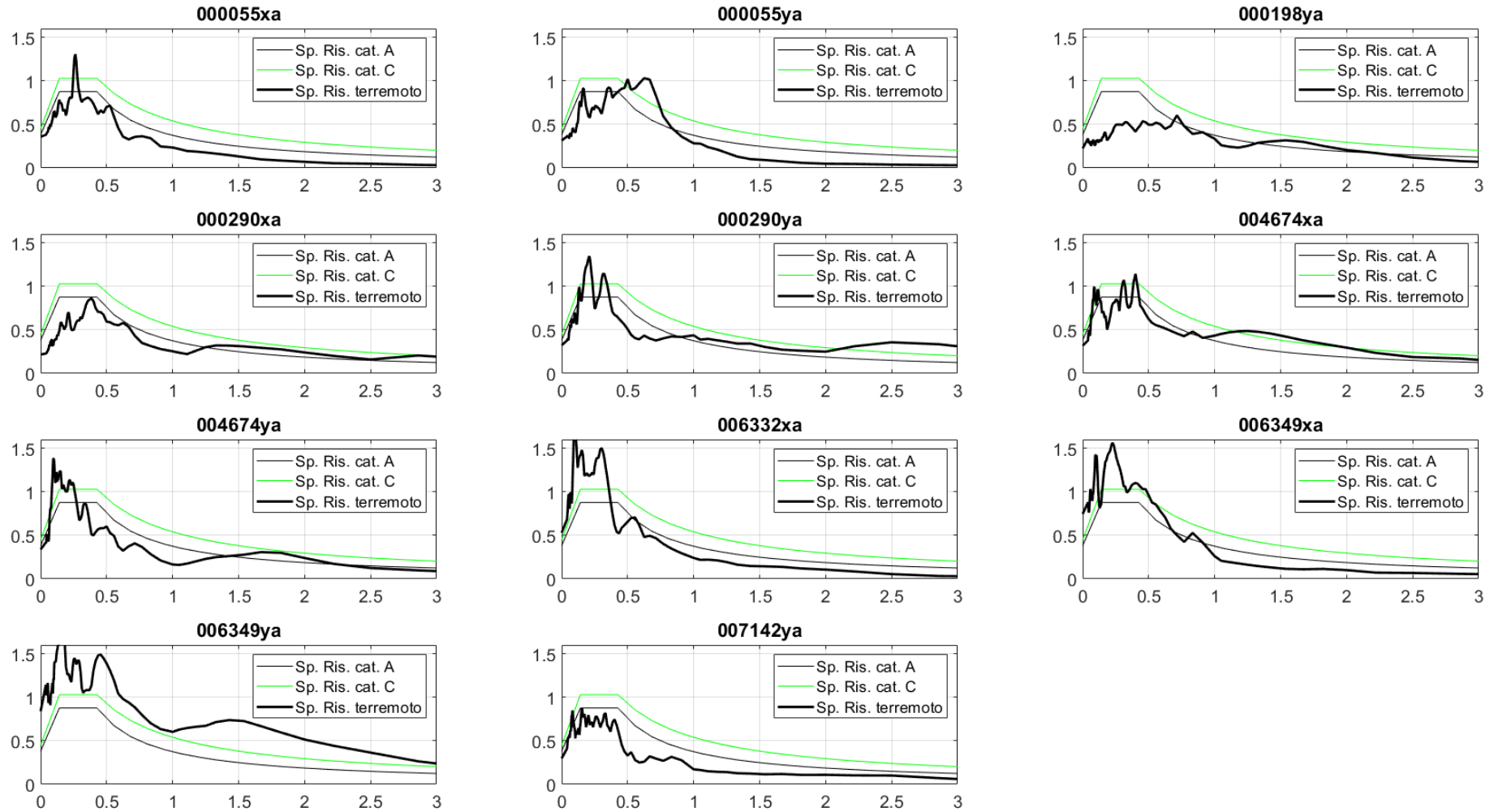


Figure 70. Response spectra of the selected earthquakes (bold black) and simplified regulatory spectra for site category A (thin black) and C (green) for SLC state, related to the Marana Capacciotti dam.

6. DELIVERABLES AND CONCLUSIONS

Following the O.P.C.M. 3274/2003, D.L. 79/2004 and with the entry into force of the NTC2008 and the NTC2018, site-specific seismotectonic studies are declared necessary as an integral part of the seismic verifications of large dams. During this PhD program, we carried out a seismotectonic study in the region of two large earth dams in Southern Italy. The seismic motion at bedrock and the dynamic characterization of the two dams, obtained from this study, were presented at the Sapienza University of Rome, which used these results as a starting point for its work, in order to complete the seismic verifications requested by the Ministry of Infrastructure and Transport. More specifically, the definition of the seismic motion at bedrock was the direct input for the geotechnical modelling carried out by the Sapienza University. These are, in fact, the deliverables necessary for defining the effects of the rapid emptying operations and the calculation of land subsidence. The seismic motion at surface is governed by local geology, which is why we conducted field surveys at the two sites in July and October 2019. Geophysical and dynamic characterization of dams and soil are, in fact, another necessary input for seismic verifications, since they provide fundamental information for the dynamic monitoring of the facilities.

While carrying out the seismic hazard reassessment through a probabilistic approach in our study area, some critical issues emerged. Among these, the intrinsic uncertainties related to the magnitude of historical events, the association of earthquakes with the respective seismogenic sources, the use of PGA and the attenuation laws that could be derived from untrustworthy data. In light of this, we decided to focus on the investigation of the site categories in which the seismic stations are housed and on the effects of soil-structure interaction. However, the standard PSHA approach itself is much debated at the present day: in fact, further methodologies are being tested and integrated, such as fault-based and time dependent models. For this reason, we tested the SHERIFS approach on our study area and we obtained four different fault-based seismicity rates, based on four different fault and multi-fault rupture scenarios. These results are thought to be used in future studies as a criterion for weighing the different input data for a fault-based PSHA model and, subsequently, to become an integration to the standard-approach models.

REFERENCES

- Abrahamson, N. A. (2006). Seismic hazard assessment: problems with current practice and future developments. In First European conference on earthquake engineering and seismology (pp. 3-8).
- Aguilar-Meléndez, A., Ordaz, M. G., Puente, J. D. L., Pujades, L., Barbat, A., Rodríguez-Lozoya, H. E., Monterrubio-Velasco, M., Escalante Martínez, J. E., Campos-Rios, A. (2018). Sensitivity analysis of seismic parameters in the Probabilistic Seismic Hazard Assessment (PSHA) for Barcelona applying the new R-CRISIS. *Computación y Sistemas*, 22(4), 1099-1122.
- Aki, K. (1965). Maximum likelihood estimate of b in the formula $\log N = a - bM$ and its confidence limits. *Bull. Earthq. Res. Inst., Tokyo Univ.*, 43, 237-239.
- Alessandrini G., Lattanzi G., Slivicki S., Sgattoni G., Castellaro S. (2019). Indagini svolte nell'ambito del Contratto di Consulenza per lo "Studio sismotettonico delle dighe Marana Capacciotti e San Pietro sul Torrente Osento e delle opere accessorie" – Consorzio di Bonifica per la Capitanata. ITACA (Italian ACcelerometric Archive. http://itaca.mi.ingv.it/ItacaNet_31/#/home).
- Ambraseys, N. N., Simpson, K. U., & Bommer, J. J. (1996). Prediction of horizontal response spectra in Europe. *Earthquake Engineering & Structural Dynamics*, 25(4), 371-400.
- Baker, J. W. (2013). An introduction to probabilistic seismic hazard analysis. White paper version, 2(1), 79.
- Barani, S., Spallarossa, D., Bazzurro, P., & Pelli, F. (2014). The multiple facets of probabilistic seismic hazard analysis: a review of probabilistic approaches to the assessment of the different hazards caused by earthquakes. *Bollettino di Geofisica Teorica ed Applicata*, 55(1).
- Basili, R., D'Amico, V., Meletti, C., & Valensise, G. (2007). Linee-guida per la redazione e le istruttorie degli studi sismotettonici relativi alle grandi dighe. Contenute nell'accordo ai sensi dell'art. 15 della L. 241/90 e s.m.i. tra la Direzione Generale per le Dighe e le Infrastrutture Idriche ed Elettriche e l'Istituto Nazionale di Geofisica e Vulcanologia.
- Basili, R., Valensise, G., Vannoli, P., Burrato, P., Fracassi, U., Mariano, S., Tiberti, M. M., & Boschi, E. (2008). The Database of Individual Seismogenic Sources (DISS), version 3: summarizing 20 years of research on Italy's earthquake geology. *Tectonophysics*, 453(1-4), 20-43.
- Bindi, D., Pacor, F., Luzi, L., Puglia, R., Massa, M., Ameri, G., & Paolucci, R. (2011). Ground motion prediction equations derived from the Italian strong motion database. *Bulletin of Earthquake Engineering*, 9(6), 1899-1920.

- Bommer, J. J., Scherbaum, F., Bungum, H., Cotton, F., Sabetta, F., & Abrahamson, N. A. (2005). On the use of logic trees for ground-motion prediction equations in seismic-hazard analysis. *Bulletin of the Seismological Society of America*, 95(2), 377-389.
- Boncio, P., Lavecchia, G., & Pace, B. (2004). Defining a model of 3D seismogenic sources for Seismic Hazard Assessment applications: the case of central Apennines (Italy). *Journal of Seismology*, 8(3), 407-425.
- Bormann, P., Baumbach, M., Bock, G., Grosser, H., Choy, G. L., & Boatwright, J. (2002). Seismic sources and source parameters, *New manual of seismological observatory practice*, P. Bormann (ed.), GeoForschungsZentrum Potsdam.
- Brune, J. N. (1970). Tectonic stress and the spectra of seismic shear waves from earthquakes. *Journal of Geophysical Research*, 75(26), 4997–5009. <https://doi.org/10.1029/JB075i026p04997>.
- BSSC - Building Seismic Safety Council. (2003). NEHRP Recommended provisions for seismic regulations for new buildings and other structures. Federal Emergency Management Agency (FEMA), Washington DC, USA, Report No. 450.
- Cao, A., & Gao, S. S. (2002). Temporal variation of seismic b-values beneath northeastern Japan island arc. *Geophysical research letters*, 29(9), 48-1.
- Castellaro, S., Mulargia, F., & Kagan, Y. Y. (2006). Regression problems for magnitudes. *Geophysical Journal International*, 165(3), 913-930.
- Castellaro, S., Alessandrini, G., Musinu, G. (2022). Seismic Station Installations and their Impact on the Recorded Signals and Derived Quantities. Manuscript submitted to SRL.
- Cauzzi, C., Faccioli, E., Vanini, M., & Bianchini, A. (2015). Updated predictive equations for broadband (0.01–10 s) horizontal response spectra and peak ground motions, based on a global dataset of digital acceleration records. *Bulletin of Earthquake Engineering*, 13(6), 1587-1612.
- CEN. (2003). Eurocode 8: Design Of Structures For Earthquake Resistance –Part 1: General Rules, Seismic Actions And Rules For Buildings. 13.
- Chartier, T., Scotti, O., & Lyon-Caen, H. (2019). SHERIFS: Open-source code for computing earthquake rates in fault systems and constructing hazard models. *Seismological Research Letters*, 90(4), 1678-1688.
- Chartier, T., Scotti, O., Lyon-Caen, H., Richard-Dinger, K., Dieterich, J. H., & Shaw, B. E. (2021). Modelling earthquake rates and associated uncertainties in the Marmara Region, Turkey. *Natural Hazards and Earth System Sciences Discussions*, 1-28.
- Ciaranfi, N., Dazzaro, L., Pieri, P., Rapisardi, L., Sardella, A. (1973). *Geologia della zona compresa fra Bisaccia (Avellino) ed il T. Olivento, presso Lavello (Potenza)*.

- Cornell, C. A. (1968). Engineering seismic risk analysis. *Bulletin of the seismological society of America*, 58(5), 1583-1606.
- Cornell, C. A., & Winterstein, S. R. (1988). Temporal and magnitude dependence in earthquake recurrence models. *Bulletin of the Seismological Society of America*, 78(4), 1522-1537.
- Cotecchia, V. (1959). Studio di geologia in Irpinia per la costruzione di un lago artificiale sul torrente Osento.
- D'Addezio, G., Pantosti, D., & Valensise, G. (1990). Caratterizzazione su basi paleosismologiche degli "antenati" del terremoto del 1980. *Proc. 9° Meeting G.N.G.T.S., Rome 1990*, 27-35.
- D'Addezio, G., Pantosti, D., & Valensise, G. (1991). Paleoearthquakes along the Irpinia fault at Pantano di S. Gregorio Magno (southern Italy). *Il Quaternario*, 4, 1, 121-136.
- D'Amico M, Felicetta C, Russo E, Sgobba S, Lanzano G, Pacor F, Luzi L (2020). Italian Accelerometric Archive v 3.1 - Istituto Nazionale di Geofisica e Vulcanologia, Dipartimento della Protezione Civile Nazionale. doi: 10.13127/itaca.3.1.
- Di Luccio, F., Fukuyama, E., & Pino, N. A. (2005). The 2002 Molise earthquake sequence: What can we learn about the tectonics of southern Italy?. *Tectonophysics*, 405(1-4), 141-154.
- Di Luccio, F., Piscini, A., Pino, N. A., & Ventura, G. (2005). Reactivation of deep faults beneath Southern Apennines: evidence from the 1990–1991 Potenza seismic sequences. *Terra Nova*, 17(6), 586-590.
- DISS Working Group (2021). Database of Individual Seismogenic Sources (DISS), Version 3.3.0: A compilation of potential sources for earthquakes larger than M 5.5 in Italy and surrounding areas. Istituto Nazionale di Geofisica e Vulcanologia (INGV). <https://doi.org/10.13127/diss3.3.0>.
- Doglioni, C., Harabaglia, P., Martinelli, G., Mongelli, F., & Zito, G. (1996). A geodynamic model of the Southern Apennines accretionary prism. *Terra Nova*, 8(6), 540-547.
- Ekström, G., M. Nettles, and A. M. Dziewonski, The global CMT project 2004-2010: Centroid-moment tensors for 13,017 earthquakes, *Phys. Earth Planet. Inter.*, 200-201, 1-9, 2012. doi:10.1016/j.pepi.2012.04.002.
- El-Isa, Z. H., & Eaton, D. W. (2014). Spatiotemporal variations in the b-value of earthquake magnitude–frequency distributions: Classification and causes. *Tectonophysics*, 615, 1-11.
- Field, E. H., Arrowsmith, R. J., Biasi, G. P., Bird, P., Dawson, T. E., Felzer, K. R., Jackson, D. D., Johnson, K. M., Jordan, T. H., Madden, C., Michael, A. J., Milner, K. R., Page, M. T., Parsons, T., Powers, P. M., Shaw, B. E., Thatcher, W. R., Weldon, R. J., & Zeng, Y. (2014). Uniform California earthquake rupture forecast, version 3 (UCERF3) - The time-independent model. *Bulletin of the Seismological Society of America*, 104(3), 1122-1180.

- Field, E. H., Biasi, G. P., Bird, P., Dawson, T. E., Felzer, K. R., Jackson, D. D., Johnson, K. M., Jordan, T. H., Madden, C., Michael, A. J., Milner, K. R., Page, M. T., Parsons, T., Powers, P. M., Shaw, B. E., Thatcher, W. R., Weldon, R. J., & Zeng, Y. (2015). Long-term time-dependent probabilities for the third Uniform California Earthquake Rupture Forecast (UCERF3). *Bulletin of the Seismological Society of America*, 105(2A), 511-543.
- Forte, G., Chioccarelli, E., De Falco, M., Cito, P., Santo, A., & Iervolino, I. (2019). Seismic soil classification of Italy based on surface geology and shear-wave velocity measurements. *Soil Dynamics and Earthquake Engineering*, 122, 79-93.
- Foti, S., Hollender, F., Garofalo, F., Albarello, D., Asten, M., Bard, P.-Y., Comina, C., Cornou, C., Cox, B., Di Giulio, G., Forbriger, T., Hayashi, K., Lunedei, E., Martin, A., Mercerat, D., Ohrnberger, M., Poggi, V., Renalier, F., Sicilia, D., & Socco, V. (2018). Guidelines for the good practice of surface wave analysis: a product of the InterPACIFIC project. *Bulletin of Earthquake Engineering*, 16(6), 2367-2420.
- Fracassi, U., & Valensise, G. (2007). Unveiling the sources of the catastrophic 1456 multiple earthquake: Hints to an unexplored tectonic mechanism in Southern Italy. *Bull. Seismol. Soc. Am.*, 97, 3, 725-748, 10.1785/0120050250.
- García-Mayordomo, J., Gaspar-Escribano, J. M., & Benito, B. (2007). Seismic hazard assessment of the Province of Murcia (SE Spain): analysis of source contribution to hazard. *Journal of Seismology*, 11(4), 453-471.
- Gardner, J. K., & Knopoff, L. (1974). Is the sequence of earthquakes in Southern California, with aftershocks removed, Poissonian?. *Bulletin of the Seismological Society of America*, 64(5), 1363-1367.
- Gasperini P., Bernardini F., Valensise G. and Boschi E. (1999). Defining Seismogenic Sources from Historical Earthquake Felt Reports, *Bull. Seism. Soc. Am.*, 89, 94-110.
- Gasperini, P., Lolli, B., & Castellaro, S. (2015). Comparative analysis of regression methods used for seismic magnitude conversions. *Bulletin of the Seismological Society of America*, 105(3), 1787-1791.
- Gerstenberger, M. C., Marzocchi, W., Allen, T., Pagani, M., Adams, J., Danciu, L., Field, E. H., Fujiwara, H., Luco, N., Ma, K. -F., Meletti, C., & Petersen, M. D. (2020). Probabilistic seismic hazard analysis at regional and national scales: State of the art and future challenges. *Reviews of Geophysics*, 58(2), e2019RG000653.
- Gómez-Novell, O., Chartier, T., García-Mayordomo, J., Ortuño, M., Masana, E., Insua-Arévalo, J. M., & Scotti, O. (2020a). Modelling earthquake rupture rates in fault systems for seismic hazard assessment: The Eastern Betics Shear Zone. *Engineering Geology*, 265, 105452.

- Gómez Novell, O., García-Mayordomo, J., Ortuño Candela, M., Masana, E., & Chartier, T. (2020b). Fault system-based probabilistic seismic hazard assessment of a moderate seismicity region: the Eastern Betics Shear Zone (SE Spain). *Frontiers In Earth Science*, 2020, vol. 8, num. 579398, p. 1-25.
- Gruppo di Lavoro, M.P.S. (2004). Redazione della mappa di pericolosità sismica prevista dall'Ordinanza PCM 3274 del 20 marzo 2003. Rapporto Conclusivo per il Dipartimento della Protezione Civile, INGV, Milano-Roma, 5.
- Grünthal, G. (1998). European macroseismic scale 1998. European Seismological Commission (ESC).
- Guidoboni, E. & Ferrari, G. (2004). Integrazione di ricerca di archeologia e storia territoriale riguardante il terremoto del 1456 e l'area molisano-campana relativamente ai terremoti prima del Mille. RPT 255/03, SGA – Storia Geofisica Ambiente, Bologna, 139 pp.
- Guidoboni E., Ferrari G., Mariotti D., Comastri A., Tarabusi G., Sgattoni G. & Valensise G. (2018) - CFTI5Med, Catalogo dei Forti Terremoti in Italia (461 a.C.-1997) e nell'area Mediterranea (760 a.C.-1500). Istituto Nazionale di Geofisica e Vulcanologia (INGV). doi: <https://doi.org/10.6092/ingv.it-cfti5>.
- Guidoboni, E., Ferrari, G., Tarabusi, G., Sgattoni, G., Comastri, A., Mariotti, D., Ciuccarelli, C., Bianchi, M. G., & Valensise, G. (2019). CFTI5Med, the new release of the catalogue of strong earthquakes in Italy and in the Mediterranean area. *Scientific Data*, 6(1), 80. <https://doi.org/10.1038/s41597-019-0091-9>.
- Gutenberg, B., & Richter, C. F. (1944). Frequency of earthquakes in California. *Bulletin of the Seismological Society of America*, 34(4), 185-188.
- Housner, G. W. (1952). Spectrum intensities of strong-motion earthquakes.
- ISPRA, Carta Geologica d'Italia alla scala 1:100 000, Foglio 175 "Cerignola" http://193.206.192.231/carta_geologica_italia/default.htm.
- ISPRA, Carta Geologica d'Italia alla scala 1:50 000, Foglio 422 "Cerignola" <http://www.isprambiente.gov.it/Media/carg/index.html>.
- ISPRA, Carta Geologica d'Italia alla scala 1:50 000, Foglio 451 "Melfi" <http://www.isprambiente.gov.it/Media/carg/index.html>.
- ITHACA Working Group (2019). ITHACA (ITaly HAZard from CAPable faulting), A database of active capable faults of the Italian territory. Version December 2019. ISPRA Geological Survey of Italy. Web Portal <http://sgi2.isprambiente.it/ithacaweb/Mappatura.aspx>.
- Kanamori, H., & Anderson, D. L. (1975). Theoretical basis of some empirical relations in seismology. *Bulletin of the seismological society of America*, 65(5), 1073-1095.

- Kiremidjian, A. S., & Anagnos, T. (1984). Stochastic slip-predictable model for earthquake occurrences. *Bulletin of the Seismological Society of America*, 74(2), 739-755.
- Kramer, S. L. (1996). *Geotechnical earthquake engineering*. Pearson Education India.
- Lanzano, G., Luzi, L., D'Amico, V., Pacor, F., Meletti, C., Marzocchi, W., Rotondi, R., & Varini, E. (2020). Ground motion models for the new seismic hazard model of Italy (MPS19): selection for active shallow crustal regions and subduction zones. *Bulletin of Earthquake Engineering*, 18(8), 3487-3516.
- Lemoine, A., Douglas, J., & Cotton, F. (2012). Testing the applicability of correlations between topographic slope and VS 30 for Europe. *Bulletin of the Seismological Society of America*, 102(6), 2585-2599.
- Locati, M., Camassi, R., Rovida, A., Ercolani, E., Bernardini, F., Castelli, V., Caracciolo, C. H., Tertulliani, A., Rossi, A., Azzaro, R., D'Amico, S., & Antonucci, A. (2021). Database Macrosismico Italiano (DBMI15), versione 3.0. Istituto Nazionale di Geofisica e Vulcanologia (INGV).
- Louie, J. N. (2001). Faster, better: shear-wave velocity to 100 meters depth from refraction microtremor arrays. *Bulletin of the Seismological Society of America*, 91(2), 347-364.
- Martino, S., Caprari, P., Fiorucci, M., & Marmoni, G. M. (2021). Il Catalogo CEDIT: dall'inventario degli effetti sismoidotti all'analisi di scenario. <https://gdb.ceri.uniroma1.it/index.php/view/map/?repository=cedit&project=Cedit>.
- McGuire, R. K. (2004). *Seismic hazard and risk analysis*. Earthquake Engineering Research Institute.
- McGuire, R. K. (2007). Probabilistic seismic hazard analysis: Early history. *Earthquake Engineering & Structural Dynamics*, 37(3), 329-338.
- McGuire, R. K., & Arabasz, W. J. (1990). An introduction to probabilistic seismic hazard analysis. In *Geotechnical an Environmental Geophysics: Volume I: Review and Tutorial* (pp. 333-354). Society of Exploration Geophysicists.
- Meletti, C., Patacca, E., Scandone, P., & Figliuolo, B. (1989). Il Terremoto del 1456 e la sua interpretazione nel quadro sismotettonico dell'Appennino Meridionale. in: B. Figliuolo (ed), *Il Terremoto del 1456, Osservatorio Vesuviano, Storia e Scienze della Terra*, 71-108 (I), 35-163 (II).
- Meletti, C., Galadini, F., Valensise, G., Stucchi, M., Basili, R., Barba, S., Vannucci, G. & Boschi, E. (2008). A seismic source zone model for the seismic hazard assessment of the Italian territory. *Tectonophysics*, 450(1-4), 85-108.
- Meletti, C., Marzocchi, W., D'Amico, V., Lanzano, G., Luzi, L., Martinelli, F., Pace, B., Rovida, A., Taroni, M., Visini, F., & Group, M. W. (2021). The new Italian seismic hazard model (MPS19). *Annals of Geophysics*.

- Molnar, S., Cassidy, J. F., Castellaro, S., Cornou, C., Crow, H., Hunter, J. A., Matsushima, S., Sánchez-Sesma, F. J., & Yong, A. (2018). Application of microtremor horizontal-to-vertical spectral ratio (MHVSR) analysis for site characterization: State of the art. *Surveys in Geophysics*, 39(4), 613-631.
- Mulargia, F., Stark, P. B., & Geller, R. J. (2017). Why is probabilistic seismic hazard analysis (PSHA) still used?. *Physics of the Earth and Planetary Interiors*, 264, 63-75.
- Nakamura, Y. (1989). A method for dynamic characteristics estimation of subsurface using microtremor on the ground surface. *Railway Technical Research Institute, Quarterly Reports*, 30(1).
- Norme Tecniche sulle Costruzioni, (2008). Decreto Ministeriale 14/01/2008, Ministry of Infrastructures and Transportations, G.U. S.O. n.29 on 4/2/2008.
- Norme Tecniche sulle Costruzioni (2018). Decreto Ministeriale 17/01/2018, Ministry of Infrastructures and Transportations, G.U. S.O. n.8 on 20/2/2018. Aggiornamento delle Norme tecniche per le costruzioni (No. 8). decreto 17-1-2018, *Gazzetta Ufficiale* 42, 20-02-2018, Ordinary Suppl.
- O.P.C.M. 3274/2003, D.L. 79/2004.
- Ordaz, M., Martinelli, F., Aguilar, A., Arboleda, J., Meletti, C., & D'Amico, V. (2017). R-CRISIS. Program and platform for computing seismic hazard.
- Ordaz, M. & Salgado-Gálvez, M.A. (2019). R-CRISIS Validation and Verification Document. ERN Technical Report. Mexico City, Mexico.
- Ortolani, F. (1974). Faglia trascorrente Pliocenica nell'Appennino campano. – TAV. I. *Bollettino della Società Geologica Italiana*, 1974, Volume 93, Fascicolo 3. pp. 609 – 622.
- Pace, B., Peruzza, L., Lavecchia, G., & Boncio, P. (2006). Layered seismogenic source model and probabilistic seismic-hazard analyses in central Italy. *Bulletin of the Seismological Society of America*, 96(1), 107-132.
- Pace, B., Visini, F., Scotti, O., & Peruzza, L. (2018). Preface: Linking faults to seismic hazard assessment in Europe. *Natural Hazards and Earth System Sciences*, 18(5), 1349-1350.
- Palano, M., Cannavò, F., Ferranti, L., Mattia, M., & Mazzella, M. E. (2011). Strain and stress fields in the Southern Apennines (Italy) constrained by geodetic, seismological and borehole data. *Geophysical Journal International*, 187(3), 1270-1282.
- Pantosti, D., Schwartz, D., P., & Valensise, G. (1993a). Paleoseismology along the 1980 surface rupture of the Irpinia fault: implications for earthquake recurrence in the southern Apennines, Italy. *J. Geophys. Res.*, 98, B4, 6561-6577.

- Pantosti, D., D'Addezio, G. & Cinti, F., R. (1993b). Paleoseismological evidence of repeated large earthquakes along the 1980 Irpinia earthquake fault. *Ann. Geofis.*, 36, 321-330.
- Patacca, E., & Scandone, P. (2001). Identificazione e valutazione di strutture sismogenetiche. Rapporto Tecnico. Convenzione ENEA—Dipartimento di Scienze della Terra Università di Pisa, Italy.
- Park, C. B., Miller, R. D., & Xia, J. (1999). Imaging dispersion curves of surface waves on multi-channel record. In *SEG Technical Program Expanded Abstracts 1998* (pp. 1377-1380). Society of Exploration Geophysicists.
- Pearson, K. (1900). X. On the criterion that a given system of deviations from the probable in the case of a correlated system of variables is such that it can be reasonably supposed to have arisen from random sampling. *The London, Edinburgh, and Dublin Philosophical Magazine and Journal of Science*, 50(302), 157-175.
- Peruzza, L., Pace, B., & Visini, F. (2011). Fault-based earthquake rupture forecast in Central Italy: Remarks after the L'Aquila M_w 6.3 event. *Bulletin of the Seismological Society of America*, 101(1), 404-412.
- Peruzza, R., Gee, B., Pace, G., Roberts, O., Scotti, F., Visini, L., Benedetti, & M. Pagani. (2016). PSHA after a strong earthquake: hints for the recovery. *Annals of Geophysics*.
- Petersen, M. D., Cao, T., Campbell, K. W., & Frankel, A. D. (2007). Time-independent and time-dependent seismic hazard assessment for the State of California: Uniform California Earthquake Rupture Forecast Model 1.0. *Seismological Research Letters*, 78(1), 99-109.
- Pino, N. A., Palombo, B., Ventura, G., Perniola, B., & Ferrari, G. (2008). Waveform modeling of historical seismograms of the 1930 Irpinia earthquake provides insight on “blind” faulting in southern Apennines (Italy). *Journal of Geophysical Research: Solid Earth*, 113(B5).
- Power, M. S., Coppersmith, K. J., Youngs, R. R., Schwartz, D. P., & Swan, R. H. (1981). Seismic Exposure Analysis for the WNP-2 and WNP-1/4 Site: Appendix 2.5 K to Amendment no. 18 Final Safety Analysis Report for WNP-2. Woodward-Clyde Consultants, San Francisco, USA.
- Reid, H. F. (1911). The elastic-rebound theory of earthquakes. *Univ. Calif. Publ. Bull. Dept. Geol. Sci.* 6, 413-444.
- Reiter, L. (1991). *Earthquake hazard analysis: issues and insights*. Columbia University Press.
- Richter, C. F. (1935). An instrumental earthquake magnitude scale. *Bulletin of the seismological society of America*, 25(1), 1-32.
- Rovida, A., Locati, M., Camassi, R., Lolli, B., & Gasperini, P. (2020). The Italian earthquake catalogue CPTI15. *Bulletin of Earthquake Engineering*, 1-32.

- Rovida A., Locati M., Camassi R., Lolli B., Gasperini P., Antonucci A. (2021). Catalogo Parametrico dei Terremoti Italiani (CPTI15), versione 3.0. Istituto Nazionale di Geofisica e Vulcanologia (INGV). <https://doi.org/10.13127/CPTI/CPTI15.3>.
- Sabetta, F., & Pugliese, A. (1996). Estimation of response spectra and simulation of nonstationary earthquake ground motions. *Bulletin of the Seismological Society of America*, 86(2), 337-352.
- Sadigh, K., Chang, C. Y., Egan, J. A., Makdisi, F., & Youngs, R. R. (1997). Attenuation relationships for shallow crustal earthquakes based on California strong motion data. *Seismological research letters*, 68(1), 180-189.
- Scandone, P. (2004). Definizione spaziale delle principali strutture sismogenetiche della penisola italiana. Progetto S2 - Schede di rendicontazione scientifica delle singole Unità di Ricerca. UR 2.15, 265-277.
- Scholz, C. H., Aviles, C. A., & Wesnousky, S. G. (1986). Scaling differences between large interplate and intraplate earthquakes. *Bulletin of the Seismological Society of America*, 76(1), 65-70.
- Schwartz, D. P., & Coppersmith, K. J. (1984). Fault behavior and characteristic earthquakes: Examples from the Wasatch and San Andreas fault zones. *Journal of Geophysical Research: Solid Earth*, 89(B7), 5681-5698.
- Scotti, O., Clément, C., & Baumont, D. (2014). Seismic hazard for design and verification of nuclear installations in France: Regulatory context, debated issues and ongoing developments. *Geofis. Teor. Appl*, 55(1), 135-148.
- Serpelloni, E., Bürgmann, R., Anzidei, M., Baldi, P., Ventura, B. M., & Boschi, E. (2010). Strain accumulation across the Messina Straits and kinematics of Sicily and Calabria from GPS data and dislocation modeling. *Earth and Planetary Science Letters*, 298(3-4), 347-360.
- SESAME. (2004). Guidelines for the implementation of the H/V spectral ratio technique on ambient vibrations measurements, processing and interpretation (No. European Commission–EVG1-CT-2000-00026 SESAME). European Commission.
- Shimazaki, K., & Nakata, T. (1980). Time-predictable recurrence model for large earthquakes. *Geophysical Research Letters*, 7(4), 279-282.
- Sieberg, A. (1930). Scala MCS (Mercalli-Cancani-Sieberg). *Geologie der Erdbeben, Handbuch der Geophysik*, 2(4), 552-555.
- SolGeo (2003). Diga di S. Pietro (AV). Indagini geofisiche con metodi sonici. Misure CROSS-HOLE. Rel. G0124_03.
- Stirling, M., McVerry, G., Gerstenberger, M., Litchfield, N., Van Dissen, R., Berryman, K., Barnes, P., Wallace, L., Villamor, P., Langridge, R., Lamarche, G., Nodder, S., Reyners, M., Bradley, B., Rhoades, D., Smith, W., Nicol, A., Pettinga, J., Clark, K., & Jacobs, K. (2012). National seismic

- hazard model for New Zealand: 2010 update. *Bulletin of the Seismological Society of America*, 102(4), 1514-1542.
- Tarabusi G., Ferrari G., Ciuccarelli C., Bianchi M.G., Sgattoni G., Comastri A., Mariotti D., Valensise G., Guidoboni E. (2020) - CFTILab, Laboratorio Avanzato di Sismologia Storica. Istituto Nazionale di Geofisica e Vulcanologia (INGV). <https://doi.org/10.13127/CFTI/CFTILAB>
- Valensise, G., Ferrari, G., Tarabusi, G., & Sgattoni, G. (2018). Il nuovo CFTI5Med: navigando tra continuità e innovazione. <https://ingvterremoti.com/2018/11/15/il-nuovo-cfti5med-navigando-tra-continuita-e-innovazione/>.
- Valentini, A., Visini, F., & Pace, B. (2017). Integrating faults and past earthquakes into a probabilistic seismic hazard model for peninsular Italy. *Natural Hazards and Earth System Sciences*, 17(11).
- Valentini, A. (2020). Allowing multi-fault earthquakes and relaxing fault segmentation in central Apennines (Italy): hints for fault-based PSHA.
- Valentini, A., Pace, B., Boncio, P., Visini, F., Pagliaroli, A., & Pergalani, F. (2018). Analisi probabilistica fault-based della pericolosità sismica volta alla definizione di input sismici: osservazioni dopo la sequenza sismica del 2016 in Italia Centrale. In 37° Convegno Nazionale di Geofisica della Terra solida (pp. 26-30).
- Valentini, A., Pace, B., Boncio, P., Visini, F., Pagliaroli, A., & Pergalani, F. (2019). Definition of seismic input from fault-based PSHA: Remarks after the 2016 central Italy earthquake sequence. *Tectonics*, 38(2), 595-620.
- Vannoli, P., & Burrato, P. (2018). I caratteri della sismotettonica in Italia: osservazioni e modelli. *Geologia dell'Ambiente*.
- Vannoli, P., Bernardi, F., Palombo, B., Vannucci, G., Console, R., & Ferrari, G. (2016). New constraints shed light on strike-slip faulting beneath the southern Apennines (Italy): The 21 August 1962 Irpinia multiple earthquake. *Tectonophysics*, 691, 375-384.
- Vezzani, L., Festa, A., & Ghisetti, F. C. (2010). Geology and tectonic evolution of the Central-Southern Apennines, Italy (Vol. 469). Geological Society of America.
- Visini, F., Pace, B., Meletti, C., Marzocchi, W., Akinci, A., Azzaro, R., Barani, S., Barberi, G., Barreca, G., Basili, R., Bird, P., Bonini, M., Burrato, P., Buseti, M., Carafa, M., Cocina, O., Console, R., Corti, G., D'Agostino, N., ... Zuccolo, E. (2021). Earthquake Rupture Forecasts for the MPS19 Seismic Hazard Model of Italy. *Annals of Geophysics*, 64(2), SE220-SE220.
- Visini, F., Valentini, A., Chartier, T., Scotti, O., & Pace, B. (2020). Computational tools for relaxing the fault segmentation in probabilistic seismic hazard modelling in complex fault systems. *Pure and Applied Geophysics*, 177(5), 1855-1877.

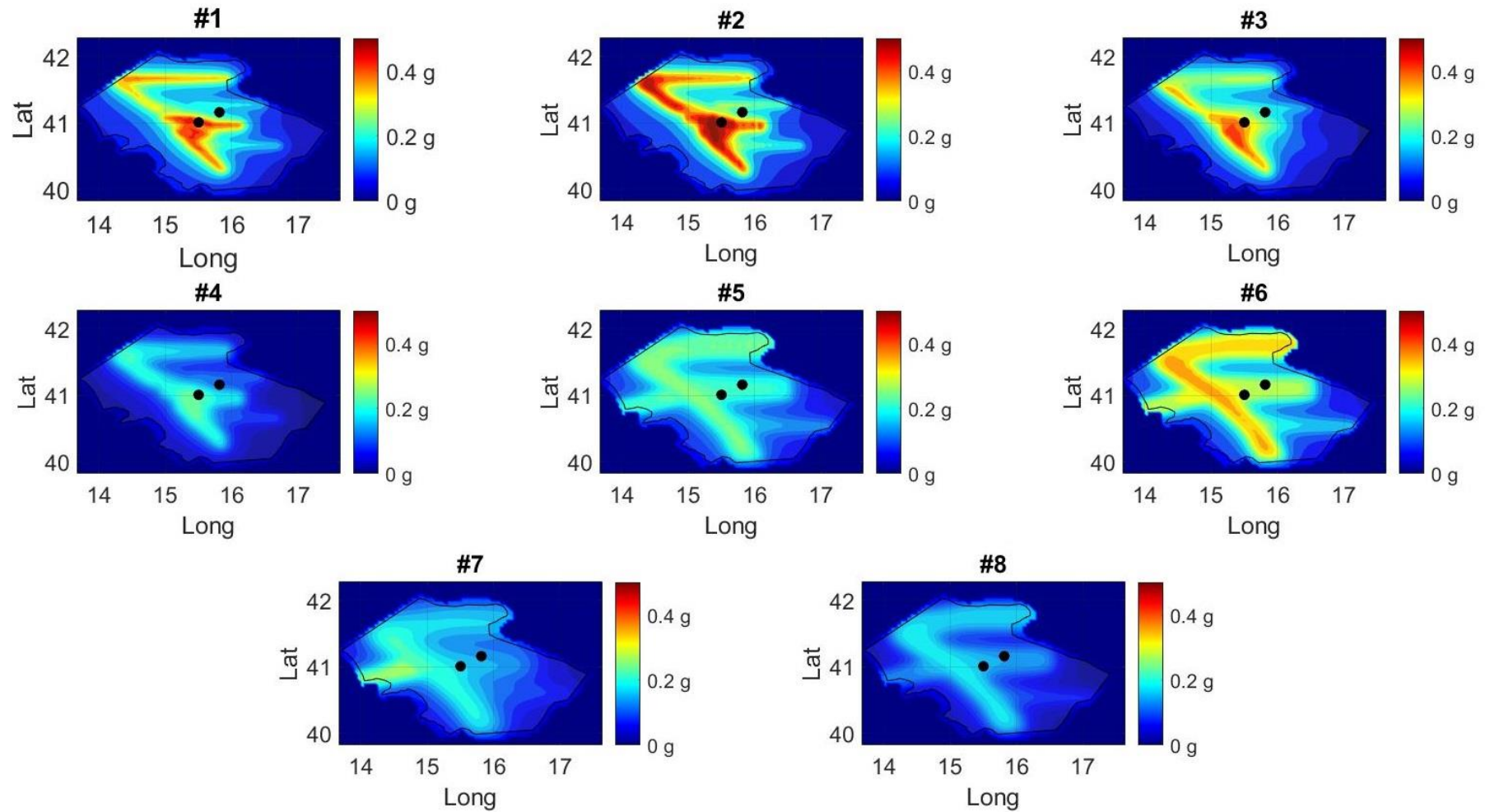
- Vitale, S., & Ciarcia, S. (2018). Tectono-stratigraphic setting of the Campania region (southern Italy). *Journal of Maps*, 14(2), 9-21.
- Wald, D. J., & Allen, T. I. (2007). Topographic slope as a proxy for seismic site conditions and amplification. *Bulletin of the Seismological Society of America*, 97(5), 1379-1395.
- Wells, D. L., & Coppersmith, K. J. (1994). New empirical relationships among magnitude, rupture length, rupture width, rupture area, and surface displacement. *Bulletin of the seismological Society of America*, 84(4), 974-1002.
- Wiemer, S., & Wyss, M. (2000). Minimum magnitude of completeness in earthquake catalogs: Examples from Alaska, the western United States, and Japan. *Bulletin of the Seismological Society of America*, 90(4), 859-869.
- Wood, H. O., & Neumann, F. (1931). Modified Mercalli intensity scale of 1931. *Bulletin of the Seismological Society of America*, 21(4), 277-283.
- Youngs, R. R., & Coppersmith, K. J. (1985). Implications of fault slip rates and earthquake recurrence models to probabilistic seismic hazard estimates. *Bulletin of the Seismological society of America*, 75(4), 939-964.

APPENDIX A

Appendix A. List of individual (ITIS) and composite (ITCS) seismogenic sources of reference for this study (DISS Working Group, 2021), grouped into the six macro-sources used for this study.

	ID code (DISS Working Group, 2021)
SOURCE 1	ITIS095 – Frosolone
	ITCS077 – Pescolanciano – Montagano
	ITIS053 – Ripabottoni
	ITIS052 – San Giuliano di Puglia
	ITIS054 – San Severo
	ITCS003 – Ripabottoni – San Severo
	ITIS022 – San Marco Lamis
	ITIS021 – San Giovanni Rotondo
	ITIS020 – Monte Sant’ Angelo
	ITCS058 – San Marco in Lamis – Mattinata
SOURCE 2	ITIS082 – Ascoli Satriano
	ITIS080 – Cerignola
	ITIS083 – Bisceglie
	ITCS004 – Castelluccio dei Sauri – Trani
SOURCE 3	ITIS089 – Carpino – Le Piane
	ITIS004 – Boiano Basin
	ITIS005 – Tammaro Basin
	ITCS024 – Miranda – Apice
	ITIS092 – Ariano Irpino
	ITCS057 – Pago Veiano – Montaguto
SOURCE 4	ITIS006 – Ufita Valley
	ITIS088 – Bisaccia
	ITIS081 – Melfi
	ITCS084 – Mirabella Eclano – Monteverde
	ITCS089 - Rapolla - Spinazzola
SOURCE 5	ITIS077 – Colliano
	ITIS079 – Pescopagano
	ITCS034 - Irpinia – Agri Valley
	ITCS087 – Conza della Campania – Tolve
	ITCS063 - Andretta Filano
	ITIS078 – San Gregorio Magno
	ITIS008 – Agri Valley
	ITIS010 – Melandro – Pergola
SOURCE 6	ITIS084 – Potenza
	ITCS005 – Baragiano - Palagianello

APPENDIX B



Appendix B. Partial seismic hazard models for the SLV limit state. For details on the choices made for each model, see Figure 21 and Figure 22. The acceleration values are expressed in g (using an absolute color palette), with a 10% exceedance probability in 100 years ($T_R = 950$ years) at $T = 0.01$ s.

APPENDIX C

Appendix C. List of faults used in the fault-based approach. Faults marked in white in the table are the Individual Seismogenic Sources reported in the DISS database, while faults highlighted in grey are the integration of Valentini et al. (2017). For each of them, we list here the dip angle, the kinematics (S = strike-slip, N = normal), the seismogenic depth range (km) and the slip rate range (mm/yr).

Fault ID	Dip (°)	Kinematics	Seismogenic depth range (km)	Slip rate range (mm/yr)
F1	70	S	11 - 25	0.4 - 0.7
F2	86	S	12 - 20	0.1 - 0.5
F3	82	S	12 - 20	0.1 - 0.5
F4	80	S	6 - 21	0.1 - 0.5
F5	80	S	0 - 12	0.4 - 0.7
F6	80	S	0 - 12	0.4 - 0.7
F7	80	S	0 - 12	0.5 - 1.2
F8	80	S	13 - 21	0.1 - 0.5
F9	80	S	11 - 22	0.1 - 0.5
F10	80	S	13 - 19	0.1 - 0.5
F11	60	N	0 - 13	0.5 - 1.2
F12	60	N	1 - 7	0.4 - 0.7
F13	55	N	1 - 12	0.4 - 0.7
F14	60	N	1 - 13	0.4 - 0.7
F15	60	N	0 - 12	0.15 - 0.35
F16	55	N	0 - 10	0.4 - 0.9
F17	70	N	11 - 25	0.4 - 0.7
F18	64	N	1 - 14	0.4 - 0.7
F19	64	N	1 - 15	0.4 - 0.7
F20	80	S	12 - 23	0.1 - 0.5
F21	70	N	1 - 10	0.4 - 0.6
F22	60	N	1 - 14	0.4 - 0.6
F23	60	N	1 - 14	0.4 - 0.6
F24	60	N	1 - 11	0.4 - 0.7
F25	60	N	1 - 13	0.4 - 0.7
F26	60	N	0 - 13	0.3 - 1
F27	60	N	0 - 12	0.3 - 1
F28	60	N	0 - 13	0.4 - 0.7
F29	60	N	0 - 13	0.8 - 1.2
F30	60	N	0 - 8	0.3 - 0.7
F31	88	S	15 - 21	0.1 - 0.5
F32	90	S	0 - 22	0.1 - 0.5
F33	60	N	0 - 13	0.2 - 0.6
F34	55	N	0 - 13	0.2 - 0.7
F35	60	N	0 - 13	0.2 - 0.3

ADDITIONAL MATERIAL

In the first part of this section, we present the complete and official reports of the ten surveyed seismic stations received by the Istituto Nazionale di Geofisica e Vulcanologia (INGV). The surveys took place during an *ad hoc* fieldwork conducted in October 2019 and the results are now available online at the ITACA database (D'Amico *et al.*, 2020). Station reports (Alessandrini *et al.*, 2019) are shown as follow:

- **ACER** – page 116
- **AND3** – page 125
- **ASR** – page 137
- **CAFE** – page 149
- **CER** – page 161
- **MRB1** – page 173
- **MRLC** – page 184
- **RNV2** – page 195
- **SGTA** – page 206
- **SNAL** – page 215

In the second part of this section (page 225), we show our study on the soil-structure interaction phenomenon. In our manuscript (Castellaro *et al.*, 2022), we propose a simple working scheme to identify the existence of potential installation-related issues and to assess the frequency range of fidelity of the response of a seismic station to the ground motion.

Giulia Alessandrini¹, Giovanni Lattanzi¹, Stephen Slivicki², Giulia Sgattoni¹, Silvia Castellaro¹

¹ *Università di Bologna, Dipartimento di Fisica e Astronomia, Viale Carlo B. Pichat 8, 40127 Bologna (Italy)*

² *University of Wisconsin-River Falls (USA)*

Site characterization of the seismic station

IV.ACER

Geophysical survey performed on
23rd October 2019 (16 pm – 18 pm)

Partly funded by Contratto di Consulenza Commissionata per lo "Studio sismotettonico delle dighe Marana Capacciotti e San Pietro sul Torrente Osento e delle opere accessorie" – Consorzio di Bonifica per la Capitanata (2019)

IV. ACER- ACERENZA

CODE	NAME	Lat. [°] WGS-84	Lon. [°] WGS-84	Elevation [m]
ACER	ACERENZA	40.786633	15.942288	690
Address	Unnamed Road, 85011 Acerenza (PZ), Basilicata			

Table 31. Code, name and WGS-84 coordinates of the seismic station.

SEISMIC STATION

SENSOR	EPISENSOR-FBA-ES-T
DIGITIZER	unknown
HOUSING	Pillar inside the meteorologic station

Table 32. Instrumental chain installed at the seismic station.

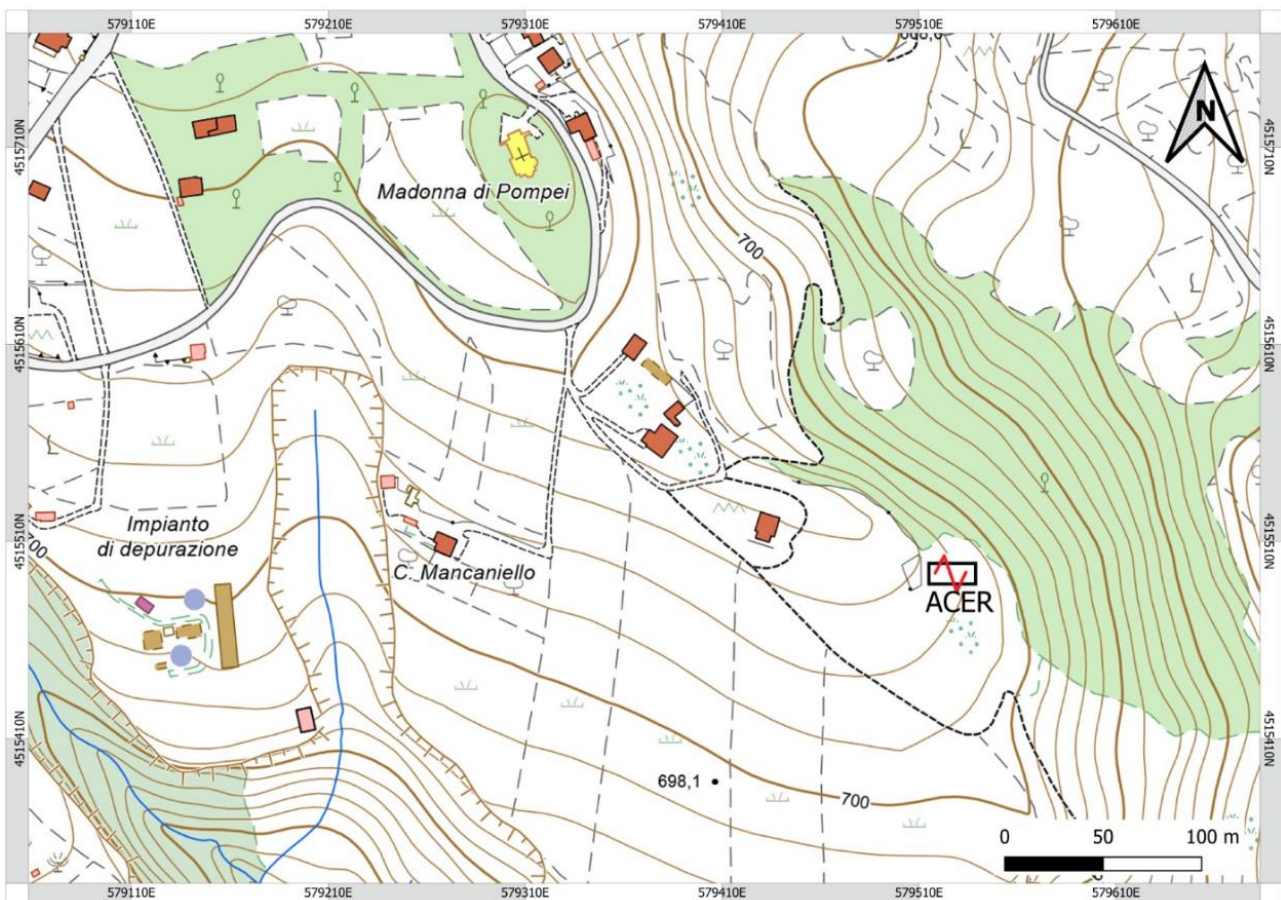


Figure 71. Location of the ACER seismic station at Acerenza (source CTR 1:5 000; the image could be rescaled, refer to the bar scale).

GEOLOGICAL AND TOPOGRAPHIC INFORMATION

According to the CARG map (Figure 72), the seismic station is located on the *Subsintema di Acerenza* (TLV_{2a}), characterized by sand and sandstone with intermediate to coarse grain-size. The maximum thickness of the sub-synthem is 50-80 m.

TYPE	NOTES	SCALE
ISPRA, carta geologica	Foglio 187, Melfi	1:100 000
CTR	Foglio 470044	1:5 000
CARG, carta geologica	Foglio 470, Potenza	1:50 000

Table 33. Geological and geotechnical cartography available for the site.

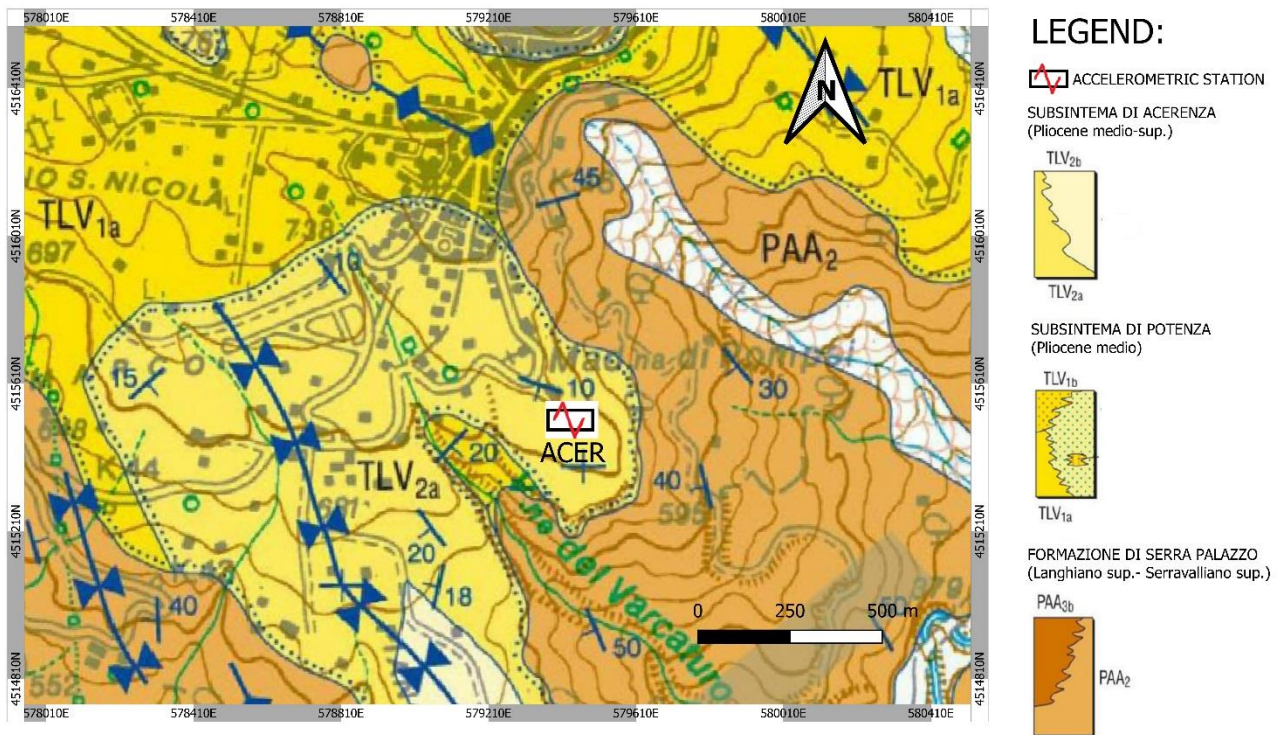


Figure 72. Geological map of the area surrounding the seismic station ACER (source CARG 1:50 000, the image could be rescaled, refer to the bar scale).

GEOPHYSICAL SURVEY

We propose an average V_s model for the site, based on the joint fit of all the acquired surface-wave dispersion and H/V curves (Table 35). Since the H/V curves are more sensitive to local geological features compared to the array dispersion curves, the average V_s model might not faithfully reproduce the H/V features at high frequency.

The theoretical H/V curve overlapped to the experimental H/V curve could be computed on a slightly different model (see footnotes, if present).

SURVEY TYPE	N.	Acquisition length	Sampling rate [Hz]	NOTES	INSTRUMENT USED
Microtremor H/V ³	4	20' each	512	All measurements on natural soil	Tromino® - MoHo srl
Active/passive 1D array ⁴	1	Active: MASW Passive: ReMi (7' recording)	512	16 geophones, 3 m inter-receiver distance	Seismograph: SoilSpy – MoHo srl Geophones: OYO - Geospace 4.5 Hz (vertical)

Table 34. List of the H/V and active/passive surface-wave arrays acquired at the site.



³ The average amplitude spectra in velocity and their standard deviation are computed for each measurement point by splitting the recorded signal into 30 second non-overlapping windows. On average, 32 to 40 signal windows are retained to compute the average H/V curve and its standard deviation. Each window is detrended, tapered with a Bartlett window, zero-padded and FF-transformed. The Fourier spectra are smoothed according to triangular windows with width equal to 10% of the central frequency, in order to keep only the significant peaks.

⁴ The vertical-component Rayleigh-wave phase-velocity dispersion curves obtained by averaging several active and passive surveys are illustrated. Only the windows showing the lowest phase velocities (with the exclusion of the alias) are retained, for their being closer to the fundamental mode dispersion curve. The phase-velocity spectra are obtained by slant-stacking the seismograms and by applying a FFT.

Figure 73. Location of the active/passive surface-wave arrays and of the H/V recordings.

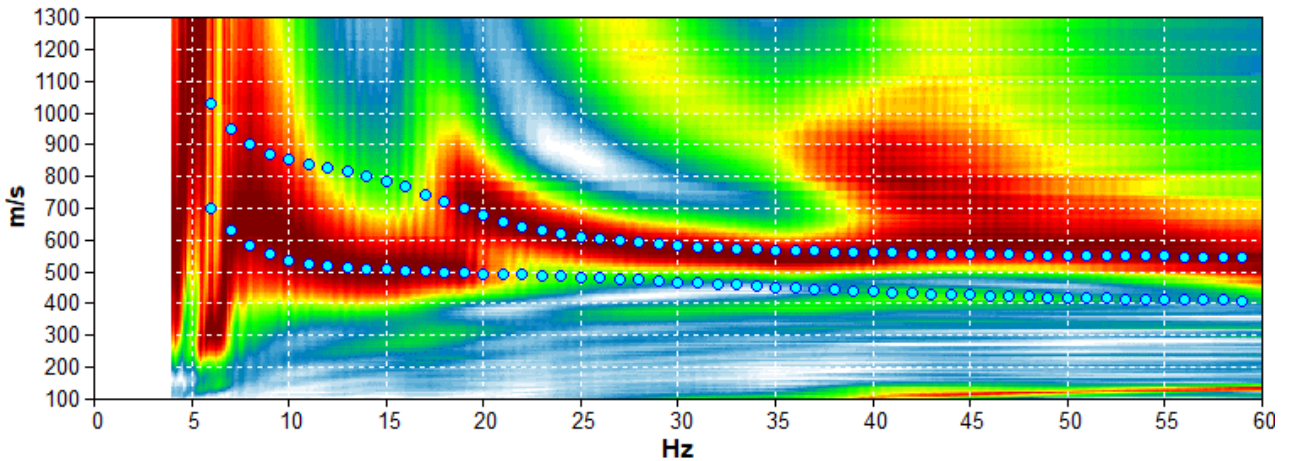


Figure 74. Average dispersion curve from the MASW and ReMi surveys. Synthetic dispersion curve for the model of Table 35 (light blue circles).

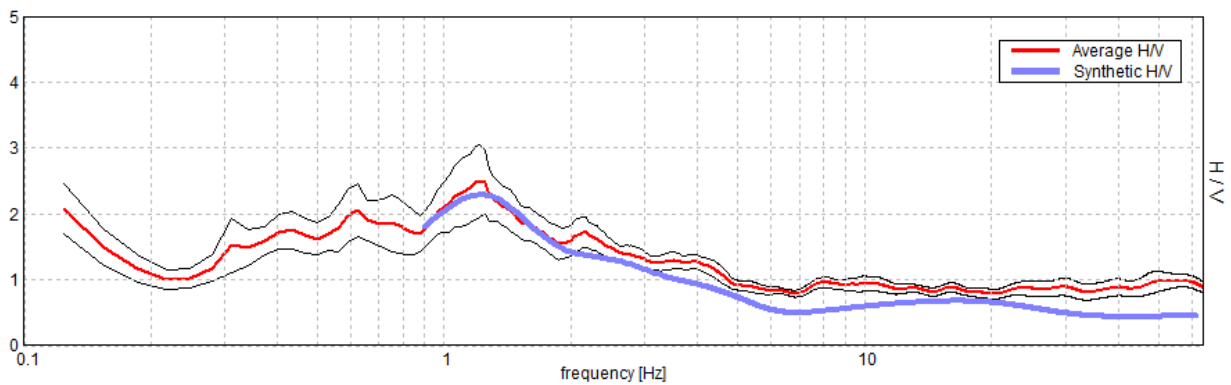


Figure 75. Experimental H/V curve acquired at site T03 (average in red, standard deviation in black). Synthetic H/V curve for the model of Table 35 (blue).

Depth at the bottom of the layer [m]	Thickness [m]	Vs [m/s]	Poisson ratio	Seismostratigraphic model obtained from:
5.00	5.00	420	0.45	0 – 45m H/V + Dispersion curve
35.00	30.00	550	0.42	
110.00	75.00	900	0.40	45 m – inf. H/V only
280.00	170.00	1300	0.40	
inf.	inf.	1800	0.38	

Table 35. Seismostratigraphic model proposed for the site.

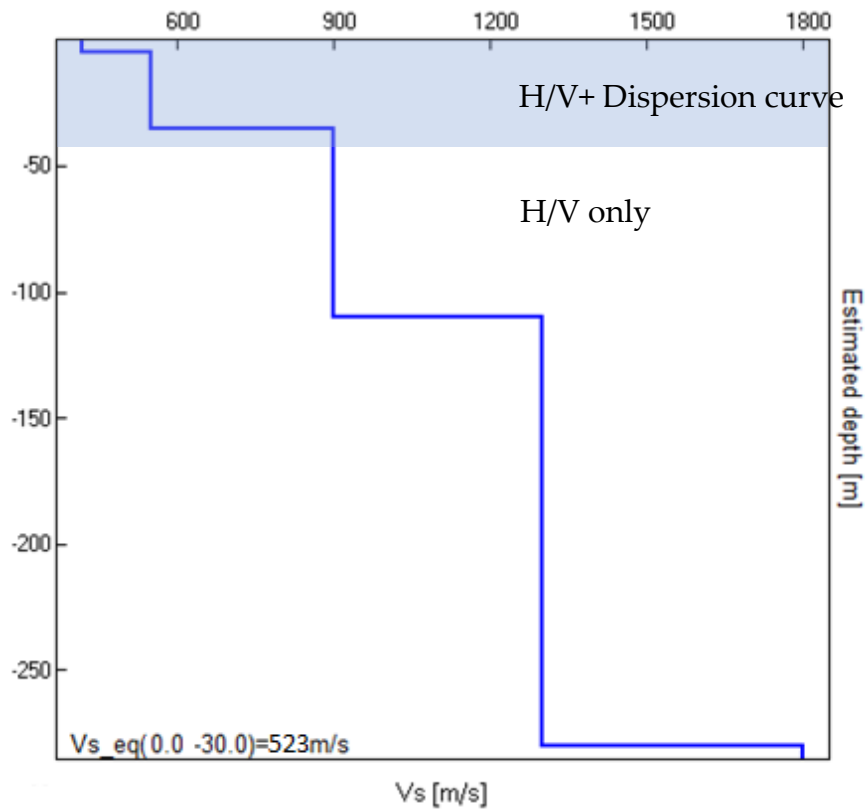


Figure 76. Vs model proposed for the site.

$$V_{seq}[0 - 30] m = 520 m/s *$$

Class B site (NTC, 2018)

* Characteristic uncertainty is 20%

ADDITIONAL MATERIAL

In this section we present the characteristic H/V curve of the site (Figure 77) together with the single spectral components used to compute it, in order for the reader to understand the stratigraphic or artefactual nature of the H/V peaks (SESAME, 2004; Castellaro, 2016). The SESAME (2004) criteria for the main H/V peak are listed in Table 36. In Figure 78 we present a selection of H/V curves acquired in the proximity of the seismic station to show the spatial variability of this function.

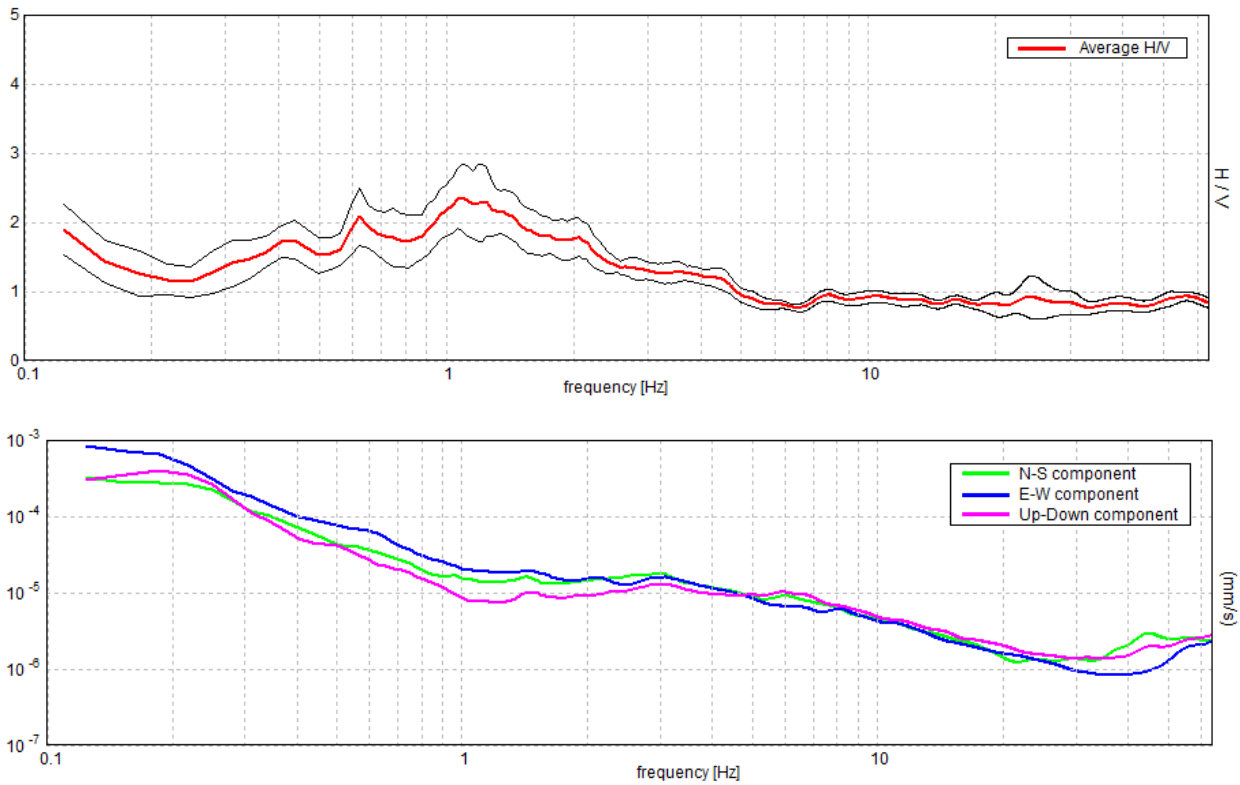


Figure 77. Top: characteristic H/V curve (average in red, standard deviation in black). Bottom: spectra of the single components of motion (NS, EW, Z) used to derive the H/V curve.

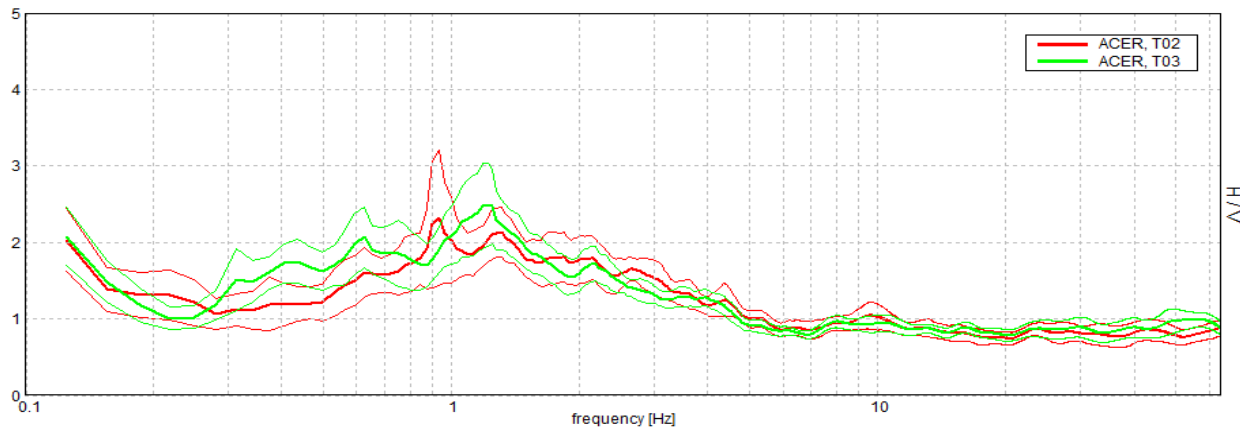


Figure 78. Comparison of the H/V curves acquired in the proximity of the seismic station (refer to Figure 73 for the location).

[According to the SESAME, 2004 guidelines]

H/V peak at 1.22 ± 0.07 Hz (in the range 0.0 - 64.0 Hz).

Criteria for a reliable H/V curve [All 3 should be fulfilled]			
$f_0 > 10 / L_w$	1.22 > 0.33	OK	
$n_c(f_0) > 200$	840.9 > 200	OK	
$\sigma_A(f) < 2$ for $0.5f_0 < f < 2f_0$ if $f_0 > 0.5\text{Hz}$ $\sigma_A(f) < 3$ for $0.5f_0 < f < 2f_0$ if $f_0 < 0.5\text{Hz}$	Exceeded 0 out of 60 times	OK	
Criteria for a clear H/V peak [At least 5 out of 6 should be fulfilled]			
Exists f^- in $[f_0/4, f_0] \mid A_{H/V}(f^-) < A_0 / 2$			NO
Exists f^+ in $[f_0, 4f_0] \mid A_{H/V}(f^+) < A_0 / 2$	4.094 Hz	OK	
$A_0 > 2$	2.50 > 2	OK	
$f_{\text{peak}}[A_{H/V}(f) \pm \sigma_A(f)] = f_0 \pm 5\%$	$ 0.05479 < 0.05$		NO
$\sigma_f < \sigma(f_0)$	0.06677 < 0.12188	OK	
$\sigma_A(f_0) < \sigma(f_0)$	0.543 < 1.78	OK	

L_w	window length
n_w	number of windows used in the analysis
$n_c = L_w n_w f_0$	number of significant cycles
f	current frequency
f_0	H/V peak frequency
σ_f	standard deviation of H/V peak frequency
$\sigma(f_0)$	threshold value for the stability condition $\sigma_f < \sigma(f_0)$
A_0	H/V peak amplitude at frequency f_0
$A_{H/V}(f)$	H/V curve amplitude at frequency f
f^-	frequency between $f_0/4$ and f_0 for which $A_{H/V}(f^-) < A_0/2$
f^+	frequency between f_0 and $4f_0$ for which $A_{H/V}(f^+) < A_0/2$
$\sigma_A(f)$	standard deviation of $A_{H/V}(f)$, $\sigma_A(f)$ is the factor by which the mean $A_{H/V}(f)$ curve should be multiplied or divided
$\sigma_{\log H/V}(f)$	standard deviation of $\log A_{H/V}(f)$ curve
$\sigma(f_0)$	threshold value for the stability condition $\sigma_A(f) < \sigma(f_0)$

Threshold values for σ_f and $\sigma_A(f_0)$					
Freq. range [Hz]	< 0.2	0.2 – 0.5	0.5 – 1.0	1.0 – 2.0	> 2.0
$\sigma(f_0)$ [Hz]	0.25 f_0	0.2 f_0	0.15 f_0	0.10 f_0	0.05 f_0
$\sigma(f_0)$ for $\sigma_A(f_0)$	3.0	2.5	2.0	1.78	1.58
$\log \sigma(f_0)$ for $\sigma_{\log H/V}(f_0)$	0.48	0.40	0.30	0.25	0.20

Table 36. SESAME (2004) criteria applied to the main resonance peak identified in the characteristic H/V curve.

GALLERY



Figure 79. Location of the H/V recordings near the ACER seismic station.

REFERENCES

Castellaro S., 2016. The complementarity of H/V and dispersion curves, *Geophysics*, 81, T323–T338

ISPRA, Carta Geologica d'Italia alla scala 1:50 000, Foglio 470 "Potenza"

Norme Tecniche sulle Costruzioni, 2018. Decreto Ministeriale 17/01/2018, Ministry of Infrastructures and Transportations, G.U. S.O. n.8 on 20/2/2018

SESAME, 2004. Guidelines for the implementation of the H/V spectral ratio technique on ambient vibrations. Measurements, processing and interpretation, WP12 European commission - Research general directorate project no. EVG1-CT-2000-0026 SESAME, report D23.12, 62 pp.

Giulia Alessandrini¹, Giovanni Lattanzi¹, Stephen Slivicki², Giulia Sgattoni¹, Silvia Castellaro¹

¹ *Università di Bologna, Dipartimento di Fisica e Astronomia, Viale Carlo B. Pichat 8, 40127 Bologna (Italy)*

² *University of Wisconsin-River Falls (USA)*

Site characterization of the seismic station

IX.AND3

Geophysical survey performed on
25th October 2019 (9 am – 11.30 am)

Partly funded by Contratto di Consulenza Commissionata per lo “Studio sismotettonico delle dighe Marana Capacciotti e San Pietro sul Torrente Osento e delle opere accessorie” – Consorzio di Bonifica per la Capitanata (2019)

IX.AND3-ANDRETTA

CODE	NAME	Lat. [°] WGS-84	Lon. [°] WGS-84	Elevation [m]
IX.AND3	Andretta	40.92980	15.33310	905
Address	Unnamed Road, 83040 Andretta AV, Italy			

Table 37. Code, name and WGS-84 coordinates of the seismic station.

SEISMIC STATION

SENSOR	unknown
DIGITIZER	unknown
HOUSING	Pillar inside a sheet metal shed

Table 38. Instrumental chain installed at the seismic station.

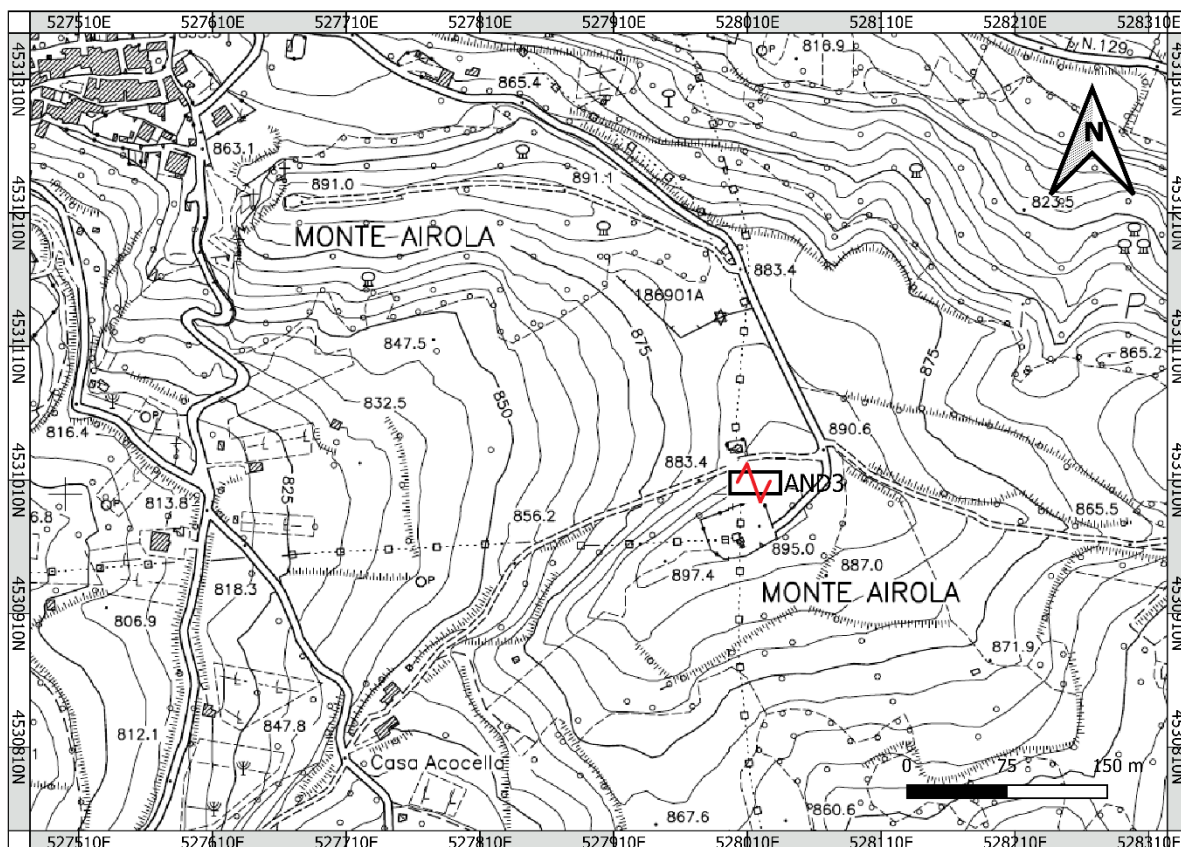


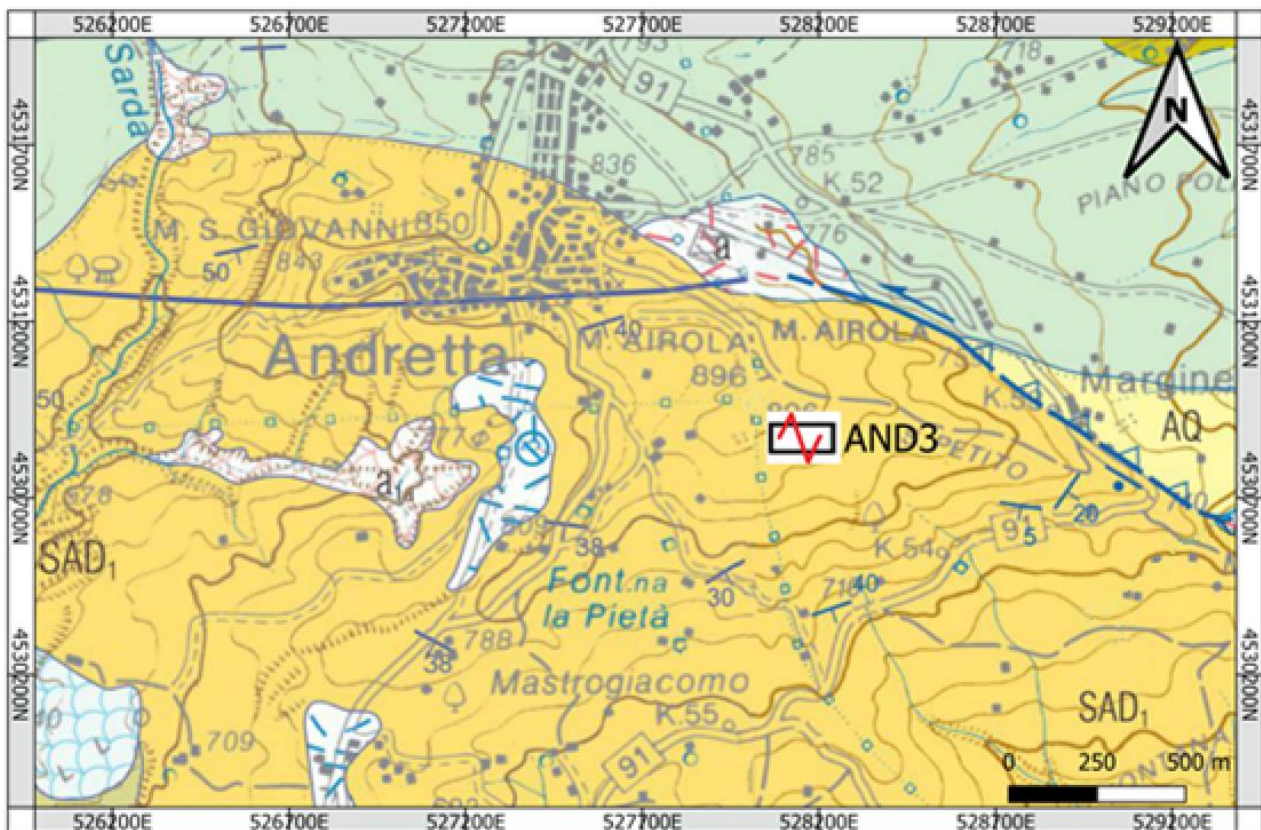
Figure 80. Location of the AND3 seismic station at Andretta (source CTR 1:5 000, the image could be rescaled, refer to the bar scale).

GEOLOGICAL AND TOPOGRAPHIC INFORMATION

According to the CARG map (Figure 81), the seismic station is located on the *Sintema di Andretta-subsintema di Monte Airola*, (SAD_1) characterized by conglomerates with intermediate sandy layer thickness. The thickness of the synthem (SAD_1) is about 100 m.

TYPE	NOTES	SCALE
CTR	Fogli 450081, 451054	1:5 000
ISPRA, carta geologica	Foglio 186, S. Angelo dei Lombardi	1:100 000
CARG, carta geologica	Foglio 450 S. Angelo dei Lombardi, 451 Melfi	1:50 000

Table 39. Geological and geotechnical cartography available for the site.



LEGEND:

-  ACCELEROMETRIC STATION
-  SAD_1
SINTEMA DI ANDRETTA
subsintema di Monte Airola
(Pliocene inf.)

Figure 81. Geological map of the area surrounding the seismic station AND3 (source CARG 1:50 000, the image could be rescaled, refer to the bar scale).

GEOPHYSICAL SURVEY

We propose an average V_s model for the site, based on the joint fit of all the acquired surface-wave dispersion and H/V curves (Table 35). Since the H/V curves are more sensitive to local geological features compared to the array dispersion curves, the average V_s model might not faithfully reproduce the H/V features at high frequency.

The theoretical H/V curve overlapped to the experimental H/V curve could be computed on a slightly different model (see footnotes, if present).

SURVEY TYPE	N.	Acquisition length	Sampling rate [Hz]	NOTES	INSTRUMENT USED
Microtremor H/V ⁵	5	20' each	512	All measurements on natural soil	Tromino® - MoHo srl
Active/passive 1D array ⁶	2	Active: MASW Passive: ReMi (7' recording)	512	16 geophones, 3 m inter-receiver distance	Seismograph: SoilSpy – MoHo srl Geophones: OYO - Geospace 4.5 Hz (vertical)

Table 40. List of the H/V and active/passive surface-wave arrays acquired at the site.

The characteristic H/V curve of the site, together with the single spectral components used to compute it, is shown in Figure 83. The H/V curves at this site show a number of artefactual peaks and troughs (arrows in Figure 83) due to the vibrations of wind turbines around the site (SESAME, 2004; Castellaro, 2016). The stratigraphic resonance of the site is at approximately 0.8 Hz. The SESAME (2004) criteria for the main H/V peak are given in Table 42.

⁵ The average amplitude spectra in velocity and their standard deviation are computed for each measurement point by splitting the recorded signal into 30 second non-overlapping windows. On average, 32 to 40 signal windows are retained to compute the average H/V curve and its standard deviation. Each window is detrended, tapered with a Bartlett window, zero-padded and FF-transformed. The Fourier spectra are smoothed according to triangular windows with width equal to 10% of the central frequency, in order to keep only the significant peaks.

⁶ The vertical-component Rayleigh-wave phase-velocity dispersion curves obtained by averaging several active and passive surveys are illustrated. Only the windows showing the lowest phase velocities (with the exclusion of the *alias*) are retained, for their being closer to the fundamental mode dispersion curve. The phase-velocity spectra are obtained by slant-stacking the seismograms and by applying a FFT.

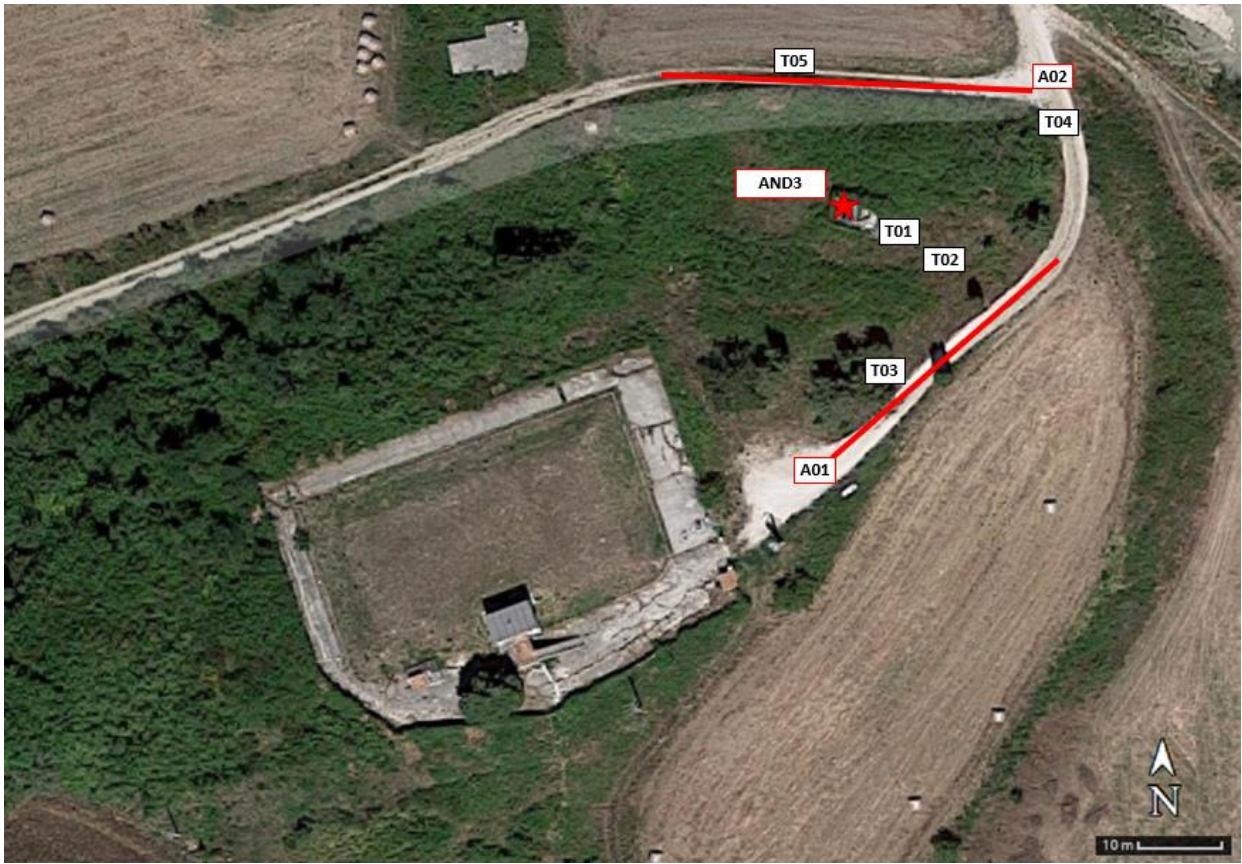


Figure 82. Location of the active/passive surface-wave arrays and of the H/V recordings.

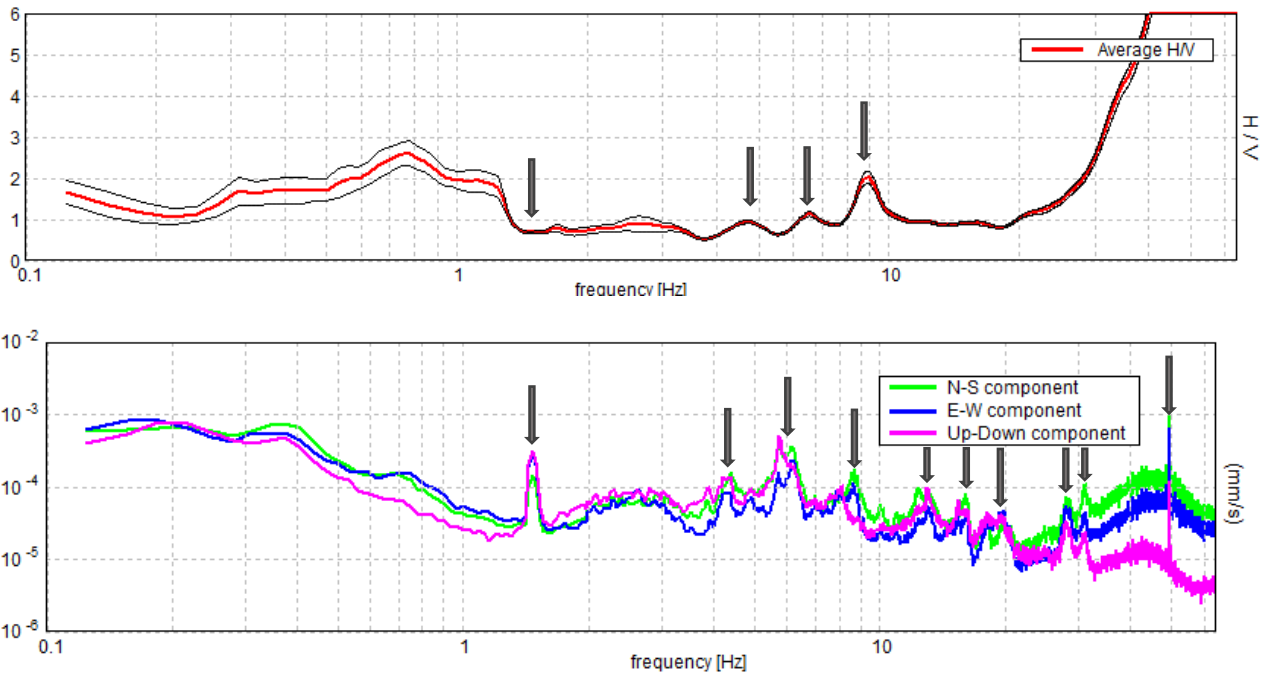


Figure 83. Experimental H/V curve acquired at site T01 (top, average in red, standard deviation in black) and non-smoothed single component spectra (bottom). The arrows indicate a number of artefacts due to the vibrations of the wind turbines around the site. These show up in the H/V curve as artefactual troughs and peaks.

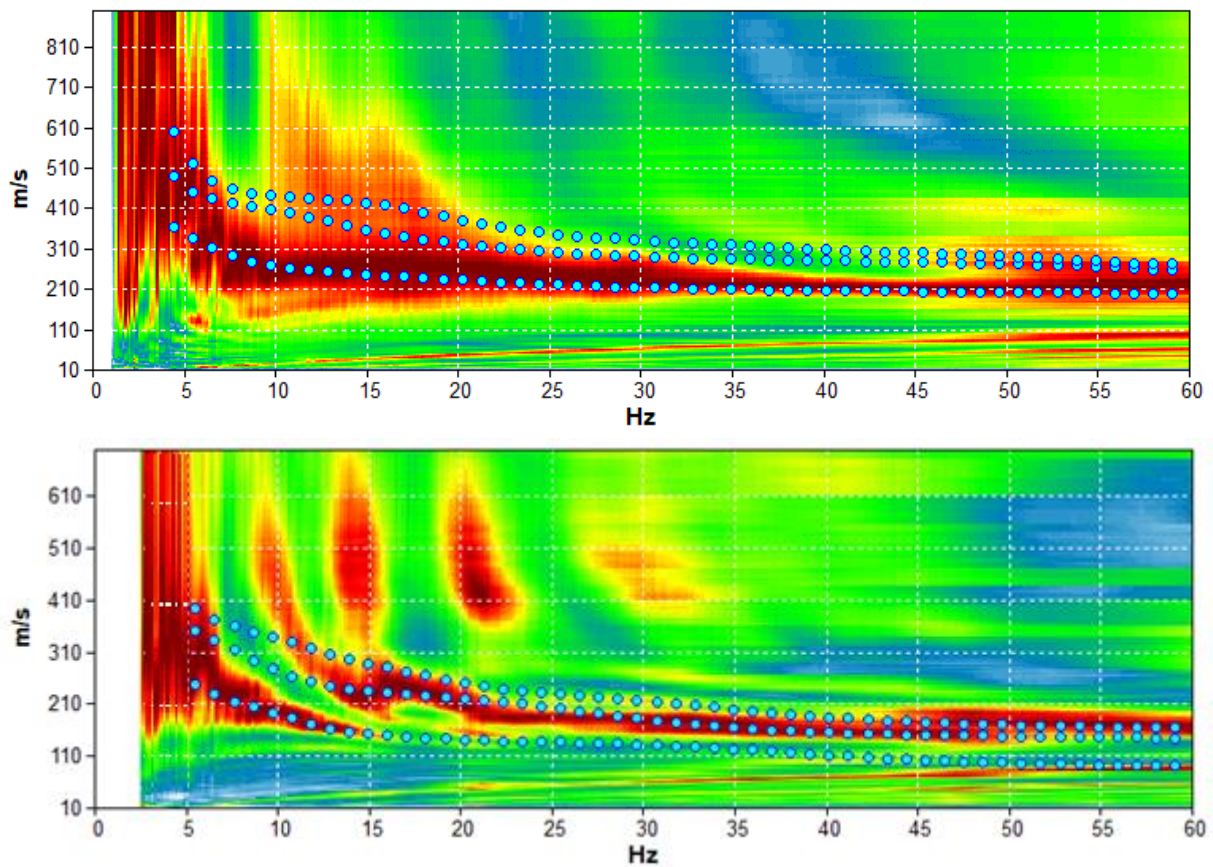


Figure 84. Dispersion curves from the MASW and ReMi surveys at site A01 (top) and A02 (bottom, Figure 73). Synthetic dispersion curves for the model of Table 35 (light blue circles).

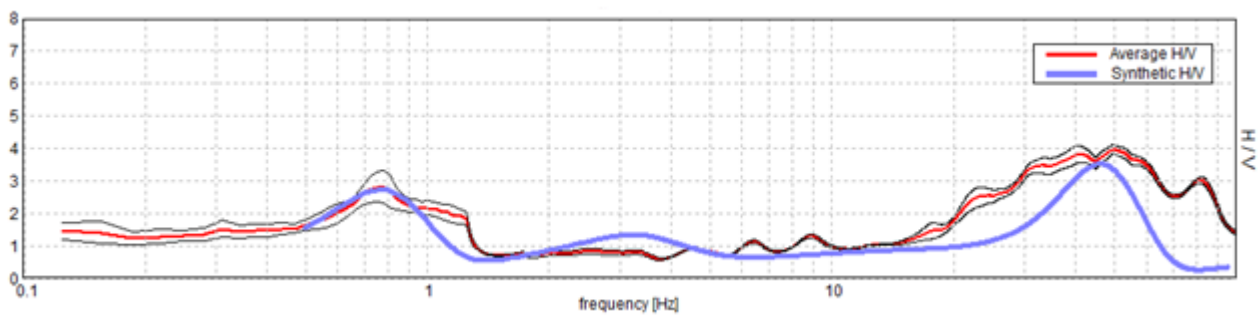


Figure 85. Experimental H/V curve acquired at site T02 (average in red, standard deviation in black). Synthetic H/V curve for the model of Table 35 (blue).

Depth at the bottom of the layer [m]	Thickness [m]	Vs [m/s]	Poisson ratio	Seismostratigraphic model obtained from:
0.60	0.60	110	0.48	0 - 28 m H/V + Dispersion curve
4.60	4.00	230	0.46	
14.60	10.00	280	0.48	
24.60	10.00	330	0.48	
134.60	110.00	430	0.46	28 m- inf.
inf.	inf.	770	0.46	H/V only

Table 41. Seismostratigraphic model proposed for the site.

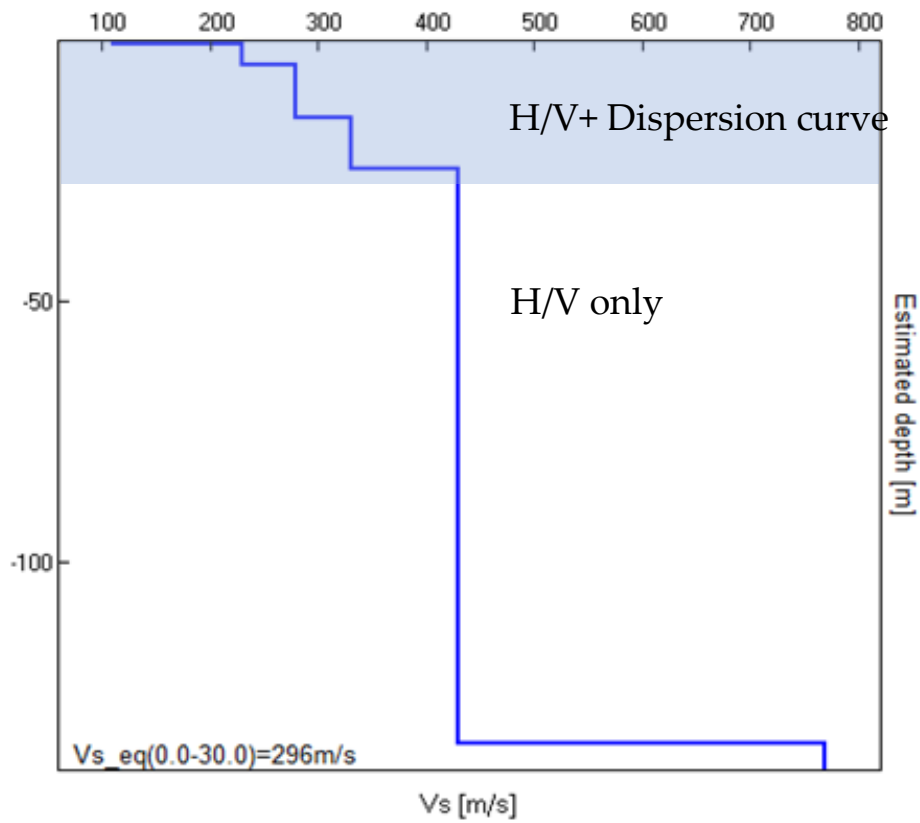


Figure 86. Vs model proposed for the site.

$V_{seq}[0 - 30] m = 300 m/s *$
 Class C site (NTC, 2018)

* Characteristic uncertainty is 20%

ADDITIONAL MATERIAL

In Figure 78 we present a selection of H/V curves acquired in the proximity of the seismic station to show the spatial variability.

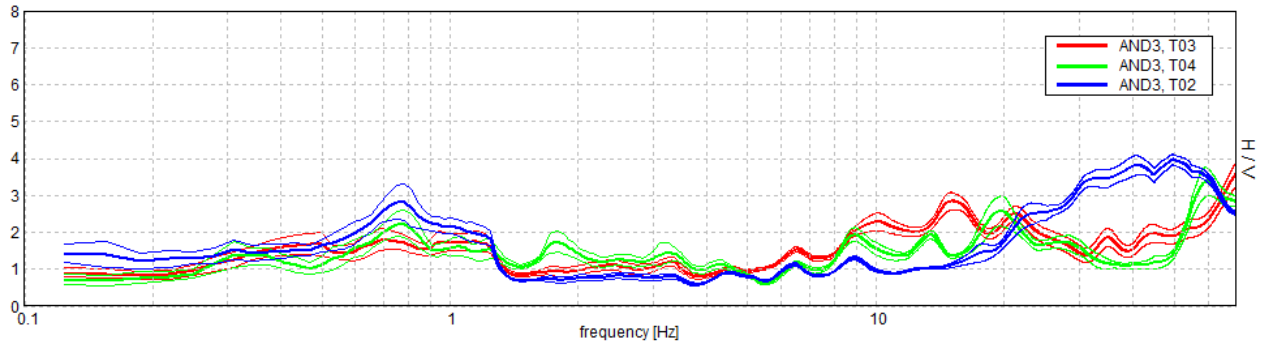


Figure 87. Comparison of the H/V curves acquired around the seismic station (refer to Figure 73 for the location).

[According to the SESAME, 2004 guidelines]

Max. H/V at 0.75 ± 0.11 Hz (in the range 0.0 - 5.0 Hz)			
Criteria for a reliable H/V curve			
[All 3 should be fulfilled]			
$f_0 > 10 / L_w$	$0.75 > 0.50$	OK	
$n_c(f_0) > 200$	$900.0 > 200$	OK	
$\kappa_A(f) < 2$ for $0.5f_0 < f < 2f_0$ if $f_0 > 0.5\text{Hz}$ $\kappa_A(f) < 3$ for $0.5f_0 < f < 2f_0$ if $f_0 < 0.5\text{Hz}$	Exceeded 0 out of 37 times	OK	
Criteria for a clear H/V peak			
[At least 5 out of 6 should be fulfilled]			
Exists f^- in $[f_0/4, f_0] \mid A_{H/V}(f^-) < A_0 / 2$	0.281 Hz	OK	
Exists f^+ in $[f_0, 4f_0] \mid A_{H/V}(f^+) < A_0 / 2$	1.281 Hz	OK	
$A_0 > 2$	$2.80 > 2$	OK	
$f_{\text{peak}}[A_{H/V}(f) \pm \kappa_A(f)] = f_0 \pm 5\%$	$ 0.15129 < 0.05$		NO
$\kappa_i < \kappa(f_0)$	$0.11347 < 0.1125$		NO
$\kappa_A(f_0) < \kappa(f_0)$	$0.4564 < 2.0$	OK	

L_w	window length
n_w	number of windows used in the analysis
$n_c = L_w n_w f_0$	number of significant cycles
f	current frequency
f_0	H/V peak frequency
σ_f	standard deviation of H/V peak frequency
$\sigma(f_0)$	threshold value for the stability condition $\sigma_f < \sigma(f_0)$
A_0	H/V peak amplitude at frequency f_0
$A_{H/V}(f)$	H/V curve amplitude at frequency f
f^-	frequency between $f_0/4$ and f_0 for which $A_{H/V}(f^-) < A_0/2$
f^+	frequency between f_0 and $4f_0$ for which $A_{H/V}(f^+) < A_0/2$
$\sigma_A(f)$	standard deviation of $A_{H/V}(f)$, $\sigma_A(f)$ is the factor by which the mean $A_{H/V}(f)$ curve should be multiplied or divided
$\sigma_{\log H/V}(f)$	standard deviation of $\log A_{H/V}(f)$ curve
$\sigma(f_0)$	threshold value for the stability condition $\sigma_A(f) < \sigma(f_0)$

Threshold values for σ_f and $\sigma_A(f_0)$					
Freq. range [Hz]	< 0.2	0.2 – 0.5	0.5 – 1.0	1.0 – 2.0	> 2.0
$\sigma(f_0)$ [Hz]	$0.25 f_0$	$0.2 f_0$	$0.15 f_0$	$0.10 f_0$	$0.05 f_0$
$\sigma(f_0)$ for $\sigma_A(f_0)$	3.0	2.5	2.0	1.78	1.58
$\log \sigma(f_0)$ for $\sigma_{\log H/V}(f_0)$	0.48	0.40	0.30	0.25	0.20

Table 42. SESAME (2004) criteria applied to the main resonance peak identified in the characteristic H/V curve.

GALLERY



Figure 88. The AND3 seismic station housing: pillar inside a sheet metal shed.



Figure 89. Location of the active/passive surface waves array A01.



Figure 90. Location of the H/V recordings near the seismic station AND3.

REFERENCES

Castellaro S., 2016. The complementarity of H/V and dispersion curves, *Geophysics*, 81, T323–T338

ISPRA, Carta Geologica d'Italia alla scala 1:50 000, Foglio 450 "S. Angelo dei Lombardi", Foglio 451 "Melfi"

Norme Tecniche sulle Costruzioni, 2018. Decreto Ministeriale 17/01/2018, Ministry of Infrastructures and Transportations, G.U. S.O. n.8 on 20/2/2018

SESAME (2004), Guidelines for the implementation of the H/V spectral ratio technique on ambient vibrations. Measurements, processing and interpretation, WP12 European commission - Research general directorate project no. EVG1-CT-2000-0026 SESAME, report D23.12, 62 pp.

Giulia Alessandrini¹, Giovanni Lattanzi¹, Stephen Slivicki², Giulia Sgattoni¹, Silvia Castellaro¹

¹ *Università di Bologna, Dipartimento di Fisica e Astronomia, Viale Carlo B. Pichat 8, 40127 Bologna (Italy)*

² *University of Wisconsin-River Falls (USA)*

Site characterization of the seismic station

IT.ASR

Geophysical survey performed on
22nd October 2019 (12 pm – 13 pm)

Partly funded by Contratto di Consulenza Commissionata per lo “Studio sismotettonico delle dighe Marana Capacciotti e San Pietro sul Torrente Osento e delle opere accessorie” – Consorzio di Bonifica per la Capitanata (2019)

IT. ASR- ASCOLI SATRIANO

CODE	NAME	Lat. [°] WGS-84	Lon. [°] WGS-84	Elevation [m]
ASR	ASCOLI SATRIANO	41.198977	15.563130	382
Address	Via Tagliamento 1, Ascoli Satriano (FG) 71022			

Table 43. Code, name and WGS-84 coordinates of the seismic station.

SEISMIC STATION

SENSOR	unknown
DIGITIZER	K2 (internal sensor) [Kinematics]
HOUSING	Fiberglass box on concrete basement approx. 1.5 x 1.5 m. The station is located between the Carabinieri station and the football field.

Table 44. Instrumental chain installed at the seismic station.

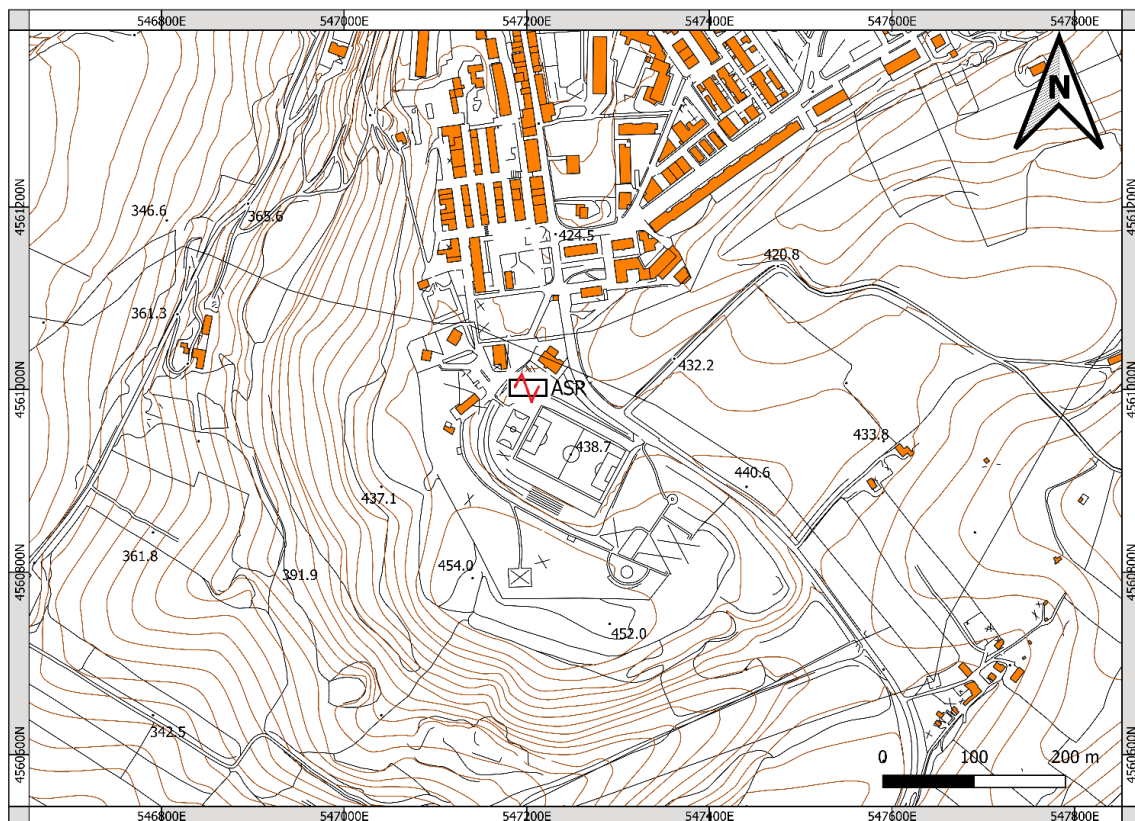


Figure 91. Location of the ASR seismic station at Ascoli Satriano (source CTR 1:5 000, the image could be rescaled, refer to the bar scale).

GEOLOGICAL AND TOPOGRAPHIC INFORMATION

According to the ENEL map (Figure 72) and to the CARG map (Foglio 421) the seismic station is located on the *Sintema di La Pezza del Tesoro (PZT)*, characterized by polygenic conglomerates interposed to sandy lenses. According to the borehole of Table 46, carried out next to the seismic station, the thickness of the conglomerates is about 16 m.

TYPE	NOTES	SCALE
CTR	Foglio 421152, 434031	1:5 000
ENEL, carta geologica	Carta geologica	1:20 000
CARG, carta geologica	Foglio 421, Ascoli Satriano	1:50 000

Table 45. Geological and geotechnical cartography available for the site.

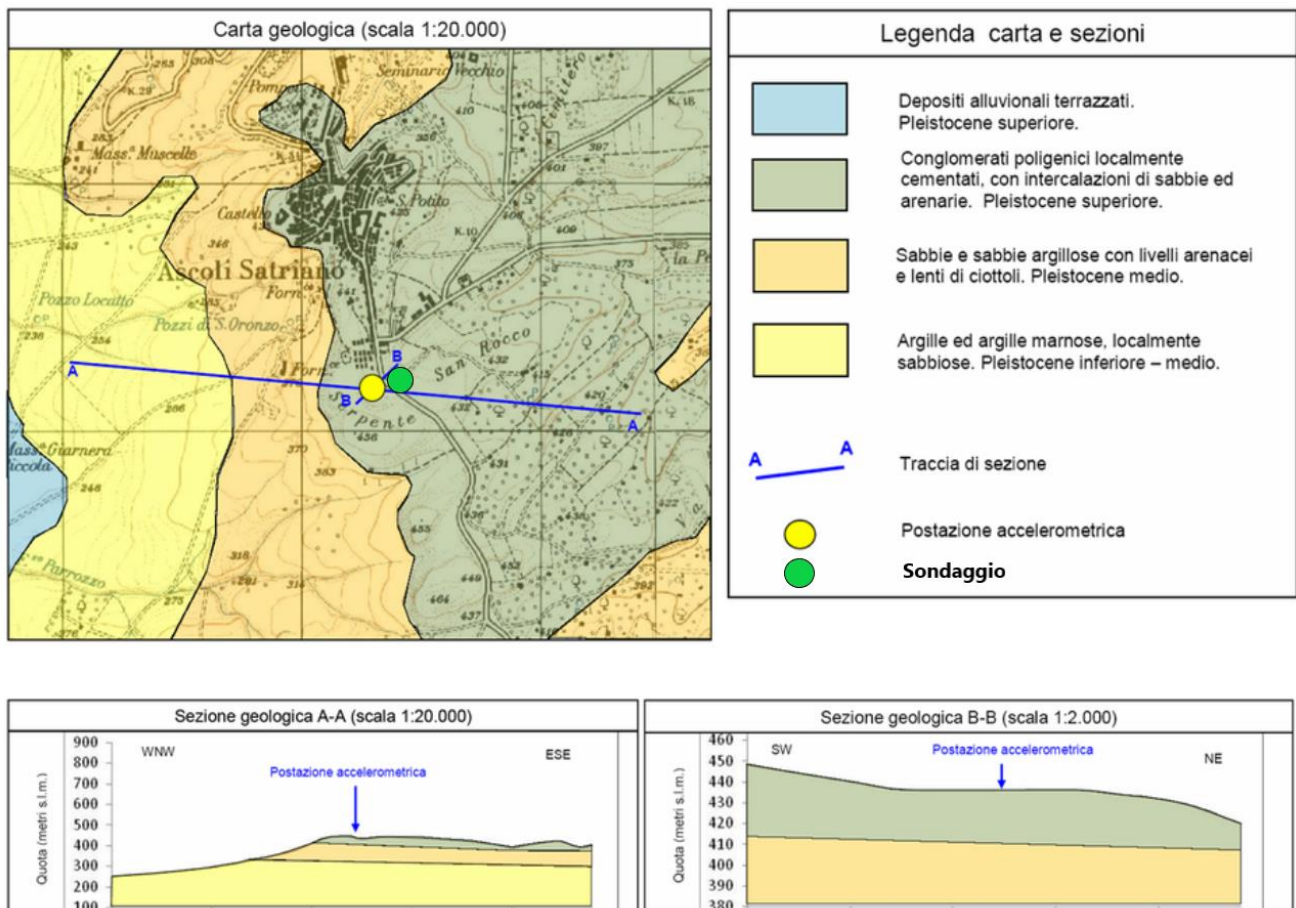


Figure 92. Geological map and cross sections of the area surrounding the seismic station ASR (source ENEL 1:20 000).

FROM DEPTH (m)	TO DEPTH (m)	THICKNESS (m)	LITHOLOGICAL DESCRIPTION
0,00	1,00	1,00	TERRENO DI RIPORTO
1,00	12,00	11,00	CONGLOMERATO A PEZZATURA VARIABILE A MATRICE TERROSA
12,00	17,00	5,00	CONGLOMERATO
17,00	36,00	19,00	SABBIA GIALLA A TRATTI CEMENTATA
36,00	41,00	5,00	ARGILLA GIALLA
41,00	46,00	5,00	LIVELLO GHIAIOSO A PEZZATURA VARIABILE
46,00	54,00	8,00	ARGILLA GIALLA CONSOLIDATA
54,00	90,00	36,00	ARGILLA BLU

Table 46. Stratigraphy of the borehole (water well 198617 ISPRA) carried out next to the seismic station (refer to Figure 72 for the location).

GEOPHYSICAL SURVEY

SURVEY TYPE	N.	Acquisition length	Sampling rate [Hz]	NOTES	INSTRUMENT USED
Microtremor H/V ⁷	4	20' each	512	All measurements on natural soil	Tromino® - MoHo srl
Active/passive 1D array ⁸	1	Active: MASW Passive: ReMi (7' recording)	512	16 geophones, 3 m inter-receiver distance	Seismograph: SoilSpy – MoHo srl Geophones: OYO - Geospace 4.5 Hz (vertical)

Table 47. List of the H/V and active/passive surface-wave arrays acquired at the site.

⁷ The average amplitude spectra in velocity and their standard deviation are computed for each measurement point by splitting the recorded signal into 30 second non-overlapping windows. On average, 32 to 40 signal windows are retained to compute the average H/V curve and its standard deviation. Each window is detrended, tapered with a Bartlett window, zero-padded and FF-transformed. The Fourier spectra are smoothed according to triangular windows with width equal to 10% of the central frequency, in order to keep only the significant peaks.

⁸ The vertical-component Rayleigh-wave phase-velocity dispersion curves obtained by averaging several active and passive surveys are illustrated. Only the windows showing the lowest phase velocities (with the exclusion of the alias) are retained, for their being closer to the fundamental mode dispersion curve. The phase-velocity spectra are obtained by slant-stacking the seismograms and by applying a FFT.



Figure 93. Location of the active/passive surface-wave arrays and of the H/V recordings.

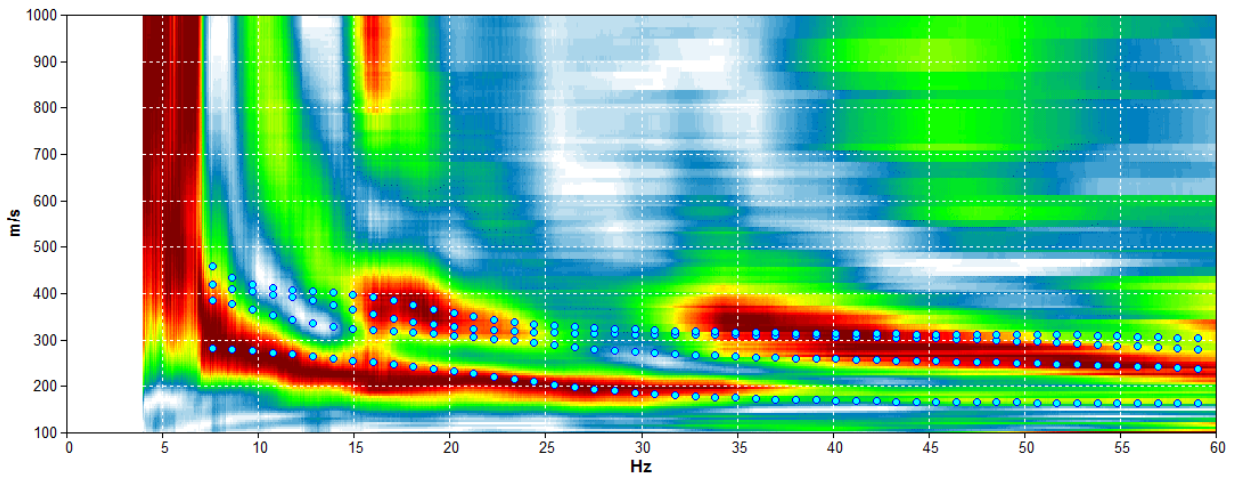


Figure 94. Average dispersion curve from the MASW and ReMi surveys. Synthetic dispersion curve for the model of Table 35 (light blue circles).

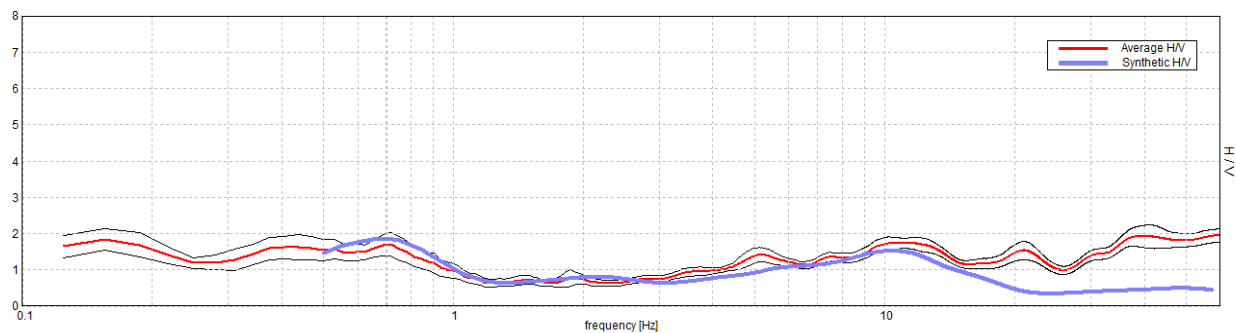


Figure 95. Experimental H/V curve acquired at site T04 (average in red, standard deviation in black). Synthetic H/V curve for the model of Table 48 (blue).

Depth at the bottom of the layer [m]	Thickness [m]	Vs [m/s]	Poisson ratio	Seismostratigraphic model obtained from:
3.00	3.00	160	0.49	0 – 22 m
9.00	6.00	270	0.48	H/V+ Dispersion curve
39.00	30.00	310	0.46	
139.00	100.00	400	0.45	22 m – inf.
inf.	inf.	630	0.45	H/V only

Table 48. Seismostratigraphic model proposed for the site.

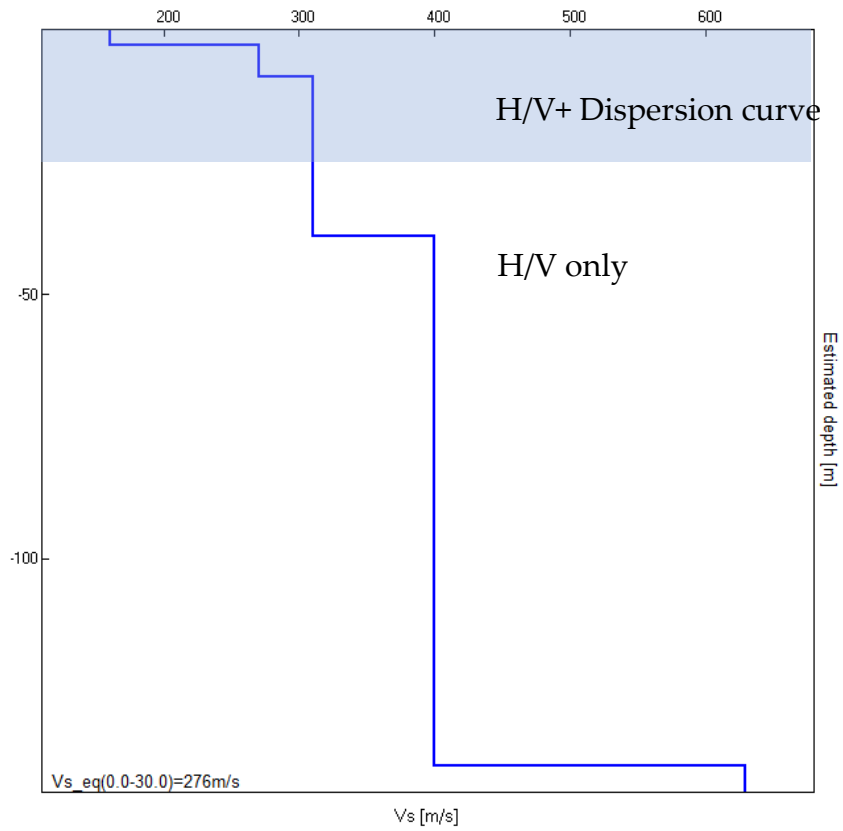


Figure 96. V_s model proposed for the site.

$$V_{s_{eq}}[0 - 30] m = 280 m/s *$$

Class C site (NTC, 2018)

* Characteristic uncertainty is 20%

ADDITIONAL MATERIAL

In this section we present the characteristic H/V curve of the site (Figure 77) together with the single spectral components used to compute it, in order for the reader to understand the stratigraphic or artefactual nature of the H/V peaks (SESAME, 2004; Castellaro, 2016). The SESAME (2004) criteria for the main H/V peak are listed in Table 36.

In Figure 78 we present a selection of H/V curves acquired in the proximity of the seismic station to show the spatial variability of this function.

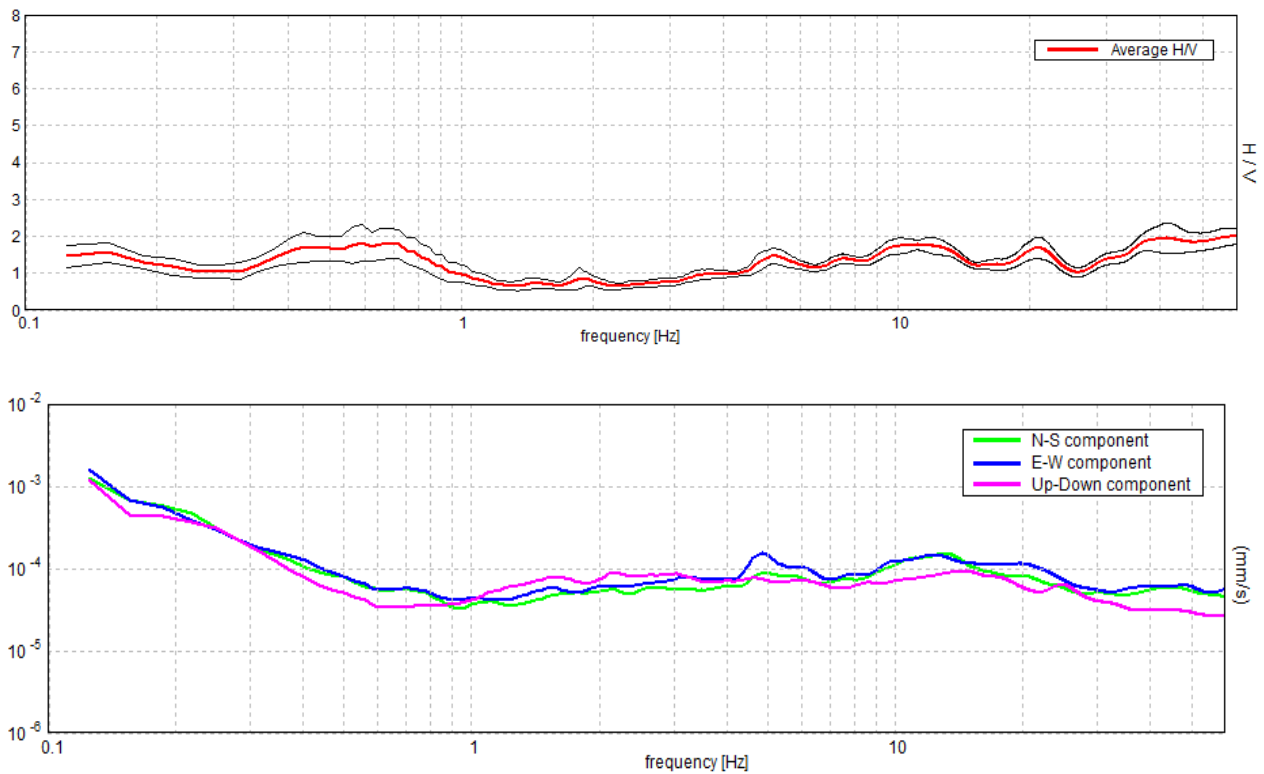


Figure 97. Top: characteristic H/V curve (average in red, standard deviation in black). Bottom: spectra of the single components of motion (NS, EW, Z) used to derive the H/V curve.

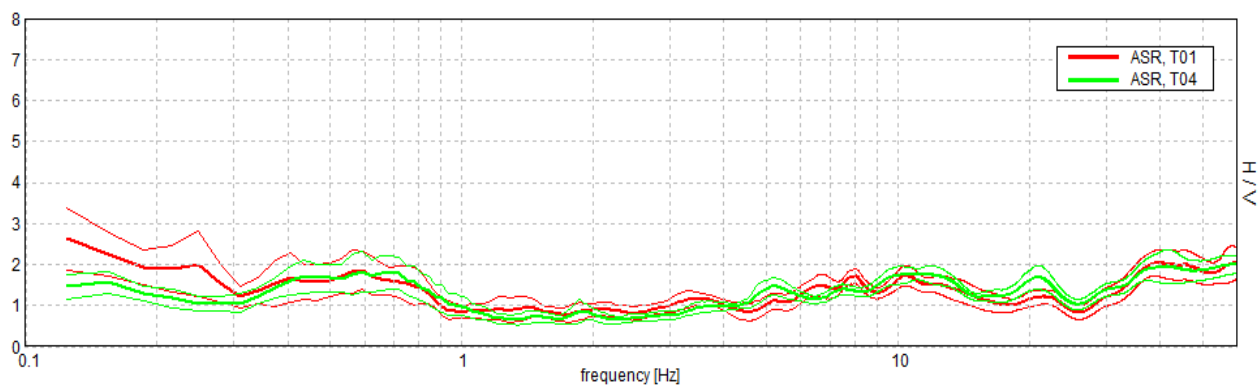


Figure 98. Comparison of the H/V curves acquired in the proximity of the seismic station (refer to Figure 73 for the location).

Max. H/V at 0.63 ± 0.09 Hz (in the range 0.3 - 5.0 Hz).

Criteria for a reliable H/V curve

[All 3 should be fulfilled]

$f_0 > 10 / L_w$	$0.63 > 0.33$	OK	
$n_c(f_0) > 200$	$300.0 > 200$	OK	
$\ast_A(f) < 2$ for $0.5f_0 < f < 2f_0$ if $f_0 > 0.5\text{Hz}$ $\ast_A(f) < 3$ for $0.5f_0 < f < 2f_0$ if $f_0 < 0.5\text{Hz}$	Exceeded 0 out of 31 times	OK	

Criteria for a clear H/V peak

[At least 5 out of 6 should be fulfilled]

Exists f^- in $[f_0/4, f_0] \mid A_{H/V}(f^-) < A_0 / 2$	0.313 Hz	OK	
Exists f^+ in $[f_0, 4f_0] \mid A_{H/V}(f^+) < A_0 / 2$	1.031 Hz	OK	
$A_0 > 2$	$2.09 > 2$	OK	
$f_{\text{peak}}[A_{H/V}(f) \pm \ast_A(f)] = f_0 \pm 5\%$	$ 0.14142 < 0.05$		NO
$\ast_f < \ast(f_0)$	$0.08839 < 0.09375$	OK	
$\ast_A(f_0) < \ast(f_0)$	$0.4276 < 2.0$	OK	

L_w	window length
n_w	number of windows used in the analysis
$n_c = L_w n_w f_0$	number of significant cycles
f	current frequency
f_0	H/V peak frequency
\ast_f	standard deviation of H/V peak frequency
$\ast(f_0)$	threshold value for the stability condition $\ast_f < \ast(f_0)$

A_0	H/V peak amplitude at frequency f_0
$A_{H/V}(f)$	H/V curve amplitude at frequency f
f^-	frequency between $f_0/4$ and f_0 for which $A_{H/V}(f^-) < A_0/2$
f^+	frequency between f_0 and $4f_0$ for which $A_{H/V}(f^+) < A_0/2$
$\sigma_A(f)$	standard deviation of $A_{H/V}(f)$, $\sigma_A(f)$ is the factor by which the mean $A_{H/V}(f)$ curve should be multiplied or divided
$\sigma_{\log H/V}(f)$	standard deviation of $\log A_{H/V}(f)$ curve
$\sigma(f_0)$	threshold value for the stability condition $\sigma_A(f) < \sigma(f_0)$

Threshold values for σ_r and $\sigma_A(f_0)$					
Freq. range [Hz]	< 0.2	0.2 – 0.5	0.5 – 1.0	1.0 – 2.0	> 2.0
$\sigma(f_0)$ [Hz]	$0.25 f_0$	$0.2 f_0$	$0.15 f_0$	$0.10 f_0$	$0.05 f_0$
$\sigma(f_0)$ for $\sigma_A(f_0)$	3.0	2.5	2.0	1.78	1.58
$\log \sigma(f_0)$ for $\sigma_{\log H/V}(f_0)$	0.48	0.40	0.30	0.25	0.20

Table 49. SESAME (2004) criteria applied to the main resonance peak identified in the characteristic H/V curve.

GALLERY



Figure 99. The ASR seismic station housing; fiberglass box on concrete basement.



Figure 100. Location of the active/passive surface waves array A01.

REFERENCES

Castellaro S., 2016. The complementarity of H/V and dispersion curves, *Geophysics*, 81, T323–T338

ISPRA, Carta Geologica d'Italia alla scala 1:50 000, Foglio 421 "Ascoli Satriano"

Norme Tecniche sulle Costruzioni, 2018. Decreto Ministeriale 17/01/2018, Ministry of Infrastructures and Transportations, G.U. S.O. n.8 on 20/2/2018

SESAME, 2004. Guidelines for the implementation of the H/V spectral ratio technique on ambient vibrations. Measurements, processing and interpretation, WP12 European commission - Research general directorate project no. EVG1-CT-2000-0026 SESAME, report D23.12, 62 pp.

Giulia Alessandrini¹, Giovanni Lattanzi¹, Stephen Slivicki², Giulia Sgattoni¹, Silvia Castellaro¹

¹ *Università di Bologna, Dipartimento di Fisica e Astronomia, Viale Carlo B. Pichat 8, 40127 Bologna (Italy)*

² *University of Wisconsin-River Falls (USA)*

Site characterization of the seismic station

IV.CAFE

Geophysical survey performed on
24th October 2019 (8.30 am – 10 am)

Partly funded by Contratto di Consulenza Commissionata per lo "Studio sismotettonico delle dighe Marana Capacciotti e San Pietro sul Torrente Osento e delle opere accessorie" – Consorzio di Bonifica per la Capitanata (2019)

IV.CAFE-CARIFE

CODE	NAME	Lat. [°] WGS-84	Lon. [°] WGS-84	Elevation [m]
CAFE	Carife	41.02800	15.23660	1070
Address	Strada Statale 91, Provincia di Avellino, Campania			

Table 50. Code, name and WGS-84 coordinates of the seismic station.

SEISMIC STATION

SENSOR	EPISENSOR-FBA-ES-T
DIGITIZER	unknown
HOUSING	Pillar inside the meteorologic station, free field

Table 51. Instrumental chain installed at the seismic station.

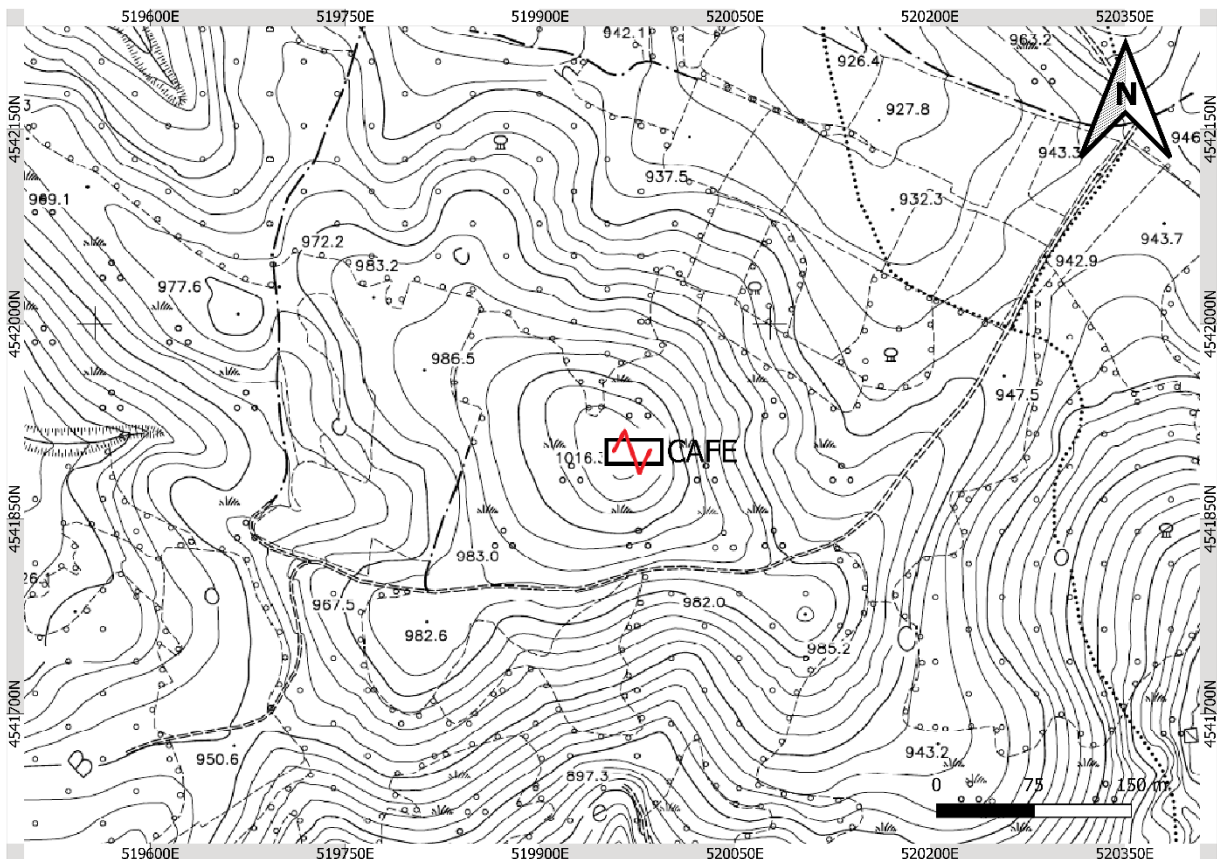


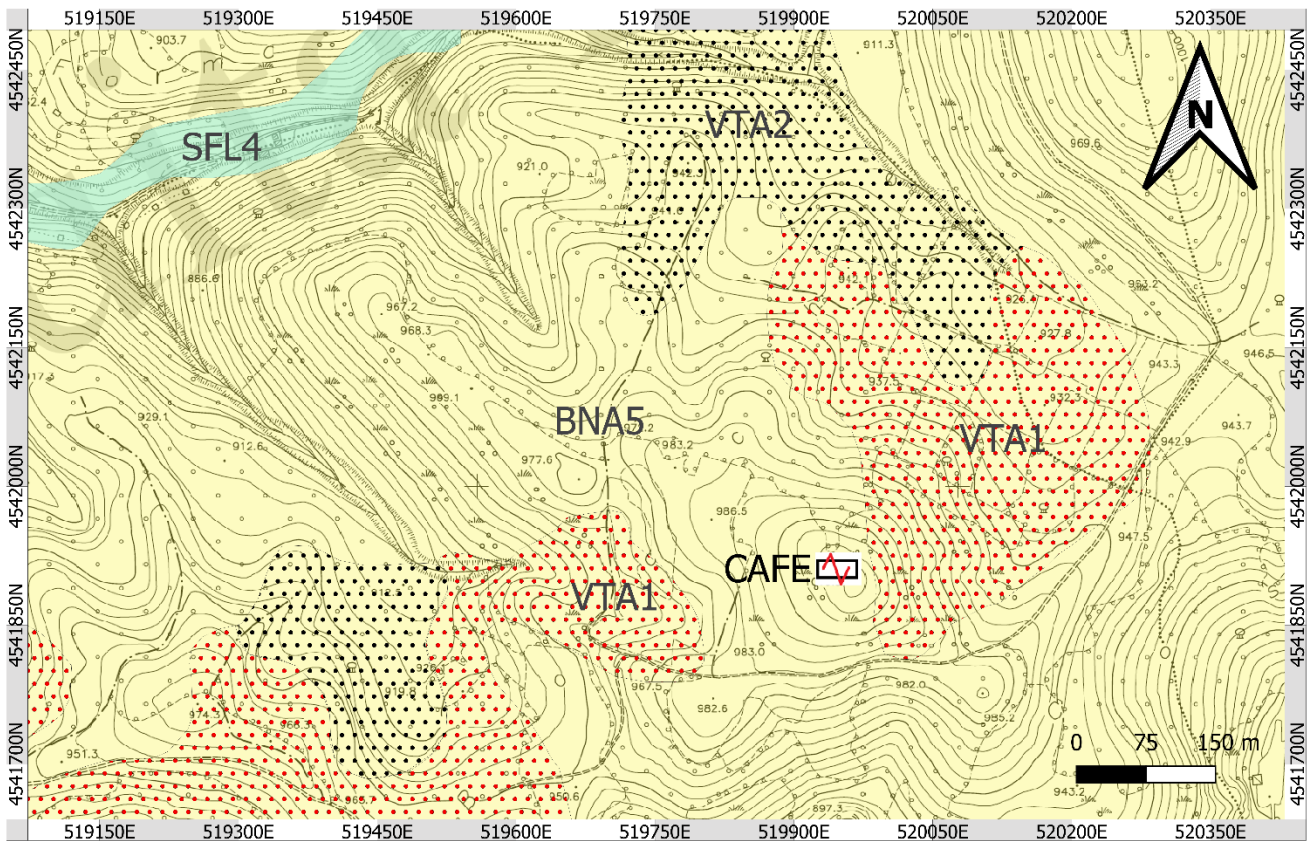
Figure 101. Location of the CAFE seismic station at Carife (source CTR 1:5 000, the image could be rescaled, refer to the bar scale).

GEOLOGICAL AND TOPOGRAPHIC INFORMATION

According to the CARG map (Figure 102), the seismic station is located on the *Formazione della Baronia - Membro conglomeratico di Trevico, (BNA₅)* characterized by very thick conglomerate layers with rare sandstone layers. The thickness of the *Membro conglomeratico di Trevico (BNA₅)* is about 400 m. The stratigraphy of a deep borehole (Trevico 01) located 900 m north of the seismic station is reported in Table 53 to give an idea of the thickness of the main units.

TYPE	NOTES	SCALE
CTR	Foglio 433151	1:5 000
CARG, carta geologica	Foglio 433, Ariano Irpino	1:50 000

Table 52. Geological and geotechnical cartography available for the site.



LEGEND:

 ACCELEROMETRIC STATION

 BNA5-FORMAZIONE DELLA BARONIA (Membro conglomeratico di Trevico)
(Pliocene inf.)

Figure 102. Geological map of the area surrounding the seismic station CAFE (modified from CARG 1:50 000; the image could be rescaled, refer to the bar scale).

FROM DEPTH (m)	TO DEPTH (m)	THICKNESS (m)	LITHOLOGICAL DESCRIPTION
0.00	395.00	395.00	CIOTTOLI E SABBIE TALORA CEMENTATE CON QUALCHE LIVELLO DI ARGILLA
395.00	534.00	139.00	SABBIE TALORA CEMENTATE CON QUALCHE INTERCALAZIONE DI ARGILLA
534.00	577.00	43.00	ARGILLE MARNOSO - SILTOSE
577.00	711.00	134.00	SABBIE E SABBIE ARGILLOSE CON INTERCALAZIONI DI ARGILLA
711.00	1373.00	662.00	ARGILLE MARNOSE TALORA SILTOSO - ARENACEE
1373.00	1475.00	102.00	SABBIE E CIOTTOLI TALORA CEMENTATI CON INTERCALAZIONI DI ARGILLE MARNOSE SCAGLIETTATE
1475.00	1562.00	87.00	ARGILLE MARNOSE SCAGLIETTATE CON SOTTILI INTERCALAZIONI DI SABBIE E CIOTTOLI TALORA CEMENTATI

Table 53. Stratigraphy of the borehole TREVICO 01 located 900 m north of the seismic station carried out by Agip.

GEOPHYSICAL SURVEY

We propose an average V_s model for the site, based on the joint fit of all the acquired surface-wave dispersion and H/V curves (Table 35). Since the H/V curves are more sensitive to local geological features compared to the array dispersion curves, the average V_s model might not faithfully reproduce the H/V features at high frequency.

The theoretical H/V curve overlapped to the experimental H/V curve could be computed on a slightly different model (see footnotes, if present).

SURVEY TYPE	N.	Acquisition length	Sampling rate [Hz]	NOTES	INSTRUMENT USED
Microtremor H/V ⁹	7	20' each	512	All measurements on natural soil	Tromino® - MoHo srl
Active/passive 1D array ¹⁰	2	Active: MASW Passive: ReMi (7' recording)	512	16 geophones: 3 m inter-receiver distance (A01); 4 m inter-receiver distance (A02)	Seismograph: SoilSpy – MoHo srl Geophones: OYO - Geospace 4.5 Hz (vertical)

Table 54. List of the H/V and active/passive surface-wave arrays acquired at the site.

The stratigraphic resonance of the site is at approximately 1.1 Hz. The SESAME (2004) criteria for the main H/V peak are given in Table 42.

⁹ The average amplitude spectra in velocity and their standard deviation are computed for each measurement point by splitting the recorded signal into 30 second non-overlapping windows. On average, 32 to 40 signal windows are retained to compute the average H/V curve and its standard deviation. Each window is detrended, tapered with a Bartlett window, zero-padded and FF-transformed. The Fourier spectra are smoothed according to triangular windows with width equal to 10% of the central frequency, in order to keep only the significant peaks.

¹⁰ The vertical-component Rayleigh-wave phase-velocity dispersion curves obtained by averaging several active and passive surveys are illustrated. Only the windows showing the lowest phase velocities (with the exclusion of the alias) are retained, for their being closer to the fundamental mode dispersion curve. The phase-velocity spectra are obtained by slant-stacking the seismograms and by applying a FFT.



Figure 103. Location of the active/passive surface-wave arrays and of the H/V recordings.

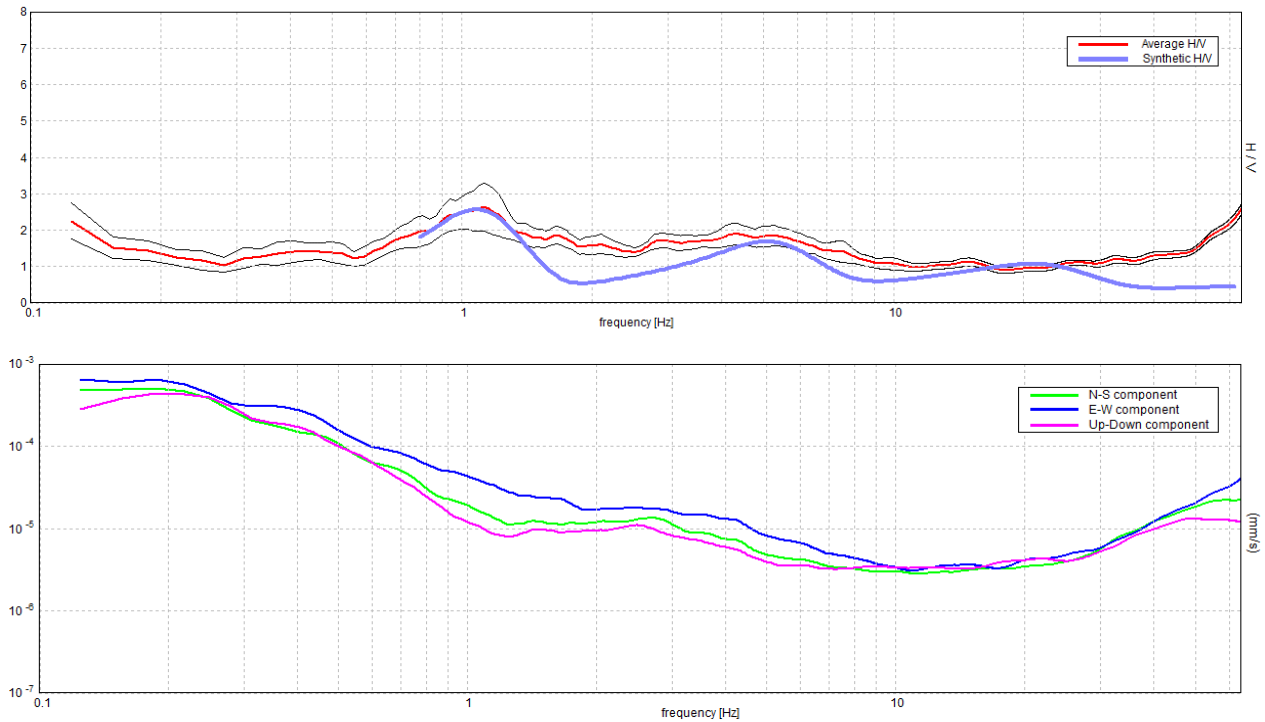


Figure 104. Experimental H/V curve acquired at site T05 (average in red, standard deviation in black) and synthetic H/V curve for the model of Table 35 (blue, top). Single component spectra (bottom).

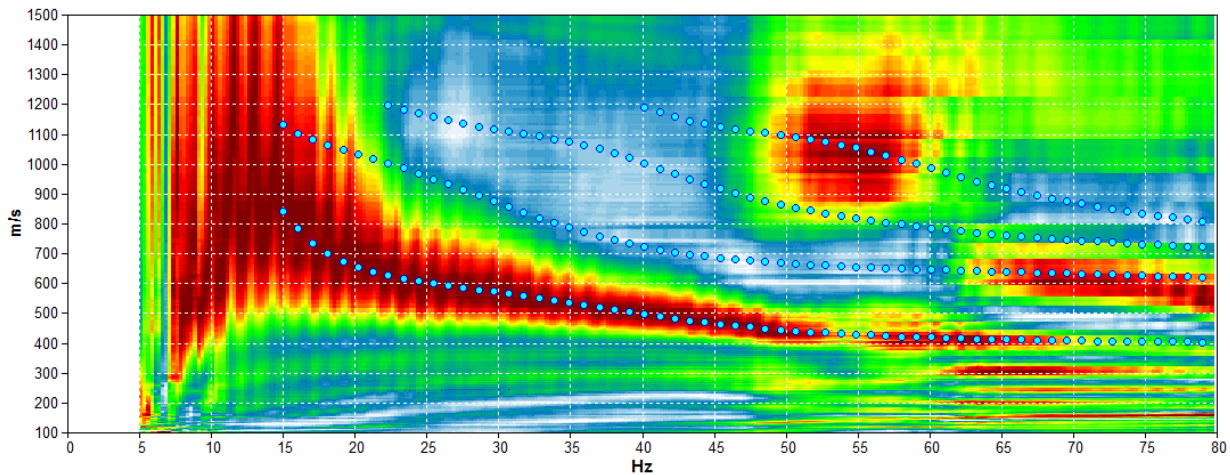


Figure 105. Dispersion curves from the MASW and ReMi surveys at site A01 (Figure 73). Synthetic dispersion curves for the model of Table 35 (light blue circles).

Depth at the bottom of the layer [m]	Thickness [m]	Vs [m/s]	Poisson ratio	Seismostratigraphic model obtained from:
4.50	4.50	420	0.42	0 – 23 m
32.50	28.00	680	0.42	H/V + Dispersion curve
252.50	220.00	1100	0.42	23 m – inf.
inf.	inf.	2050	0.40	H/V only

Table 55. Seismostratigraphic model proposed for the site.

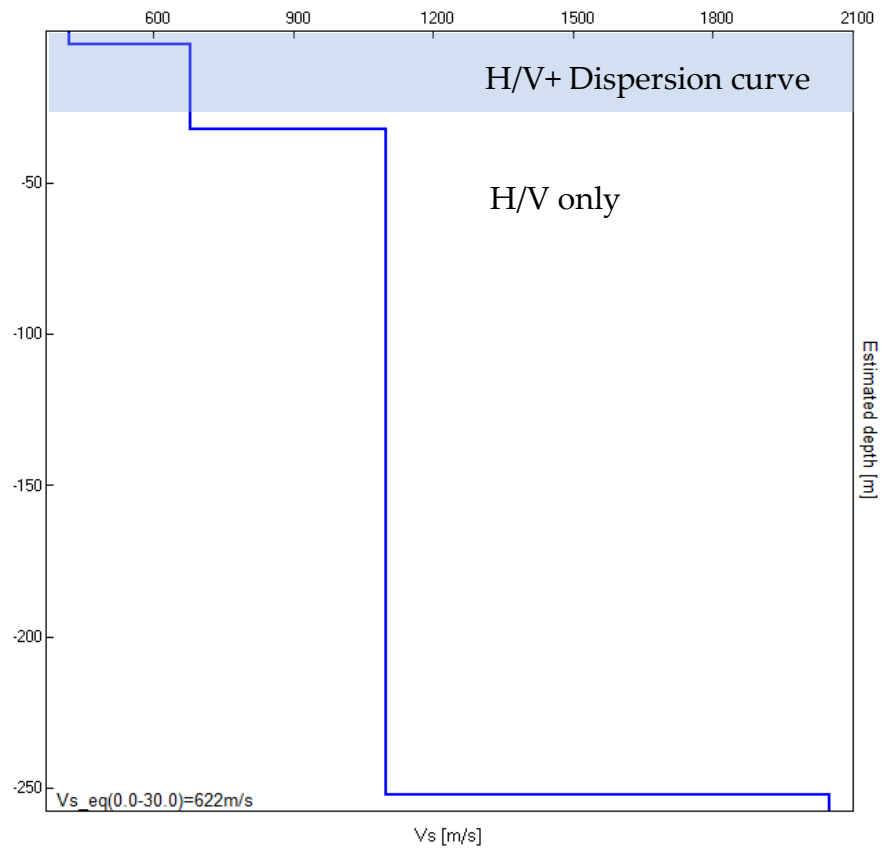


Figure 106. Vs model proposed for the site.

$V_{seq}[0 - 30] m = 620 m/s *$

Class B site (NTC, 2018)

* Characteristic uncertainty is 20%

ADDITIONAL MATERIAL

In Figure 78 we present a selection of H/V curves acquired in the proximity of the seismic station to show the spatial variability.

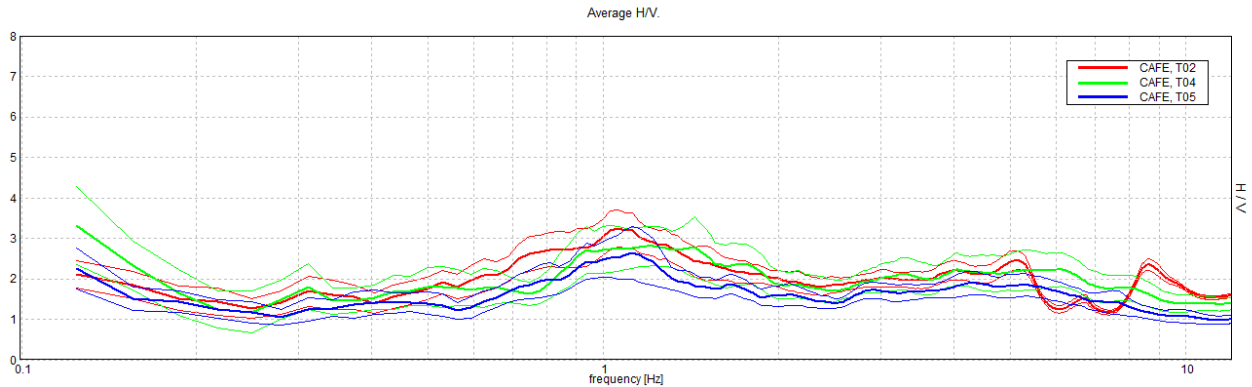


Figure 107. Comparison of the H/V curves acquired around the seismic station (refer to Figure 73 for the location).

[According to the SESAME, 2004 guidelines]

Max. H/V at 1.13 ± 0.19 Hz (in the range 0.2 - 25.0 Hz).

Criteria for a reliable H/V curve

[All 3 should be fulfilled]

$f_0 > 10 / L_w$	$1.13 > 0.50$	OK	
$n_c(f_0) > 200$	$810.0 > 200$	OK	
$\ast_A(f) < 2$ for $0.5f_0 < f < 2f_0$ if $f_0 > 0.5\text{Hz}$ $\ast_A(f) < 3$ for $0.5f_0 < f < 2f_0$ if $f_0 < 0.5\text{Hz}$	Exceeded 0 out of 55 times	OK	

Criteria for a clear H/V peak

[At least 5 out of 6 should be fulfilled]

Exists f^- in $[f_0/4, f_0] \mid A_{H/V}(f^-) < A_0 / 2$	0.594 Hz	OK	
Exists f^+ in $[f_0, 4f_0] \mid A_{H/V}(f^+) < A_0 / 2$			NO
$A_0 > 2$	$2.59 > 2$	OK	
$f_{\text{peak}}[A_{H/V}(f) \pm \ast_A(f)] = f_0 \pm 5\%$	$ 0.17155 < 0.05$		NO
$\ast_f < \ast(f_0)$	$0.19299 < 0.1125$		NO
$\ast_A(f_0) < \ast(f_0)$	$0.4426 < 1.78$	OK	

L_w	window length
n_w	number of windows used in the analysis
$n_c = L_w n_w f_0$	number of significant cycles
f	current frequency
f_0	H/V peak frequency
σ_f	standard deviation of H/V peak frequency
$\sigma(f_0)$	threshold value for the stability condition $\sigma_f < \sigma(f_0)$
A_0	H/V peak amplitude at frequency f_0
$A_{H/V}(f)$	H/V curve amplitude at frequency f
f^-	frequency between $f_0/4$ and f_0 for which $A_{H/V}(f^-) < A_0/2$
f^+	frequency between f_0 and $4f_0$ for which $A_{H/V}(f^+) < A_0/2$
$\sigma_A(f)$	standard deviation of $A_{H/V}(f)$, $\sigma_A(f)$ is the factor by which the mean $A_{H/V}(f)$ curve should be multiplied or divided
$\sigma_{\log H/V}(f)$	standard deviation of $\log A_{H/V}(f)$ curve
$\sigma(f_0)$	threshold value for the stability condition $\sigma_A(f) < \sigma(f_0)$

Threshold values for σ_f and $\sigma_A(f_0)$					
Freq. range [Hz]	< 0.2	0.2 – 0.5	0.5 – 1.0	1.0 – 2.0	> 2.0
$\sigma(f_0)$ [Hz]	$0.25 f_0$	$0.2 f_0$	$0.15 f_0$	$0.10 f_0$	$0.05 f_0$
$\sigma(f_0)$ for $\sigma_A(f_0)$	3.0	2.5	2.0	1.78	1.58
$\log \sigma(f_0)$ for $\sigma_{\log H/V}(f_0)$	0.48	0.40	0.30	0.25	0.20

Table 56. SESAME (2004) criteria applied to the main resonance peak identified in the characteristic H/V curve.

GALLERY



Figure 108. Location of the H/V recording at site T02 near the CAFE seismic station.



Figure 109. Location of the H/V recording AT SITE t01 near the CAFE seismic station.

REFERENCES

- Castellaro S., 2016. The complementarity of H/V and dispersion curves, *Geophysics*, 81, T323–T338
- ISPRA, Carta Geologica d'Italia alla scala 1:50 000, Foglio 433 "Ariano Irpino"
- Norme Tecniche sulle Costruzioni, 2018. Decreto Ministeriale 17/01/2018, Ministry of Infrastructures and Transportations, G.U. S.O. n.8 on 20/2/2018
- SESAME (2004), Guidelines for the implementation of the H/V spectral ratio technique on ambient vibrations. Measurements, processing and interpretation, WP12 European commission - Research general directorate project no. EVG1-CT-2000-0026 SESAME, report D23.12, 62 pp.

Giulia Alessandrini¹, Giovanni Lattanzi¹, Stephen Slivicki², Giulia Sgattoni¹, Silvia Castellaro¹

¹ *Università di Bologna, Dipartimento di Fisica e Astronomia, Viale Carlo B. Pichat 8, 40127 Bologna (Italy)*

² *University of Wisconsin-River Falls (USA)*

Site characterization of the seismic station

IT.CER

Geophysical survey performed on
22nd October 2019 (9 am – 10 am)

Partly funded by Contratto di Consulenza Commissionata per lo “Studio sismotettonico delle dighe Marana Capacciotti e San Pietro sul Torrente Osento e delle opere accessorie” – Consorzio di Bonifica per la Capitanata (2019)

IT.CER-CERIGNOLA

CODE	NAME	Lat. [°] WGS-84	Lon. [°] WGS-84	Elevation [m]
CER	Cerignola	41.25950	15.91020	176
Address	Via dei Salici, 6-8, 71042 Cerignola FG, Italy			

Table 57. Code, name and WGS-84 coordinates of the seismic station.

SEISMIC STATION

SENSOR	Episensor FBA ES-T [Kinometrics]
DIGITIZER	unknown
HOUSING	Fiberglass box on concrete basement. The station is located inside the primary school of Cerignola.

Table 58. Instrumental chain installed at the seismic station.

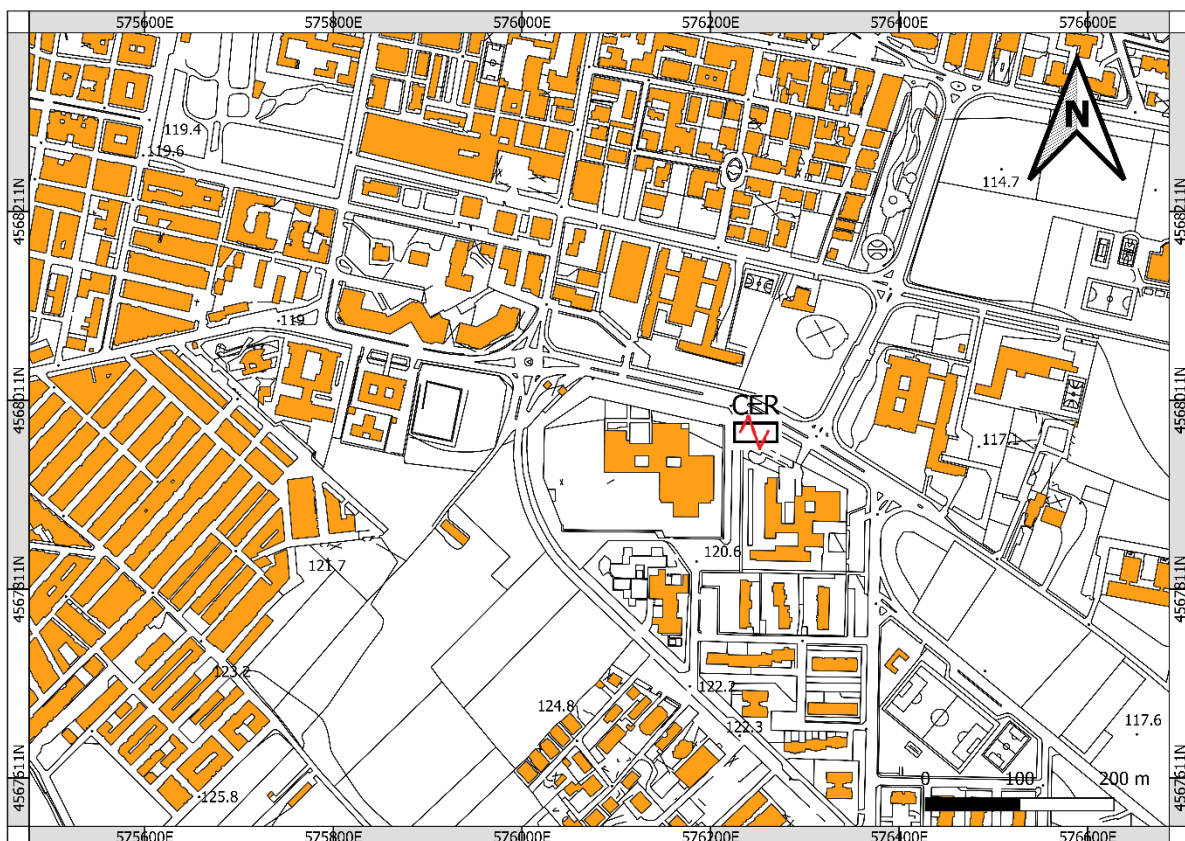


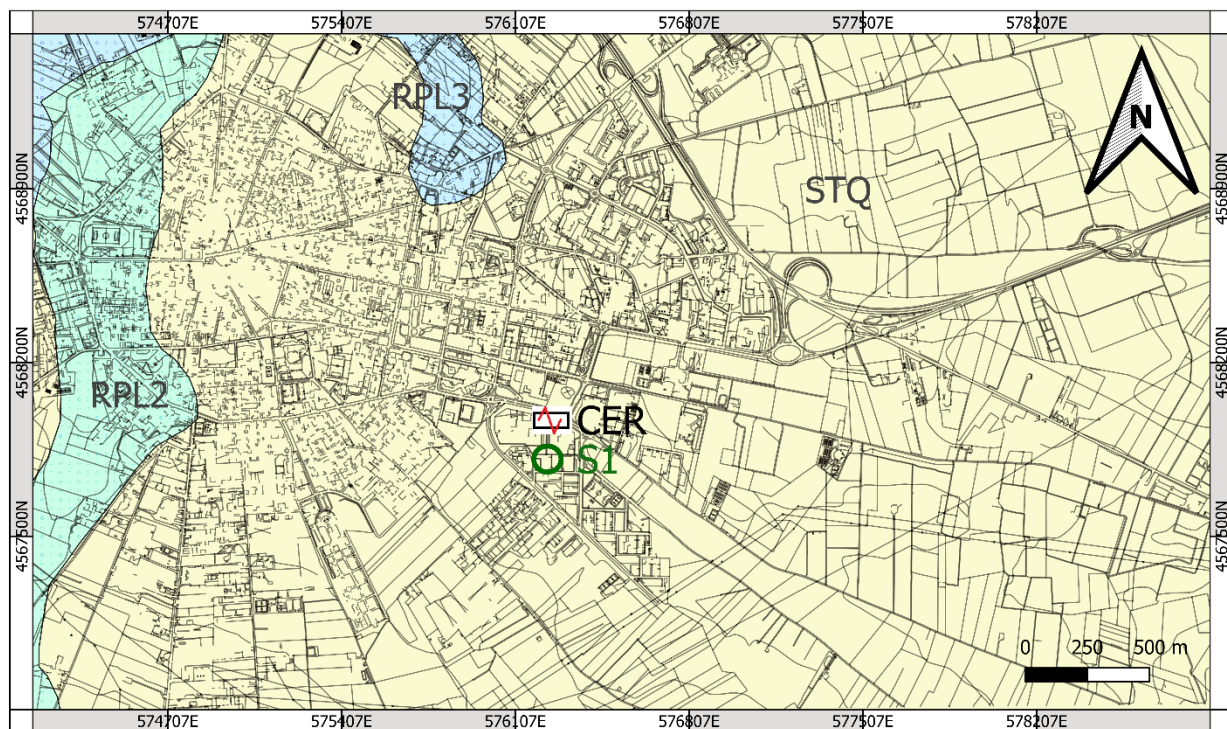
Figure 110. Location of the CER seismic station at Cerignola (source CTR 1:5 000, the image could be rescaled, refer to the bar scale).

GEOLOGICAL AND TOPOGRAPHIC INFORMATION

According to the CARG map (Figure 111), the seismic station is located on the *Sintema di Cerignola - Sabbie di Torre Quarto* (STQ) characterized by weakly cemented sand with fine to medium particle size. According to the CARG map and to the borehole S1 carried out next to the station, the thickness of the unit *Sabbie di Torre Quarto* (STQ) is about 50 m.

TYPE	NOTES	SCALE
CTR	Foglio 422112	1:5 000
ISPRA, carta geologica	Foglio 175, Cerignola	1:100 000
CARG, carta geologica	Foglio 422 Cerignola	1:50 000

Table 59. Geological and geotechnical cartography available for the site.



LEGEND:

▲ ACCELEROMETRIC STATION

○ S1-WATER WELL

■ STQ- SINTEMA DI CERIGNOLA (Sabbie di Torre Quarto)
(Pleistocene medio)

Figure 111. Geological map of the area surrounding the seismic station CER (modified from CARG 1:50 000; the image could be rescaled, refer to the bar scale). The lithological description of the borehole S1 is given in Table 60.

FROM DEPTH (m)	TO DEPTH (m)	THICKNESS (m)	LITHOLOGICAL DESCRIPTION
0.00	2.00	2.00	TERRENO VEGETALE
2.00	25.20	23.20	SABBIE FINI CON RARI CIOTTOLI ARROTONDATI DI PICCOLE DIMENSIONI IN PREVALENZA DI ORIGINE QUARZOSA GIALLE ED A LUOGHI ROSSASTRE. FACIES PLEISTOCENICA
25.20	50.00	24.80	SABBIE GRIGIASTRE CON INCLUSIONI DI LENTI CIOTTOLOSE ARENACEE O DI LIMI GRIGIASTRI
50.00	60.00	10.00	ARGILLE SUBAPPENNINICHE

Table 60. Stratigraphy of the borehole (water well 199390 ISPRA) carried out next to the seismic station (refer to Figure 111 for the location).

GEOFYSICAL SURVEY

We propose an average V_s model for the site, based on the joint fit of all the acquired surface-wave dispersion and H/V curves (Table 62). Since the H/V curves are more sensitive to local geological features compared to the array dispersion curves, the average V_s model might not faithfully reproduce the H/V features at high frequency.

The theoretical H/V curve overlapped to the experimental H/V curve could be computed on a slightly different model (see footnotes, if present).

SURVEY TYPE	N.	Acquisition length	Sampling rate [Hz]	NOTES	INSTRUMENT USED
Microtremor H/V ¹¹	4	20' each	512	All measurements on natural soil	Tromino® - MoHo srl
Active/passive 1D array ¹²	1	Active: MASW Passive: ReMi (7' recording)	512	16 geophones, 3 m inter-receiver distance	Seismograph: SoilSpy – MoHo srl Geophones: OYO - Geospace 4.5 Hz (vertical)

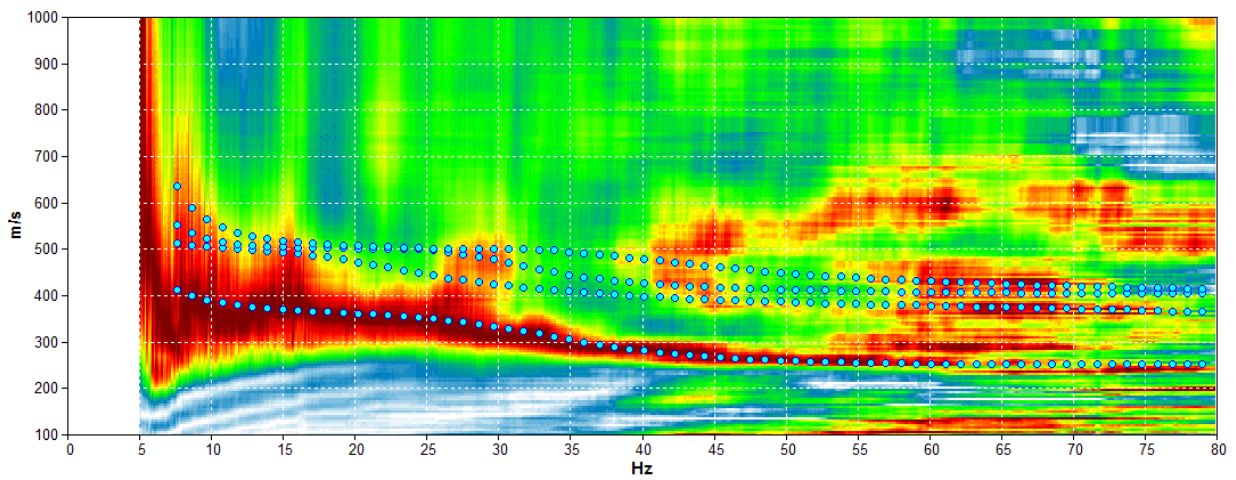
¹¹ The average amplitude spectra in velocity and their standard deviation are computed for each measurement point by splitting the recorded signal into 30 second non-overlapping windows. On average, 32 to 40 signal windows are retained to compute the average H/V curve and its standard deviation. Each window is detrended, tapered with a Bartlett window, zero-padded and FF-transformed. The Fourier spectra are smoothed according to triangular windows with width equal to 10% of the central frequency, in order to keep only the significant peaks.

¹² The vertical-component Rayleigh-wave phase-velocity dispersion curves obtained by averaging several active and passive surveys are illustrated. Only the windows showing the lowest phase velocities (with the exclusion of the alias) are retained, for their being closer to the fundamental mode dispersion curve. The phase-velocity spectra are obtained by slant-stacking the seismograms and by applying a FFT.

Table 61. List of the H/V and active/passive surface-wave arrays acquired at the site.



Figure 112. Location of the active/passive surface-wave arrays and of the H/V recordings.



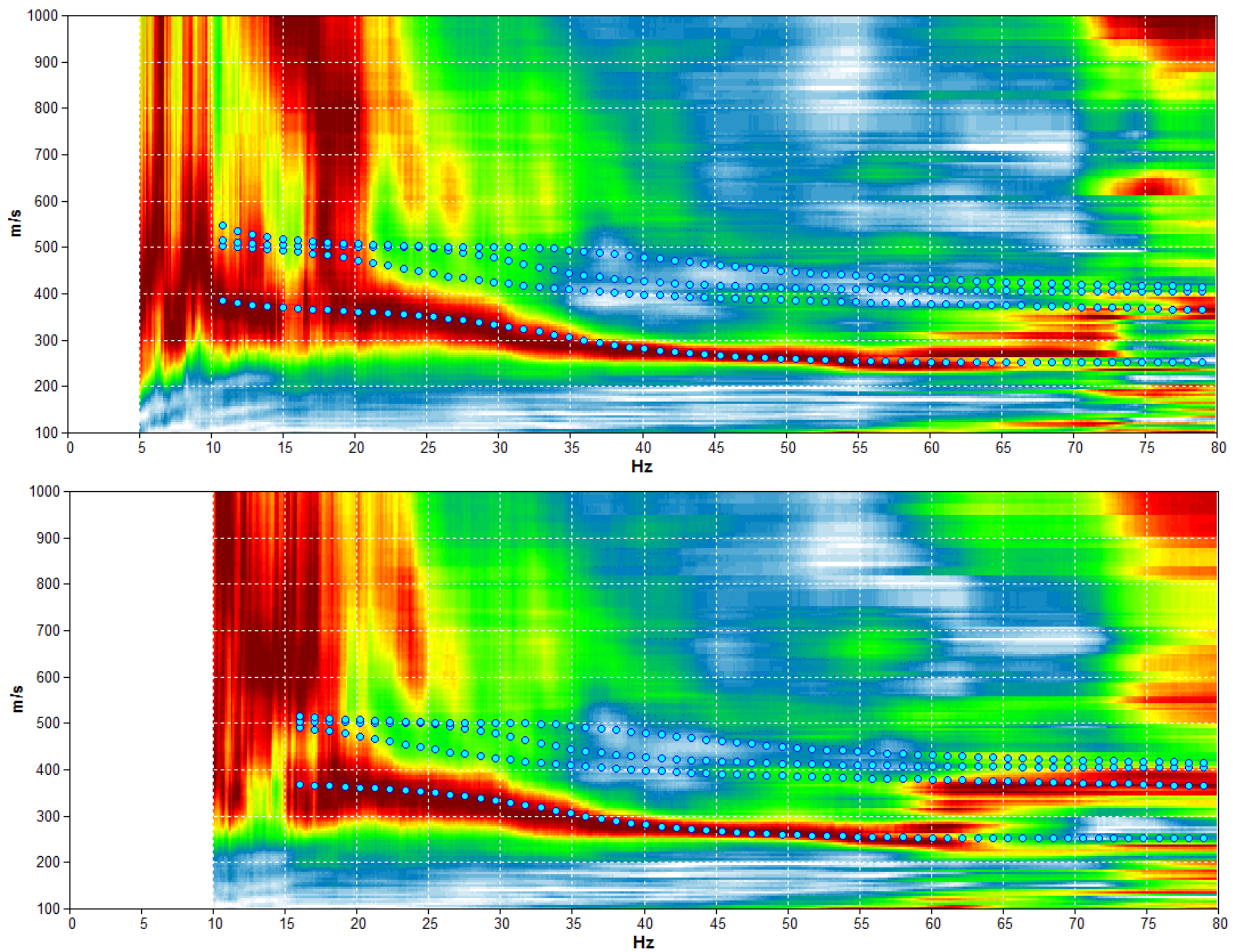


Figure 113. A selection of dispersion curves from the MASW and ReMi surveys at site A01 (Figure 73). Synthetic dispersion curves for the model of Table 62 (light blue circles).

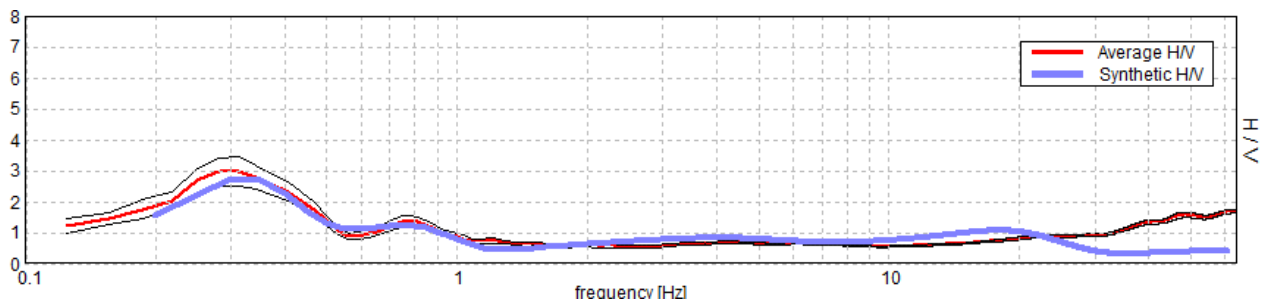


Figure 114. Experimental H/V curve acquired at site T01 (average in red, standard deviation in black). Synthetic H/V curve for the model of Table 62 (blue).

Depth at the bottom of the layer [m]	Thickness [m]	Vs [m/s]	Poisson ratio	Seismostratigraphic model obtained from:
1.00	1.00	290	0.48	0 – 25 m H/V + Dispersion curve
3.00	2.00	240	0.48	
23.00	20.00	400	0.48	

173.00	150.00	500	0.47	25 m – inf.
673.00	500.00	850	0.46	H/V only
inf.	inf.	1300	0.45	

Table 62. Seismostratigraphic model proposed for the site.

$V_{seq}[0 - 30] m = 400 m/s *$ Class B site (NTC, 2018)

* *Characteristic uncertainty is 20%*

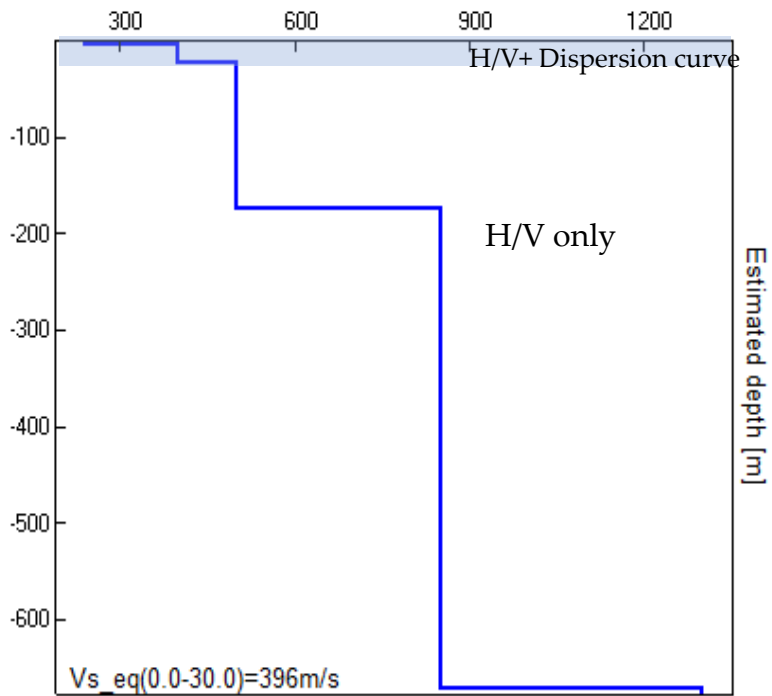
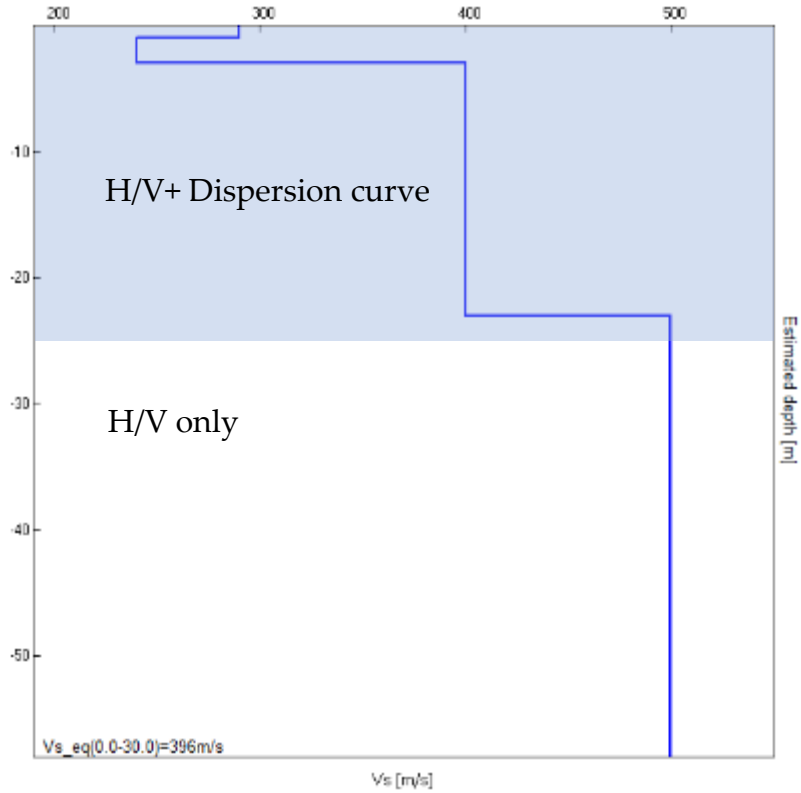


Figure 115. *Top*: Vs model proposed for the site from 0 to 60 m depth. *Bottom*: Vs model proposed for the site from 0 to ≈ 700 m depth to fit the 0.3 Hz H/V peak.

ADDITIONAL MATERIAL

In this section we present the characteristic H/V curve of the site (Figure 116) together with the single spectral components used to compute it, in order for the reader to understand the stratigraphic or artefactual nature of the H/V peaks (SESAME, 2004; Castellaro, 2016). The SESAME (2004) criteria for the main H/V peak are listed in Table 63.

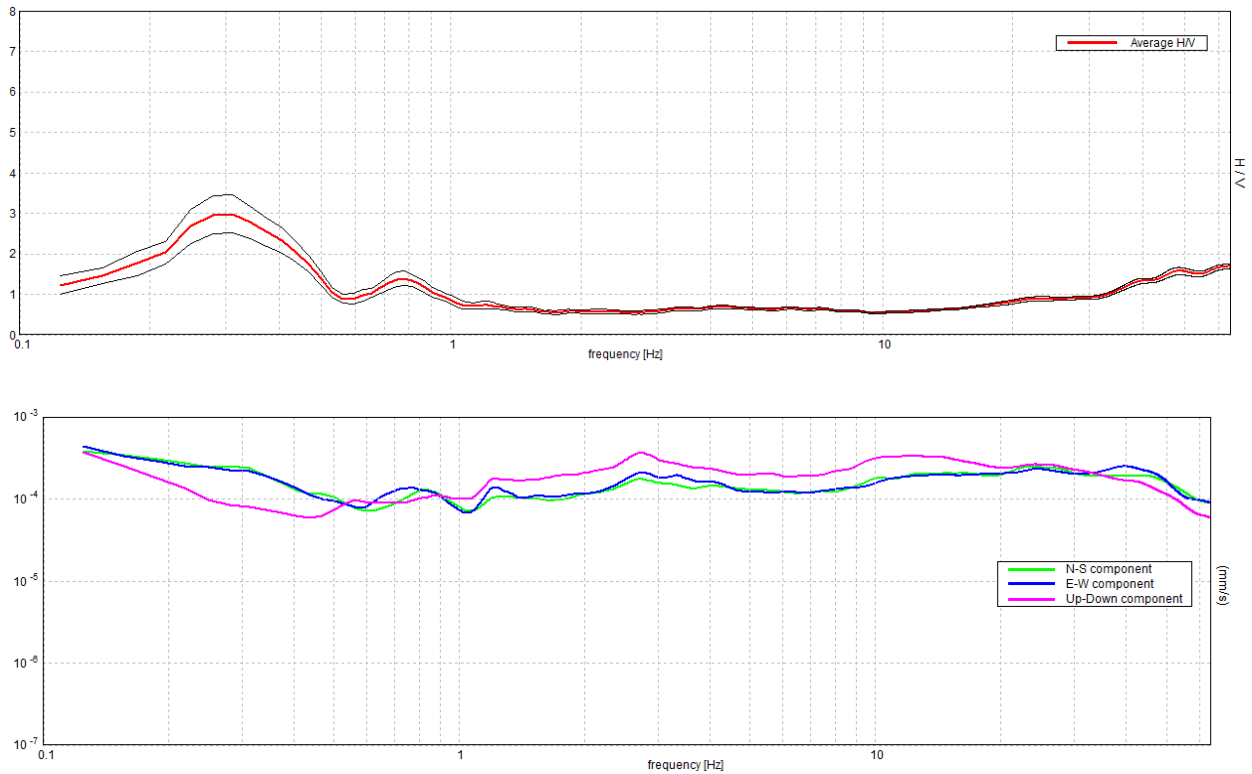


Figure 116. Top: characteristic H/V curve (average in red, standard deviation in black). Bottom: spectra of the single components of motion (NS, EW, Z) used to derive the H/V curve.

In Figure 78 we present a selection of H/V curves acquired in the proximity of the seismic station to show the spatial variability.

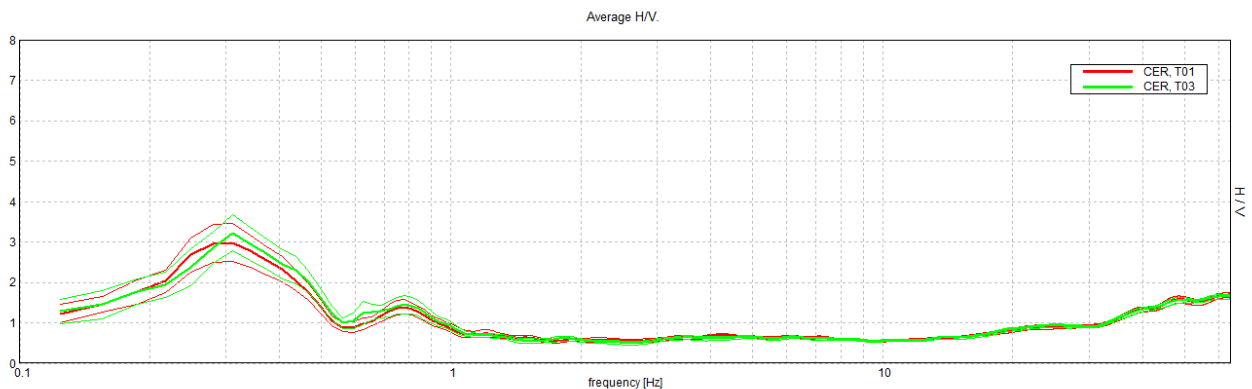


Figure 117. Comparison of the H/V curves acquired around the seismic station (refer to Figure 73 for the location).

[According to the SESAME, 2004 guidelines]

Max. H/V at 0.31 ± 0.02 Hz (in the range 0.0 - 30.0 Hz).

Criteria for a reliable H/V curve			
[All 3 should be fulfilled]			
$f_0 > 10 / L_w$	$0.31 > 0.50$		NO
$n_c(f_0) > 200$	$375.0 > 200$	OK	
$\sigma_A(f) < 2$ for $0.5f_0 < f < 2f_0$ if $f_0 > 0.5\text{Hz}$ $\sigma_A(f) < 3$ for $0.5f_0 < f < 2f_0$ if $f_0 < 0.5\text{Hz}$	Exceeded 0 out of 16 times	OK	
Criteria for a clear H/V peak			
[At least 5 out of 6 should be fulfilled]			
Exists f^- in $[f_0/4, f_0] \mid A_{H/V}(f^-) < A_0 / 2$	0.188 Hz	OK	
Exists f^+ in $[f_0, 4f_0] \mid A_{H/V}(f^+) < A_0 / 2$	0.5 Hz	OK	
$A_0 > 2$	$3.21 > 2$	OK	
$f_{\text{peak}}[A_{H/V}(f) \pm \sigma_A(f)] = f_0 \pm 5\%$	$ 0.07638 < 0.05$		NO
$\sigma_f < \sigma(f_0)$	$0.02387 < 0.0625$	OK	
$\sigma_A(f_0) < \sigma(f_0)$	$0.4531 < 2.5$	OK	

L_w	window length
n_w	number of windows used in the analysis
$n_c = L_w n_w f_0$	number of significant cycles
f	current frequency
f_0	H/V peak frequency
σ_f	standard deviation of H/V peak frequency
$\sigma(f_0)$	threshold value for the stability condition $\sigma_f < \sigma(f_0)$
A_0	H/V peak amplitude at frequency f_0
$A_{H/V}(f)$	H/V curve amplitude at frequency f
f^-	frequency between $f_0/4$ and f_0 for which $A_{H/V}(f^-) < A_0/2$
f^+	frequency between f_0 and $4f_0$ for which $A_{H/V}(f^+) < A_0/2$
$\sigma_A(f)$	standard deviation of $A_{H/V}(f)$, $\sigma_A(f)$ is the factor by which the mean $A_{H/V}(f)$ curve should be multiplied or divided
$\sigma_{\log H/V}(f)$	standard deviation of $\log A_{H/V}(f)$ curve

$\sigma(f_0)$	threshold value for the stability condition $\sigma_A(f) < \sigma(f_0)$
---------------	---

Threshold values for σ_f and $\sigma_A(f_0)$					
Freq. range [Hz]	< 0.2	0.2 – 0.5	0.5 – 1.0	1.0 – 2.0	> 2.0
$\sigma(f_0)$ [Hz]	$0.25 f_0$	$0.2 f_0$	$0.15 f_0$	$0.10 f_0$	$0.05 f_0$
$\sigma(f_0)$ for $\sigma_A(f_0)$	3.0	2.5	2.0	1.78	1.58
$\log \sigma(f_0)$ for $\sigma_{\log H/V}(f_0)$	0.48	0.40	0.30	0.25	0.20

Table 63. SESAME (2004) criteria applied to the main resonance peak identified in the characteristic H/V curve.

GALLERY



Figure 118. H/V recordings near the CER seismic station.



Figure 119. Location of the active/passive surface waves array A01 and H/V recordings.

REFERENCES

- Castellaro S., 2016. The complementarity of H/V and dispersion curves, *Geophysics*, 81, T323–T338
- ISPRA, Carta Geologica d'Italia alla scala 1:50.000, Foglio 422 (Cerignola)
- Norme Tecniche sulle Costruzioni, 2018. Decreto Ministeriale 17/01/2018, Ministry of Infrastructures and Transportations, G.U. S.O. n.8 on 20/2/2018
- SESAME (2004), Guidelines for the implementation of the H/V spectral ratio technique on ambient vibrations. Measurements, processing and interpretation, WP12 European commission - Research general directorate project no. EVG1-CT-2000-0026 SESAME, report D23.12, 62 pp.

Giulia Alessandrini¹, Giovanni Lattanzi¹, Stephen Slivicki², Giulia Sgattoni¹, Silvia Castellaro¹

¹ *Università di Bologna, Dipartimento di Fisica e Astronomia, Viale Carlo B. Pichat 8, 40127 Bologna (Italy)*

² *University of Wisconsin-River Falls (USA)*

Site characterization of the seismic station

IV.MRB1

Geophysical survey performed on
24th October 2019 (11.30 am – 12.30 pm)

Partly funded by Contratto di Consulenza Commissionata per lo “Studio sismotettonico delle dighe Marana Capacciotti e San Pietro sul Torrente Osento e delle opere accessorie” – Consorzio di Bonifica per la Capitanata (2019)

IV.MRB1-MONTE ROCCHETTA

CODE	NAME	Lat. [°] WGS-84	Lon. [°] WGS-84	Elevation [m]
MRB1	Monte Rocchetta	41.12270	14.96815	688
Address	Unnamed Road, 82021 Apice BN, Campania			

Table 64. Code, name and WGS-84 coordinates of the seismic station.

SEISMIC STATION

SENSOR	Episensor FBA ES-T [Kinometrics]
DIGITIZER	unknown
HOUSING	Pillar inside the meteorologic station, free field

Table 65. Instrumental chain installed at the seismic station.

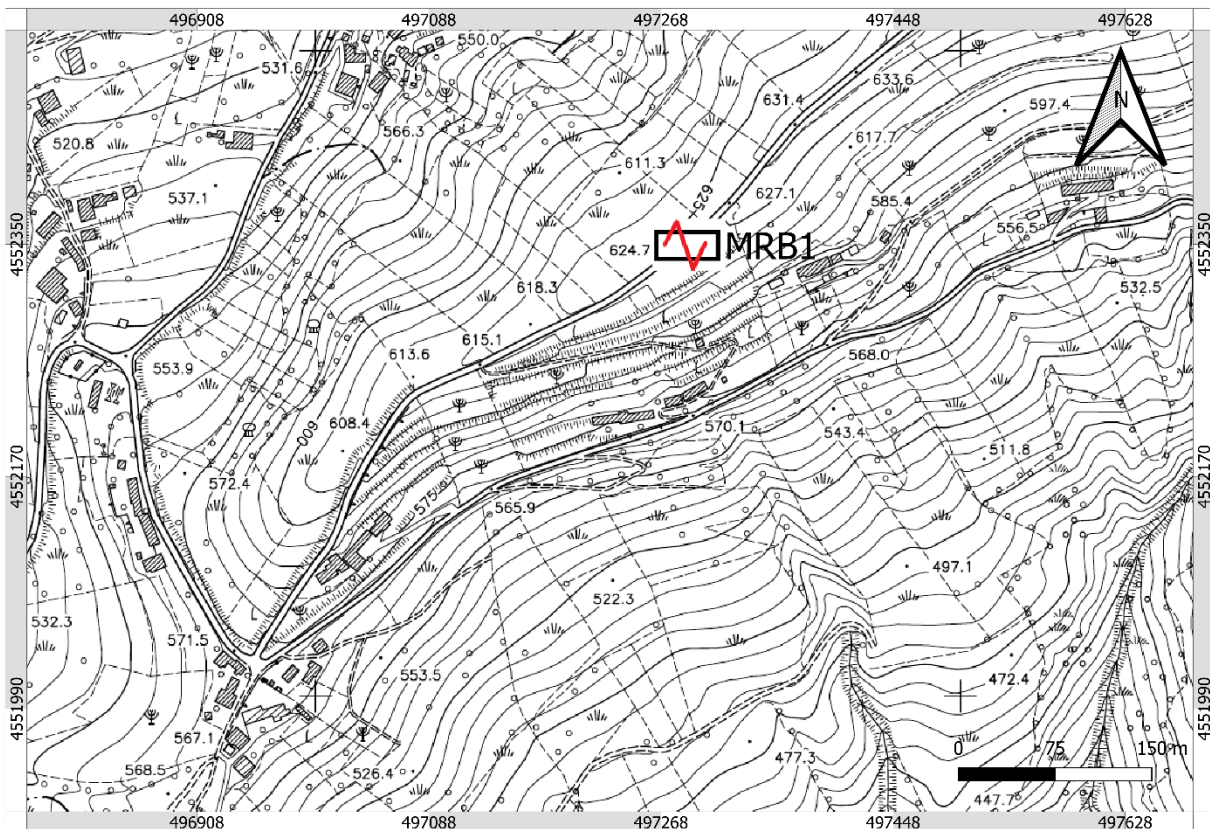


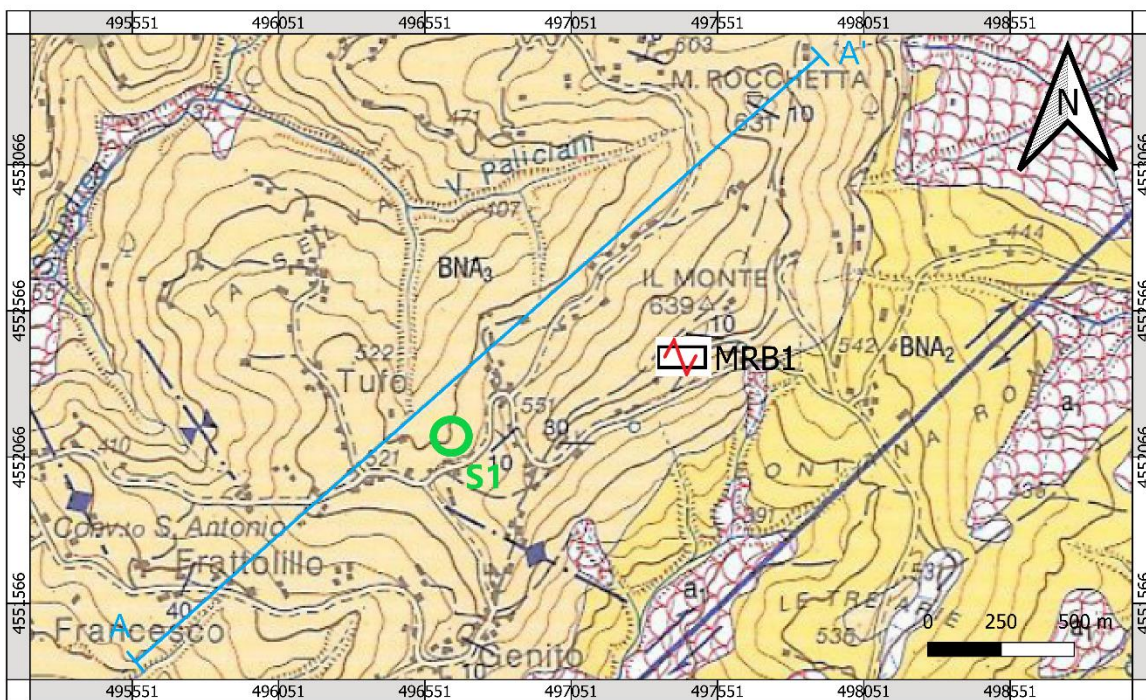
Figure 120. Location of the MRB1 seismic station at Monte Rocchetta (source CTR 1:5 000, the image could be rescaled, refer to the bar scale).

GEOLOGICAL AND TOPOGRAPHIC INFORMATION

According to the CARG map (Figure 121), the seismic station is located on the *Formazione della Baronia – Membro sabbioso di Apollosa (BNA₃)* characterized by medium and thick layers of sand and sandstone. The maximum thickness of this member varies between 100 and 250 m.

TYPE	NOTES	SCALE
CTR	Foglio 432082	1:5 000
CARG, carta geologica	Foglio 432, Benevento	1:50 000

Table 66. Geological and geotechnical cartography available for the site.



LEGEND:

▲ ACCELEROMETRIC STATION

○ WATER WELL

■ BNA₃- FORMAZIONE DELLA BARONIA (membro sabbioso di Apollosa)
(Pliocene inferiore - medio)

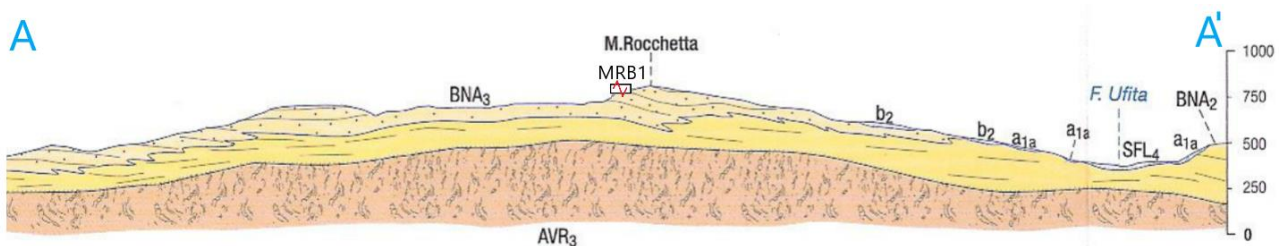


Figure 121. Geological map and cross-section of the area surrounding the seismic station MRB1 (modified from CARG 1:50 000; the image could be rescaled, refer to the bar scale). The stratigraphy of water well S1 is described in Table 53.

FROM DEPTH (m)	TO DEPTH (m)	THICKNESS (m)	LITHOLOGICAL DESCRIPTION
0.00	1.00	1.00	SILTOSO SABBIOSO GIALLASTRO
1.00	6.00	5.00	SABBIA GIALLASTRA MEDIAMENTE ADDENSATA
6.00	41.00	35.00	GHIAIA SILTOSA
41.00	70.00	29.00	ARGILLA GRIGIA

Table 67. Stratigraphy of the water well 170967 ISPRA carried out next to the seismic station (refer to Figure 121

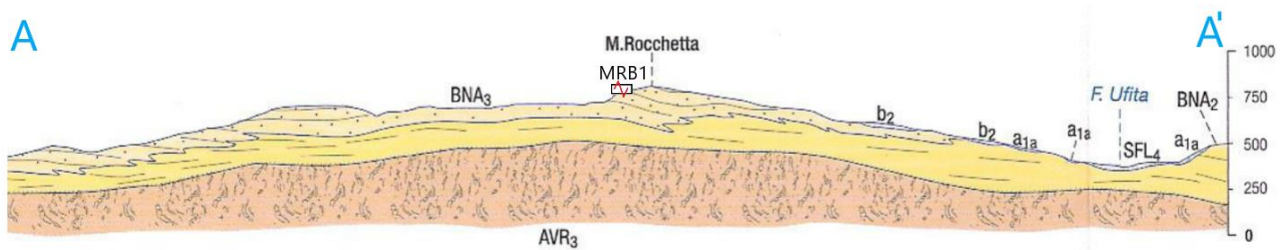


Figure 121 for the location).

GEOPHYSICAL SURVEY

We propose an average Vs model for the site, based on the joint fit of all the acquired surface-wave dispersion and H/V curves (Table 68). Since the H/V curves are more sensitive to local geological features compared to the array dispersion curves, the average Vs model might not faithfully reproduce the H/V features at high frequency.

The theoretical H/V curve overlapped to the experimental H/V curve could be computed on a slightly different model (see footnotes, if present).

SURVEY TYPE	N.	Acquisition length	Sampling rate [Hz]	NOTES	INSTRUMENT USED
Microtremor H/V ¹³	6	20' each	512	All measurements on natural soil	Tromino® - MoHo srl
Active/passive 1D array ¹⁴	1	Active: MASW Passive: ReMi (7' recording)	512	16 geophones, 3 m inter-receiver distance	Seismograph: SoilSpy – MoHo srl Geophones: OYO - Geospace 4.5 Hz (vertical)

Table 68. List of the H/V and active/passive surface-wave arrays acquired at the site.

¹³ The average amplitude spectra in velocity and their standard deviation are computed for each measurement point by splitting the recorded signal into 30 second non-overlapping windows. On average, 32 to 40 signal windows are retained to compute the average H/V curve and its standard deviation. Each window is detrended, tapered with a Bartlett window, zero-padded and FF-transformed. The Fourier spectra are smoothed according to triangular windows with width equal to 10% of the central frequency, in order to keep only the significant peaks.

¹⁴ The vertical-component Rayleigh-wave phase-velocity dispersion curves obtained by averaging several active and passive surveys are illustrated. Only the windows showing the lowest phase velocities (with the exclusion of the alias) are retained, for their being closer to the fundamental mode dispersion curve. The phase-velocity spectra are obtained by slant-stacking the seismograms and by applying a FFT.

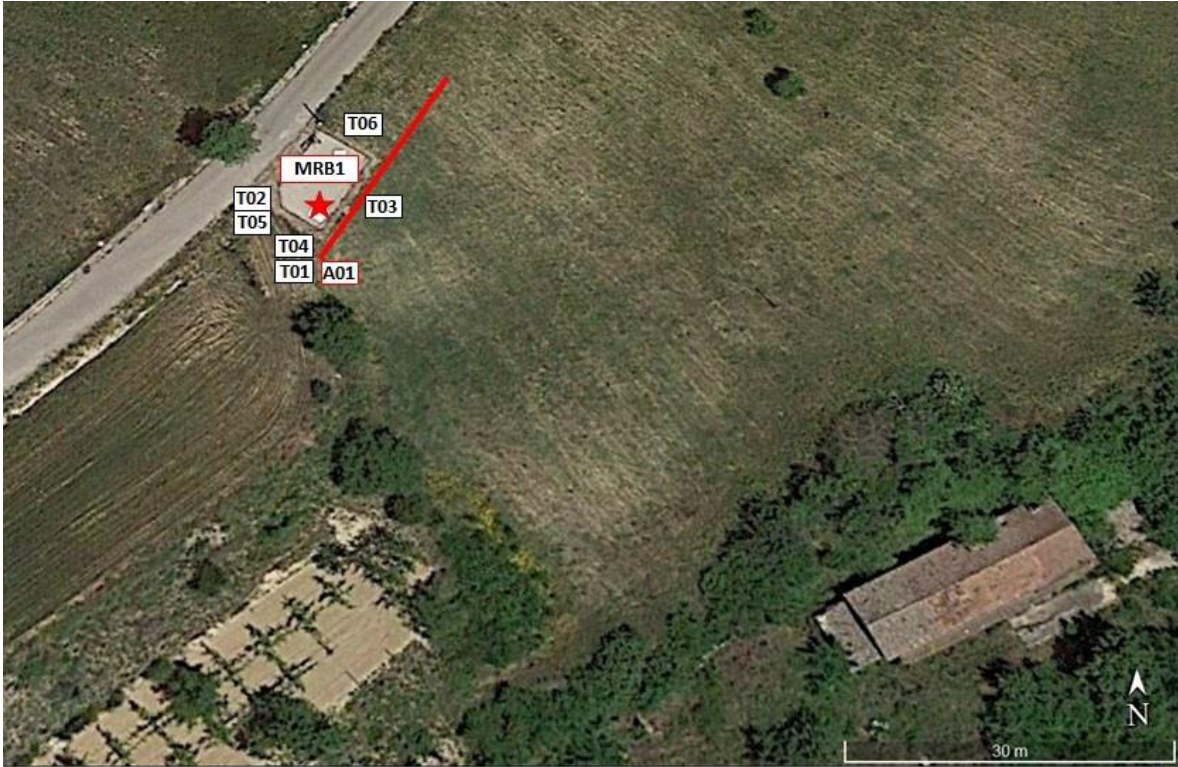


Figure 122. Location of the active/passive surface-wave arrays and of the H/V recordings.

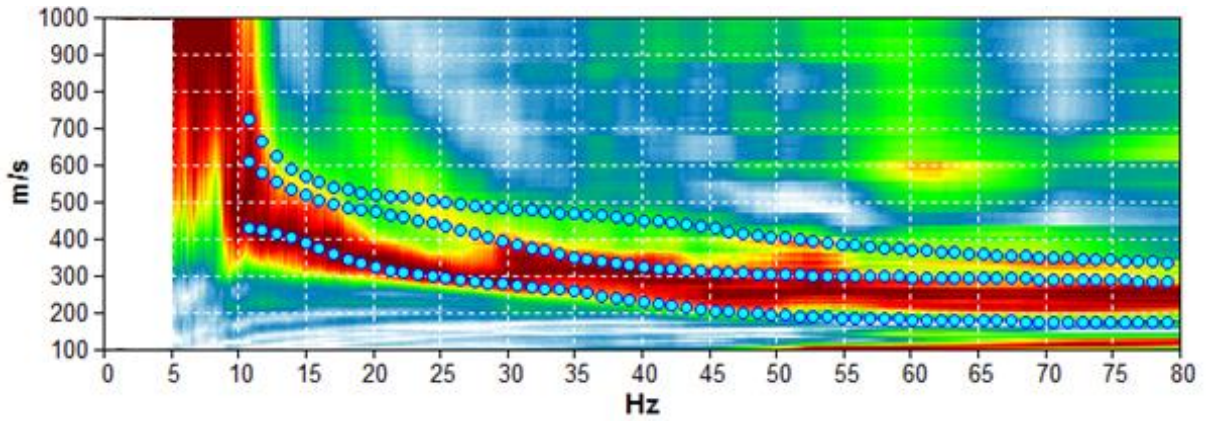


Figure 123. Dispersion curve from the MASW and ReMi surveys at site A01 (Figure 73). Synthetic dispersion curves for the model of Table 69 (light blue circles).

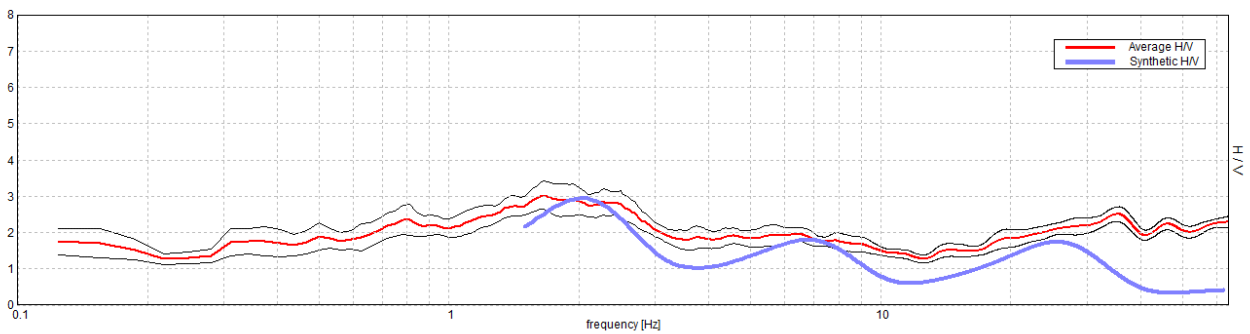


Figure 124. Experimental H/V curve acquired at site T06 (average in red, standard deviation in black). Synthetic H/V curve for the model of Table 69.

Depth at the bottom of the layer [m]	Thickness [m]	Vs [m/s]	Poisson ratio	Seismostratigraphic model obtained from:
2.00	2.00	210	0.47	0 – 22 m
14.00	12.00	370	0.47	H/V + Dispersion curve
54.00	40.00	640	0.46	
99.00	45.00	810	0.45	22 m – inf.
inf.	inf.	1150	0.44	H/V only

Table 69. Seismostratigraphic model proposed for the site.

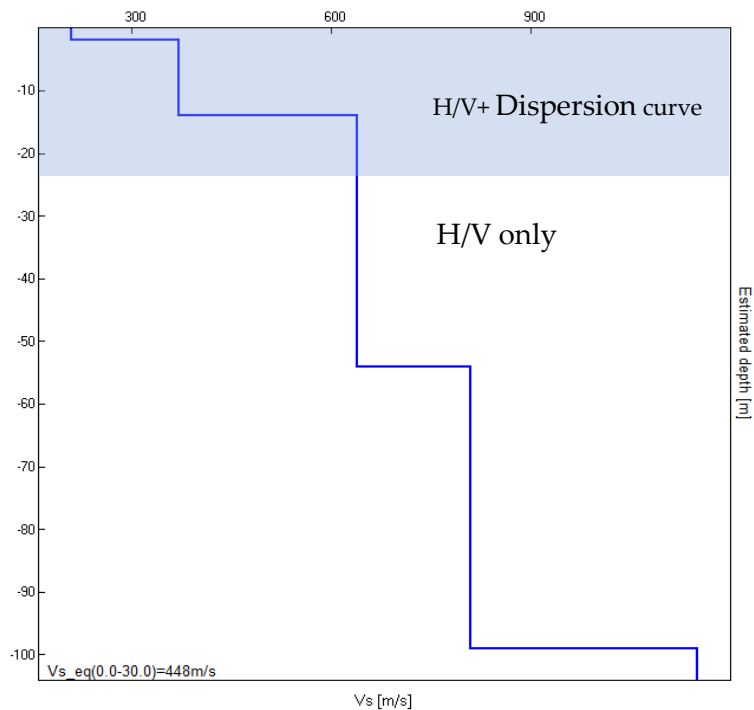


Figure 125. Vs model proposed for the site.

$V_{Seq}[0 - 30] m = 450 m/s^*$

Class B site (NTC, 2018)

* Characteristic uncertainty is 20%

ADDITIONAL MATERIAL

In this section we present the characteristic H/V curve of the site (Figure 116) together with the single spectral components used to compute it, in order for the reader to understand the stratigraphic or artefactual nature of the H/V peaks (SESAME, 2004; Castellaro, 2016). The SESAME (2004) criteria for the main H/V peak are listed in Table 42.

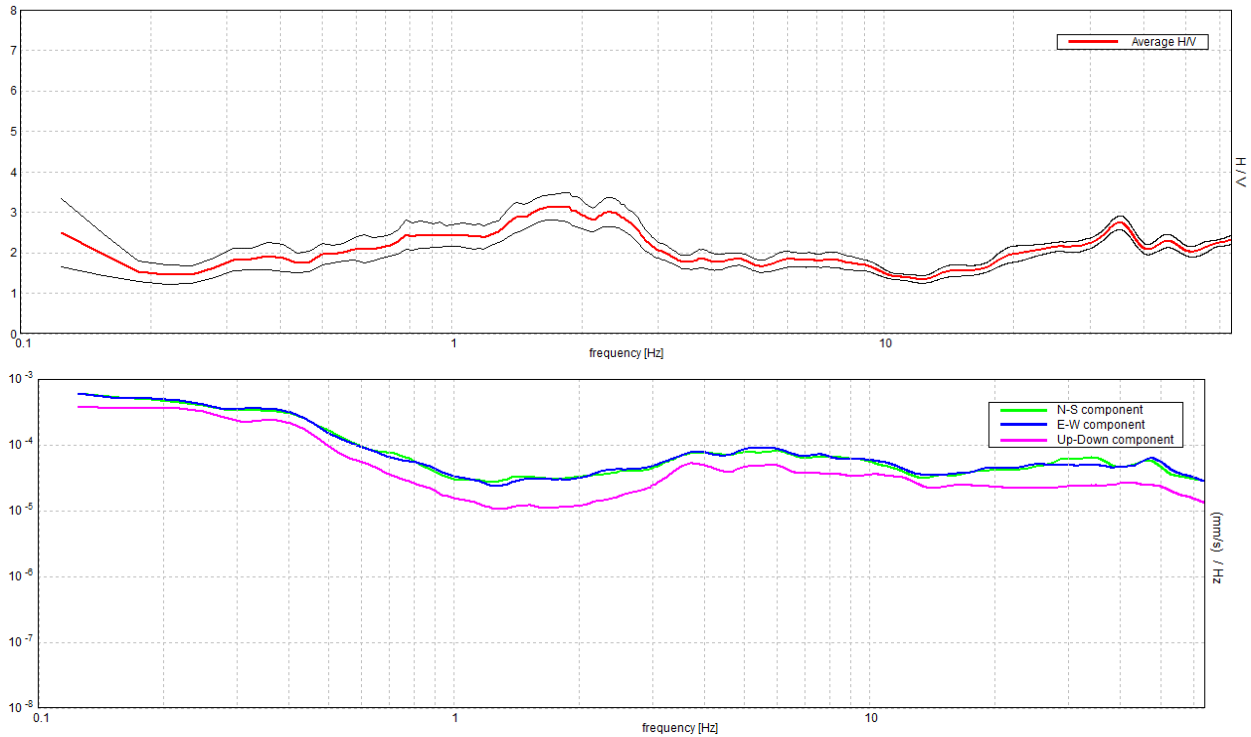


Figure 126. Top: characteristic H/V curve (average in red, standard deviation in black). Bottom: spectra of the single components of motion (NS, EW, Z) used to derive the H/V curve.

In Figure 78 we present all the H/V curves acquired in the proximity of the seismic station to show the spatial variability.

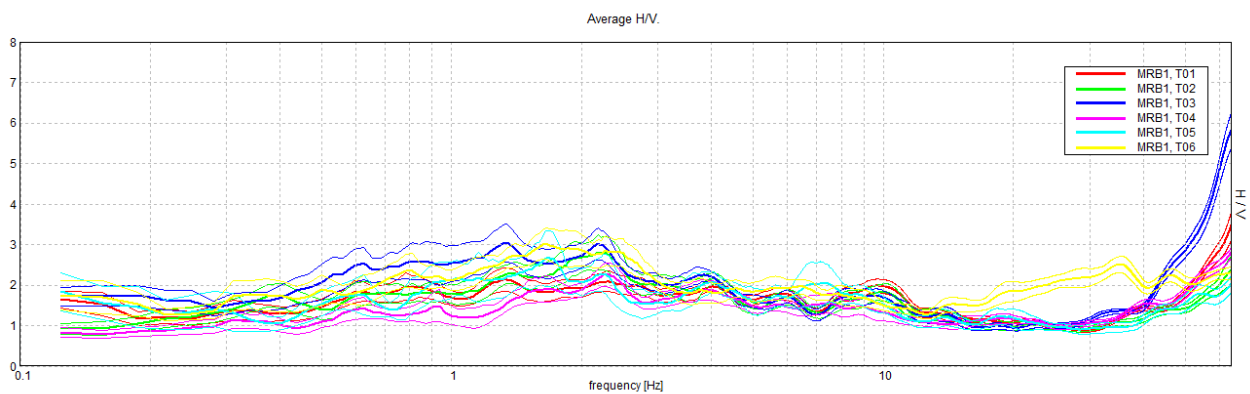


Figure 127. Comparison of the H/V curves acquired around the seismic station (refer to Figure 73 for the location).

[According to the SESAME, 2004 guidelines]

Max. H/V at 1.75 ± 0.17 Hz (in the range 0.0 - 20.0 Hz).

Criteria for a reliable H/V curve

[All 3 should be fulfilled]

$f_0 > 10 / L_w$	$1.75 > 0.50$	OK	
$n_c(f_0) > 200$	$1155.0 > 200$	OK	
$\ast_A(f) < 2$ for $0.5f_0 < f < 2f_0$ if $f_0 > 0.5\text{Hz}$ $\ast_A(f) < 3$ for $0.5f_0 < f < 2f_0$ if $f_0 < 0.5\text{Hz}$	Exceeded 0 out of 85 times	OK	

Criteria for a clear H/V peak

[At least 5 out of 6 should be fulfilled]

Exists f^- in $[f_0/4, f_0] \mid A_{H/V}(f^-) < A_0 / 2$			NO
Exists f^+ in $[f_0, 4f_0] \mid A_{H/V}(f^+) < A_0 / 2$			NO
$A_0 > 2$	$3.02 > 2$	OK	
$f_{\text{peak}}[A_{H/V}(f) \pm \ast_A(f)] = f_0 \pm 5\%$	$ 0.09556 < 0.05$		NO
$\ast_f < \ast(f_0)$	$0.16723 < 0.175$	OK	
$\ast_A(f_0) < \ast(f_0)$	$0.3929 < 1.78$	OK	

L_w	window length
n_w	number of windows used in the analysis
$n_c = L_w n_w f_0$	number of significant cycles
f	current frequency
f_0	H/V peak frequency
σ_f	standard deviation of H/V peak frequency
$\sigma(f_0)$	threshold value for the stability condition $\sigma_f < \sigma(f_0)$
A_0	H/V peak amplitude at frequency f_0
$A_{H/V}(f)$	H/V curve amplitude at frequency f
f^-	frequency between $f_0/4$ and f_0 for which $A_{H/V}(f^-) < A_0/2$
f^+	frequency between f_0 and $4f_0$ for which $A_{H/V}(f^+) < A_0/2$
$\sigma_A(f)$	standard deviation of $A_{H/V}(f)$, $\sigma_A(f)$ is the factor by which the mean $A_{H/V}(f)$ curve should be multiplied or divided
$\sigma_{\log H/V}(f)$	standard deviation of $\log A_{H/V}(f)$ curve
$\sigma(f_0)$	threshold value for the stability condition $\sigma_A(f) < \sigma(f_0)$

Threshold values for σ_f and $\sigma_A(f_0)$

Freq. range [Hz]	< 0.2	0.2 – 0.5	0.5 – 1.0	1.0 – 2.0	> 2.0
$\omega(f_0)$ [Hz]	$0.25 f_0$	$0.2 f_0$	$0.15 f_0$	$0.10 f_0$	$0.05 f_0$
$\omega(f_0)$ for $\omega_A(f_0)$	3.0	2.5	2.0	1.78	1.58
$\log \omega(f_0)$ for $\omega_{\log H/V}(f_0)$	0.48	0.40	0.30	0.25	0.20

Table 70. SESAME (2004) criteria applied to the main resonance peak identified in the characteristic H/V curve.

GALLERY



Figure 128. H/V recordings near the MRB1 seismic station.



Figure 129. Location of the active/passive surface waves array A01.

REFERENCES

- Castellaro S., 2016. The complementarity of H/V and dispersion curves, *Geophysics*, 81, T323–T338
- ISPRA, Carta Geologica d'Italia alla scala 1:50 000, Foglio 432 "Benevento"
- Norme Tecniche sulle Costruzioni, 2018. Decreto Ministeriale 17/01/2018, Ministry of Infrastructures and Transportations, G.U. S.O. n.8 on 20/2/2018
- SESAME, 2004. Guidelines for the implementation of the H/V spectral ratio technique on ambient vibrations. Measurements, processing and interpretation, WP12 European commission - Research general directorate project no. EVG1-CT-2000-0026 SESAME, report D23.12, 62 pp.

Giulia Alessandrini¹, Giovanni Lattanzi¹, Stephen Slivicki², Giulia Sgattoni¹, Silvia Castellaro¹

¹ *Università di Bologna, Dipartimento di Fisica e Astronomia, Viale Carlo B. Pichat 8, 40127 Bologna (Italy)*

² *University of Wisconsin-River Falls (USA)*

Site characterization of the seismic station

IV.MRLC

Geophysical survey performed on
24th October 2019 (16.30 pm – 18 pm)

Partly funded by Contratto di Consulenza Commissionata per lo "Studio sismotettonico delle dighe Marana Capacciotti e San Pietro sul Torrente Osento e delle opere accessorie" – Consorzio di Bonifica per la Capitanata (2019)

IV.MRLC – MURO LUCANO

CODE	NAME	Lat. [°] WGS-84	Lon. [°] WGS-84	Elevation [m]
MRLC	MURO LUCANO	40.756366	15.488696	605
Address	Via Pianello, 76, 85054 Muro lucano PZ, Italy			

Table 71. Code, name and WGS-84 coordinates of the seismic station.

SEISMIC STATION

SENSOR	Episensor FBA ES-T [Kinematics]
DIGITIZER	unknown
HOUSING	Masonry shed

Table 72. Instrumental chain installed at the seismic station.

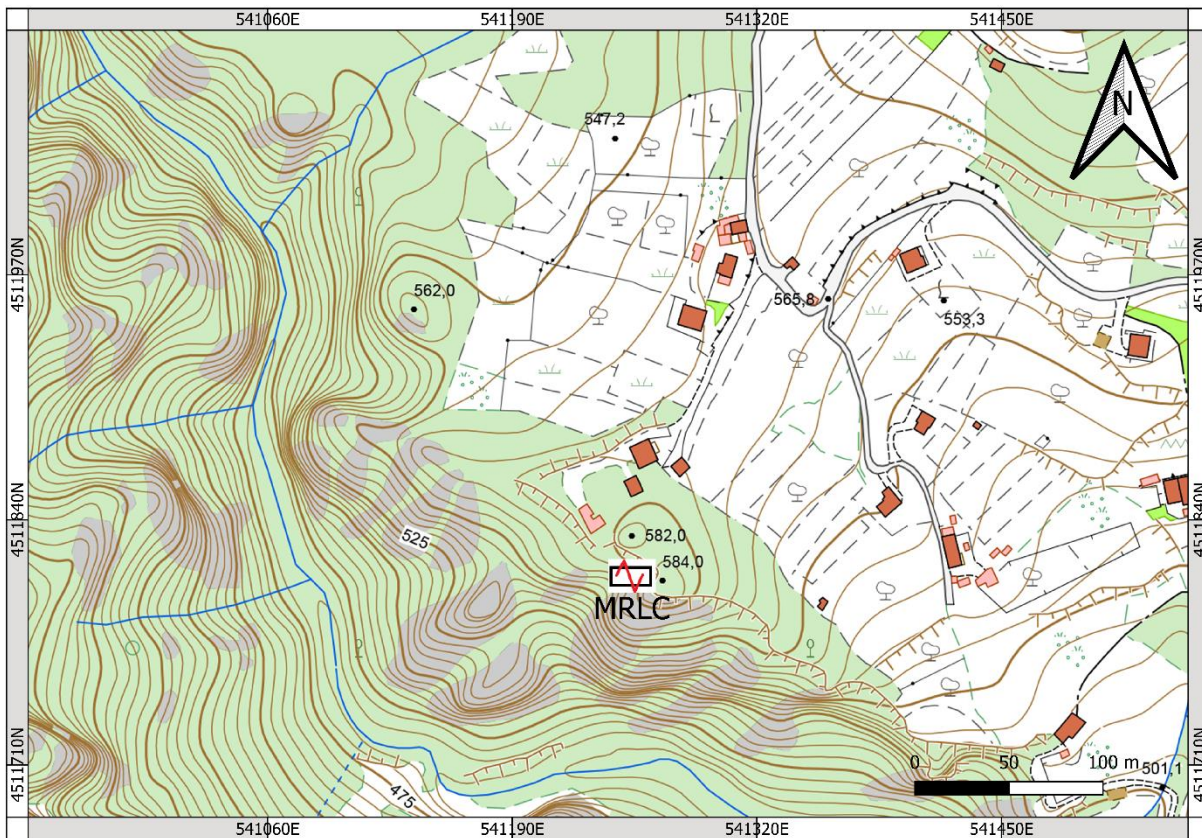


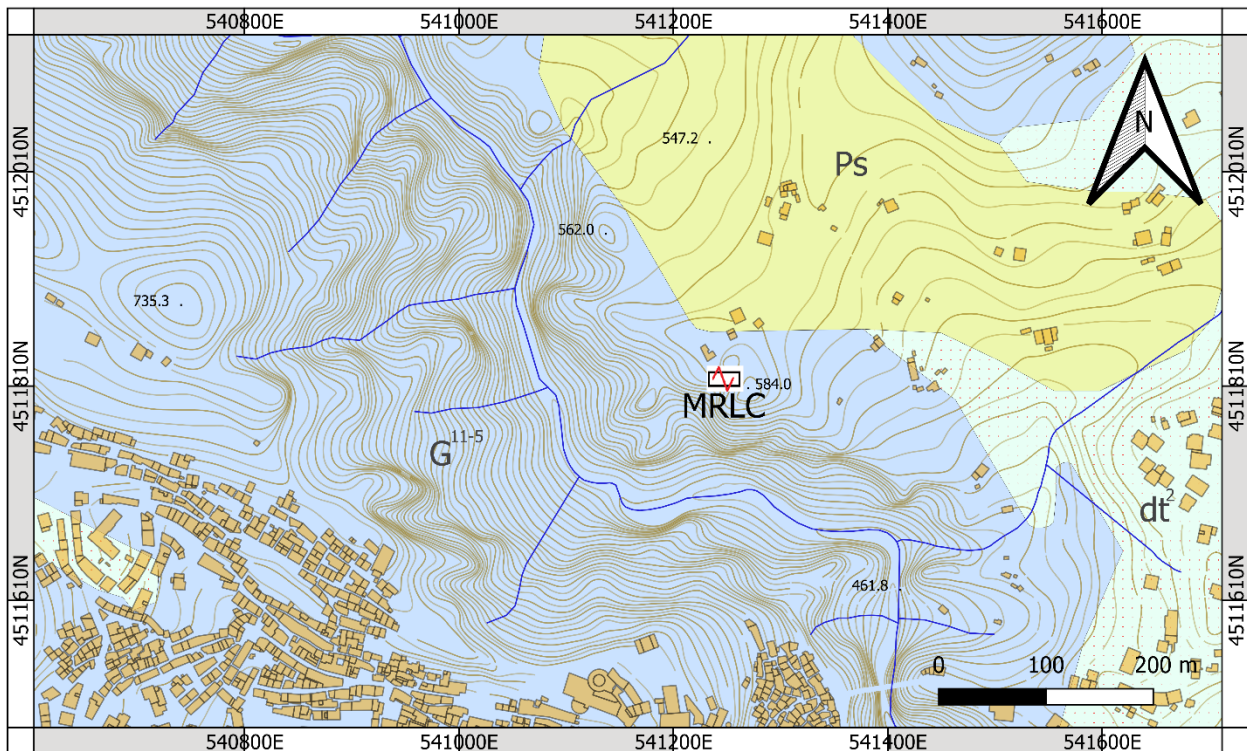
Figure 130. Location of the MRLC seismic station at Muro Lucano (source CTR 1:5 000, the image could be rescaled, refer to the bar scale).

GEOLOGICAL AND TOPOGRAPHIC INFORMATION

According to the ISPRA 1:100 000 Carta Geologica d'Italia map (Figure 72), the seismic station is located on the Jurassic oolitic limestone (G^{11-5}).

TYPE	NOTES	SCALE
CTR	Foglio 469022	1:5 000
ISPRA, carta geologica	Foglio 187, Melfi	1:100 000

Table 73. Geological and geotechnical cartography available for the site.



LEGEND:

-  ACCELEROMETRIC STATION
-  dt² Detrito di falda (Pleistocene-Olocene)
-  Ps Sabbie giallastre (Pliocene medio-inf.)
-  G¹¹⁻⁵ Calcari oolitici avana, calcilutiti, calcareniti (Malm-Dogger)

Figure 131. Geological map of the area surrounding the seismic station MRLC (source ISPRA 1:100 000, the image could be rescaled, refer to the bar scale).

GEOPHYSICAL SURVEY

We propose an average V_s model for the site, based on the joint fit of all the acquired surface-wave dispersion and H/V curves (Table 35). Since the H/V curves are more sensitive to local geological features compared to the array dispersion curves, the average V_s model might not faithfully reproduce the H/V features at high frequency.

The theoretical H/V curve overlapped to the experimental H/V curve could be computed on a slightly different model (see footnotes, if present).

SURVEY TYPE	N.	Acquisition length	Sampling rate [Hz]	NOTES	INSTRUMENT USED
Microtremor H/V ¹⁵	4	20' each	512	All measurements on natural soil	Tromino® - MoHo srl
Active/passive 1D array ¹⁶	2	Active: MASW Passive: ReMi (7' recording)	512	16 geophones: 3 m inter-receiver distance (A01); 4 m inter-receiver distance (A02)	Seismograph: SoilSpy – MoHo srl Geophones: OYO - Geospace 4.5 Hz (vertical)

Table 74. List of the H/V and active/passive surface-wave arrays acquired at the site.

¹⁵The average amplitude spectra in velocity and their standard deviation are computed for each measurement point by splitting the recorded signal into 30 second non-overlapping windows. On average, 32 to 40 signal windows are retained to compute the average H/V curve and its standard deviation. Each window is detrended, tapered with a Bartlett window, zero-padded and FF-transformed. The Fourier spectra are smoothed according to triangular windows with width equal to 10% of the central frequency, in order to keep only the significant peaks.

¹⁶The vertical-component Rayleigh-wave phase-velocity dispersion curves obtained by averaging several active and passive surveys are illustrated. Only the windows showing the lowest phase velocities (with the exclusion of the alias) are retained, for their being closer to the fundamental mode dispersion curve. The phase-velocity spectra are obtained by slant-stacking the seismograms and by applying a FFT.

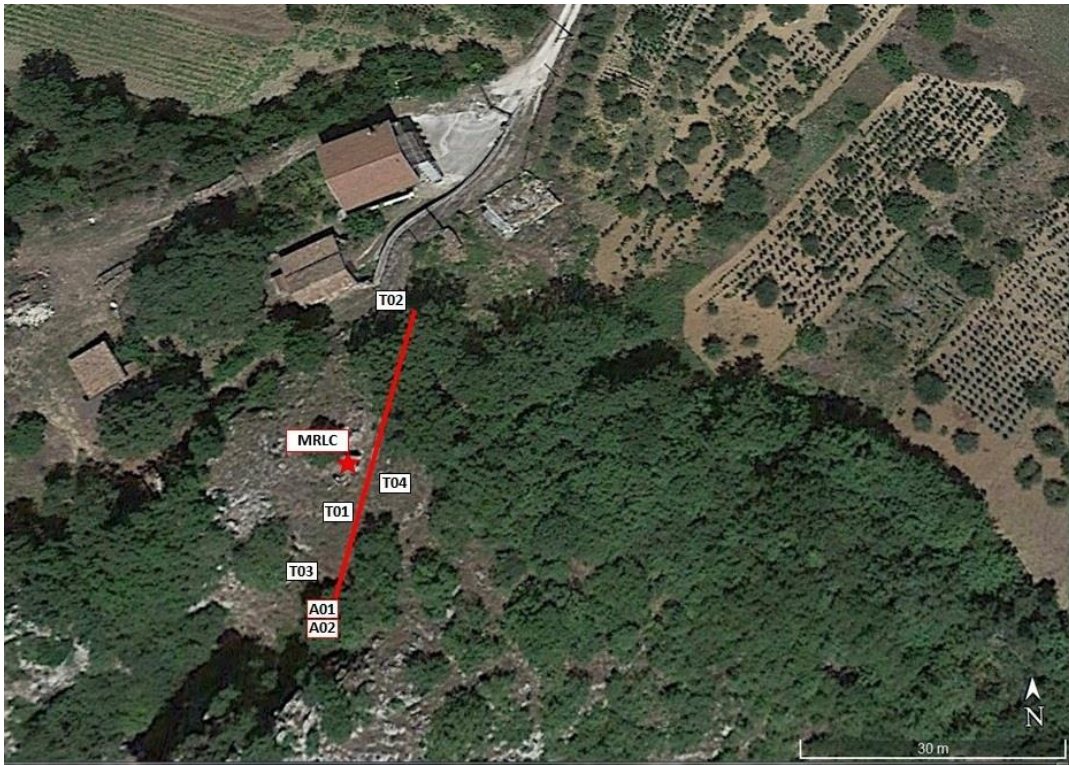


Figure 132. Location of the active/passive surface-wave arrays and of the H/V recordings.

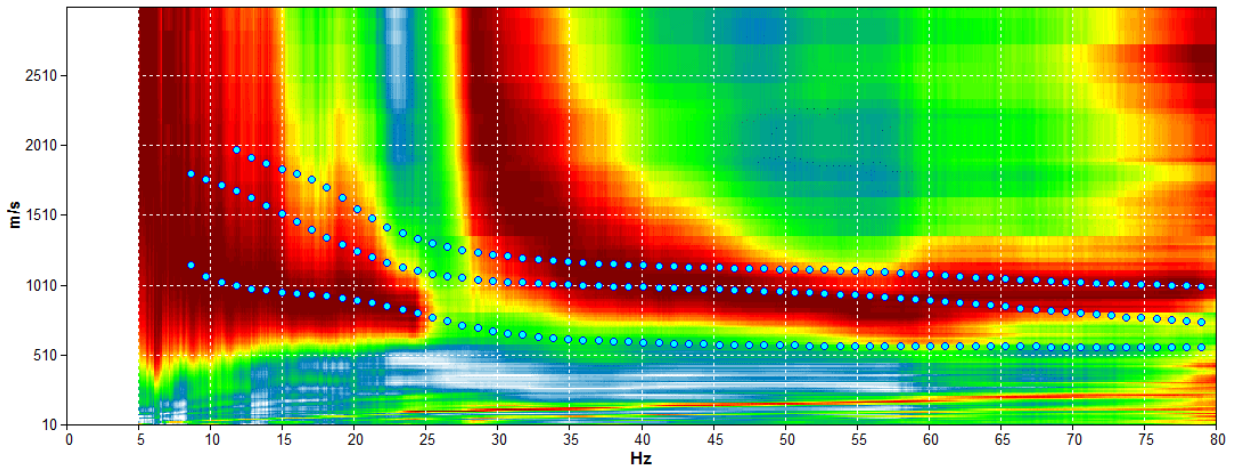


Figure 133. Average dispersion curve from the MASW and ReMi surveys at site A02. Synthetic dispersion curve for the model of Table 35 (light blue circles).

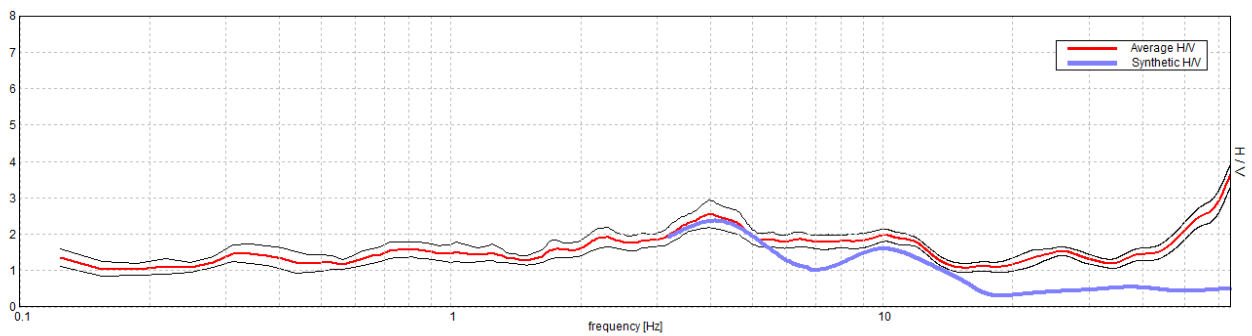


Figure 134. Experimental H/V curve acquired at site T01 (average in red, standard deviation in black). Synthetic H/V curve¹⁷ for the model of Table 35 (blue).

Depth at the bottom of the layer [m]	Thickness [m]	Vs [m/s]	Poisson ratio	Seismostratigraphic model obtained from:
10.00	10.00	600	0.42	0 – 74 m
65.00	55.00	1100	0.42	H/V + Dispersion curve
inf.	inf.	2000	0.40	74 m – inf. H/V only

Table 75. Seismostratigraphic model proposed for the site.

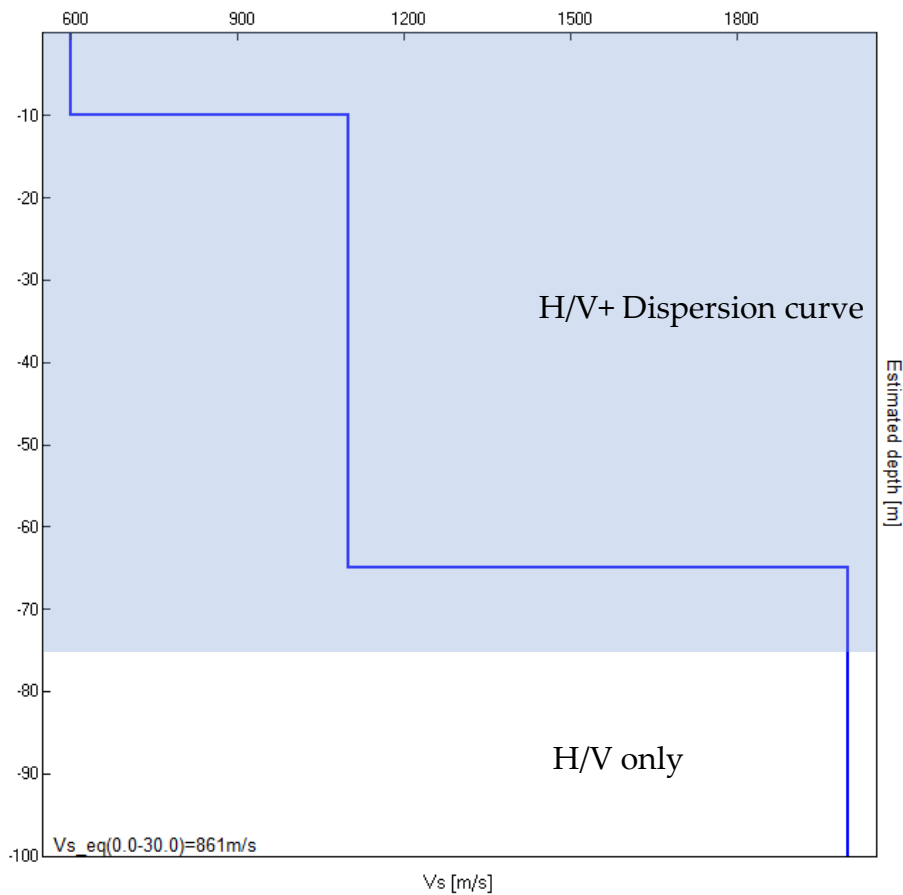


Figure 135. Vs model proposed for the site.

$$V_{seq}[0 - 10] m = 600 m/s *$$

¹⁷ At high frequencies, the synthetic H/V curve has a different fit if compared to the average Vs model obtained from the dispersion curve.

$$V_{s30}[0 - 30] m = 860 m/s *$$

Class B site (NTC, 2018)

Class A/B site (NTC, 2008)

* Characteristic uncertainty is 20%

ADDITIONAL MATERIAL

In this section we present the characteristic H/V curve of the site (Figure 77) together with the single spectral components used to compute it, in order for the reader to understand the stratigraphic or artefactual nature of the H/V peaks (SESAME, 2004; Castellaro, 2016). The SESAME (2004) criteria for the main H/V peak are listed in Table 36. In Figure 78 we present a selection of H/V curves acquired in the proximity of the seismic station to show the spatial variability of this function.

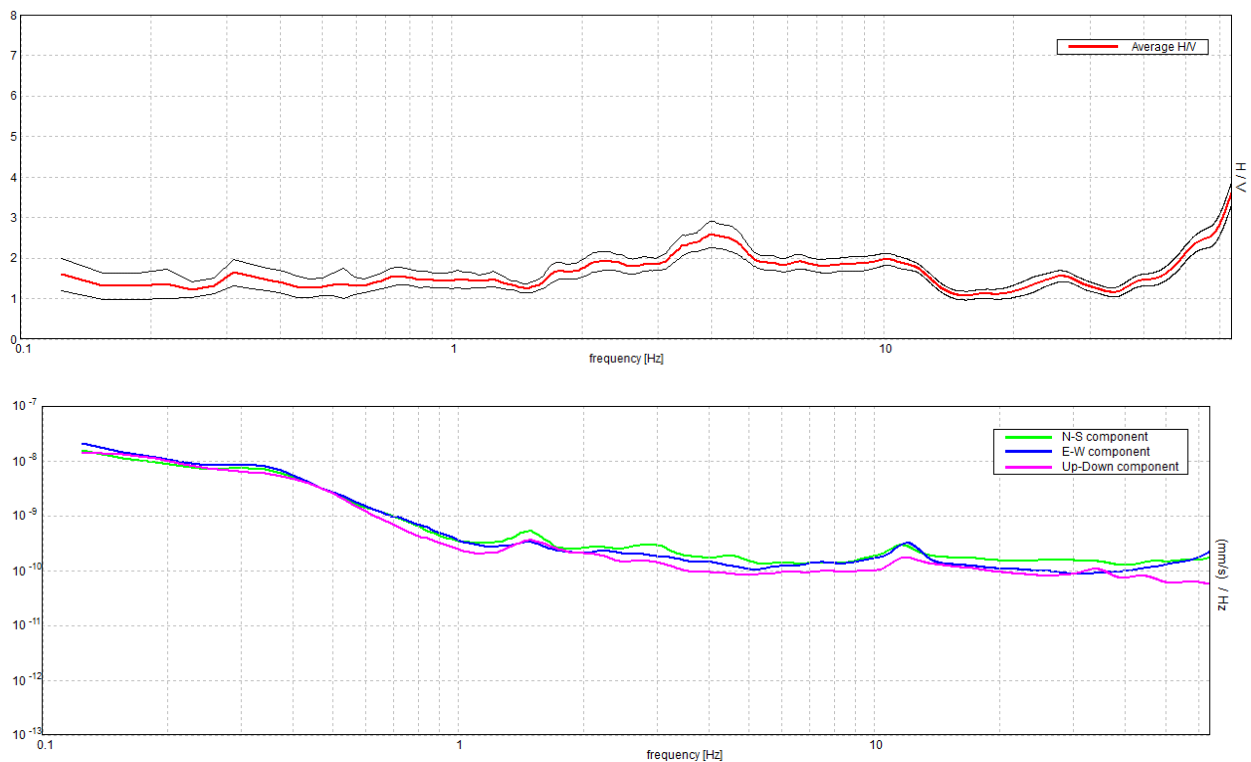


Figure 136. Top: characteristic H/V curve (average in red, standard deviation in black). Bottom: spectra of the single components of motion (NS, EW, Z) used to derive the H/V curve.

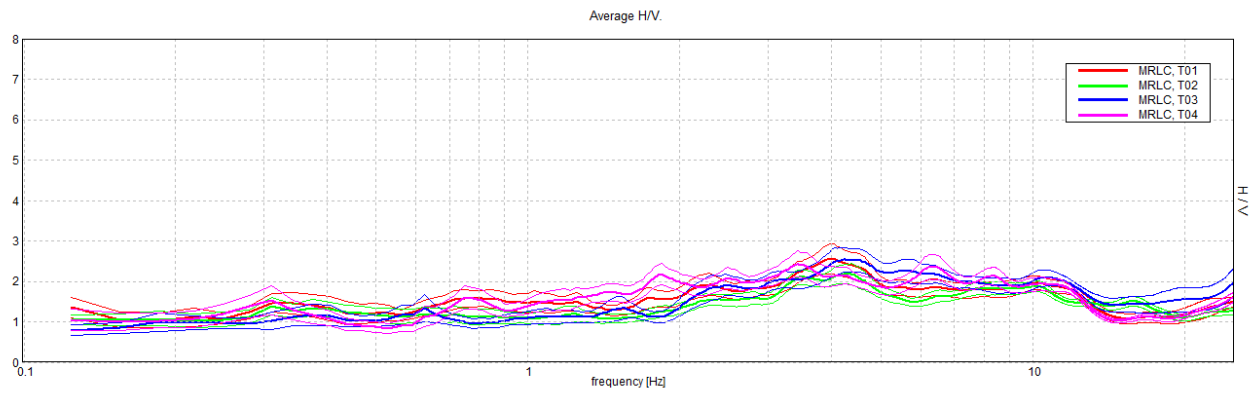


Figure 137. Comparison of the H/V curves acquired in the proximity of the seismic station (refer to Figure 73 for the location).

[According to the SESAME, 2004 guidelines]

Max. H/V at 4.03 ± 2.45 Hz (in the range 0.0 - 20.0 Hz).

Criteria for a reliable H/V curve

[All 3 should be fulfilled]

$f_0 > 10 / L_w$	$4.03 > 0.50$	OK	
$n_c(f_0) > 200$	$3870.0 > 200$	OK	
$\sigma_A(f) < 2$ for $0.5f_0 < f < 2f_0$ if $f_0 > 0.5\text{Hz}$ $\sigma_A(f) < 3$ for $0.5f_0 < f < 2f_0$ if $f_0 < 0.5\text{Hz}$	Exceeded 0 out of 194 times	OK	

Criteria for a clear H/V peak

[At least 5 out of 6 should be fulfilled]

Exists f^- in $[f_0/4, f_0] \mid A_{H/V}(f^-) < A_0 / 2$	1.531 Hz	OK	
Exists f^+ in $[f_0, 4f_0] \mid A_{H/V}(f^+) < A_0 / 2$	13.5 Hz	OK	
$A_0 > 2$	$2.58 > 2$	OK	
$f_{\text{peak}}[A_{H/V}(f) \pm \sigma_A(f)] = f_0 \pm 5\%$	$ 0.60848 < 0.05$		NO
$\sigma_f < \sigma(f_0)$	$2.45292 < 0.20156$		NO
$\sigma_A(f_0) < \sigma(f_0)$	$0.3245 < 1.58$	OK	

L_w	window length
n_w	number of windows used in the analysis
$n_c = L_w n_w f_0$	number of significant cycles
f	current frequency
f_0	H/V peak frequency
σ_f	standard deviation of H/V peak frequency
$\sigma(f_0)$	threshold value for the stability condition $\sigma_f < \sigma(f_0)$
A_0	H/V peak amplitude at frequency f_0
$A_{H/V}(f)$	H/V curve amplitude at frequency f
f^-	frequency between $f_0/4$ and f_0 for which $A_{H/V}(f^-) < A_0/2$
f^+	frequency between f_0 and $4f_0$ for which $A_{H/V}(f^+) < A_0/2$
$\sigma_A(f)$	standard deviation of $A_{H/V}(f)$, $\sigma_A(f)$ is the factor by which the mean $A_{H/V}(f)$ curve should be multiplied or divided
$\sigma_{\log H/V}(f)$	standard deviation of $\log A_{H/V}(f)$ curve
$\sigma(f_0)$	threshold value for the stability condition $\sigma_A(f) < \sigma(f_0)$

Threshold values for σ_f and $\sigma_A(f_0)$

Freq. range [Hz]	< 0.2	0.2 – 0.5	0.5 – 1.0	1.0 – 2.0	> 2.0
$\sigma(f_0)$ [Hz]	$0.25 f_0$	$0.2 f_0$	$0.15 f_0$	$0.10 f_0$	$0.05 f_0$

$\sigma(f_0)$ for $\sigma_A(f_0)$	3.0	2.5	2.0	1.78	1.58
$\log \sigma(f_0)$ for $\sigma_{\log H/V}(f_0)$	0.48	0.40	0.30	0.25	0.20

Table 76. SESAME (2004) criteria applied to the main resonance peak identified in the characteristic H/V curve.

GALLERY



Figure 138. Location of the H/V recording near the MRLC seismic station.



Figure 139. Location of the active/passive surface waves arrays A01 – A02 and H/V T01 recording.

REFERENCES

Castellaro S., 2016. The complementarity of H/V and dispersion curves, *Geophysics*, 81, T323–T338

ISPRA, Carta Geologica d'Italia alla scala 1:100 000, Foglio 187 "Melfi"

Norme Tecniche sulle Costruzioni, 2008. Decreto Ministeriale 14/01/2008, Ministry of Infrastructures and Transportations, G.U. S.O. n.29 on 4/2/2008

Norme Tecniche sulle Costruzioni, 2018. Decreto Ministeriale 17/01/2018, Ministry of Infrastructures and Transportations, G.U. S.O. n.8 on 20/2/2018

SESAME, 2004. Guidelines for the implementation of the H/V spectral ratio technique on ambient vibrations. Measurements, processing and interpretation, WP12 European commission - Research general directorate project no. EVG1-CT-2000-0026 SESAME, report D23.12, 62 pp.

Giulia Alessandrini¹, Giovanni Lattanzi¹, Stephen Slivicki², Giulia Sgattoni¹, Silvia Castellaro¹

¹ *Università di Bologna, Dipartimento di Fisica e Astronomia, Viale Carlo B. Pichat 8, 40127 Bologna (Italy)*

² *University of Wisconsin-River Falls (USA)*

Site characterization of the seismic station

IT.RNV2

Geophysical survey performed on
23rd October 2019 (13 pm – 14.30 pm)

Partly funded by Contratto di Consulenza Commissionata per lo “Studio sismotettonico delle dighe Marana Capacciotti e San Pietro sul Torrente Osento e delle opere accessorie” – Consorzio di Bonifica per la Capitanata (2019)

IT. RNV2 – RIONERO IN VULTURE

CODE	NAME	Lat. [°] WGS-84	Lon. [°] WGS-84	Elevation [m]
RNV2	RIONERO IN VULTURE	40.92838	15.66907	683
Address	Via delle Falene, 46, 85028 Rionero In Vulture PZ, Italy Basilicata			

Table 77. Code, name and WGS-84 coordinates of the seismic station.

SEISMIC STATION

SENSOR	MS2007+ [Syscom]
DIGITIZER	130-01/3 [Refttek]
HOUSING	Fiberglass box on concrete basement.

Table 78. Instrumental chain installed at the seismic station.

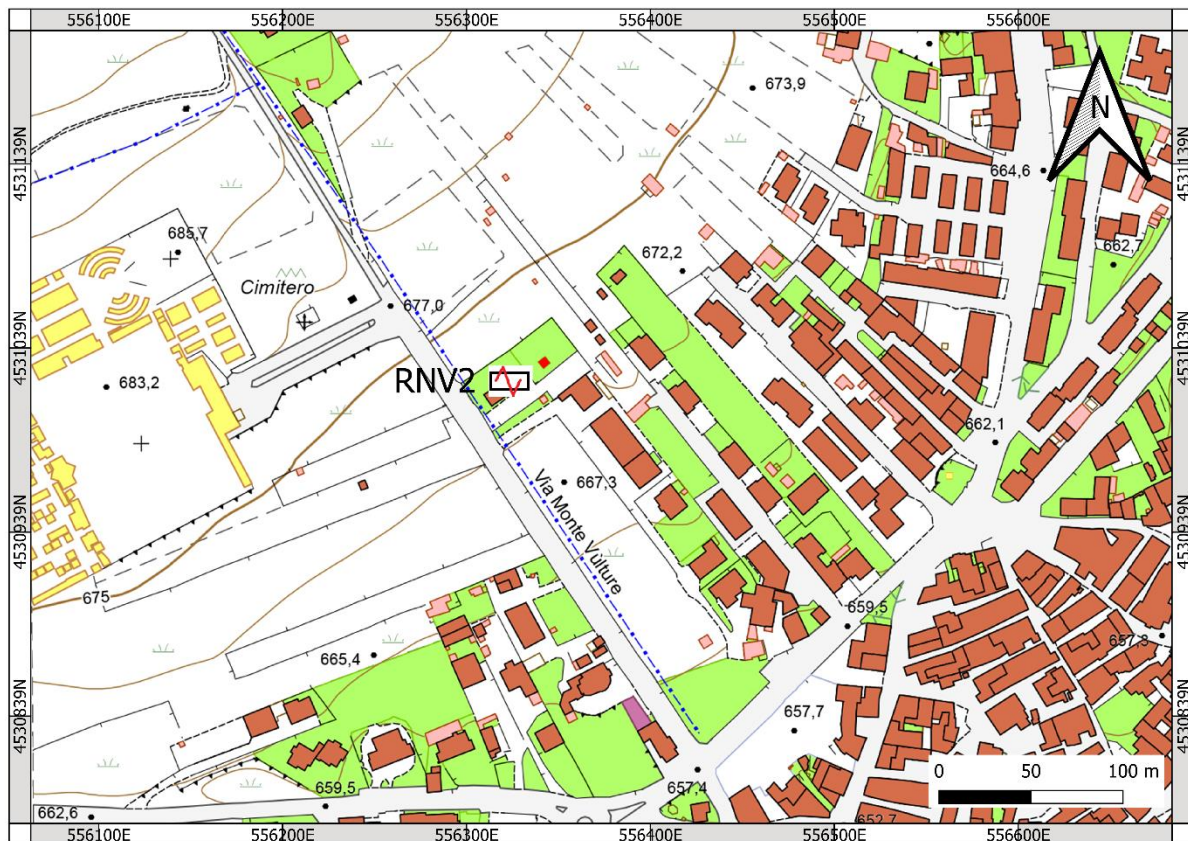


Figure 140. Location of the RNV2 seismic station at Rionero in Vulture (source CTR 1:5 000, the image could be rescaled, refer to the scale bar).

GEOLOGICAL AND TOPOGRAPHIC INFORMATION

According to the ENEL map and cross-section (Figure 72), the seismic station is located on volcanic tuffs. In the CARG map, tuffs are classified as *Subsistema di Vulture-San Michele (SBL₃)*, characterized by single pyroclastic flow units 10-15 m thick.

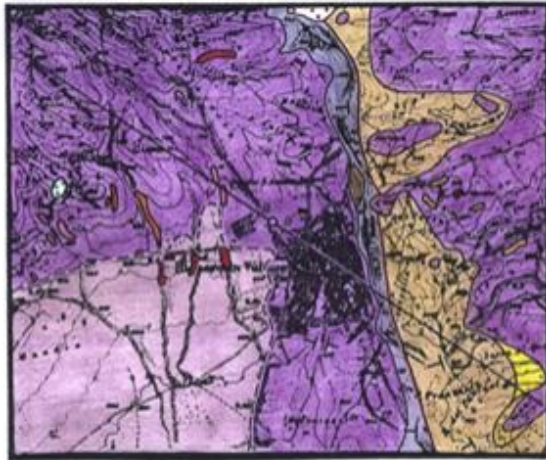
TYPE	NOTES	SCALE
CTR	Foglio 452054	1:5 000
ISPRA, carta geologica	Foglio 173, Benevento	1:100 000
CARG, carta geologica	Foglio 452 Rionero in Vulture	1:50 000
ENEL, carta geologica	Carta geologica	1:25 000

Table 79. Geological and geotechnical cartography available for the site.

Postazione di RIONERO IN VULTURE (NUOVA)

CARTA GEOLOGICA

Scala 1:25.000

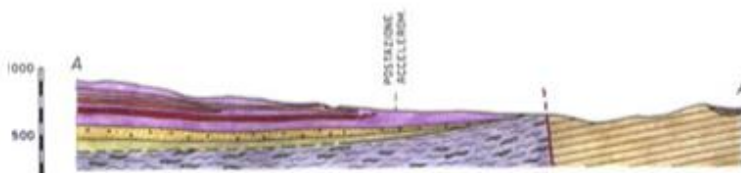


LEGENDA

- DETRITO DI FALDA.
- FORMAZIONI VULCANICHE**
- TUFFI SCURI SUBAEREI, NORMALMENTE STRATIFICATI, DI COLORE VARIABILE DAL GRIGIO AL BRUNO-SCURO, PIÙ O MENO COERENTI. A RIONERO DEPOSITI CON CARATTERE POZZOLANICO (a). DEPOSITI DI "LAHAR" (b).
- TEFRITI DI COLORE PREVALENTE GRIGIO-FERRO, IN COLATE SINGOLE O IN PIÙ COLATE SOVRAPPOSTE (c); BASANITI DI COLOR GRIGIO-NERO (w); SCORIE (sc).

Postazione di RIONERO IN VULTURE (NUOVA)

SEZIONE GEOLOGICA A-A'



- PLEISTOCENE**
- LAVI FIDITICHE IN COLATE SINGOLE O IN PIÙ COLATE SOVRAPPOSTE, A VOLTE CON CARATTERI DI TRANSIZIONE FRA LE MAFITI E LE FONOLITI.
- TUFFI CHIARI SUBAEREI GENERALMENTE NON STRATIFICATI DI COMPOSIZIONE TRACHITICA E FONOLITICA, RIFERIBILI ALLE MANIFESTAZIONI INIZIALI.
- CIOTTOLAMI POLIGENICI, PROBABILMENTE FLUVIO-LACUSTRI.
- UNITÀ IRPINE**
- MIOCENE**
- FORMAZIONE DI SERRA PALAZZO: ALTERNANZE DI ARENARIE QUARZOSE-FELDSPATICO-MICACEE, MARNE GRIGIASTRE, CALCARI MARNOSI, A VOLTE SOSTITUITE ETEROPICAMENTE DA MOLASSE IN BANCATE (TORTONIANO-LANGHIANO SUP).
- FORMAZIONE DI STIGLIANO: ARENARIE QUARZOSE CON INTERCALAZIONI DI ARGILLOSCISTI VERDASTRI (LANGHIANO SUP - AQUITANIANO).
- COMPLESSO SICILIDE**
- ARGILLE VARICOLORI: ARGILLE E ARGILLOSCISTI PIÙ O MENO SCAGLIOSI, ROSSASTRI O VERDASTRI, CON INTERCALAZIONI DI CALCARI MARNOSI, CALCARENITI E BRECCIOLE NUMMULITICHE (MIOCENE - OLIGOCENE).
- FAGLIA.
- ✓ ORIENTAZIONE DEGLI STRATI.
- + STRATI ORIZZONTALI.
- A — A' TRACCIA DELLE SEZIONI.
- POSTAZIONE ACCELEROMETRICA.

LEGENDA

- FORMAZIONI VULCANICHE**
- TUFFI SCURI SUBAEREI, NORMALMENTE STRATIFICATI, DI COLORE VARIABILE DAL GRIGIO AL BRUNO-SCURO, PIÙ O MENO COERENTI. A RIONERO DEPOSITI CON CARATTERE POZZOLANICO.
- TEFRITI DI COLORE PREVALENTE GRIGIO-FERRO, IN COLATE SINGOLE O IN PIÙ COLATE SOVRAPPOSTE (c); BASANITI DI COLOR GRIGIO-NERO (w).
- LAVI FIDITICHE IN COLATE SINGOLE O IN PIÙ COLATE SOVRAPPOSTE, A VOLTE CON CARATTERI DI TRANSIZIONE FRA LE MAFITI E LE FONOLITI.
- TUFFI CHIARI SUBAEREI GENERALMENTE NON STRATIFICATI DI COMPOSIZIONE TRACHITICA E FONOLITICA, RIFERIBILI ALLE MANIFESTAZIONI INIZIALI.
- DEPOSITI FLUVIO-LACUSTRI E LACUSTRI FINEMENTE STRATIFICATI, CON INTERCALAZIONI DI TUFFI SUBAEREI.
- CIOTTOLAMI POLIGENICI, PROBABILMENTE FLUVIO-LACUSTRI.
- UNITÀ IRPINE (MIOCENE)**
- FORMAZIONE DI SERRA PALAZZO: ALTERNANZE DI ARENARIE QUARZOSE-FELDSPATICO-MICACEE, MARNE GRIGIASTRE, CALCARI MARNOSI, A VOLTE SOSTITUITE ETEROPICAMENTE DA MOLASSE IN BANCATE (TORTONIANO-LANGHIANO SUP).
- COMPLESSO SICILIDE**
- ARGILLE VARICOLORI: ARGILLE E ARGILLOSCISTI PIÙ O MENO SCAGLIOSI, ROSSASTRI O VERDASTRI, CON INTERCALAZIONI DI CALCARI MARNOSI, CALCARENITI E BRECCIOLE NUMMULITICHE (MIOCENE - OLIGOCENE).

Figure 141. Geological map of the area surrounding the seismic station RNV2 (source ENEL 1:25 000, the image could be rescaled, refer to the scale bar).

GEOPHYSICAL SURVEY

We propose an average V_s model for the site, based on the joint fit of all the acquired surface-wave dispersion and H/V curves (Table 35). Since the H/V curves are more sensitive to local geological features compared to the array dispersion curves, the average V_s model might not faithfully reproduce the H/V features at high frequency.

The theoretical H/V curve overlapped to the experimental H/V curve could be computed on a slightly different model (see footnotes, if present).

SURVEY TYPE	N.	Acquisition length	Sampling rate [Hz]	NOTES	INSTRUMENT USED
Microtremor H/V ¹⁸	5	20' each	512	All measurements on natural soil	Tromino® - MoHo srl
Active/passive 1D array ¹⁹	1	Active: MASW Passive: ReMi (7' recording)	512	16 geophones, 3 m inter-receiver distance	Seismograph: SoilSpy – MoHo srl Geophones: OYO - Geospace 4.5 Hz (vertical)

Table 80. List of the H/V and active/passive surface-wave arrays acquired at the site.

¹⁸ The average amplitude spectra in velocity and their standard deviation are computed for each measurement point by splitting the recorded signal into 30 second non-overlapping windows. On average, 32 to 40 signal windows are retained to compute the average H/V curve and its standard deviation. Each window is detrended, tapered with a Bartlett window, zero-padded and FF-transformed. The Fourier spectra are smoothed according to triangular windows with width equal to 10% of the central frequency, in order to keep only the significant peaks.

¹⁹ The vertical-component Rayleigh-wave phase-velocity dispersion curves obtained by averaging several active and passive surveys are illustrated. Only the windows showing the lowest phase velocities (with the exclusion of the alias) are retained, for their being closer to the fundamental mode dispersion curve. The phase-velocity spectra are obtained by slant-stacking the seismograms and by applying a FFT.

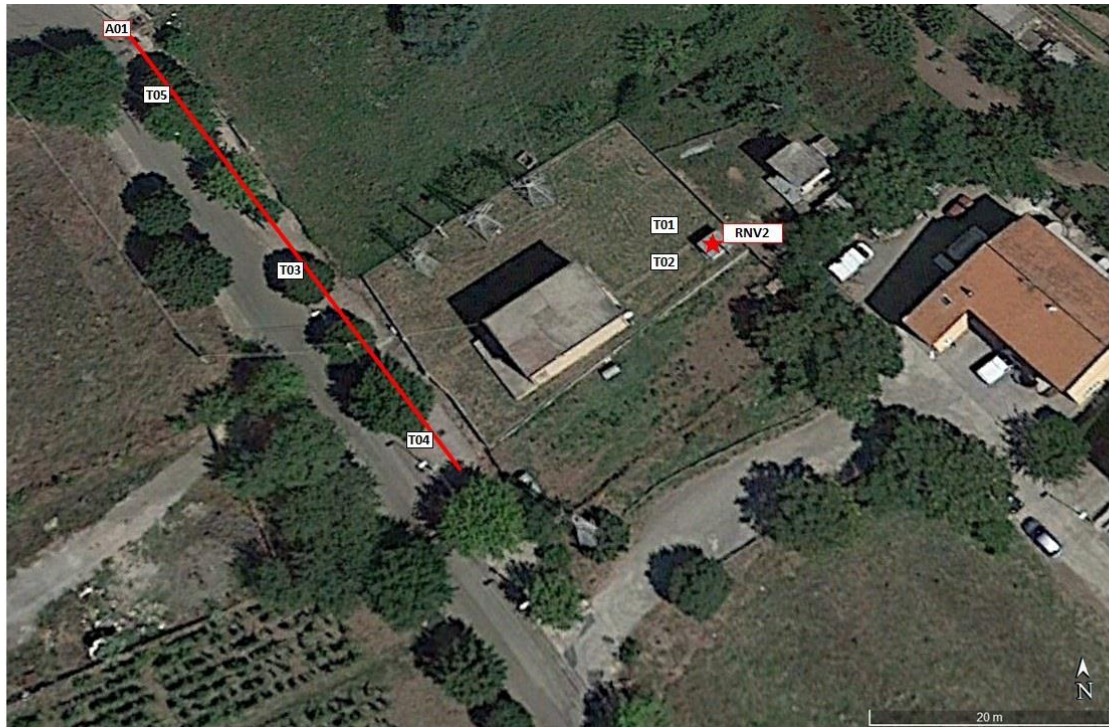


Figure 142. Location of the active/passive surface-wave arrays and of the H/V recordings.

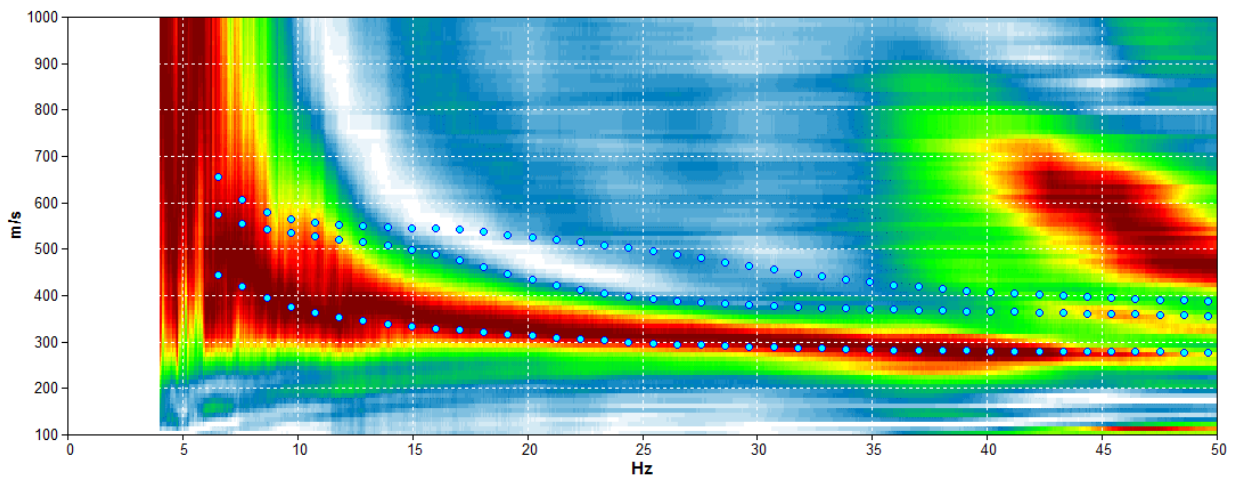


Figure 143. Average dispersion curve from the MASW and ReMi surveys at site A01. Synthetic dispersion curve for the model of Table 35 (light blue circles).

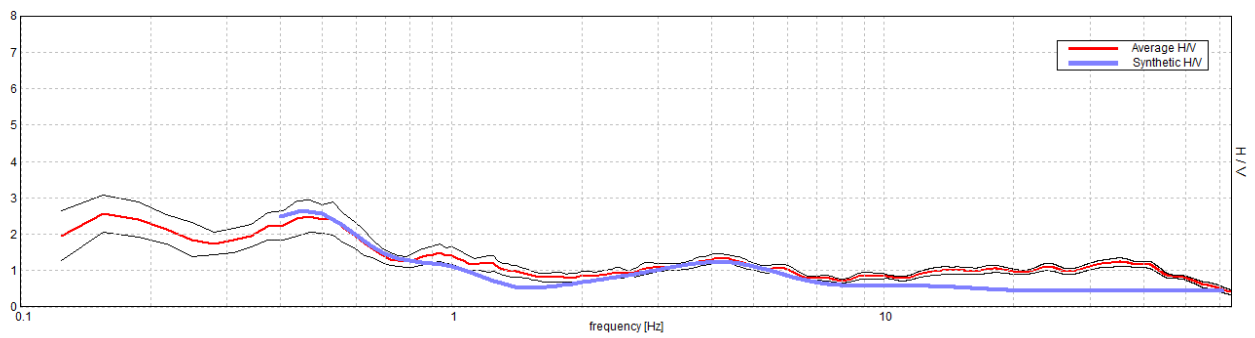


Figure 144. Experimental H/V curve acquired at site T03 (average in red, standard deviation in black). Synthetic H/V curve for the model of Table 35 (blue).

Depth at the bottom of the layer [m]	Thickness [m]	Vs [m/s]	Poisson ratio	Seismostratigraphic model obtained from:
6.00	6.00	290	0.48	0 – 40m
21.00	15.00	370	0.47	H/V + Dispersion curve
151.00	130.00	540	0.46	
511.00	360.00	920	0.43	40 m – inf.
inf.	inf.	1300	0.42	H/V only

Table 81. Seismostratigraphic model proposed for the site.

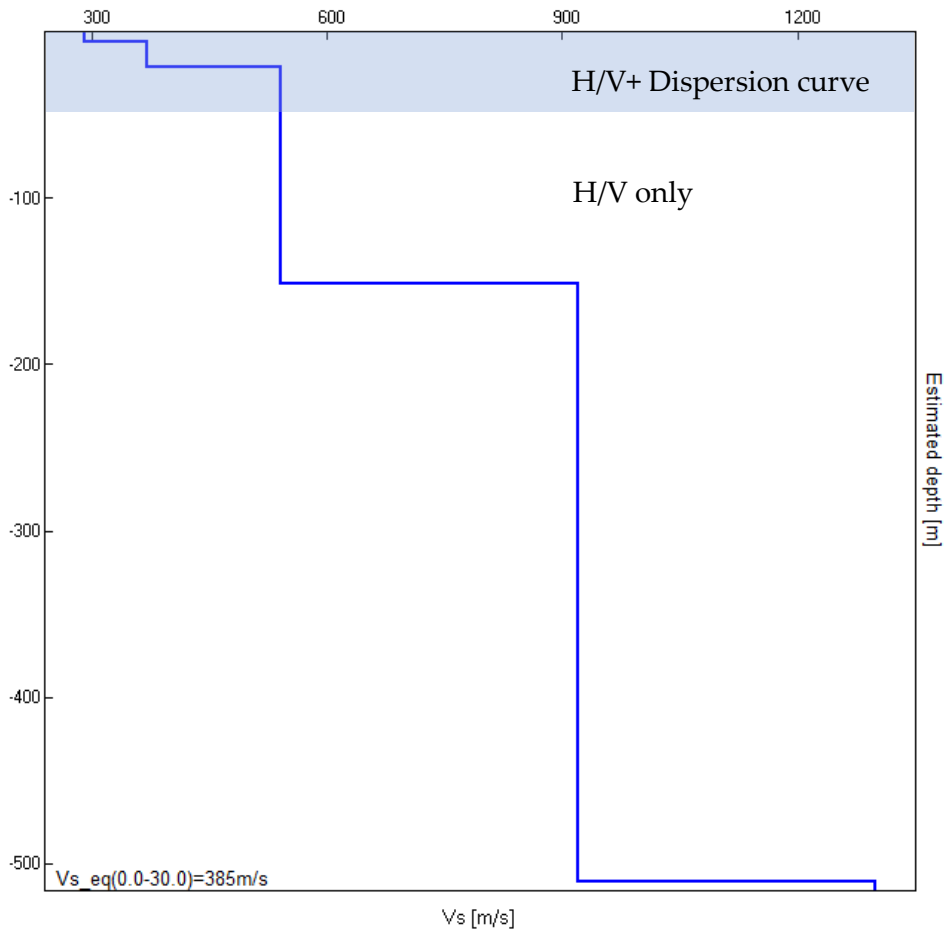


Figure 145. Vs model proposed for the site.

$$V_{s_{eq}}[0 - 30] m = 380 m/s^*$$

Class B site (NTC, 2018)

* Characteristic uncertainty is 20%

ADDITIONAL MATERIAL

In this section we present the characteristic H/V curve of the site (Figure 77) together with the single spectral components used to compute it, in order for the reader to understand the stratigraphic or artefactual nature of the H/V peaks (SESAME, 2004; Castellaro, 2016). The SESAME (2004) criteria for the main H/V peak are listed in Table 82.

In Figure 78 we present a selection of H/V curves acquired in the proximity of the seismic station to show the spatial variability of this function.

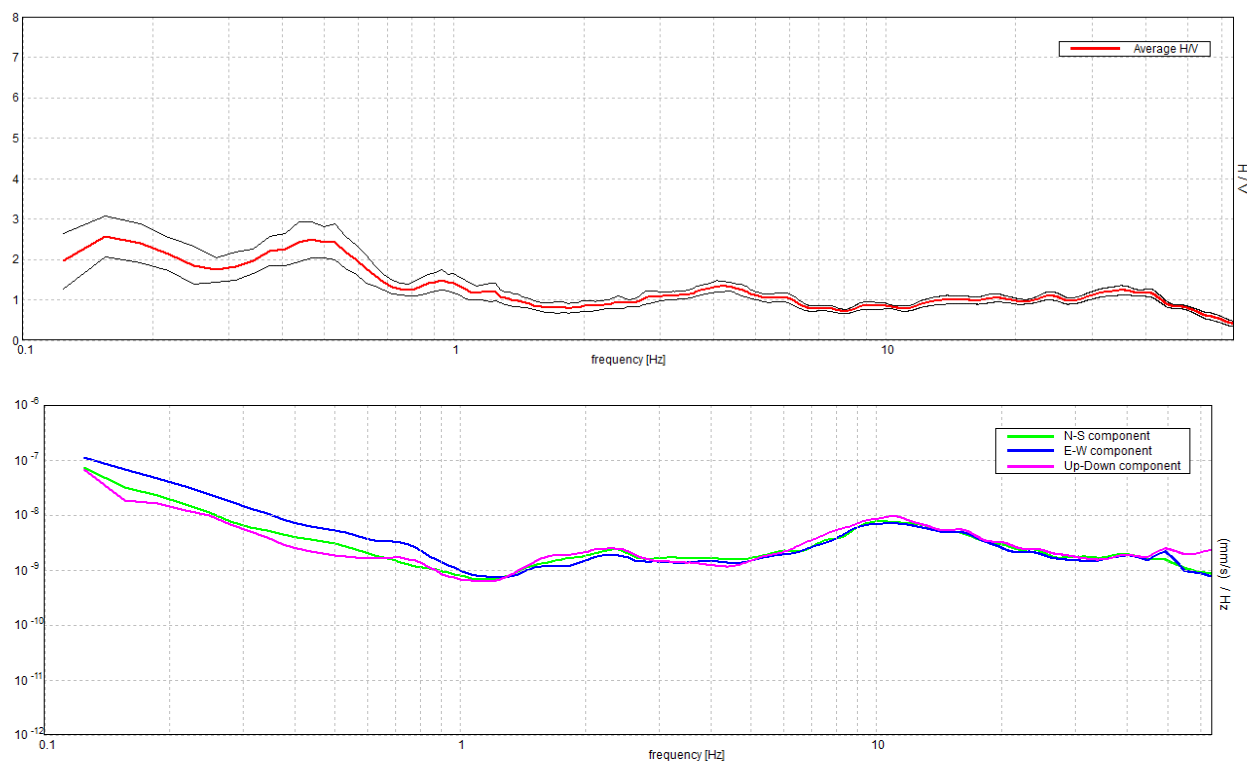


Figure 146. Top: characteristic H/V curve (average in red, standard deviation in black). Bottom: spectra of the single components of motion (NS, EW, Z) used to derive the H/V curve.

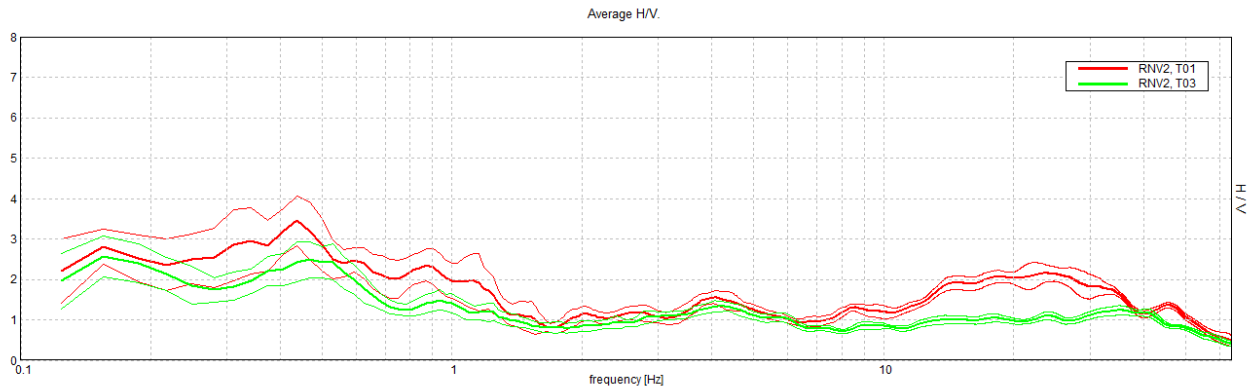


Figure 147. Comparison of the H/V curves acquired in the proximity of the seismic station (refer to Figure 73 for the location).

[According to the SESAME, 2004 guidelines]

Max. H/V at 0.53 ± 0.05 Hz (in the range 0.3 - 1.0 Hz).

Criteria for a reliable H/V curve

[All 3 should be fulfilled]

$f_0 > 10 / L_w$	$0.53 > 0.50$	OK	
$n_c(f_0) > 200$	$308.1 > 200$	OK	
$\kappa_A(f) < 2$ for $0.5f_0 < f < 2f_0$ if $f_0 > 0.5\text{Hz}$ $\kappa_A(f) < 3$ for $0.5f_0 < f < 2f_0$ if $f_0 < 0.5\text{Hz}$	Exceeded 0 out of 26 times	OK	

Criteria for a clear H/V peak

[At least 5 out of 6 should be fulfilled]

Exists f^- in $[f_0/4, f_0]$ $A_{H/V}(f^-) < A_0 / 2$			NO
Exists f^+ in $[f_0, 4f_0]$ $A_{H/V}(f^+) < A_0 / 2$	1.188 Hz	OK	
$A_0 > 2$	$2.32 > 2$	OK	
$f_{\text{peak}}[A_{H/V}(f) \pm \kappa_A(f)] = f_0 \pm 5\%$	$ 0.0867 < 0.05$		NO
$\kappa_f < \kappa(f_0)$	$0.04606 < 0.07969$	OK	
$\kappa_A(f_0) < \kappa(f_0)$	$0.3978 < 2.0$	OK	

L_w	window length
n_w	number of windows used in the analysis
$n_c = L_w n_w f_0$	number of significant cycles
f	current frequency
f_0	H/V peak frequency

σ_f	standard deviation of H/V peak frequency
$\sigma(f_0)$	threshold value for the stability condition $\sigma_f < \sigma(f_0)$
A_0	H/V peak amplitude at frequency f_0
$A_{H/V}(f)$	H/V curve amplitude at frequency f
f^-	frequency between $f_0/4$ and f_0 for which $A_{H/V}(f^-) < A_0/2$
f^+	frequency between f_0 and $4f_0$ for which $A_{H/V}(f^+) < A_0/2$
$\sigma_A(f)$	standard deviation of $A_{H/V}(f)$, $\sigma_A(f)$ is the factor by which the mean $A_{H/V}(f)$ curve should be multiplied or divided
$\sigma_{\log H/V}(f)$	standard deviation of $\log A_{H/V}(f)$ curve
$\sigma(f_0)$	threshold value for the stability condition $\sigma_A(f) < \sigma(f_0)$

Threshold values for σ_f and $\sigma_A(f_0)$					
Freq. range [Hz]	< 0.2	0.2 – 0.5	0.5 – 1.0	1.0 – 2.0	> 2.0
$\sigma(f_0)$ [Hz]	0.25 f_0	0.2 f_0	0.15 f_0	0.10 f_0	0.05 f_0
$\sigma(f_0)$ for $\sigma_A(f_0)$	3.0	2.5	2.0	1.78	1.58
$\log \sigma(f_0)$ for $\sigma_{\log H/V}(f_0)$	0.48	0.40	0.30	0.25	0.20

Table 82. SESAME (2004) criteria applied to the main resonance peak identified in the characteristic H/V curve.

GALLERY



Figure 148. Location of the H/V recording near the RNV2 seismic station.



Figure 149. Location of the active/passive surface waves array A01 and H/V T05 recording.

REFERENCES

- Castellaro S., 2016. The complementarity of H/V and dispersion curves, *Geophysics*, 81, T323–T338
- ISPRA, Carta Geologica d'Italia alla scala 1:50 000, Foglio 452 "Rionero in Vulture"
- Norme Tecniche sulle Costruzioni, 2018. Decreto Ministeriale 17/01/2018, Ministry of Infrastructures and Transportations, G.U. S.O. n.8 on 20/2/2018
- SESAME, 2004. Guidelines for the implementation of the H/V spectral ratio technique on ambient vibrations. Measurements, processing and interpretation, WP12 European commission - Research general directorate project no. EVG1-CT-2000-0026 SESAME, report D23.12, 62 pp.

Giulia Alessandrini¹, Giovanni Lattanzi¹, Stephen Slivicki², Giulia Sgattoni¹, Silvia Castellaro¹

¹ *Università di Bologna, Dipartimento di Fisica e Astronomia, Viale Carlo B. Pichat 8, 40127 Bologna (Italy)*

² *University of Wisconsin-River Falls (USA)*

Site characterization of the seismic station

IV.SGTA

Geophysical survey performed on
22nd October 2019 (16.30 pm – 17.30 pm)

Partly funded by Contratto di Consulenza Commissionata per lo “Studio sismotettonico delle dighe Marana Capacciotti e San Pietro sul Torrente Osento e delle opere accessorie” – Consorzio di Bonifica per la Capitanata (2019)

IV. SGTA – SANT’AGATA DI PUGLIA

CODE	NAME	Lat. [°] WGS-84	Lon. [°] WGS-84	Elevation [m]
SGTA	SANT’AGATA DI PUGLIA	41.135577	15.365384	890
Address	Unnamed Road, 71028, Sant’Agata di Puglia, FG, Italy			

Table 83. Code, name and WGS-84 coordinates of the seismic station.

SEISMIC STATION

SENSOR	unknown
DIGITIZER	unknown
HOUSING	Pillar inside the meteorologic station, free field

Table 84. Instrumental chain installed at the seismic station.

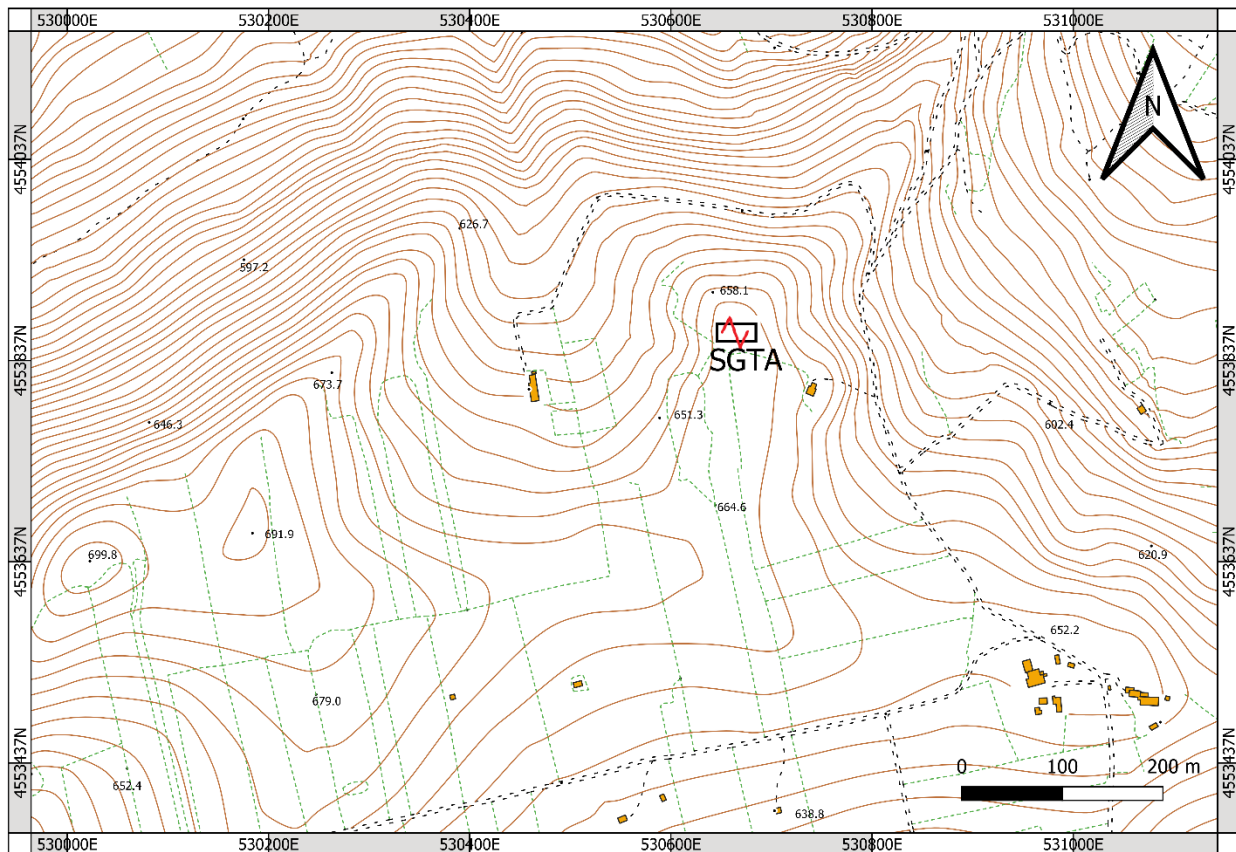


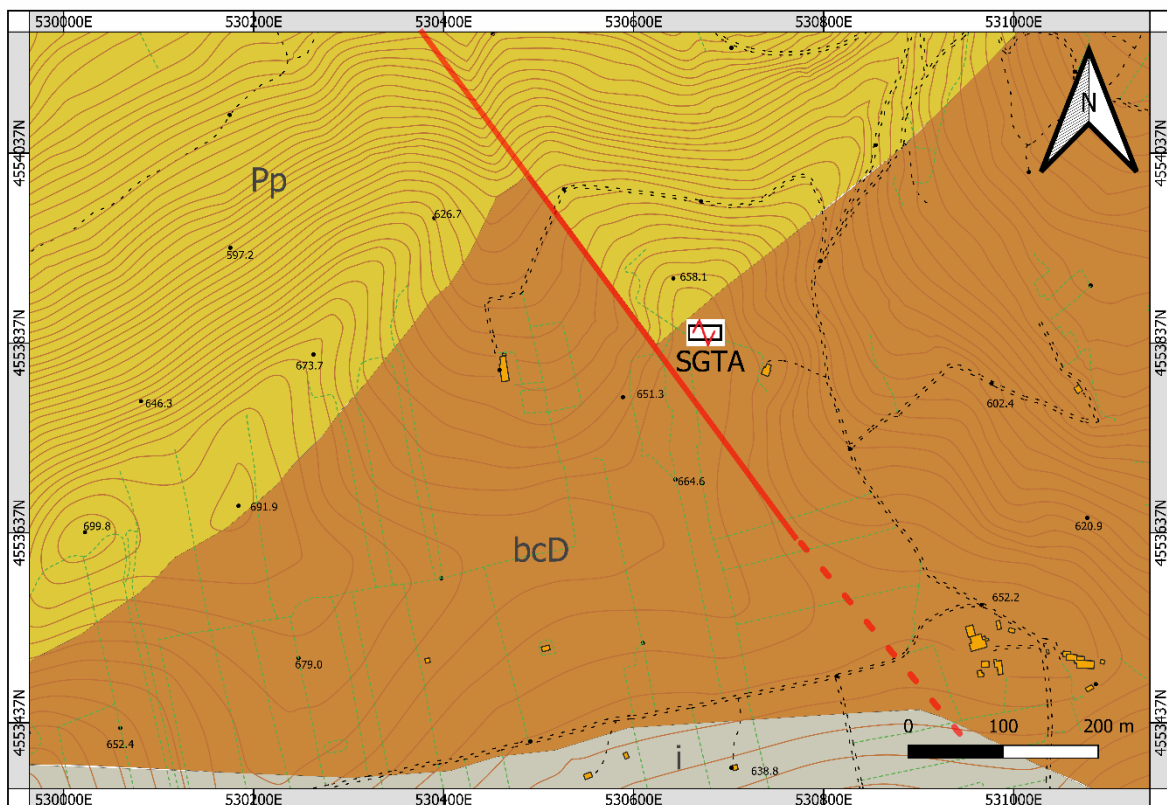
Figure 150. Location of the SGTA seismic station at Sant’Agata di Puglia (source CTR 1:5 000, the image could be rescaled, refer to the scale bar).

GEOLOGICAL AND TOPOGRAPHIC INFORMATION

According to the geologic map ISPRA 1:100 000 (Figure 72), the seismic station is located on the *Daunia formation (bcD)*, characterized by conglomerates and calcarenites alternating with marls and clay.

TYPE	NOTES	SCALE
CTR	Foglio 434054	1:5 000
ISPRA, carta geologica	Foglio 174, Ariano Irpino	1: 100 000

Table 85. Geological and geotechnical cartography available for the site.



LEGEND:

-  ACCELEROMETRIC STATION
-  Pp Puddinghe poligeniche (Pliocene)
-  bcD Formazione della Daunia (Miocene)
-  i Complesso indifferenziato

Figure 151. Geological map of the area surrounding the seismic station SGTA (source ISPRA 1:100 000, the image could be rescaled, refer to the scale bar).

GEOPHYSICAL SURVEY

We propose an average Vs model for the site, based on the joint fit of all the acquired surface-wave dispersion and H/V curves (Table 35). Since the H/V curves are more sensitive to local geological features compared to the array dispersion curves, the average Vs model might not faithfully reproduce the H/V features at high frequency.

The theoretical H/V curve overlapped to the experimental H/V curve could be computed on a slightly different model (see footnotes, if present).

SURVEY TYPE	N.	Acquisition length	Sampling rate [Hz]	NOTES	INSTRUMENT USED
Microtremor H/V ²⁰	4	20' each	512	All measurements on natural soil	Tromino® - MoHo srl
Active/passive 1D array ²¹	2	Active: MASW Passive: ReMi (7' recording)	512	16 geophones: 3 m inter-receiver distance (A01); 4 m inter-receiver distance (A02)	Seismograph: SoilSpy – MoHo srl Geophones: OYO - Geospace 4.5 Hz (vertical)

Table 86. List of the H/V and active/passive surface-wave arrays acquired at the site.

²⁰ The average amplitude spectra in velocity and their standard deviation are computed for each measurement point by splitting the recorded signal into 30 second non-overlapping windows. On average, 32 to 40 signal windows are retained to compute the average H/V curve and its standard deviation. Each window is detrended, tapered with a Bartlett window, zero-padded and FF-transformed. The Fourier spectra are smoothed according to triangular windows with width equal to 10% of the central frequency, in order to keep only the significant peaks.

²¹ The vertical-component Rayleigh-wave phase-velocity dispersion curves obtained by averaging several active and passive surveys are illustrated. Only the windows showing the lowest phase velocities (with the exclusion of the alias) are retained, for their being closer to the fundamental mode dispersion curve. The phase-velocity spectra are obtained by slant-stacking the seismograms and by applying a FFT.



Figure 152. Location of the active/passive surface-wave arrays and of the H/V recordings.

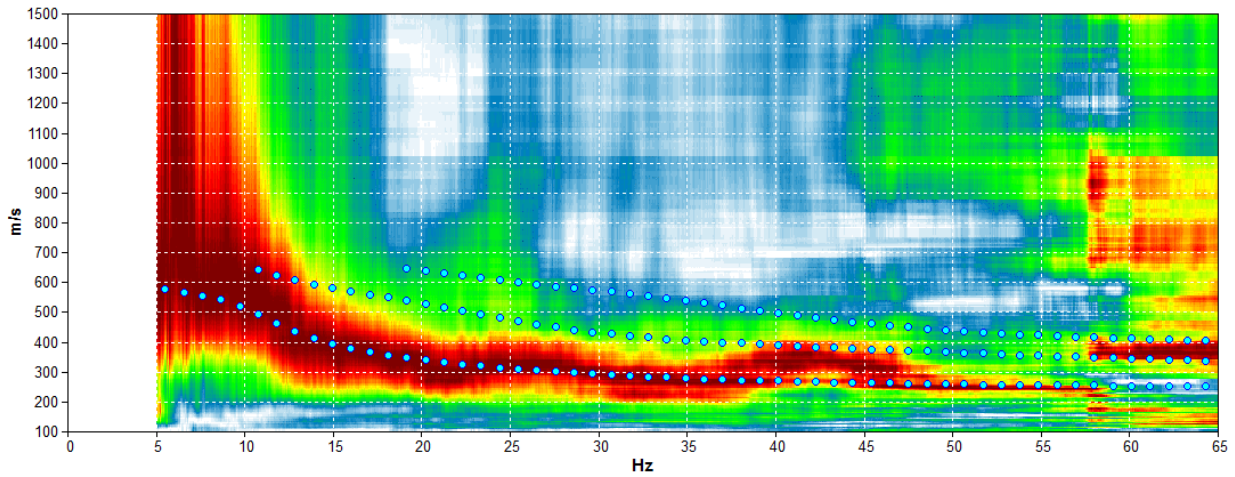


Figure 153. Average dispersion curves from the MASW and ReMi surveys at site A01. Synthetic dispersion curve for the model of Table 35 (light blue circles).

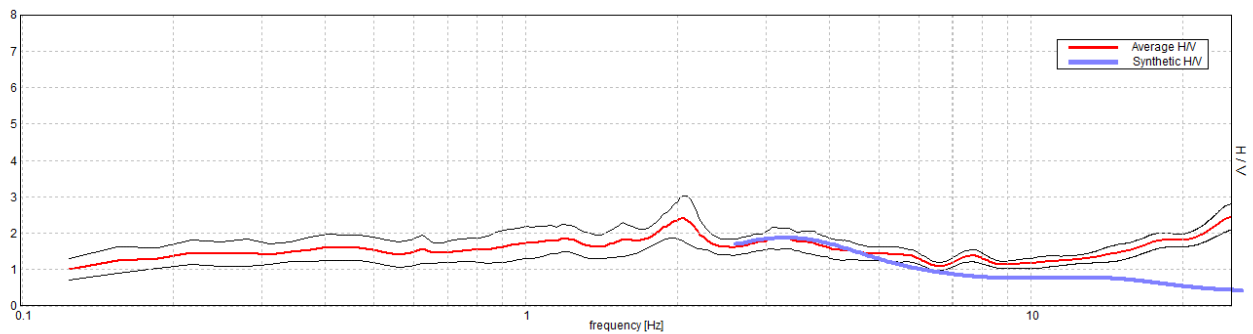


Figure 154. Experimental H/V curve acquired at site T01 (average in red, standard deviation in black). Synthetic H/V curve for the model of Table 35 (blue).

Depth at the bottom of the layer [m]	Thickness [m]	Vs [m/s]	Poisson ratio	Seismostratigraphic model obtained from:
4.00	4.00	260	0.48	0 – 45m H/V + Dispersion curve
8.00	4.00	350	0.47	
20.00	12.00	400	0.46	45 m – inf. H/V only
45.00	25.00	550	0.44	
inf.	inf.	700	0.42	

Table 87. Seismostratigraphic model proposed for the site.

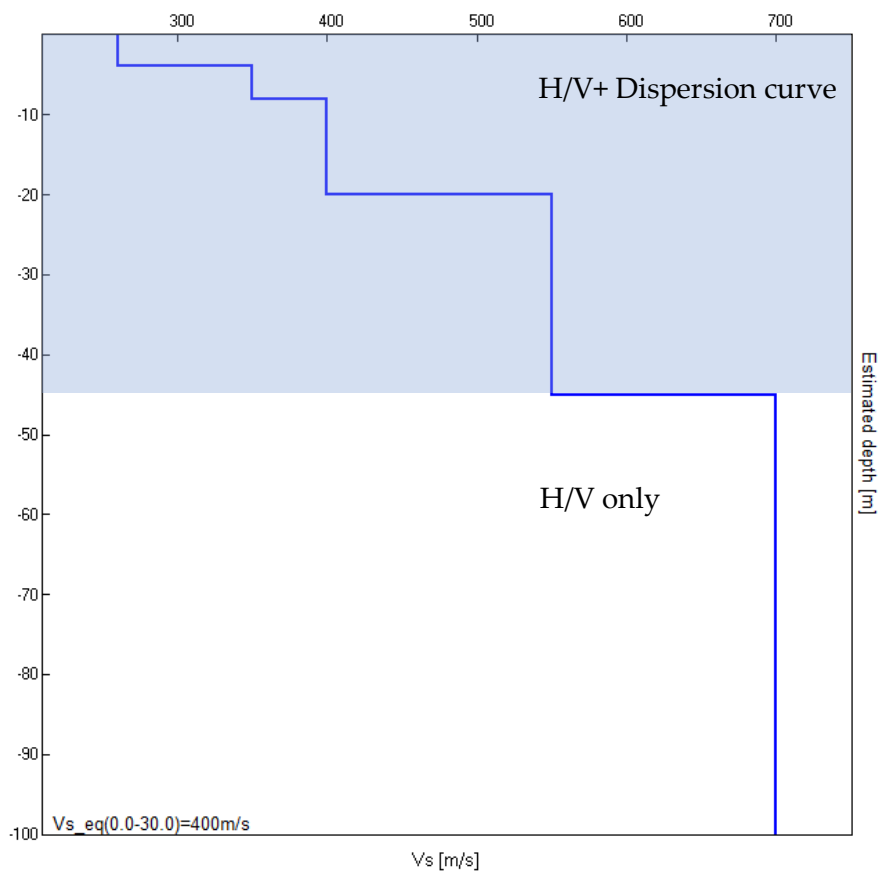


Figure 155. Vs model proposed for the site.

$V_{Seq}[0 - 30] m = 400 m/s *$

Class B site (NTC, 2018)

* Characteristic uncertainty is 20%

ADDITIONAL MATERIAL

In this section we present the characteristic H/V curve of the site (Figure 77) together with the single spectral components used to compute it, in order for the reader to understand the stratigraphic or artefactual nature of the H/V peaks (SESAME, 2004; Castellaro, 2016).

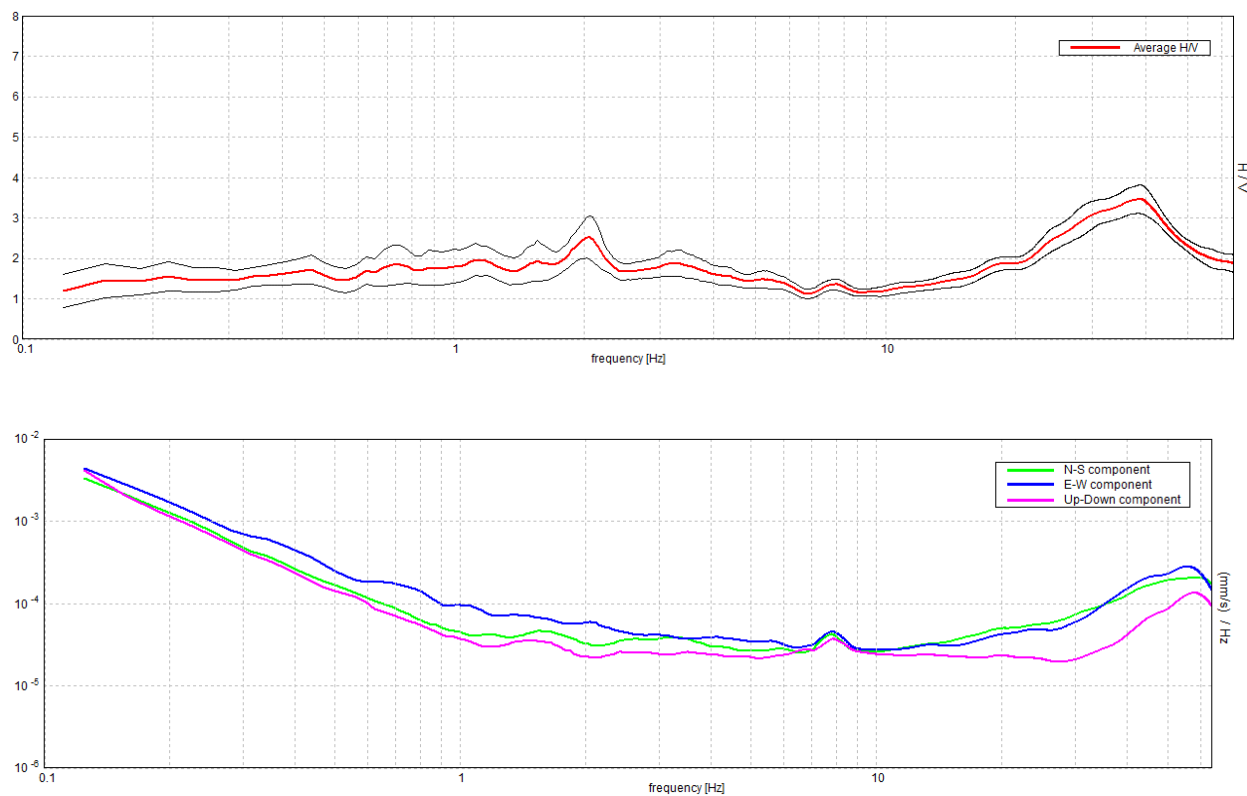


Figure 156. Top: characteristic H/V curve (average in red, standard deviation in black). Bottom: spectra of the single components of motion (NS, EW, Z) used to derive the H/V curve.

GALLERY



Figure 157. H/V recording at site T01 near the meteorological station.



Figure 158. H/V recording at site T03 near the SGTA seismic station.

REFERENCES

- Castellaro S., 2016. The complementarity of H/V and dispersion curves, *Geophysics*, 81, T323–T338
- Norme Tecniche sulle Costruzioni, 2018. Decreto Ministeriale 17/01/2018, Ministry of Infrastructures and Transportations, G.U. S.O. n.8 on 20/2/2018
- SESAME, 2004. Guidelines for the implementation of the H/V spectral ratio technique on ambient vibrations. Measurements, processing and interpretation, WP12 European commission - Research general directorate project no. EVG1-CT-2000-0026 SESAME, report D23.12, 62 pp.

Giulia Alessandrini¹, Giovanni Lattanzi¹, Stephen Slivicki², Giulia Sgattoni¹, Silvia Castellaro¹

¹ *Università di Bologna, Dipartimento di Fisica e Astronomia, Viale Carlo B. Pichat 8, 40127 Bologna (Italy)*

² *University of Wisconsin-River Falls (USA)*

Site characterization of the seismic station

IV.SNAL

Geophysical survey performed on
24th October 2019 (13.30 pm – 14.30 pm)

Partly funded by Contratto di Consulenza Commissionata per lo "Studio sismotettonico delle dighe Marana Capacciotti e San Pietro sul Torrente Osento e delle opere accessorie" – Consorzio di Bonifica per la Capitanata (2019)

IV.SNAL – SANT'ANGELO DEI LOMBARDI

CODE	NAME	Lat. [°] WGS-84	Lon. [°] WGS-84	Elevation [m]
SNAL	SANT'ANGELO DEI LOMBARDI	40.92542	15.20908	874
Address	Unnamed Road, 83054, Sant'Angelo dei Lombardi, AV, Italy			

Table 88. Code, name and WGS-84 coordinates of the seismic station.

SEISMIC STATION

SENSOR	unknown
DIGITIZER	unknown
HOUSING	Pillar inside the meteorologic station

Table 89. Instrumental chain installed at the seismic station.

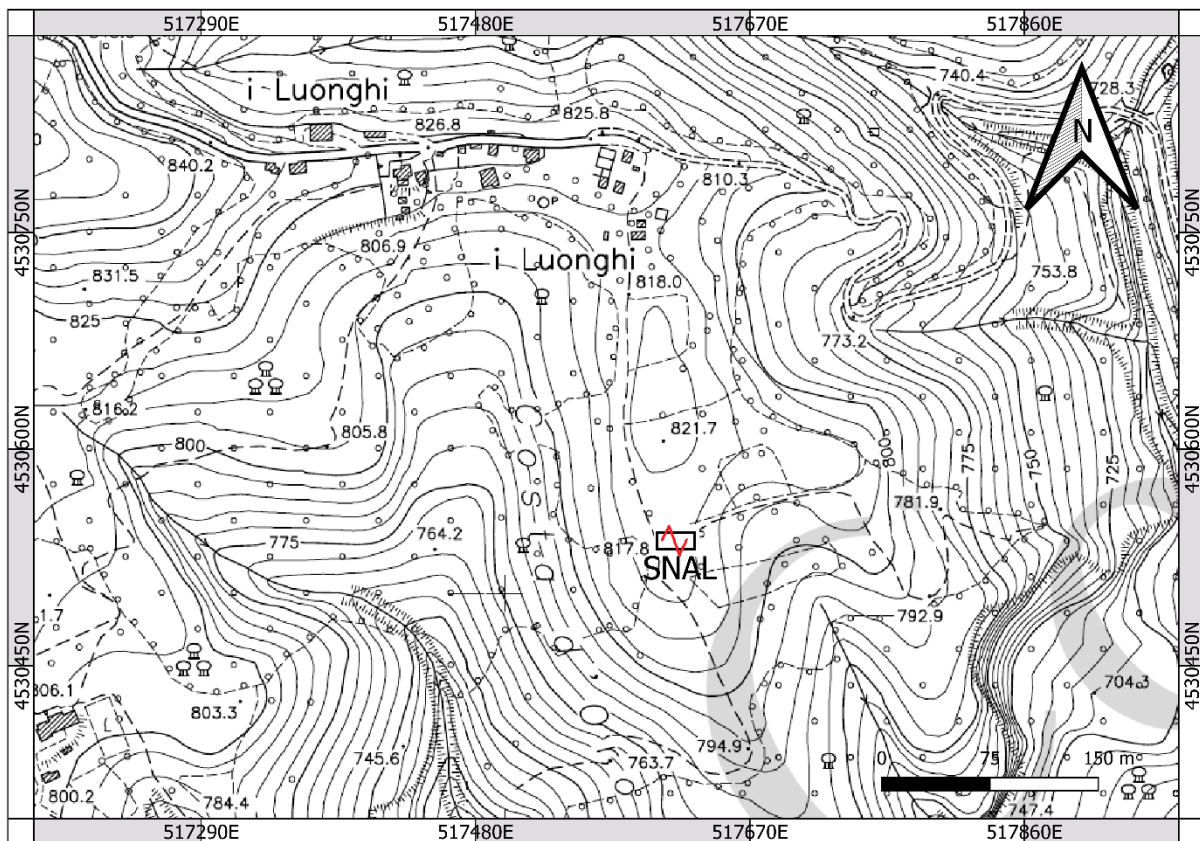


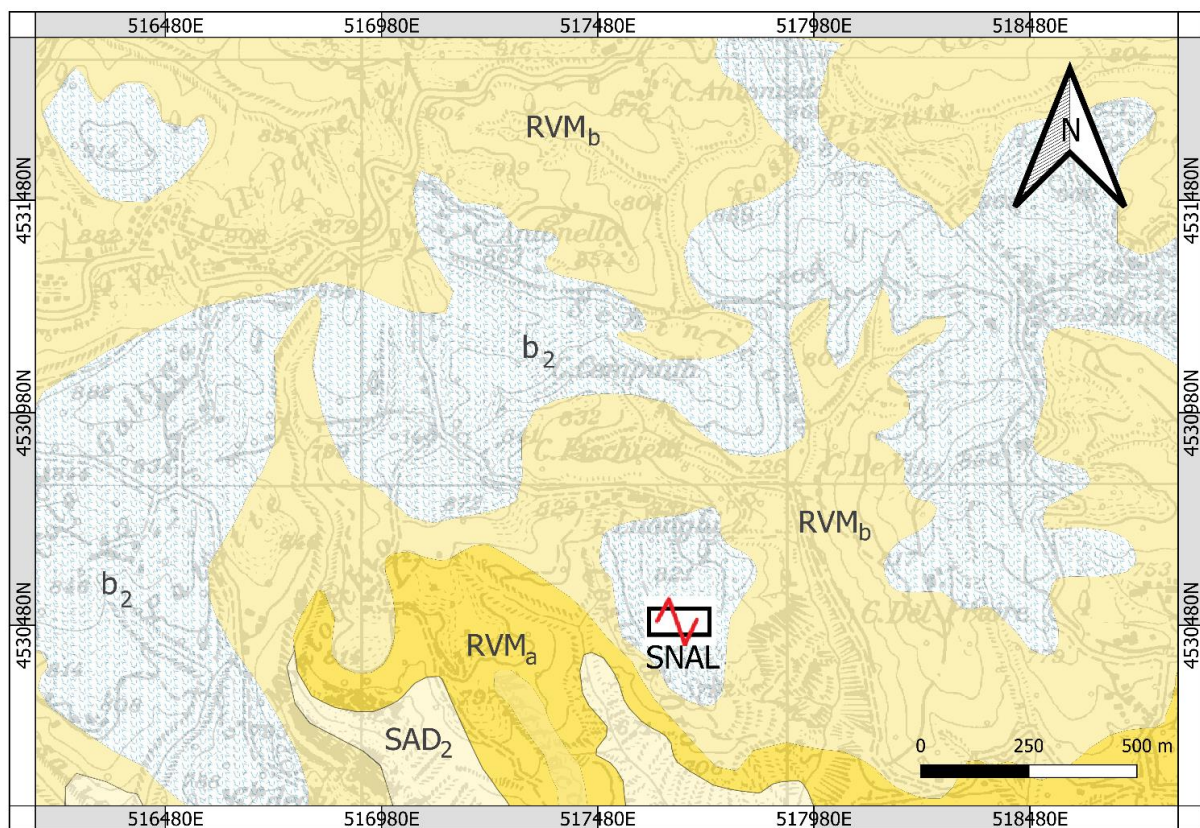
Figure 159. Location of the SNAL seismic station at Sant'Angelo dei Lombardi (source CTR 1:5 000, the image could be rescaled, refer to the scale bar).

GEOLOGICAL AND TOPOGRAPHIC INFORMATION

According to the CARG map (Figure 72), the seismic station is located on eluvial-colluvial deposits (b_2) which can reach maximum thickness of 2 m. These shallow deposits overlay the *sintema di Ruvo del Monte* deposits (RVM_b) characterized by conglomerates and sand. The maximum thickness of this litofaces is about 120 m.

TYPE	NOTES	SCALE
CTR	Foglio 450071 450074	1:5 000
CARG, carta geologica	Foglio 450, Sant Angelo dei Lombardi	1:50 000
ISPRA, carta geologica	Foglio 186, Sant' Angelo dei Lombardi	1:100 000

Table 90. Geological and geotechnical cartography available for the site.



LEGEND:

-  ACCELEROMETRIC STATION
-  b_2 Coltre eluvio-colluviale (Olocene)
-  RVM_a Sintema di Ruvo del Monte - Litofaces arenaceo sabbiosa (Pliocene inf.-Pliocene sup.)
-  RVM_b Sintema di Ruvo del Monte - Litofaces conglomeratico sabbiosa (Pliocene inf.-Pliocene sup.)
-  SAD_2 Sintema di Andretta - subsintema di Vallicella (Pliocene inf.)

Figure 160. Geological map of the area surrounding the seismic station SNAL (source CARG 1:50 000, the image could be rescaled, refer to the scale bar).

GEOPHYSICAL SURVEY

We propose an average V_s model for the site, based on the joint fit of all the acquired surface-wave dispersion and H/V curves (Table 35). Since the H/V curves are more sensitive to local geological features compared to the array dispersion curves, the average V_s model might not faithfully reproduce the H/V features at high frequency.

The theoretical H/V curve overlapped to the experimental H/V curve could be computed on a slightly different model (see footnotes, if present).

SURVEY TYPE	N.	Acquisition length	Sampling rate [Hz]	NOTES	INSTRUMENT USED
Microtremor H/V ²²	5	20' each	512	All measurements on natural soil	Tromino® - MoHo srl
Active/passive 1D array ²³	1	Active: MASW Passive: ReMi (7' recording)	512	16 geophones, 3 m inter-receiver distance	Seismograph: SoilSpy – MoHo srl Geophones: OYO - Geospace 4.5 Hz (vertical)

Table 91. List of the H/V and active/passive surface-wave arrays acquired at the site.

²² The average amplitude spectra in velocity and their standard deviation are computed for each measurement point by splitting the recorded signal into 30 second non-overlapping windows. On average, 32 to 40 signal windows are retained to compute the average H/V curve and its standard deviation. Each window is detrended, tapered with a Bartlett window, zero-padded and FF-transformed. The Fourier spectra are smoothed according to triangular windows with width equal to 10% of the central frequency, in order to keep only the significant peaks.

²³ The vertical-component Rayleigh-wave phase-velocity dispersion curves obtained by averaging several active and passive surveys are illustrated. Only the windows showing the lowest phase velocities (with the exclusion of the alias) are retained, for their being closer to the fundamental mode dispersion curve. The phase-velocity spectra are obtained by slant-stacking the seismograms and by applying a FFT.



Figure 161. Location of the active/passive surface-wave arrays and of the H/V recordings.

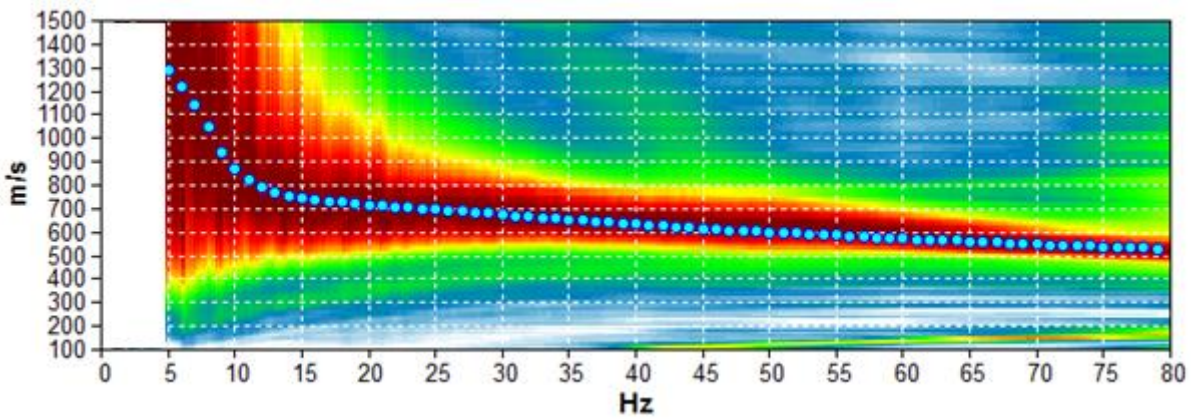


Figure 162. Average dispersion curve from the MASW and ReMi surveys at site A01. Synthetic dispersion curve for the model of Table 35 (light blue circles).

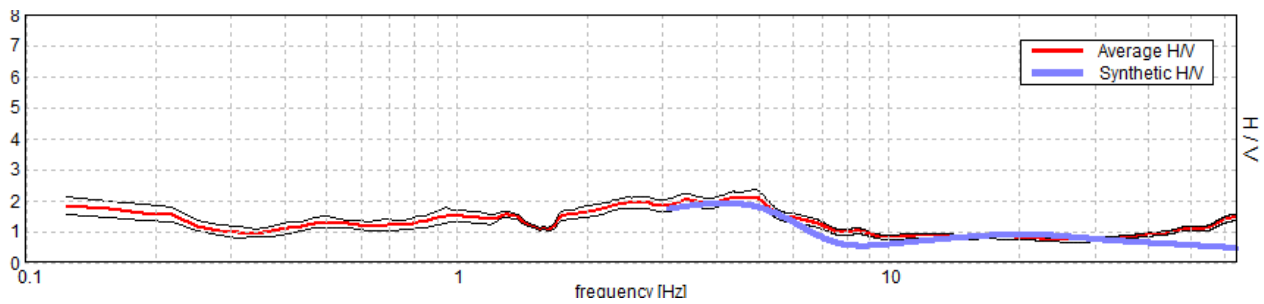


Figure 163. Experimental H/V curve acquired at site T04 (average in red, standard deviation in black). Synthetic H/V curve for the model of Table 35 (blue).

Depth at the bottom of the layer [m]	Thickness [m]	Vs [m/s]	Poisson ratio	Seismostratigraphic model obtained from:
3.00	3.00	500	0.47	0 – 55 m H/V + Dispersion curve
9.00	6.00	670	0.44	
41.00	32.00	800	0.43	55 m – inf. H/V only
131.00	90.00	1400	0.40	
inf.	inf.	1700	0.40	

Table 92. Seismostratigraphic model proposed for the site.

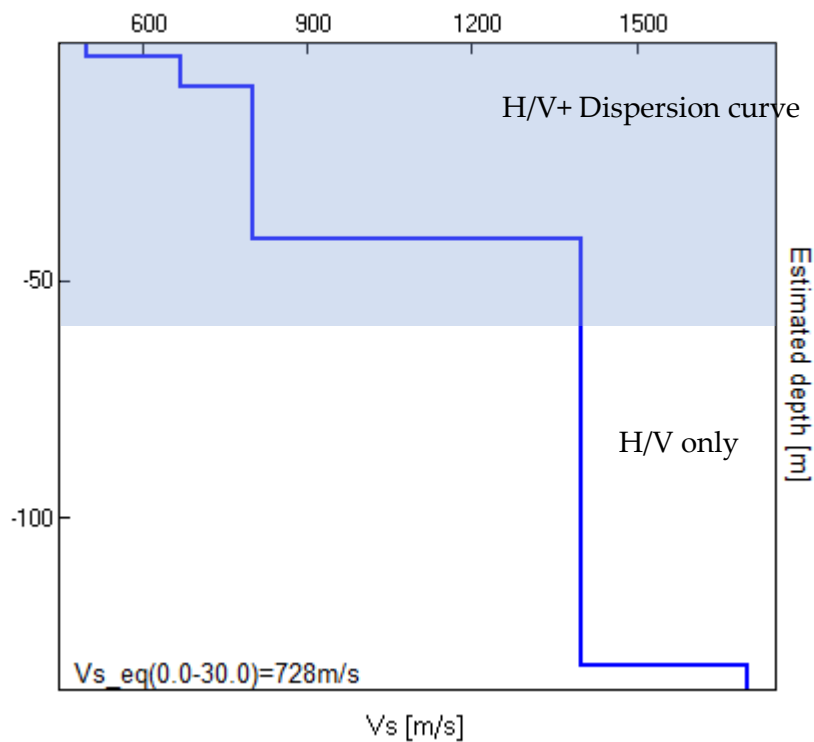


Figure 164. Vs model proposed for the site.

$V_{Seq}[0 - 9] m = 600 m/s *$
 $V_{S_{30}}[0 - 30] m = 730 m/s *$
 Class B site (NTC, 2018)
 Class B site (NTC, 2008)

* Characteristic uncertainty is 20%

ADDITIONAL MATERIAL

In this section we present the characteristic H/V curve of the site (Figure 77) together with the single spectral components used to compute it, in order for the reader to understand the stratigraphic or artefactual nature of the H/V peaks (SESAME, 2004; Castellaro, 2016). The SESAME (2004) criteria for the main H/V peak are listed in Table 82.

In Figure 78 we present a selection of H/V curves acquired in the proximity of the seismic station to show the spatial variability of this function.

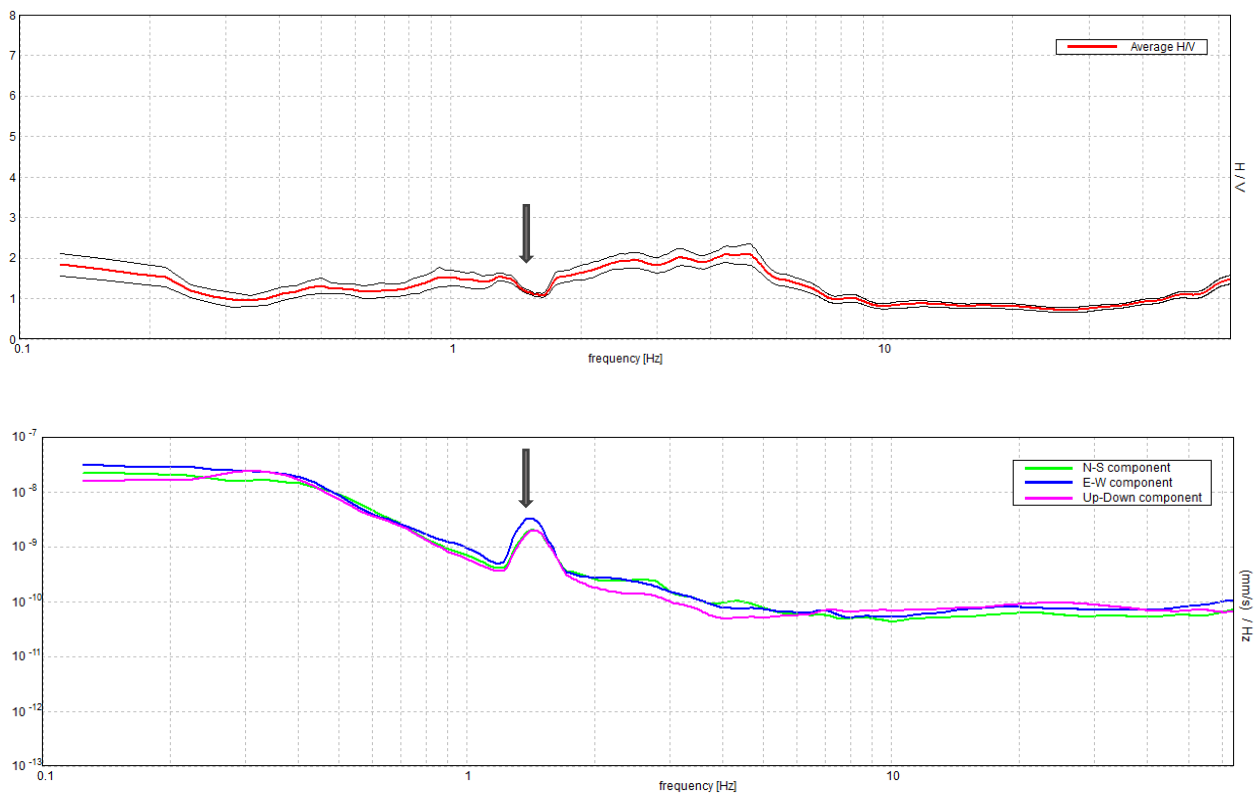


Figure 165. Top: characteristic H/V curve (average in red, standard deviation in black). Bottom: spectra of the single components of motion (NS, EW, Z) used to derive the H/V curve. The arrow indicates an artefact that shows up in the H/V curve as a trough.

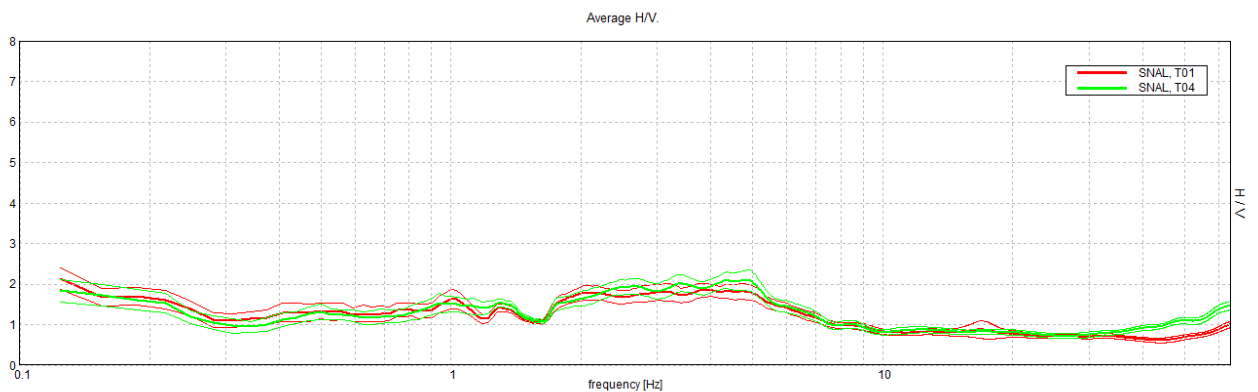


Figure 166. Comparison of the H/V curves acquired in the proximity of the seismic station (refer to Figure 73 for the location).

[According to the SESAME, 2004 guidelines]

Max. H/V at 4.31 ± 1.04 Hz (in the range 0.2 - 64.0 Hz).

Criteria for a reliable H/V curve			
[All 3 should be fulfilled]			
$f_0 > 10 / L_w$	$4.31 > 0.50$	OK	
$n_c(f_0) > 200$	$4053.8 > 200$	OK	
$\sigma_A(f) < 2$ for $0.5f_0 < f < 2f_0$ if $f_0 > 0.5\text{Hz}$ $\sigma_A(f) < 3$ for $0.5f_0 < f < 2f_0$ if $f_0 < 0.5\text{Hz}$	Exceeded 0 out of 208 times	OK	
Criteria for a clear H/V peak			
[At least 5 out of 6 should be fulfilled]			
Exists f^- in $[f_0/4, f_0] \mid A_{H/V}(f^-) < A_0 / 2$	1.625 Hz	OK	
Exists f^+ in $[f_0, 4f_0] \mid A_{H/V}(f^+) < A_0 / 2$	7.344 Hz	OK	
$A_0 > 2$	$2.12 > 2$	OK	
$f_{\text{peak}}[A_{H/V}(f) \pm \sigma_A(f)] = f_0 \pm 5\%$	$ 0.2423 < 0.05$		NO
$\sigma_f < \sigma(f_0)$	$1.04491 < 0.21563$		NO
$\sigma_A(f_0) < \sigma(f_0)$	$0.2052 < 1.58$	OK	

L_w	window length
n_w	number of windows used in the analysis
$n_c = L_w n_w f_0$	number of significant cycles
f	current frequency
f_0	H/V peak frequency
σ_f	standard deviation of H/V peak frequency
$\sigma(f_0)$	threshold value for the stability condition $\sigma_f < \sigma(f_0)$
A_0	H/V peak amplitude at frequency f_0
$A_{H/V}(f)$	H/V curve amplitude at frequency f
f^-	frequency between $f_0/4$ and f_0 for which $A_{H/V}(f^-) < A_0/2$
f^+	frequency between f_0 and $4f_0$ for which $A_{H/V}(f^+) < A_0/2$
$\sigma_A(f)$	standard deviation of $A_{H/V}(f)$, $\sigma_A(f)$ is the factor by which the mean $A_{H/V}(f)$ curve should be multiplied or divided
$\sigma_{\log H/V}(f)$	standard deviation of $\log A_{H/V}(f)$ curve
$\sigma(f_0)$	threshold value for the stability condition $\sigma_A(f) < \sigma(f_0)$

Threshold values for ω_r and $\omega_A(f_0)$					
Freq. range [Hz]	< 0.2	0.2 – 0.5	0.5 – 1.0	1.0 – 2.0	> 2.0
$\omega(f_0)$ [Hz]	$0.25 f_0$	$0.2 f_0$	$0.15 f_0$	$0.10 f_0$	$0.05 f_0$
$\omega(f_0)$ for $\omega_A(f_0)$	3.0	2.5	2.0	1.78	1.58
$\log \omega(f_0)$ for $\omega_{\log H/V}(f_0)$	0.48	0.40	0.30	0.25	0.20

Table 93. SESAME (2004) criteria applied to the main resonance peak identified in the characteristic H/V curve.

GALLERY



Figure 167. Location of the H/V recording on the SNAL seismic station.

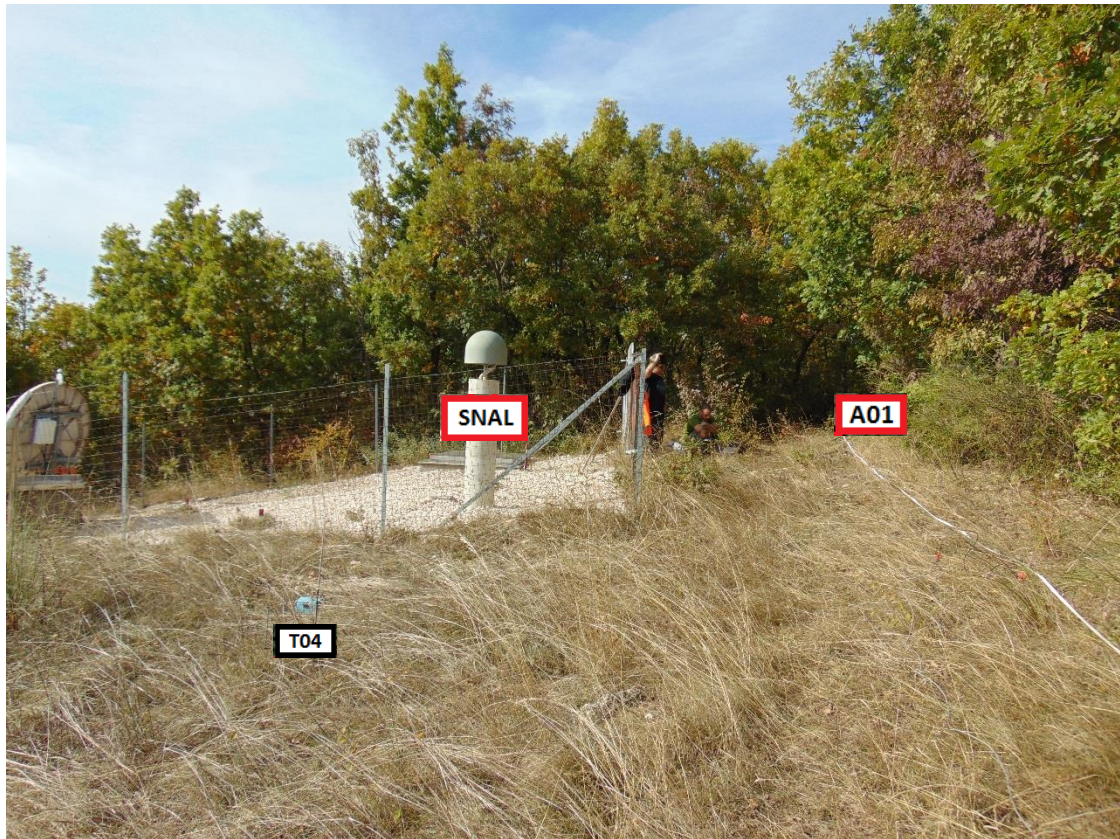


Figure 168. Location of the active/passive surface waves array A01 and H/V T05 recording.

REFERENCES

- Castellaro S., 2016. The complementarity of H/V and dispersion curves, *Geophysics*, 81, T323–T338
- ISPRA, Carta Geologica d'Italia alla scala 1:50 000, Foglio 450 "Sant' Angelo dei Lombardi"
- Norme Tecniche sulle Costruzioni, 2008. Decreto Ministeriale 14/01/2008, Ministry of Infrastructures and Transportations, G.U. S.O. n.29 on 4/2/2008
- Norme Tecniche sulle Costruzioni, 2018. Decreto Ministeriale 17/01/2018, Ministry of Infrastructures and Transportations, G.U. S.O. n.8 on 20/2/2018
- SESAME, 2004. Guidelines for the implementation of the H/V spectral ratio technique on ambient vibrations. Measurements, processing and interpretation, WP12 European commission - Research general directorate project no. EVG1-CT-2000-0026 SESAME, report D23.12, 62 pp.

Seismic Station Installations and their Impact on the Recorded Signals and Derived Quantities

Silvia Castellaro¹, Giulia Alessandrini¹, Giuseppe Musinu²

¹Dipartimento di Fisica e Astronomia, Alma Mater Studiorum Università di Bologna, viale C. B. Pichat 8,
Italy

²ENSER srl, viale A. Baccarini 29, Faenza, Ravenna – Italy

Abstract

The role of local geology in controlling ground motion has long been acknowledged. Consequently, increasing attention is paid to the assessment of the geophysical properties of the soils at the seismic stations, which impact the station recordings and a series of related quantities, particularly those referring to seismic hazard estimates. Not the same level of attention is commonly dedicated to the seismic station installation, to the point that it is generally believed that housings/shelters containing seismic instruments are of no interest because they can only affect frequencies well above the engineering range of interest. By using examples from seismic and accelerometric stations, we describe the 1) housing, 2) foundation and 3) pillar effects on the seismic records. We propose a simple working scheme to identify the existence of potential installation-related issues and to assess the frequency fidelity range of response of a seismic station to ground motion. The hope is that, besides the parameters (V_{s30} , soil classes etc.) that start to be routinely introduced in the seismic archives, the assessment of the maximum reliable frequency, under which no soil-structure interaction is expected, also becomes a mandatory information. In our experience, for some installation sites, the maximum reliable frequency can even be less than a very few Hz.

Introduction

At the early stages of seismology, seismic stations were installed on stiff rock (Bormann, 2002), to minimize the effects of the fine sediments/rock weathering on the recorded seismic waves. The size

of permanent installation seismometers, their need for screws, levelling, batteries and cables led to place them on artificial ground, such as *ad hoc* concrete slabs. There is also sometimes the perception that something stiff as a concrete slab or pillar between the sensor and the object of measurement improves the coupling between the two. In addition, to ensure protection from environmental conditions and vandalism, many seismic stations were placed inside small or large structures.

The need for homogenous and dense seismic networks progressively required seismic stations to be installed on any type of geological condition and, in parallel, increasing attention started to be paid to the characterization of the geophysical properties of the soils at the seismic stations (see Cultrera et al., 2021, for a review). In fact, their impact on the station recordings and on the subsequent hazard estimates can be large. On the opposite, not enough attention is still paid to the seismic station installation. It is generally recognized that this can affect the seismic recordings, but it is usually believed that housings/shelters can affect only frequencies well above the engineering range of interest. This led to the habit of naming ‘free-field stations’, stations that are not under free-field conditions (see also Hollender *et al.*, 2020, who noted the same issues).

The seismic sensor installation can affect seismometer recordings, both under microtremor and earthquake excitation, essentially in 3 strongly interconnected ways that we will discuss in the paper:

- 1) *Housing effect*: the structure/cabin inside which the sensor is installed has its own dynamics, ruled by its vibration modes. This motion is transmitted to the ground and recorded by the seismometer, even when the latter is placed on a pillar isolated from the foundation by means of a cut all around (Figure 169).
- 2) *Foundation effect*: stiff foundations (e.g., concrete slab on soft soils) perturb the incident wavefield. Typically, the horizontal motion recorded on the top of a foundation is strongly deamplified, compared to the free-field motion, at all the wavelengths smaller than and comparable to the foundation size.
- 3) *Pillar effect*: sensors are often placed on concrete pillars, detached from the foundation by means of a cut, with the intention of dynamically isolating the sensor from the surrounding foundation/structure. We will show that the proximity of the pillar to the foundation and the connection between the two provided by the ground, does not warrant the desired effect.

The effect of foundations on seismic motion was studied by several authors (e.g. Bycroft, 1980; Crouse and Husmand, 1989; Luco *et al.*, 1986; 1990; Castellaro and Mulargia, 2011; Cavalieri *et al.*,

2021). Luco *et al.* (1990), as an example, studied 12 different foundation geometries and performed a parametric study, by changing the size, the embedment depth, the extension above the surface. These results, however, strongly depended on the specific input used to study the phenomenon and the conclusions, though very relevant, were difficult to be used because they lacked generality.

Bycroft (1977, 1980) recommended the use of large and thick foundations on nuclear power plants to reduce the seismic input to the overlying structures. If this reduction is clearly welcome in the case of structures to protect them from seismic inputs, it is definitely unwelcome in the case of seismic stations, which are expected to faithfully record the incoming signal (at points 1 or 3 in Figure 169) and not its downsized version on the top of the foundation (point 2 in Figure 169).

The soil-structure interaction and the soil-city interaction were studied by even more authors (*Soil-structure*: Jennings, 1970; Wong and Trifunac, 1975; Bycroft 1977; Safak, 1998; Guéguen *et al.*, 2000; Chavez-Garcia and Cardenas-Soto, 2002; Guéguen *et al.*, 2002; Mucciarelli *et al.*, 2003; Cornou *et al.*, 2004; Gallipoli *et al.*, 2004; Guéguen and Bard, 2005; Gallipoli *et al.*, 2006; Kham *et al.*, 2006; Ditommaso *et al.*, 2010a,b; Laurenzano *et al.*, 2010; Massa *et al.*, 2010; Castellaro and Mulargia, 2011; Castellaro *et al.*, 2013; Sotiriadis *et al.*, 2019; Hollender *et al.*, 2020. *Soil-city*: Wirgin and Bard, 1996; Guéguen *et al.*, 2000; Cloteau and Aubry, 2001; Guéguen *et al.*, 2002; Kham *et al.*, 2006; Schwan *et al.*, 2016; Isbilibiroglu *et al.*, 2015; Kurand and Narayan, 2018).

All these studies had little impact on the practical procedures behind seismic installations, also because their effect is hard to predict and to remove.

A recent trend is to move seismometers inside dedicated small fiber-glass cabins (e.g., CER panel in Figure 170): the smaller the foundations, the smaller the range of wavelengths affected by the foundation itself. The smaller the protection structure, the larger its eigen-frequencies (thus beyond the frequency range of engineering interest). However, small fiber-glass structures have much lower stiffness k and mass m compared to traditional structures and since the eigen-frequency of a structure is proportional to $\sqrt{\frac{k}{m}}$, these values can still fall inside the frequency range of engineering interest, altering the motion recorded by the seismometer.

In this paper we provide some examples about: a) the elements that can affect the seismic station fidelity to ground motion, b) how to experimentally assess such fidelity.

Considering the variety of seismic installations that depends on national procedures, on specific soil conditions, on local construction habits, on seismic instrumentation and so on, we do not attempt

any systematic/parametric study, but we illustrate the problems by using real examples from seismic stations belonging to the Italian National Seismic or Accelerometric (strong motion, IT) networks. We focus on a few stations only, but the potential diffusion of the problem will be discussed at the end of the paper and, as noted by Hollender *et al.* (2020), it is not confined to single nations.

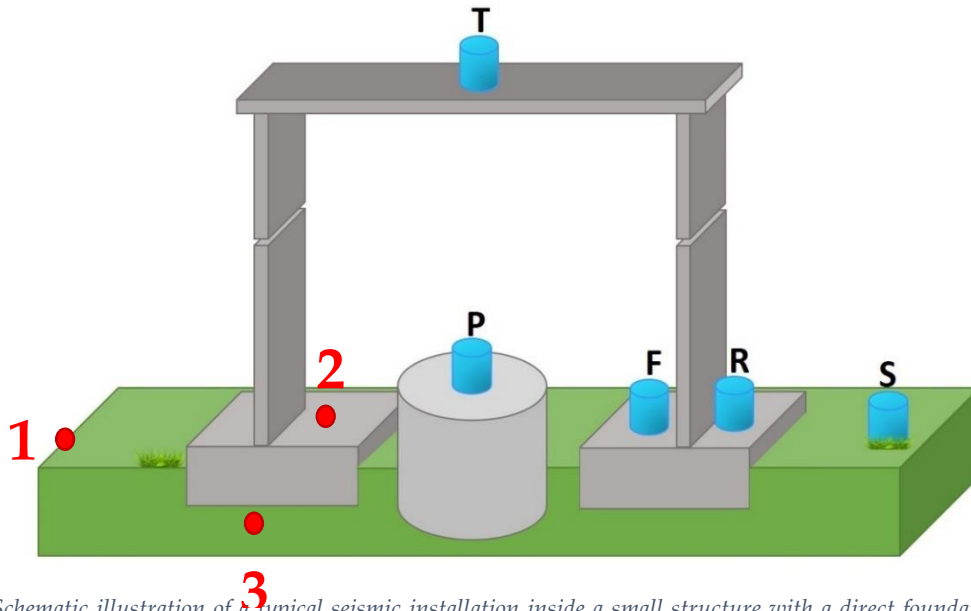


Figure 169. Schematic illustration of a typical seismic installation inside a small structure with a direct foundation. T (top) is the measurement point on the top of the structure (to characterize its fundamental mode), P on the pillar, F on the foundation, R on the foundation rim and S on natural soil.

Elements that can affect the seismic station fidelity to ground motion

We refer to typical seismic stations settled inside big or small structures (Figure 169) and discuss the 1) housing, 2) foundation and 3) pillar impact. These are strongly interconnected, therefore sometimes the discussion will necessarily mix them up.

We use examples from the Italian seismic/accelerometric stations illustrated in Figure 170. For each example we provide the station code, a picture and the soil type synthesized by means of its Vs30. Additional information about each station can be found by searching the station code in the [INGV Itaca](#) database (D'Amico *et al.*, 2020). At the example sites, we collected simultaneous ambient noise measurements at the T (top), P (pillar), F (foundation), R (foundation rim), S (natural soil) locations given in Figure 169.

For all measurements we used Tromino® Blu 3-component portable velocity/acceleration sensors by MoHo srl (Italy), after checking that their response was identical. The signal was acquired at all

sites for a minimum of 30 minutes, then split into non overlapping window. The FFT was applied to each window and the resulting spectra were smoothed with triangular functions having a width equal to 3 per cent of the central frequency. In the end, the average spectra and their standard deviations were computed.

<p align="center">MRN Mirandola (Italy), $V_{s30} = 210$ m/s</p>	<p align="center">FRN Fornovo di Taro (Italy), $V_{s30} = 350$ m/s</p>	<p align="center">CER Cerignola $V_{s30} = 400$ m/s</p>	
			
<p align="center">NAS Naso (Sicily, Italy) $V_{s30} = 310$ m/s</p>	<p align="center">CRL Corleone (Sicily, Italy) $V_{s30} = 370$ m/s</p>	<p align="center">PNN Pennabilli (Italy) $V_{s30} = 350$ m/s</p>	<p align="center">ALF Alfonsine (Italy) $V_{s30} = 240$ m/s</p>
			

Figure 170. A set of stations of the Italian accelerometric (IT) and seismic (IV) network: small housing (MRN), tower-structures of the national electric service (FRN, NAS, CRL, PNN, ALF) and fiber-glass cabin (CER). A typical pillar with the cut separating it from the foundation is also shown for the MRN station. The pillar is present in most of the Italian installations and can also be square in shape, as in the case of CER. The instruments used for this survey can be seen in the panel of MRN and CER (blue and red boxes). The letter P stands for pillar, F for foundation, R for foundation rim.

The housing effect

Phenomenological evidence

The influence of buildings on ground motion recorded by sensors inside or in their proximity is widely acknowledged (see references in the Introduction). Less acknowledged is the direct influence of the housing on the seismometer recordings that it should protect.

The motion of structures is ruled by the superposition of the motions occurring at their natural frequencies, $f_{i=0,\dots,n}^{Stru}$. When a structure vibrates - due to earthquakes, microtremor, wind - part of this vibration is radiated to the soil and dissipated. The fraction of motion radiated back to the foundation can roughly be estimated by measuring the spectral amplitude of motion on the top of the structure (T in Figure 169) and on its foundation (F or R in Figure 169) or just off the foundation (S in Figure 169), at the same frequencies f_i^{Stru} and time. In practice, this fraction of motion is recorded also by the sensors placed on the pillar (P in Figure 169) because the vibration is efficiently transmitted through the ground.

To show this, we compare the spectra of the motion recorded on the top of the cabins with those recorded at the same time on the pillar or foundation (T/P and T/F ratios) and just outside the cabin (T/S ratios). We also compare the motion recorded on the pillar or foundation with the motion recorded in free-field (P/S, F/S ratios). When no effect is present, we expect these last two ratios to be equal to 1 at all frequencies.

We start from the case of the MRN station, which is hosted in a small cabin (approx. 4 m x 3 m x 4 m, Figure 170), whose bending frequencies are 10 and 17 Hz in the transversal direction, as evident in the T/S_{ref} and T/F spectral ratios of Figure 171. We focus on the transversal direction because it is associated to the lowest resonance frequency, but the same discussion would apply to the longitudinal direction, along which the first bending mode is 15 Hz. We see that the F/S_{ref} and P/S_{ref} spectral ratios are identical, which means that the pillar sensor measures the same things as the foundation sensor, despite the cut all around it. This was observed also in Mucciarelli *et al.* (2003) and Castellaro and Mulargia (2009).

The F/S_{ref} ratio illustrates the role of the foundation on the incoming waves in respect to the real free-field condition. If the foundation had no effect, this ratio should be equal 1 at all frequencies, which is not. S_i/S_{ref} is the ratio between the recording acquired on the soil just off the station (S_i) and on the soil at a few meters distance from the station (usually less than 5 m, S_{ref}). This ratio tends to 1 but there are still some minor differences due to the foundation still very close to S_i.

We note that if the pillar were isolated from the surrounding structure, we should not see any amplification in the P/S_{ref} spectra at the resonance frequencies of the structure. Figure 171 shows that

this is not the case: the pillar is affected by the vibration modes of the overlying cabin, in the same way in which the foundation is (F/S_{ref}).

Despite the limited size of the hosting structure, we can assess, from the F/S_{ref} and P/S_{ref} ratios, that the motion recorded from this station is perturbed at frequencies larger than 8 Hz.

As a further example, we present in Figure 172 the spectral ratios recorded on the foundation vs. natural soil at two other larger-in-size stations (NAS and PNN, Figure 170). Again, we see that the seismic motion recorded at these sites is perturbed by the eigen-frequencies of the cabin at ≈ 7 Hz in one case and ≈ 5 Hz in the other case. These are frequencies of large engineering interest, but the motion recorded from the seismometers at these sites is not a faithful reproduction of the seismic input above ≈ 6.5 and 4 Hz, respectively.

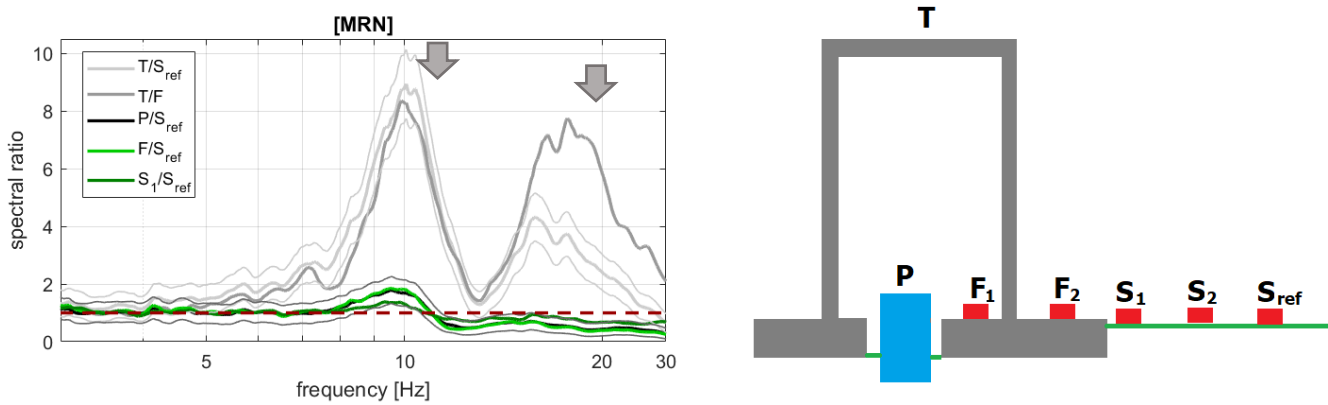


Figure 171. Spectral ratios of the motion recorded along the transversal direction of the cabin MRN at different locations, whose symbols are given in the right panel. The T/S_{ref} and T/F spectral ratios show the natural vibration modes of the structure (gray arrows at 10 Hz, 17 Hz). The P/S_{ref} and F/S_{ref} ratios show the effect of the foundation on the incoming waves in respect to the real free-field condition. If the foundation induced no effect, these ratios should be equal 1 at all frequencies. S_1/S_{ref} is the ratio between the recording acquired on the soil just off the station (S_1) and on the soil at a few meters distance from the station (usually 3-5 m from the foundation rim). S_1/S_{ref} tends to 1 but the eigen-mode of the structure is still visible.

The standard deviation of the spectral ratios is shown only in the two extreme cases, not to impair the readability of the plots. It was checked that its amplitude is in the same order of magnitude also when not shown.

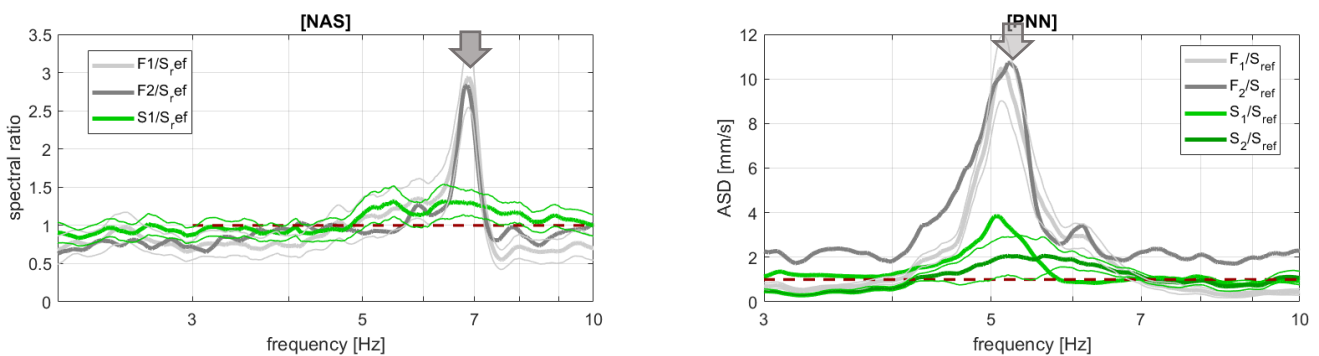


Figure 172. Spectral ratios of the motion recorded along the transversal direction of the cabins NAS and PNN at different locations, whose symbols are given in the right panel of Figure 171. In the F/S_{ref} ratios the natural vibration modes of the structure (6.8 Hz and

5.2 Hz for NAS and PNN, respectively) can be clearly identified. These are progressively less noticeable in the S_1/S_{ref} and S_2/S_{ref} ratios. Thick lines are the average values, thin lines indicate the standard deviations.

Effects on derived quantities

On H/V

Let us now consider case of CRL station in Sicily (Figure 170). The H/V curve computed from the data recorded by the official instrument installed on the pillar and provided by the national seismic agency is shown on the left panel of Figure 173. It exhibits two peaks passing the SESAME (2004) criteria. In the official station report, the 0.28 Hz frequency peak is indicated as fundamental mode of the site, while the 6 Hz frequency peak is marked as an additional site frequency and it passes even more SESAME (2004) criteria than the fundamental peak.

At this site we performed some measurements inside the niche in the wall of the cabin (red circle in Figure 169) and on the perimeter of the foundation, on natural soil. The spectra of these measurements (right panel in Figure 173) clearly show that the natural modes of the cabin are 7, 18, 30 Hz and are not visible in the free-field S recording, with the only exception of the small disturbance in the vertical component at the fundamental frequency of the structure (7 Hz), which is an effect of structural rocking. This typically has an amplitude which is 1/10 of the horizontal component amplitude.

The 6 Hz H/V peak frequency, identified in the official station report as 'reliable', is thus not a soil property but the vibration mode of the cabin, as recorded by the pillar sensor. As a consequence, automatic peak recognition algorithms in the case of sensors installed inside structures of any type should be avoided.

We take this opportunity to note that, despite its large use even on structures, the H/V method (here providing a peak at 6 Hz) is not suitable to detect the resonance of structures (in this case 7 Hz). By dividing the horizontal and vertical components, the H/V ratio mixes different structural behaviors, acting in different directions and occurring at different frequencies. This easily result in a biased estimate of the structure eigenfrequencies, as in this case.

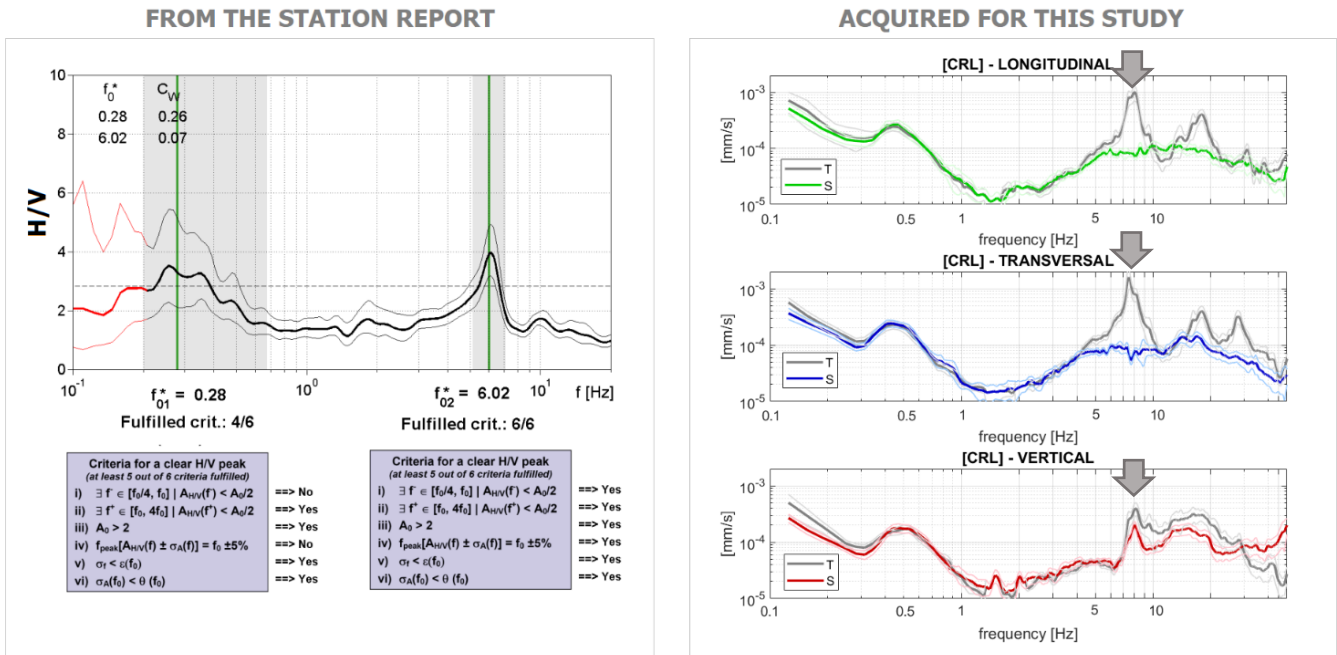


Figure 173. Left panel: H/V curve computed on the data acquired from the official instrument installed on the pillar at the CRL station. According to the station report, 2 peaks pass the SESAME (2004) criteria. Our measurements (right panel), performed on the top of the cabin (T) and on the natural soil just off the station (S) clearly show that the 6 Hz peak is the eigen-period of the cabin and not a soil property. Thick lines are the average values, thin lines indicate the standard deviations.

On response spectra

Let us now consider an intermediate size event (PGA = 0.25 g) recorded in real free-field conditions (black curves in Figure 174) at the MRN site. We treat the MRN housing as single degree of freedom oscillator with natural frequency and damping as directly measured (10 Hz for the transversal component, Figure 171, and 5% damping as computed by the DECÒ method in Castellaro, 2016a). We ignore higher modes because they fall at frequencies of poor engineering interest. Alternatively, they could be considered by mode superposition. We compute the acceleration time series expected on the top of the cabin for the selected input earthquake (red curves in Figure 174a) by means of the Newmark integration approach (e.g., in Clough and Penzien, 1975).

From the T/P ratio in Figure 171 we know the fraction of the cabin motion transmitted to the pillar at all frequencies (e.g., 1/8 for the fundamental frequency), at least under ambient noise excitation. We can thus estimate the free-field motion that would be recorded by the seismometer on the pillar (cyan lines in Figure 174b). This calculation is not conservative, in the sense that under non-linear behavior it could underestimate the real impact.

We now compute the response spectra of the same input earthquake as it would be computed from the pillar recording and from the free-field recording, and compare them in Figure 174c. The response spectrum calculated from the signal collected on the pillar, P , is much larger than the response spectrum computed from the free-field signal (S) at periods close to the natural periods of the housing.

In Figure 174d, e, f we show the same procedure applied to the FRN station (Figure 170). Since the FRN housing eigen-frequencies are lower than the MRN ones (5 Hz vs 10 Hz), the effect on the response spectrum is expected at larger periods, as it is in panel f.

Beyond the hypotheses and assumptions, these examples show that the response spectra computed from a recording performed on a pillar influenced by the surrounding structure can be severely affected at periods close to the structure eigen-period. PGA is also affected but to a minor extent (cyan, P , vs black, S , curves in Figure 174b, e).

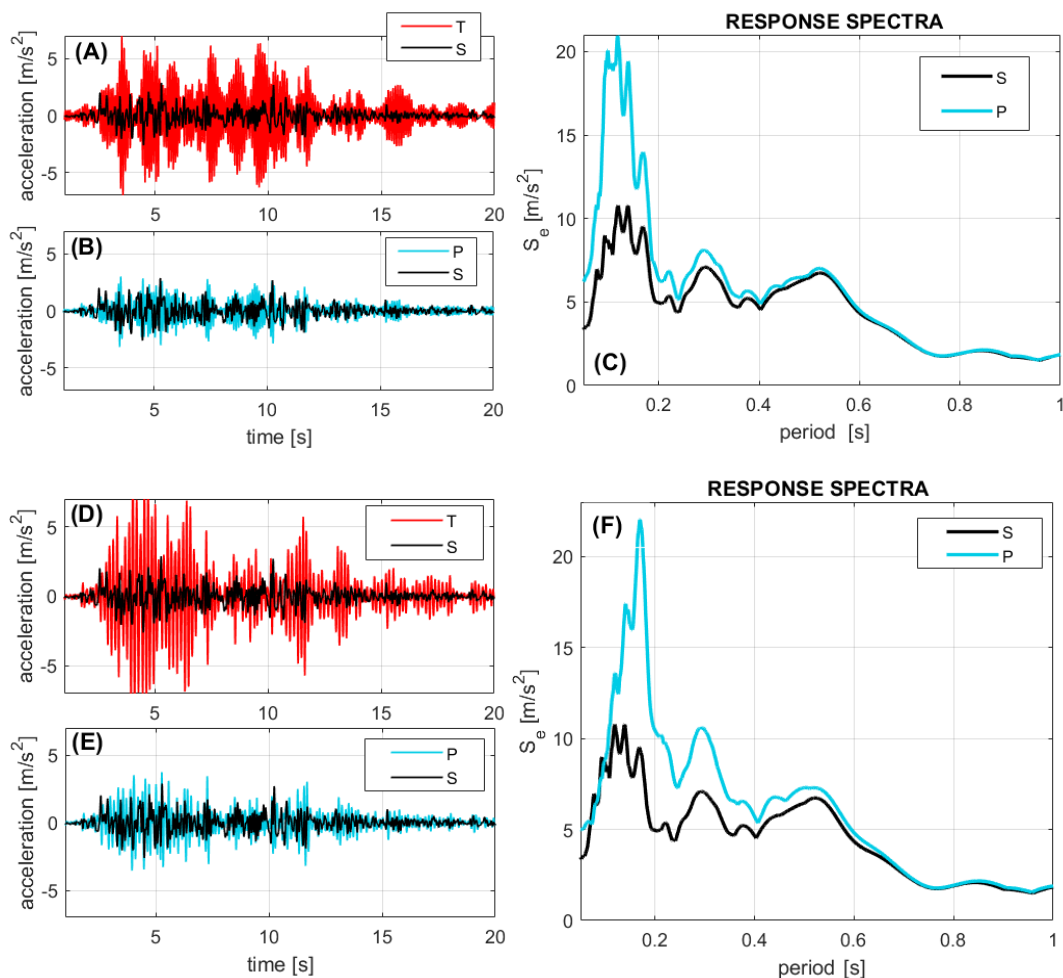


Figure 174. Free-field earthquake records and response spectra (S , black) compared to those recorded on the top of a seismic station (T , red) and on the pillar inside the station (P , cyan). Panels a , b , c refers to the MRN station. Panels d , e , f to the FRN one.

The results above come from models as no earthquake recordings were available on the top of the station, on the pillar and on the surrounding real free-field conditions at the same time. However, to reproduce these findings with real data, we used ambient noise recordings acquired simultaneously on the pillar and on the garden surrounding the MRN station. As it can be seen in Figure 175, the response spectrum computed from the ambient noise recording acquired on the pillar (cyan) shows the resonance modes of the cabin at 0.06 and 0.1 s (16 and 10 Hz) as dominant peaks, while this is not the case for the response spectrum from ambient noise acquired on the garden surrounding the structure. The two response spectra, in general, are very different.

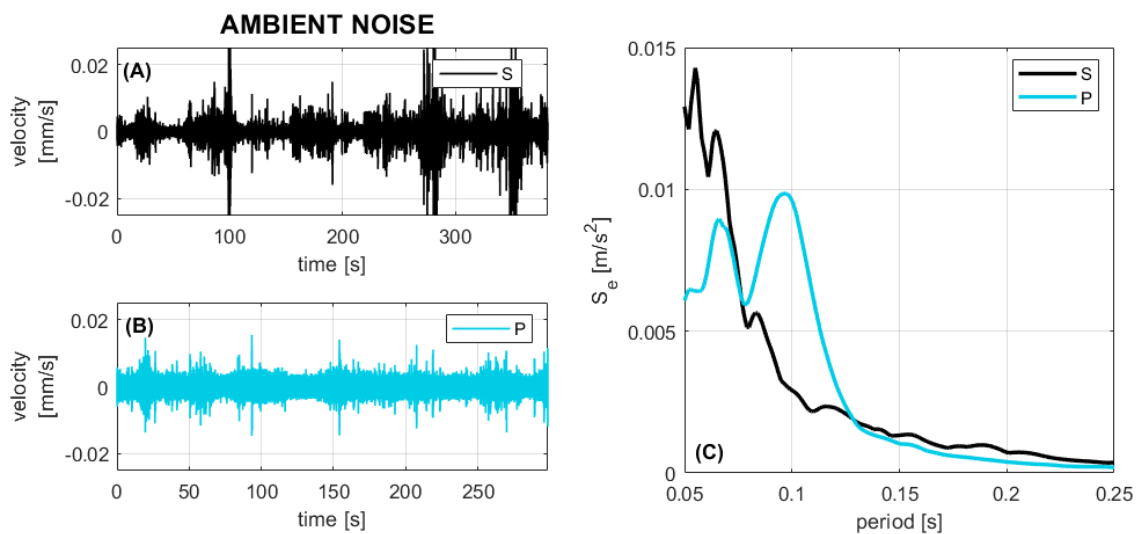


Figure 175. Ambient noise recording acquired in (A) free-field conditions, (B) on the station pillar and response spectra in the two cases (C) for the MRN station.

The foundation effect

General issues

After the initial installations on rock, in more recent times seismic stations started to be installed on soft sedimentary covers, both to improve the spatial coverage of seismic networks as well as to capture the so-called seismic site effects (stratigraphic amplification, resonances, etc.). However, the standards of seismic installations (concrete slabs or pillars inside the foundations of hosting structures), did not vary with the underground geology and seismic stations keep on being installed following the original principles.

When an interface has to be placed between the object to measure and the measurement device, the impedance between the interface and the object to measure must be as close as possible, to avoid

modifications of the signal due to the interface. This is well acknowledged in the down-hole and cross-hole seismic testing, where, according to ASTM D7400/D7400M-19, the plastic hole casing must be coupled to the ground by using a filling material with seismic impedance as close as possible to the ground itself. On the opposite, this seems to be completely disregarded in seismic station installations. However, while a concrete slab over stiff rocks is theoretically not expected to perturb seismic waves in a significant way, being the rock-to-concrete transition virtually continuous, a concrete slab on soft sediments is expected to perturb seismic waves significantly.

Foundations can be thought as stiff artificial layers that, when overlying softer ones, configure a 'velocity inversion'. This effect on microtremors was largely discussed in Castellaro and Mulargia (2009). They showed both empirically and analytically that whenever a stiffer layer overlies softer ones, the spectra recorded on the stiff layer show deamplified horizontal components compared to the case with no velocity inversion. The vertical component is generally less affected, to the point that a velocity inversion is typically marked by H/V ratios persistently lower than 1.

When a seismic wave hits a stiffer interface, the reflection coefficient is larger than the transmission coefficient (Zoeppritz, 1919). With reference to the red dots in Figure 169:

- 1) incoming surface waves hitting the foundation are reflected backwards and only a fraction of the incoming waves propagate through the medium, from point 1 to 3,
- 2) body waves travelling from the bottom to the surface are identically reflected downwards and only a fraction of the incoming wave propagates from point 2 to 3,
- 3) the foundation generates a velocity inversion, which inhibits the existence of the fundamental mode of Love waves (Castellaro, 2016b).

The waves affected by the aforementioned phenomena are, dominantly, those with wavelengths 2λ comparable to or smaller than the foundation dimensions. The real effect is however more extensive and complex (see references in the Introduction).

A decay in the horizontal spectra recorded on the foundation or pillar (F, R, P sites in Figure 169) compared to the real free-field conditions (site S in Figure 169) is thus expected and effectively measured. This effect can easily be observed by taking two short measurements one on the foundation/pillar and one on the natural soil just around the foundation, as we are going to show.

Phenomenological evidence

We consider the ALF and MRN seismic stations (Figure 169) and compare the spectra of the recordings taken on the pillar (P), on the foundation (F), on the foundation rim (R) and on the natural soil just outside the station (S), at the same time (Figure 176). We clearly see that while moving from the foundation center to its rim, to the natural soil, the amplitude of the horizontal spectra significantly increases. The effect is clear from 4 Hz and 10 Hz upwards, for ALF and MRN respectively, and essentially depends on the foundation width, more than on its thickness (Castellaro and Mulargia, 2009). Again, there is no significant difference between the motion acquired on the pillars – just theoretically but not effectively isolated from the rest of the foundation – and the motion on the foundation. They both severely alter the recorded motion, compared to the soil one, of a factor up to 10 times in amplitude.

In Figure 176 (gray arrows) we clearly see that the F, P, R spectra are also severely affected by the natural frequencies of the housings (4 Hz for ALF and the already mentioned 10 Hz for MRN).

The foundation effect (decay in the horizontal spectral components) and the housing effect (peaks of increased amplitude in the horizontal components at the eigen-frequencies of the housing) overlap and are both present in the foundation (F) and pillar (P) recordings.

To stress out that this issue is not typical only of foundations on soft soils, in Figure 177 we present the H/V curves acquired on a seismic station in Bulgaria (Sofia) installed inside a tunnel in rock (granite). The acquisition performed on the rock shows a flat H/V with amplitude equal to 1, as expected. The acquisition performed on the concrete platform constructed to host a number of instruments on the rock, shows a significantly deamplified H/V ratio from 7 Hz upwards, due to the deamplification of the horizontal components.

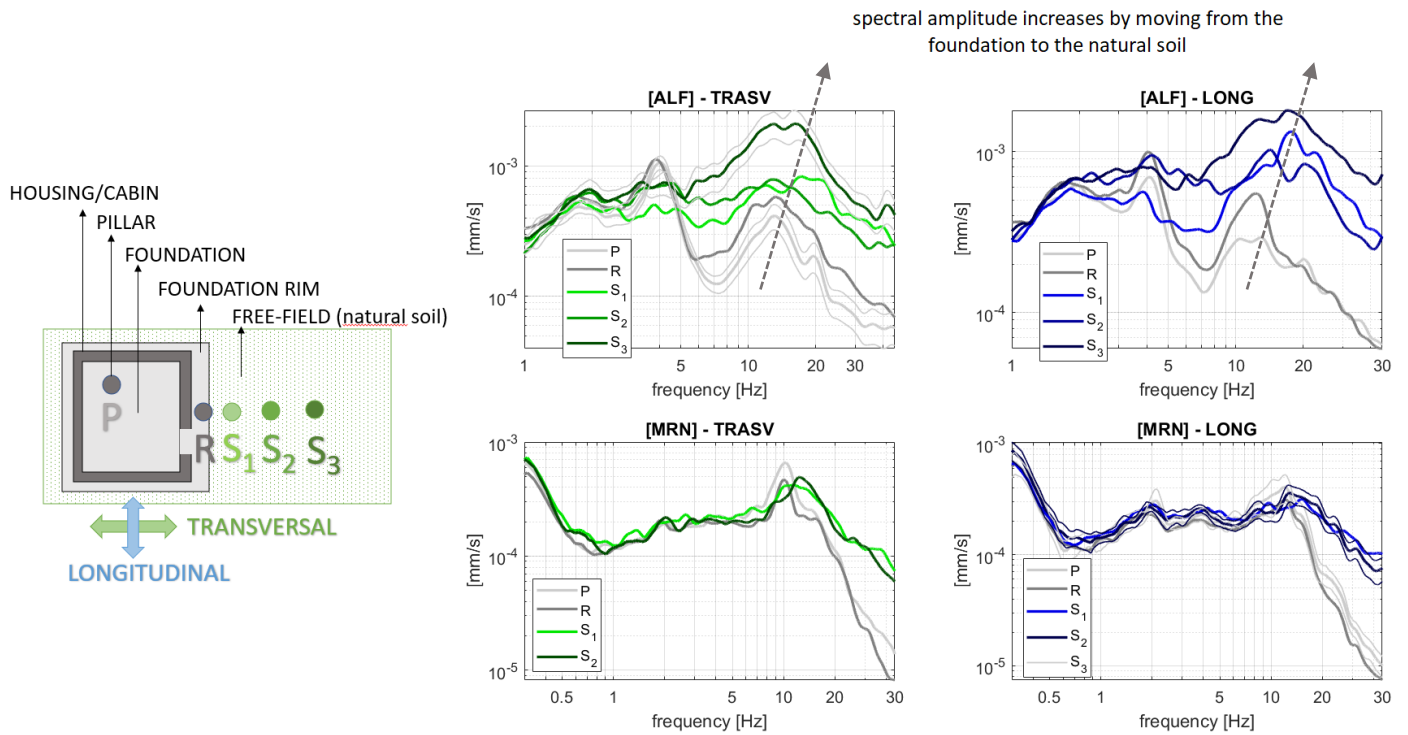


Figure 176. Velocity spectra recorded at different sites at the ALF and MRN sites, by moving from the pillar to the foundation to the surrounding soil. Both the housing effect (peaks at 4 Hz for ALF, at 10 Hz for MRN) and the foundation effect (deamplification of the horizontal components of motion at P and R compared to the soil sites S) are visible. The standard deviation of the spectra is shown only in some extreme cases, not to impair the readability of the plots. Its amplitude is approximately the same also when not shown.

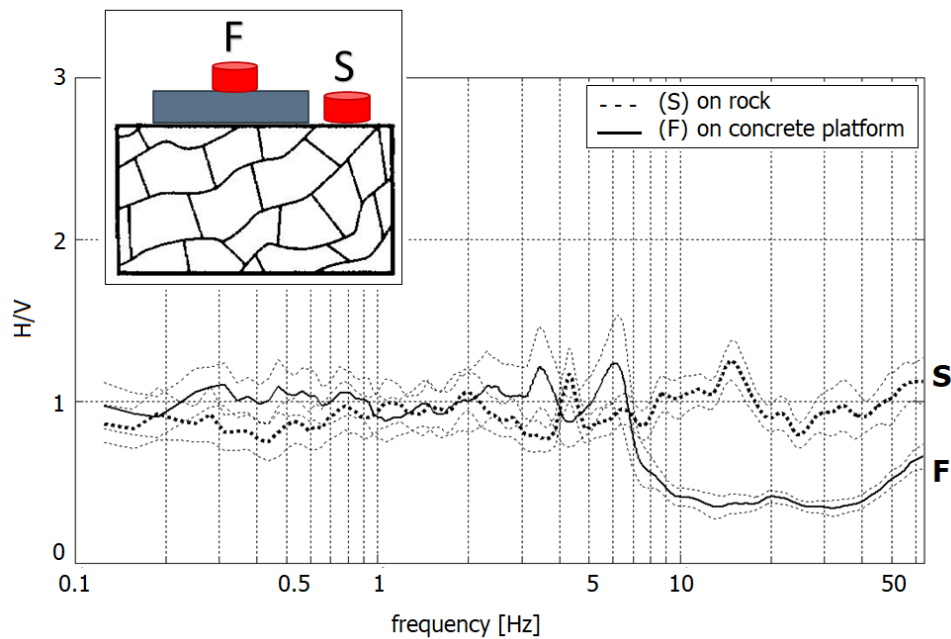


Figure 177. Microtremor H/V ratio recorded on a granite rock (dashed line) and on a concrete slab on the rock (black line). The concrete platform, being stiffer than the rock, produces a deamplified H/V curve at frequencies larger than 7 Hz.

Other possible consequences

The deamplification of the horizontal components (H) due to a stiff foundation might sometime lead to the wrong conclusion that the dominant component of motion during an earthquake is the vertical one (V). By analyzing 123 response spectra of motion recorded at 41 alluvial sites, Bozorgnia *et al.* (1995) noted that the H/V spectral ratios of motion were well below the assumed 1 to 2/3 value at frequencies larger than 6-10 Hz. This is reported to be common in the near field (Chopra, 1966), but this could also be partly or fully explained by the fact that near earthquakes are rich in high frequencies and that seismic installations – particularly those settled on soft soils – modify the seismic input at high frequency, specifically decreasing its H/V ratio.

Luzi *et al.* (2013) observed that, during the May 20th 2012 Mw 5.9 earthquake, the closest-to-the-epicentre MRN station recorded a vertical acceleration larger than the horizontal ones (Figure 178). A number of authors mentioned this as one of the reasons for many of the observed collapses (Vannucchi *et al.*, 2012; Romeo, 2012; Ercolino *et al.*, 2012; Andreini *et al.*, 2014; Decanini *et al.*, 2012; Carydis *et al.*, 2012). It is true that the Peak Ground Acceleration (PGA) recorded by the MRN station occurred in the vertical component (Figure 178 top line), but the earthquake spectra (Figure 178 bottom line) show that the vertical component was larger than the horizontal ones only at frequencies larger than ≈ 10 Hz.

This very same pattern ($H/V < 1$ at $f > 10$ Hz) is visible in the microtremor H/V spectra collected on the station pillar but it is no more visible in the recordings collected at just 2 m distance from the station, in real free-field conditions (Figure 179). We thus propose that in the case of this earthquake the dominant vertical component of PGA was possibly not a real feature of the earthquake, but once more an artifact induced by the foundation around the seismic sensor, that strongly deamplified the high frequency horizontal components.

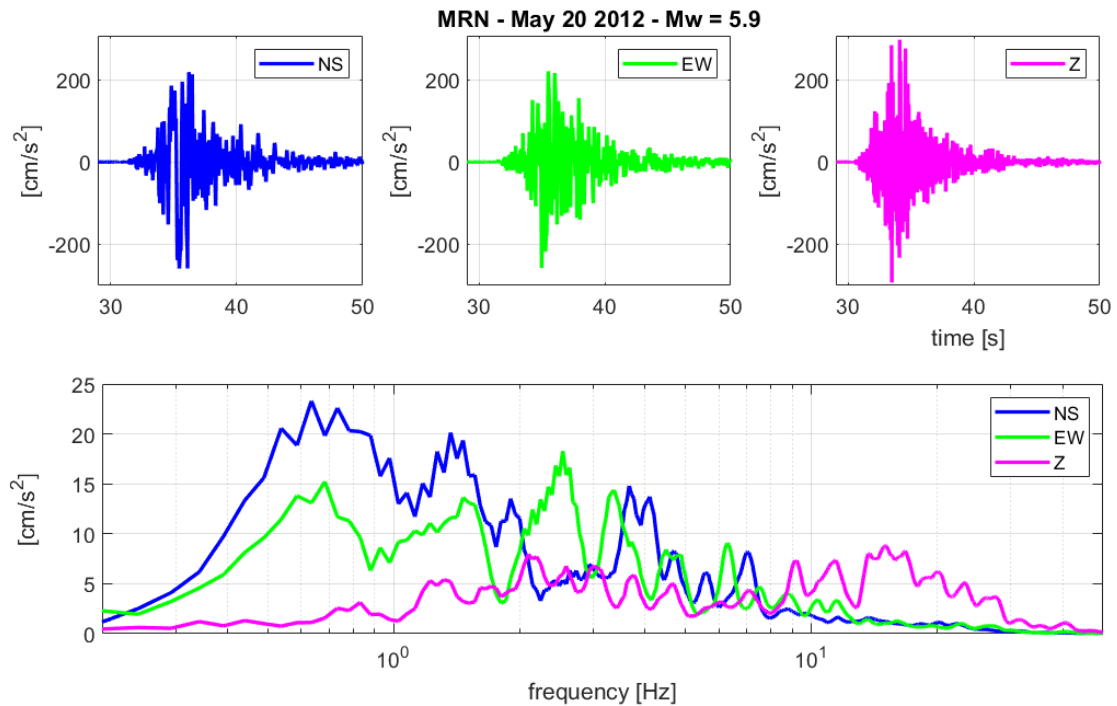


Figure 178. 3C recordings of the Mirandola May 20th 2012 earthquake recorded at the MRN station. Top: time series. Bottom: acceleration amplitude spectra.

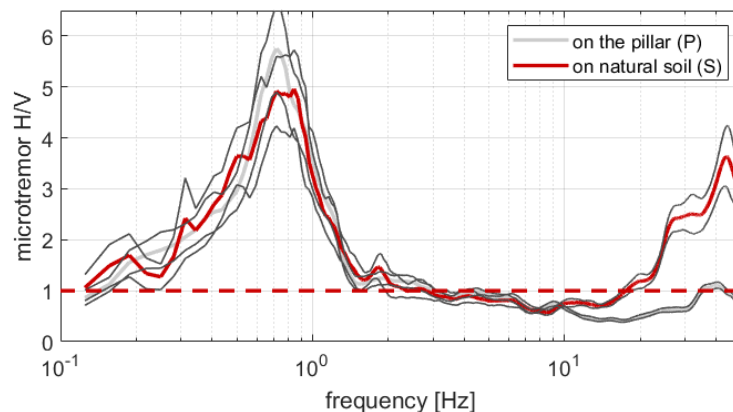


Figure 179. Microtremor H/V ratios recorded at the MRN station on the pillar (P) and in free-field (S). The foundation effect is clear at frequencies larger than 10 Hz.

The pillar effect

As anticipated, the intention of letting the seismometers be independent from the surrounding housings led to the cut of the foundations and to the construction of pillars, directly set into the ground in the middle or on the corner of foundations (Figure 169, MRN in Figure 170). Pillars are typically cylinders of 0.6 m diameter and 1.5 m height, set into the ground for at least 0.5 m. As seen, this cut is not much effective because the structure and the pillar are rooted on the same soil and the transmission of the reciprocal motion is warranted by the soil itself.

Another potential problem emerges. Also pillars have their own vibration modes that are certainly recorded by the sensor applied on their top. Do these modes occur at frequencies of engineering interest? Concrete pillars typically installed in seismic stations are ‘beams’ dominated by shear, rather than flexural deformation and their eigen-modes are expected to occur at several tens of hertz, well beyond the range of interest in engineering seismology.

By using the FE numerical tools Ansys Academy 2020R1, we modelled a pillar with the dimensions given above, density $\rho = 2.4 \cdot 10^3 \text{ kg/m}^3$, Young modulus $E = 30 \text{ GPa}$, stuck for 0.5 m into a soil with $\rho = 2 \cdot 10^3 \text{ kg/m}^3$, $E = 45 \text{ MPa}$, $V_s = 150 \text{ m/s}$ (Figure 180). By applying an impulse in horizontal direction with $V_0 = 1 \text{ m/s}$ and observing the free oscillations, we found that the eigen-frequency of the pillar is 28 Hz. This is hard to measure in real cases because the pillars are thick and the displacement under microtremor very weak, however we can expect that on average this kind of pillars vibrates at frequencies around 30 Hz and this value increases if, e.g., they are stuck at shallower depth.

It can be expected that the pillar moves independently from the foundation during an earthquake. However, the reduction in the horizontal components due to the foundation effect on surface waves still exist, as well as the transmission of the housing eigen-modes through the soil, as we have shown in the previous examples.

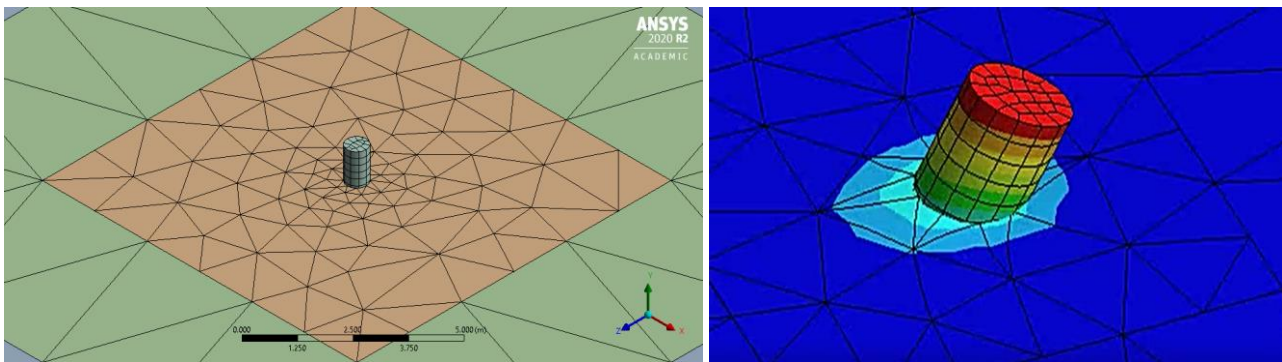


Figure 180. FE model of a homogenous pillar stuck into a soft soil.

Diffusion and identification of the problem

We estimated that as of 2021, in Italy, at least 35% of the ≈ 600 accelerometric IT stations are hosted inside 4-5 m side, 7-9 m height towers of the electrical national service (Figure 181). A further 3% are hosted in other types of buildings and 18% inside minihouses, that is structures like the MRN case we discussed. Most of them is also settled on soft soils (C, D, E categories according to EC8), where

soil-structure interaction is expected to be large. We thus expect that the aforementioned issues affect at least half of the accelerometric IT Italian network (clearly with different severity according to the specific conditions), but this is certainly not an issue restricted to Italy (see also Hollender *et al.*, 2020).

We propose a simple way to identify the existence of a potential installation-induced problem and assess the range of fidelity of the response of a seismic station to the ground motion. The approach is based on the following actions:

- 1) take a recording on the top of the seismic cabin (T) to identify its natural frequency,
- 2) take a set of simultaneous recordings on the pillar (P), on the foundation (F) and under truly free-field conditions (S). We are aware that at some sites a 'truly free-field' condition cannot even be achieved. We also warn that 'simultaneous' here means just at the same time but with no need for a real synchronization of all instruments, as no phase but only amplitude spectra are analyzed,
- 3) compare T and P (or T and F) spectra: these will immediately reveal the degree of rocking of the housing and tell what fraction of the housing motion is radiated to the foundation under weak motion,
- 4) compute the F/S or P/S spectral ratios. This will reveal to what extent the sensors placed on the foundation/pillar record a deamplified horizontal motion compared to the real free-field conditions and in what frequency interval. Expect that the larger the foundation size, and the softer the soil compared to the foundation, the larger the frequency interval affected by these issues.

We warn that the recordings to assess the structure eigen-frequencies (item 1) should be done along the structural main axes, but these may not coincide with the NS-EW axes of the seismometer/accelerometer installed inside the structure. In this case, *ad hoc* axis rotations should be performed.

We also warn that in order to perform the comparisons above, some spectral smoothing is mandatory but this should not exceed a few percent of the central frequency otherwise the spectral peaks due to the housing eigenmodes will appear less clear.

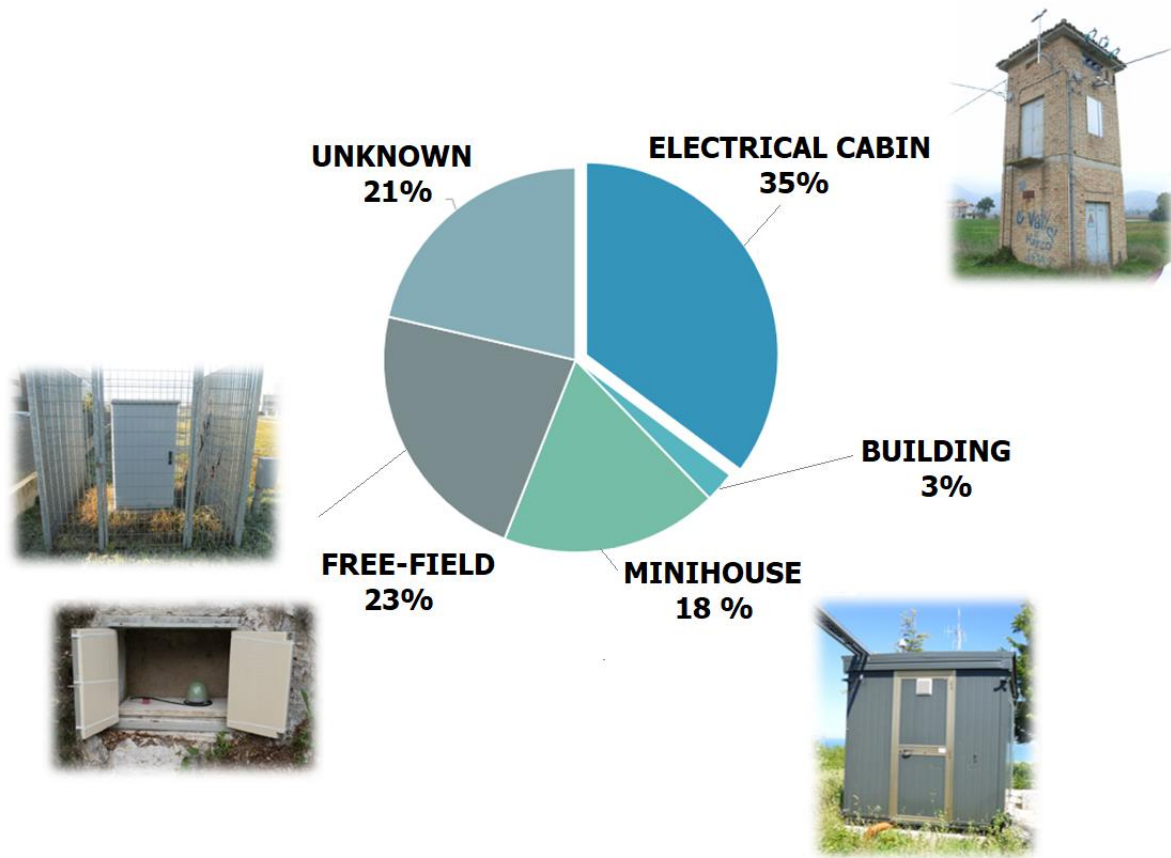


Figure 181. Percentage of the seismic installations of the Italian accelerometric network, as of 2021.

Discussion and Conclusions

Bormann *et al.* (2002, chapter 7) wrote that seismic site selection is not often given the amount of study it requires. Maybe also the hosting structure is not given the consideration it requires (Hollender *et al.*, 2020) as the design and construction of seismic stations has not much evolved over time.

The presence of a structure around an instrument perturbs the recorded motion in three ways.

The first one is the transmission of the structure own motion to the foundation and the surrounding ground. Sensors placed inside the structure record, therefore, a composite signal, made of seismic waves and of the response of the structure to them. We showed that cutting the foundation around the sensor pillars gives no benefits in isolating the sensor from the housing motion, as the vibrations are transmitted in a very efficient way through the common soil.

The second effect is that a foundation, typically made of reinforced concrete, acts as a layer with seismic impedance much higher than any natural soil. Seismic waves travelling upwards and surface waves striking an extended rigid layer like a foundation, will be mostly reflected downwards

or backwards as they hit the foundation. They will shake the structure, but only a small fraction of them will cross the foundation and will be recorded by the instruments installed on the foundation. Foundations violate the principle of physical measurements according to which when an interface is needed between an instrument and the object of measurement (the ground) then the interface must have an impedance as close as possible to the object of measurement, to minimize the perturbation of the wavefield. Concrete slabs/pillars do not have this property, not even always when installed on very stiff rock.

As a consequence, in seismic tremor or seismic events recordings carried out inside a structure, a fraction of waves is missing.

The third issue is related to the pillar that can alter the recorded motion by means of its own eigenmodes. This effect, however, is mostly confined to frequencies beyond the range of engineering interest.

We noted that particularly the first problem can affect even the modern fibre-glass installations since their smaller mass and stiffness combination turns into natural frequencies of vibration still falling within the range of engineering interest. Fiber-glass cabins are also often hosted on large concrete slabs where other instruments (typically meteorological) are installed. This makes the frequency interval, where deamplification of horizontal motion recorded by the seismometer is measured, wider.

Installing seismic stations inside structures does not affect the earthquake magnitude estimates, that are usually performed at very long periods and does not affect the hypocentral estimates, which are based on the arrival times of specific waves.

However, even by excluding the installations inside proper buildings, the soil-structure interaction at the seismic stations can, in our experience, produce artefactual patterns at least down to 2 Hz, (this depends on the size and properties of the housing). The influence of the cabin self-modes on the recordings also leads to artefactual spikes in the response spectra typically on the plateau. The opposite (a reduction in the response spectra) effect is expected because of the velocity inversion induced by the foundation.

Besides the fact that these two effects can partly compensate in the response spectra, an issue remains about the reliability of the motion recorded from the seismic stations at high frequency. This bias has consequences in the assessment of seismic site effects in terms of PGA, on the computation of

attenuation laws and ground motion prediction equations but probably also on the often observed unexpected large vertical motion compared to the horizontal one during earthquakes.

In conclusion, we believe that besides the parameters (V_{s30} , soil classes etc.) that start to be routinely introduced in the seismic archives, assessing the maximum reliable frequency f_{max} of earthquake and microtremor recordings (under which no soil-structure interaction is expected) is a mandatory step. To this aim, it should also be reminded that due to the possible non-elastic behavior under strong motion, such f_{max} established under weak motion could even be overestimated. This is because the eigen-frequencies of structures under strong-motion can be lower than under ambient noise excitation again due to the soil-structure interaction. We provided a simple scheme to assess this maximum reliable frequency f_{max} .

Data and Resources

The data collected at the seismic station installations were collected by the authors and by those mentioned in the acknowledgments. The accelerometric records used in this paper were provided by ITACA (D'Amico *et al.*, 2020).

Declaration of Competing Interests

The authors acknowledge there are no conflicts of interest recorded.

Acknowledgments

We thank Giovanni Lattanzi for Figure 1, Martina Delvecchio and Anna Ferrara for the computations used to build Figure 181, Antonella Gorini from Dipartimento della Protezione Civile for providing access to the MRN station and the two workers from ENEL who assisted us during the measurements. We thank Alfredo Pitullo and the Consorzio per la Bonifica della Capitanata (Contratto di Consulenza Commissionata tra Consorzio per la Bonifica della Capitanata e Dipartimento di Fisica e Astronomia dell'Alma Mater Studiorum – Università di Bologna 2019-2021) for funding some of the presented surveys. We thank Umberto Borgia, Luigi Perricone and Riccardo Panzeri for their help, in 2014, in collecting many of the measurements here presented, in the frame of the DPC-INGV-S2-2014 Project “Constraining Observations into Seismic Hazard”, which is here

acknowledged, too. Long time has passed since then, but the memory of those days is still alive. Thank you.

References

- Andreini, M., A. De Falco, L. Giresini L., M. Sassu (2014). Structural damage in the cities of Reggiolo and Carpi after the earthquake on May 2012 in Emilia Romagna, *Bull. Earthquake Eng.* **12** 2445-2480.
- Bormann, P. (2012). New Manual of Seismological Observatory Practice (NMSOP-2), Potsdam: Deutsches GeoForschungszentrum GFZ; IASPEI <https://doi.org/10.2312/GFZ.NMSOP-2>
- Bozorgnia, Y., M. Niazi, K.W. Cambell (1995). Characteristics of Free-Field Vertical Ground Motion during the Northridge Earthquake, *Earth. Spectra* **11** 515-525.
- Bycroft, G.N. (1977). Soil-structure interaction at higher frequency factors, *Earthq. Eng. Struct. Dyn.* **5** 235-248.
- Bycroft, G.N. (1980). Soil-foundation interaction and differential ground motions, *Earthq. Eng. Struct. Dyn.* **8** 235-248.
- Castellaro, S. (2016a). Soil and structure damping from single station measurements, *Soil Dyn. Earthq. Eng.* **90** 480-493.
- Castellaro, S. (2016b). The complementarity of H/V and dispersion curves, *Gephysics* **81** T323-T338.
- Castellaro, S., F. Mulargia (2009). The effect of velocity inversions on H/V, *Pure and Applied Geophysics* **166** 567-592.
- Castellaro, S., F. Mulargia (2010). How far from a building starts the tremor free-field? The case of three most famous Italian towers and of a modern building, *Bull. Seism. Soc. Am.* **100** 2080-2094.
- Castellaro, S., L.A. Padron, F. Mulargia (2013). The different response of apparently identical structures: a far-filed lesson from the Mirandola 20th May 2012 earthquake, *Bull. Earthq. Eng.*, **12**, 2481-2493.
- Cavaliere, F., A.A. Correia, R. Pinho, (2021). Variations between foundation-level recordings and free-field earthquake ground motions: numerical study at soft-soil sites, *Soil Dynamics and Earthquake Engineering* **141** 106511.
- Carydis, P., C. Castiglioni, E. Lekkas, I. Kostaki, N. Lebesis, A. Drei (2012). The Emilia Romagna, May 2012

- earthquake sequence. The influence of the vertical earthquake component and related geoscientific and engineering aspects, *Ingegneria Sismica* **2-3**, 31-58.
- Chavez-Garcia, F.J., M. Cardenas-Soto (2002). The contribution of the built environment to the free-field ground motion in Mexico City, *Soil Dyn. Earthq. Eng.* **22** 773–780.
- Chopra, A.K. (1966). The importance of the vertical component of earthquake motions, *Bull. Seism. Soc. Am.* **56** 1163-1175.
- Clough, R.W., J. Penzien (1975). *Dynamics of structures*, Mc-Graw Hill.
- Clouteau, D., D. Aubry (2001). Modifications of the ground motion in dense urban areas, *J. Computational Acoustics* **9** 1659-1675.
- Cornou, C., P. Guéguen, P.-Y. Bard, E. Haghshenas (2004). Ambient noise energy bursts observation and modeling: Trapping of harmonic structure-soil induced-waves in a topmost sedimentary layer, *J. Seismol.* **8** 507–524.
- Crouse, C.B., B. Husmand (1989). Soil-structure interaction at CDMG and USGS accelerograph stations, *Bull. Seismol. Soc. Am.* **79** 1–14.
- Cultrera, G., C. Cornou, G. Di Giulio, P.-Y. Bard (2021). Indicators for site characterization at seismic station: recommendation from a dedicated survey, *Bull. Earthquake Eng.* **19** 4171–4195
- D'Amico, M.C., C. Felicetta, E. Russo, S. Sgobba, G. Lanzano, F. Pacor, L. Luzi (2020). Italian ACcelerometric Archive (ITACA), version 3.1, Istituto Nazionale di Geofisica e Vulcanologia (INGV) <https://doi.org/10.13127/itaca.3.1>
- Decanini, L.D., D. Liberatore, L. Liberatore, L. Sorrentino (2012). Preliminary Report on the 2012, May 20, Emilia Earthquake, v.1, <http://www.eqclearinghouse.org/2012-05-20-italy-it/>
- Ditommaso, R., M.R. Gallipoli, M. Mucciarelli, F.C. Ponzio (2010a). Effect of a single vibrating building on free-field ground motion: numerical and experimental evidences, *Bulletin of Earthquake Engineering* **8** DOI: 10.1007/s10518-009-9134-5.
- Ditommaso, R., S. Parolai, M. Mucciarelli, S. Eggert, M. Sobiesiak, J. Zschau (2010b). Monitoring the response and the back-radiated energy of a building subjected to ambient vibration and impulsive action: the Falkenhof Tower (Potsdam, Germany), *Bulletin of Earthquake Engineering* **8** DOI: 10.1007/s10518-009-9151-4.
- Ercolino, M., G- Magliulio, G. Manfredi (2016). *The lesson learnt after Emilia-Romagna earthquakes on precast RC structures: a case-study*, 1st International Conference on Natural Hazards & Infrastructure
28-30 June, Chania, Greece.

- Gallipoli, M.R., M. Mucciarelli, R.R. Castro, G. Monachesi, P. Contri (2004). Structure, soil-structure response and effects of damage based on observations of horizontal-to-vertical spectral ratios of microtremors, *Soil Dyn. Earthq. Eng.* **24** 487-495.
- Gallipoli, M.R., M. Mucciarelli, F. Ponzio, M. Dolce, E. D'Alema, M. Maistrello (2006) Buildings as a seismic source: analysis of a release test at Bagnoli, Italy, *Bull. Seism. Soc. Am.* **96** 2457- 2464.
- Guéguen, P., P.-Y. Bard, C.S. Oliveira (2000). Experimental and numerical analysis of soil motion caused by free vibration of a building model, *Bull. Seism. Soc. Am.* **90** 1464-1479.
- Guéguen, P., P.-Y. Bard, F.J. Chavez-Garcia (2002). Site-city seismic interaction in Mexico Citylike environments: An analytic study, *Bull. Seism. Soc. Am.* **92** 794- 811.
- Guéguen, P., P.-Y. Bard (2005). Soil-structure and soil-structure-soil interaction: experimental evidence at the Volvi test site, *J. Earthq. Eng.*, **9**, 657–693.
- Hollender, F., Z. Roumelioti, E. Maufroy, P. Traversa, A. Mariscal (2020). Can we trust high-frequency content in strong-motion database signals? Impact of housing, coupling, and installation depth of seismic sensors, *Seismological Research Letters* **91** 2192-2205.
- Isbiliroglu, Y., R. Taborda, J. Bielak, (2015). Coupled Soil-Structure Interaction Effects of Building Clusters during Earthquakes, *Earthq. Spectra* **31** 463-500.
- Jennings, P.C. (1970). Distant motion from a building vibration test, *Bull. Seism. Soc. Am.* **60** 2037-2043.
- Kham, M., J.-F. Semblat, P.-Y. Bard, P. Dangla. (2006). Seismic site–city interaction: main governing phenomena through simplified numerical models, *Bull. Seism. Soc. Am.* **96** 1934-1951.
- Kumar N., J.P. Narayan, 2018. Quantification of site–city interaction effects on the response of structure under double resonance condition, *Geophysical Journal International* **212** 422–441.
- Laurenzano, G., E. Priolo, M.R. Gallipoli, M. Mucciarelli, F.C. Ponzio (2010). Effect of vibrating buildings on free-field motion and on adjacent structures: the Bonafro (Italy) case history, *Bull. Seism. Soc. Am.* **100** 802-818.
- Luco, J.E., J.G. Anderson, M. Georgevich (1990). Soil-structure interaction effects on strong motion accelerograms recorded on instrument shelters, *Earthq. Eng. Struct. Dyn.* **19** 119-131.
- Luco, J., H.L. Wong (1986). Response of a rigid foundation to a spatially random ground motion, *Earthq. Eng. Struct. Dyn.* **14** 891-908.

- Luzi, L., F. Pacor, G. Ameri, R. Puglia, P. Burrato, M. Massa, P. Augliera, G. Franceschina, S. Lovati, R. Castro (2013). Overview on the Strong-Motion Data Recorded during the May–June 2012 Emilia Seismic Sequence, *Seismological Research Letters*, **84** 629-644.
- Massa, M., S. Marzorati, C. Ladina, S. Lovati (2010). Urban seismic stations: soil-structure interaction assessment by spectral ratio analyses, *Bull. Earthquake Eng.* **8** 723–738.
- Mucciarelli, M., M.R. Gallipoli, F.C. Ponzio, M. Dolce (2003). Seismic waves generated by oscillating building, *Soil Dyn. Earthq. Eng.* **23** 255-262.
- Romeo, R. (2012). Emilia (Italy) M5.9 earthquake on 20 May 2012: an unusual pattern of liquefaction, *Italian J. Eng. Geol. Environ.* **2** 75-84.
- Şafak, E. (1998), New approach to analyzing soil-building systems, *Soil Dyn.and Earthq. Engin.* **17** 509-517.
- Schwan, L., C. Boutin, L.A. Padron, M.S. Dietz, P.-Y. Bard, C. Taylor (2016). Seismology Site-city interaction: theoretical, numerical and experimental crossed-analysis, *Geophys. J. Int.* **205** 1006–1031.
- SESAME (2004). Guidelines for the implementation of the H/V spectral ratio technique on ambient vibrations: Measurements, processing and interpretation, SESAME European Research Project WP12, deliverable no. D23.12, http://sesame.geopsy.org/Delivrables/D08-02_Texte.pdf.
- Sotiriadis, D., N. Klimis, B. Margaritis *et al.*, 2019. Influence of structure–foundation–soil interaction on ground motions recorded within buildings *Bull. Earthquake Eng.* **17** 5867–5895.
- Vannucchi, G., T. Crespellani, J. Facciorusso, A. Ghinelli, C. Madaia, A. Puliti, S. Renzi (2012). Soil liquefaction phenomena observed in recent seismic events in Emilia-Romagna Region, Italy, *Ingegneria Sismica* **2-3** 20-29.
- Wirgin, A., P.-Y. Bard (1996). Effects of building on the duration and amplitude of ground motion in Mexico City, *Bull. Seism. Soc. Am.* **86** 914-920.
- Wong, H.L., M.D. Trifunac (1975). Two dimensional antiplane building-soil-building interaction for two or more buildings and for incident plane SH waves, *Bull. Seismol. Soc. Am.* **65** 1863-1865.
- Zoepprtiz, K. (1919). On reflection and propagation of seismic waves, *Gottinger Nachrichten* **1** 66-84.